DEGREE PROJECT

Advanced system integration of hydrogen production in Stockholm

A case study of Stockholm Exergi

Sustainable Energy Engineering, master's level
2023

Luleå University of Technology
Department of Engineering Sciences and Mathematics

LULEÅ UNIVERSITY OF TECHNOLOGY

[This page intentionally left blank]

Acknowledgement

I want to hereby thank my academic supervisor Professor Andrea Toffolo and supervisor Erik Dahlen for guidance, presenting excellence in the field of energy engineering.
In addition to official supervision, I want to thank Ph.D. Fabian Levihn, for the insight of economic performance, and Professor Kentaro Umeki for feedback regarding gasification processes, who initiated my interest in power plant engineering with mathematical simulations in the first place.

I also want to thank Stockholm Exergi for the opportunity to investigate and contribute, to the development affirming climate action in the nation's interest.

Fred Goldbech Birath,
In pursuit of Title: Master of Science in Sustainable Energy Engineering.

Abstract

The production of electrofuels is becoming a desired part of the transition toward the target of emission neutrality. In this thesis, a techno-economic analysis regarding the opportunities for system integration of hydrogen production is completed.

The mapping of production methods in an urban environment is investigated, with the combination of district heating and power production services. By co-production of products valuable for the current energy system, process design, and mathematical programming are utilized to create physically applicable models for Stockholm Exergi´s existing plants, where placement is estimated as feasible. Empirical theory with kinetic models is applied, calculating the gasifier plant processes C/BFB and FB, accounting for diffusivity, geometry, particle model, or other aspects influencing the reaction. EF is handled with only basic calculation since modeling the reaction in detail comes with uncertainties. The analysis of electrolysis explores the time, membrane, and temperature-derived interference with production.

Full utilization of by-products in combination with CCS, heating of return water, and CCU is investigated and valued in order to calculate the economical performance of each proposed model. In addition, the boilers residing in Värtahamnen, Högdalen, and Brista are modeled to connect to the proposed hydrogen production, thus the technical feasibility is determined. It can be concluded that all proposed models work without any major technical penalty to the current system in theory.

An economical benchmarking is performed by comparing the technologies independently. By using the resulting economic performance indicators, it can be concluded that the CFB gasifier replacing the existing boiler P3, render the most profitable overall, presenting an NPV of 4087.6 MSEK and IRR of 53%, with a total investment of 628.4 MSEK. Regarding electrolyzers, the AEL platform with a fuel cell is the most profitable, rendering an NPV of 667.4 and IRR of 48%, while having a total investment cost of 131.6 MSEK. The sensitive analysis performed showcases a similar result, as the CFB gasifier is the most prominent choice.

Strategical analysis showcases the supply dynamics of constructed plants over time, indicating the compatibility of integration in the current system. The supply of district heating, balancing services, and hydrogen storage are quantified as part of the strategic analysis. The result indicates that the reliability of the gasification system is higher than electrolysis, except if PPA is utilized, generating a constant supply of product from the electrolyzer. Utilization of PPA, restricted fuel cell usage, and alternative configuration of the electrolyzer platform are investigated as part of the sensitivity analysis to evaluate the most cost-efficient operation method.

The conclusion of all results indicates that hydrogen production is feasible, economically beneficial, and promotes the utilization of CCS, in the case of Stockholm Exergi.

.

Contents

Nomenclature

AEL	Alkaline electrolyzer
aFRR	Automatic frequency restoration reserve
ASU	Air separation unit
BECCS	Bioenergy with carbon capture and storage
BFB	Bubbling fluidized bed
CAPEX	Capital investment expenses
CCS	Carbon capture and storage
CCU	Carbon capture and utilization
CFB	Circulating fluidized bed
CHP	Combined heat and power
CW	Cooling water
CSTR	Continuous stirred tank reactor
DH	District heating
EF	Entrained flow
FB	Fixed bed
FC	Fuel cell
FCR	frequency containment reserve
FFR	Fast frequency reserve
FGC	Fluegas condensation
FGR	Fluegas recycling
GtP	Gas to power
HEX	Heat exchager
IRR	Internal rate of return
MSW	Municipal solid waste
mFRR	Manual frequency restoration reserve
NCF	Net cash flow
NPV	Net present value
OPEX	Operational investment expenses
PBT	Pay back time
PEM	Proton exchange membrane electrolyzer
PFR	Plug flow reactor
PtG	Power to gas
PtGtP	Power to gas to power
PPA	Purchase power agreement
PVQ	Present value quota
PSA	Pressure swing adsorption
SC	Steam cycle
ST	Steam turbine
TOC	Total organic carbon
WGS	Water gas shift
WGSR	Water gas shift reaction

A	Area or Frequency factor
D	Diffusivity or factor
E	Activation energy (kJ/mol)
ρ	Density (kg/m^3)
U	thermal transmittance (W/m^{2}K)
M	Molar mass (g/mol)
p	Pressure (bar)
P	Power (W)
n	Number of moles
L	Length (m)
Q	Heat Flow (W)
k	Thermal conductivity (W/m)
T	Temperature (K)
SB	Ratio of steam to biomass (kg/kg)
η	Efficiency (%)
h	Enthalpy (kJ/kg)
Q	Energy/heat (W)
$\dot{m}$	Mass flow (kg/s)
X	specie conversion rate (mol)
c_p	Specific heat capacity (J/(kg K))
t	Time (seconds, hours)
V	Volume (m3)
J	Potential (V)
ϵ	void fraction
C	Cost (Sek)
z	Current lifetime (years)
i	Current (A)
R	Universal gas constant or Resistance
v	velocity (m/s)
ν	Viscosity (pa s)
d	Diameter (m)
b	Data for gas constant
c	concentration (g/mol)
γ_a	Radiation losses boiler (%)
γ_g	Specific heat ratio (%)
K	reaction rate
λ_{ER}	Air excess ratio
f	Scaling exponent
α	exchange constants

1 Introduction

Hydrogen has recently been discussed as an alternative to fossil fuels in the coming energy transition and already has a demand in the steel as well as in the chemical industry. In order to satisfy the demand for hydrogen, it is then necessary to establish a market, which can compete with the current production of fossil fuels and existing hydrogen production. Hydrogen is also seen as a solution to provide a more flexible energy supply, in line with the share of intermittent electricity production that is installed and gives the hydrogen the potential to act as energy storage. The European Commission has produced legislative proposals and regulations, and grants to facilitate the integration of hydrogen in our society as both fuel and energy storage. What remains then is how hydrogen production can take place in a cost-effective manner that attracts investors. The reason why hydrogen is relevant to replace our fossil fuels is that hydrogen is classified as a renewable product that produces no emissions if it produced from solar, wind, or BECCS, which coincides with the EU's goal of climate neutrality in 2045.

1.1 Stockholm Exergi

Stockholm Exergi is a supplier of electricity, district heating, additional to cooling in the Stockholm region, and thus is responsible for the majority of production residing in the area. In addition to power and heat, Stockholm Exergi is also a provider in advancements regarding carbon dioxide storage of Biogen emissions called Bio-CCS or BECCS, as by 2026 they plan to offer fossil-free and emission-negative energy production. This has been classified as one of the flagships in Europe, which has been recognized through research support from the European Union (Exergi, 2023b). In addition to storing carbon dioxide, Stockholm Exergi also has an investment in sequestering carbon dioxide, as carbon dioxide has value as a product in the food and chemical industry.

1.2 Objective

Stockholm Exergi intends to investigate the possibilities of hydrogen production, in order to participate in the energy transition that is taking place across Europe, in addition to exploring the advantages of byproducts. Since Stockholm is the largest city in Sweden in terms of population and is responsible for a relatively large share of emissions related to transport, it is of interest to investigate how this can be prevented, as hydrogen is an alternative that can relieve the need for electricity, which under current circumstances year 2023, is in short supply. The research on hydrogen in combination with existing systems is something that is meant to make hydrogen production more profitable, thus determining at what pace society can cope with the transition without risking economic collapse, poverty, and the production halt of important chemicals based on fossil fuels. Investigating the possibility of implementing hydrogen production in Stockholm is in the nation's interest and may in the near future set an example for cities in Sweden or the EU that share similar conditions.

This case study is targeted at the future market of Stockholm, as at least 4.3 TWh of hydrogen are required to replace the current demand of heavy transportation fuels (Miljöförvaltningen, 2023). Hydrogen produced in the region can also be utilized in national or international trading of green hydrogen and as a tool to take advantage of different net support services. By-products of the hydrogen production are also considered as valued streams when for example excess heat is exploited in district heating, or oxygen as performance enhancers for planned Bio-CCS installations.

1.3 Aim of Thesis

The primary target of this thesis is to analyze the opportunities to integrate hydrogen production in Stockholm, by a techno-economic evaluation. The areas that this research will encompass, can be broken into the following;

- To map the technical possibilities for the integration of hydrogen production in an existing district heating system.
- To investigate the actual impact new technology has on the production measures of electricity and district heating.
- Simulate and outline the contemporary production of hydrogen gas and district heating in these facilities in a way that makes it physically applicable.

- To investigate the value of byproducts in combination with BECCS and district heating.
- To determine the overall economic performance of the different production methods of hydrogen, suitable for the integration with local combined heat and power plants.
- To create, in a dynamic market for electricity and heat, an economic model that utilizes the possibility of storing energy in the form of hydrogen, thereby increasing the feasibility of strategic investment.
- Finally, present techno-economic results of the technical and economical performances of each proposed method, with the premise that the hydrogen is produced with negative or net emissions.

1.4 Boundaries

The research is executed with an academic approach, meaning that all technical equipment is described as a scientific generalization connected to theoretical values, and not specific for a manufacturer, unless specifically stated. The approach for this thesis is bound to the technical depth so that the technologies investigated have at least utilization of fluid mechanics, temperature variation, and stoichiometry into account in each system.

The boundaries for the system analysis and approach are limited to the independent plants, and do not include the distribution of gas or physical implementations, outside the process models. In the calculation and results, the process model is designed to meet the purity grade for hydrogen only, all other chemical products will be assumed to be in the acceptable range for achieving their market value. The outside temperature and variation of fuel quality for all the process models are assumed constant, thus project boundaries are set so seasonal changes are not considered within the technical calculation.

2 Background

In this section, the background of the fundamental processes and other subjects of relevance for this thesis is explained and elaborated.

2.1 Hydrogen production

There are several methods for producing hydrogen, ranging from fossil-based production to the splitting of water molecules. In the case of producing hydrogen in a city environment during the time of energy transition, the selection of alternatives comes down to renewable or carbon-neutral methods. When further investigating economically viable opportunities of hydrogen production, electrolysis is the primary target for adaption to the portfolio of both heat and power production by Stockholm Exergi, though gasification has other economical opportunities than previously thought, since in this particular case, the carbon dioxide infrastructure is available from the year 2026. This means that carbon dioxide is stored (CCS) or can be considered a product (CCU) that generates an income, which means that the conditions in this case study differ from previous research (Machhammer et al., 2016).

No initial plan of hydrogen production methods was investigated at Stockholm Exergi, so mapping of existing possibilities for hydrogen production and integration is investigated. After a thorough analysis, it can be concluded that hydrogen from gasification and reforming, or electrolysis fits the profile of the company, delivering carbon-neutral products in a city environment (Valente et al., 2020).

2.1.1 Electrolysis

Hydrogen can be produced purely from water and energy, by splitting the water molecules into hydrogen and oxygen molecules, and have the possibility of being classified as fully renewable, if the electricity derives from renewable sources. The process, that is connected to the water splitting, is called electrolysis. To initiate this process an anode and cathode separated by a membrane are required, filling the void with water and additives. Direct current is added to the electrodes on both sides, which causes the water molecules to split. This effect produces hydrogen at the cathode and oxygen at the anode. The basic reaction is described by Equation (1).

$$H_2O + Energy \rightarrow H_2 + \tfrac{1}{2}O_2 \tag{1}$$

There exist several types of electrolysis techniques for hydrogen production that are considered relevant for future production and differentiated in the way of achieving electrolysis. In this thesis three methods are investigated, alkaline (AEL), which utilizes electrolytes to operate, polymer electrode membrane (PEM), which utilizes pressure, and solid oxide (SOEC), which uses high temperature to initiate the process. Despite obtaining different methods of operation, they all function according to the same principle of splitting water molecules, and their overall reaction follows Equation (1).

Table 1: List of performance indicators based on electrolyzer technology (Schmidt et al., 2017) (Ji & Wang, 2021).

Technology	AEL	PEM	SOEC
Technical availability	Mature	Commercial	Semi-commercial
Temperature (°C)	60-80	50-90	500-1000
Electrolyte	KOH	Polymer	ZrO_2
Ramp time (min)	20-30	5-20	20-30
Dynamic operation	Limited	Yes	Limited
Load interval (%)	20-100	0-100	30-100
Lifetime (10^3 h)	60-90	20-60	$<$10
Efficiency (%)	62-82	67-84	81-100

In Table 1 the properties of each electrolysis technology are shown. In this thesis, only commercial and mature methods will be investigated since the feasibility of integration is valued for actual implementation.

Table 2: List of performance indicators based on fuel cell technology(Sjölin & Holmgren, 2019) (Ji & Wang, 2021).

Technology	PEMFC	SOFC	MCFC
Technical availability	Commercial	Commercial	Semi-commercial
Temperature (℃)	50-100	500-1000	500-600
Electrolyte	polymer	ZrO_2	H_2CO_3
Ramp time (min)	<5	>5	20-30
Dynamic operation	Yes	Limited	Limited
Lifetime (10^3 h)	20-80	20-90	25-30
Efficiency (%)	50-60	60	50

In Table 2 the properties of some selected fuel cell technology are presented, with PEMFC being the investigated technology in this study. The choice of PEM is due to the multipurpose adaption of membrane-based technology, that is both used in transport and industrial applications. From a brief analysis, PEM, AEL, and PEMFC are the technologies assumed to be of relevance for the study, because of their respective availability on the market.

2.1.2 Water gas shift and steam reforming

Steam reforming and water gas shifting are utilized in the process and chemical industry to produce synthetic materials and fuels. In steam reforming, the main process involves reacting steam with methane, producing hydrogen gas and carbon dioxide as byproducts described in reaction 2. This reaction occurs in the presence of a catalyst consisting of nickel or platinum, at high temperatures and pressures.

$$CH_4 + H_2O \rightarrow CO + 3H_2 \tag{2}$$

The approach of water gas shift utilizes the concentrations of carbon monoxide and abundant steam in processes involved in decomposition, to create synthetic gasses from solid fuels, which can, in theory, be any material containing carbon. The water gas shift process is carried out using catalysts such as iron oxide or copper oxide. These catalysts help to accelerate the reaction and increase its efficiency. Depending on the catalyst, secondary purposes are applicable for the material, for example, carbon dioxide adsorption (Jansen et al., 2013). Water gas shifting utilizes the same procedure but reacts with carbon monoxide from synthetic gas to create hydrogen and carbon dioxide, utilizing low-temperature steam proportionally to steam reforming. The desired conditions for the water gas shift reaction vary depending on the specific catalyst being used but still follow the principle of the main reaction described in Equation 3 (LeValley et al., 2014).

$$CO + H_2O \rightarrow CO_2 + H_2 \tag{3}$$

Steam reforming and water gas shifting are methods to produce quantities of hydrogen gas for industrial-scale applications, for example, ammonia production. The process also has the additional potential of reducing greenhouse gas emissions by capturing and storing the carbon dioxide produced during the reaction. However, steam reforming does have its drawbacks in the application of renewable hydrogen production. It requires proportionally large amounts of energy to sustain high temperatures and pressures relative to water gas shift and requires methane, which can be derived from fossil fuels. Syngas derived from gasification contains methane levels lower than 20% in medium-temperature processes. Due to the lack of potential for hydrogen extraction and energy-intense production requirements, steam reforming will not be applicable to the investigated case as a primary approach to reforming.

2.2 Electrolyzers

The technologies presented in this subsection are the suggested production technologies with electrolysis, as hydrogen is created from electricity.

2.2.1 AEL

Alkaline water electrolysis is the most mature and established method of producing hydrogen by electrolysis. The process operates at temperatures around 60-80°C and utilizes low-grade metals as membrane material. The charge carrier or electrolyte in this particular process is the hydroxide ion, OH^-, that reacts as described in Equation (4) and (5) to split the water molecules. The power consumed from a separate cell is approximately

4,5 - 5,5 kWh per cubic meter of hydrogen, resulting in an internal efficiency of 50-70 % (Chi & Yu, 2018).

$$2OH^- \rightarrow \frac{1}{2}O_2 + H_2O + 2e^- \tag{4}$$

$$2H_2O + 2e^- \rightarrow H_2 + 2OH^- \tag{5}$$

In general, the electrolyte is made up of potassium hydroxide (KOH) or sodium hydroxide (NaOH), with varying concentrations below 35 wt%. A membrane is also required to separate the hydrogen and oxygen as presented in Figure 1. The choice of diaphragm is essential for cell efficiency and lifetime, it is a wettable and highly durable material that has been improved by a considerable amount in recent years, as porous materials are a recent alternative for this membrane and decrease the cell's use of energy by increasing the active reaction area (Ji & Wang, 2021).

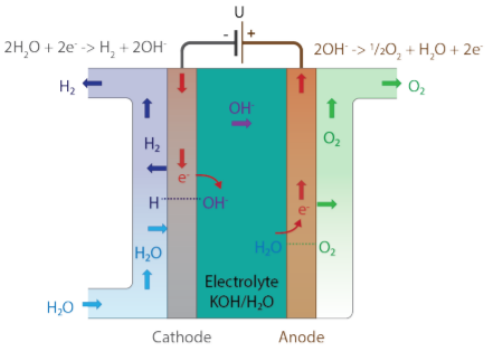

Figure 1: Overview of an AEL cell.Gallandat et al., 2017

In industrial applications, several cells are combined into a stack. This stack is coupled to a water and power source, additionally to a cooling system to regulate the cell working temperature. A simplified setup with three electrolysis stacks is shown in Figure 2, as the dark cylinders represent the bolted cells, and red piping an isolated central liquid cooling circuit.

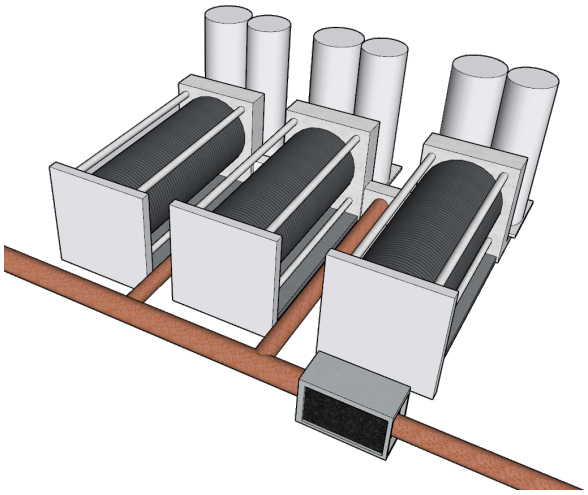

Figure 2: Industrial scale AEL stacks coupled to a central cooling circuit.

2.2.2 PEM

In the polymer electrolyte membrane, also called proton exchange membrane electrolysis, acidic polymer membranes replace the diaphragm and electrolyte commonly used in AEL technology. The PEM Charge Carrier is essential in this process by facilitating proton transport across the membrane. In the cells, electrodes consist of precious metals, often connected to higher component cost in relation to AEL, but potential to achieve higher

efficiency relative to Alkaline cells (Ji & Wang, 2021).

$$H_2O \rightarrow \frac{1}{2}O_2 + 2H^+ + 2e^- \tag{6}$$

$$2H^+ + 2e^- \rightarrow H_2 \tag{7}$$

Figure 3 provides an overview of the PEM technology, and the reaction for the anode and cathode is presented in Equation (6) and the carrier reaction elaborated in Equation 7 (Chi & Yu, 2018).

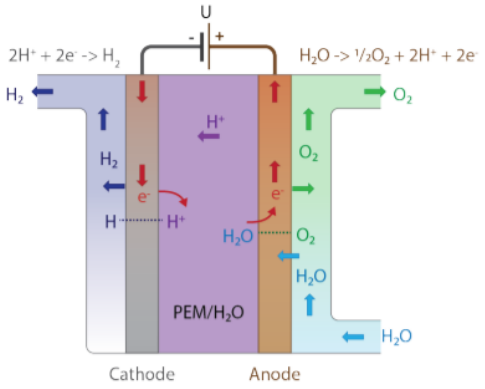

Figure 3: Overview of a PEM cell (Gallandat et al., 2017).

In industrial applications PEM stacks consume water, and electrical energy to initiate the electrolysis process and mechanical to build pressure. The benefits of utilizing this pressure-controlled method are the relatively small stack size in comparison to AEL and optional alignment, also this process allows the utilization to be more dynamically controlled.

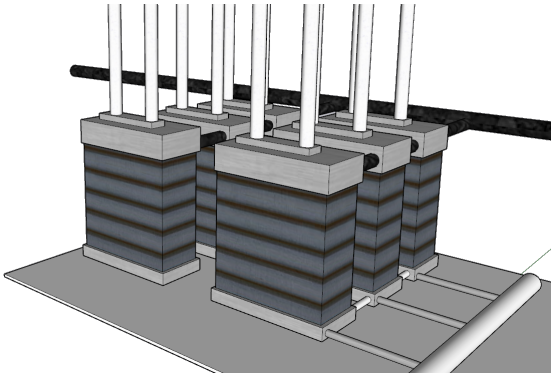

Figure 4: Industrial scale PEM units coupled to the central cooling unit.

In similarity to the AEL stack, PEM stacks can be placed in proximity to each other and coupled to a central cooling control system, combining the supply of water feed to independent cells. In Figure 4 the cooling circuit is indicated in black, while water feed and product flows are indicated in white. This figure is only a graphical example since stacks can have varying layouts, appearance, and process connections. In regards to PEMFC, it obtains similar physical proportions as the PEM stacks and inherits compact dimensions due to scaling limitations (Reyes, 2023).

2.3 Gasification

To create hydrogen derived from coal, biomass, or solid waste, gasification is the primary method for creating the synthetic gas that will be reformed. Gasification is a process that converts material fuels into gas over a range of temperatures (>700 ℃), which can be utilized to generate electricity, heat, or reformed to chemicals by different applications. The process involves heating the fuel in an oxygen-starved environment, which breaks down the molecules into gaseous compounds, for example, hydrogen and carbon monoxide. Combustion of material is required to maintain the reduction, with a share of the carbon being combusted to sustain gasification temperature. In a gasifier, the combustion of materials can primarily be described with reactions 8,

$$C + \tfrac{1}{2}O_2 \rightarrow CO \quad or \quad C + O_2 \rightarrow CO_2, \tag{8}$$

and gaseous combustion in reaction 9 additional to reaction 10.

$$H_2 + \tfrac{1}{2}O_2 \rightarrow H_2O \tag{9}$$

$$CO + \tfrac{1}{2}O_2 \rightarrow CO_2 \tag{10}$$

The exothermic reactions then supply the heat for endothermic gasification reactions of solids, and the internal water gas reaction 11,

$$C + H_2O \rightarrow CO + H_2 \tag{11}$$

Boduard reaction 12 after product gas and volatile material begin fast pyrolysis to produce carbon monoxide in the absence of oxygen,

$$C + CO_2 \rightarrow 2CO \tag{12}$$

and methanization of solids fuel materials by Fisher-tropsch reaction 13.

$$C + 2H_2 \rightarrow CH_4 \tag{13}$$

During gas acclimation, water gas shift reactions occur between CO and excess steam inside the reactor. These reactions may differ since methods, catalysts and other parameters determine the detailed process, this can be explained with detailed kinetics elaborated in Section 3 and is based on the selection of gasifier technology. The general setup for gasifier operation is composed of a fuel flow, reaction agent, and air, as oxidizer in stand-alone application. Gasifier types operate at various temperatures and render char and tar conversions at different rates, which can greatly impact the system efficiency depending on fuel. This conversion rate is also connected to residence time and to the fuel efficiency of the technology, and tar produces syngas of reduced material, as described in the tar creaking reaction 14 (Rudra & Tesfagaber, 2019).

$$Tar \rightarrow CO_2 + CO + H_2 + CH_4 \tag{14}$$

The efficiency of gasifiers is determined by measuring the output gas energy content. The efficiency is thus connected to solid conversion efficiency and the ratio of which high-energy gaseous molecules is produced. The conversion is altered by parameters such as steam to fuel ratio for increasing water gas shifting rate in the reactor, thus, the fuel-to-hydrogen efficiency. This applies to both gasifier and downstream equipment, i.e. for example temperature, which has certain detrimental effects on reactor efficiency. The increase of temperature and ratio of excess steam is, as described, beneficial to increase the conversion of CO. Parameters such as temperature, gasifying agent and excess air ratio are those to adjust for optimal utilization of processed fuel, and will determine the performance of the reactor conversion behavior (Rudra & Tesfagaber, 2019).

Commercial types of gasifier technology can be split up into three major types as described in Table 3, as the most common configuration is applied.

Table 3: List of performance indicators based on gasifier technology.(Williams & Kaffka, 2015)(Lian et al., 2021)(Weerachanchai et al., 2008)

Technology	B-/CFB	FB	EF
Agent	Air/steam	Air	Air
Temperature (°C)	700-1000	300-1000	1000-1400
Fuel	Bio/MSW/Coal	Bio/MSW/Coal	Bio/Coal
Fuel roughness (mm)	1-100	1-150	<0.5
Pressurized	Possible	Atmospheric	Possible
Residence time	Minutes	Hours	Seconds
Max efficiency cold gas (%)	80	83	78
Size range (MW)	10-700	0-10	40-1200

The efficiency of each technology is counted as cold gas efficiency, meaning the chemical energy stored in the gas compared to the energy of solid fuel without considering the production of heat.

2.3.1 Fluidized bed gasifier

Fluidized bed gasifiers and boilers share similar traits, as a fluidization agent, air or steam, moves the bed material and creates a state when the bed material can be described acting as a fluid. The fluidization of bed material, consisting of hot sand or limestone, promotes complete combustion of the fuel and heat dissipation. The mixture of bed material is heated to a high temperature, which causes the fuel to decompose into a gaseous state, that is then extracted as a product out of the gasifier.

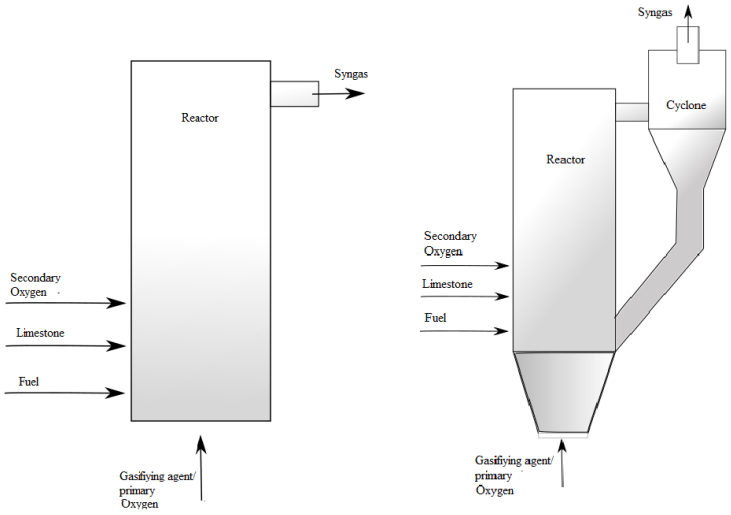

Figure 5: A illustration describing the process parameters over a Bubbling fluidized bed to the left, and circulating bed to the right, showcasing primary and secondary streams.

In gasifier reactors, the fluidization agent can be a mixture of both air and steam, the gasifying agent achieves increased particle contact and prevent lumping in the bed material. A fluidized bed has two main different configurations, Bubbling and Circulating. In the Bubbling gasifier, the bed material is only moved at low velocity inside the reactor as the bed is only moved by fluidization. In Circulating bed gasifiers, particulates, sand, and other volatile material enters a cyclone before exiting the gasifier island (Leckner et al., 2011). The material entering the cyclone is separated from the gas stream and re-enters the reactor from below as shown in Figure 5.

2.3.2 Entrained flow gasifier

High-temperature gasification, such as Entrained flow reactors, uses direct oxidation of material and high pressure to achieve fast reaction rates, thus creating product gas in large volumes. The internal separation of water, tar, and ash occurs in the lower part of the gasifier by water quenching, thus creating a slurry of slag water as described in Figure 6.

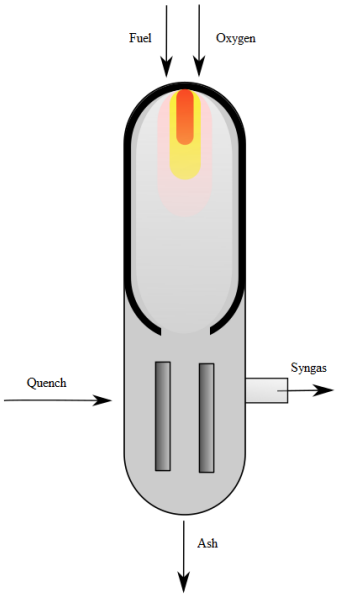

Figure 6: A illustration of the general setup of a entrained flow gasifier reactor.

Due to the fast volatilizing process, this has some drawbacks regarding fuel efficiency and dependability of high carbon pulverized fuel in order to reach operation temperatures. The sensitivity of this gasification process also renders this process not suitable for mixing steam and oxygen, since cooling the combustion with water counteracts the idea of having low combustion delay and high-temperature gasification. However, there are some setups that allow coal slurry blends and steam mixing, but with penalties, for example, higher oxygen feed and increased CO2 content in product gas (Gong, 2014).

2.3.3 Fixed bed gasifier

Fixed bed gasifiers depend on a gravimetric process, as drying, gasification, and combustion is separated into different stages in the gasifying reactor. The bed is fixed, as the accumulated solids land on the bottom and create a bed of inert and volatile material. The method of the fixed bed relies on height, so the main factor of product will depend on residential time. Fixed bed reactors have two primary setups, downdraft, and updraft, describing how the feed of fuel and gas is directed. A simplified explanation of the process of a downdraft gasifier is shown in Figure 7.

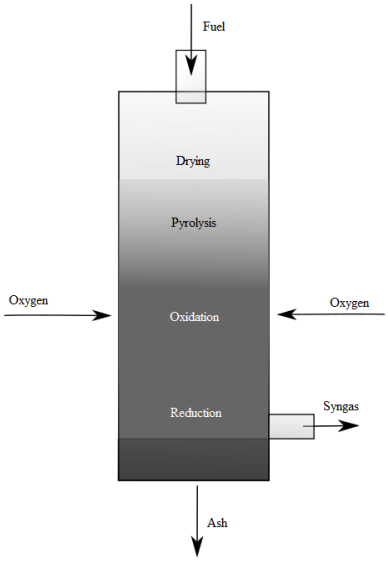

Figure 7: A illustration of a updraft(concurrent) Fixed bed gasifier.

In updraft configuration, gasifying agent enters from the bottom of the reactor and the gas outlet near the top, with little to no separation of the internal processes.
Fixed bed gasifiers have in general the lowest reactor temperature in comparison to the other mentioned techniques, as it does not require high temperature relative to BFB and EF for delivering product gas, and instead rely on longer conversion time. This technology is not receptive towards mixing oxygen with steam since the possibility of the extinguishing combustion process, together with low heat distribution inside the bed, is too uncertain to operate (Gøbel et al., 2007).

2.3.4 Dual bed gasification and combustion

Gasification with co-combustion of tar and other carbonated material is a recent development of gasification technology. It utilizes the separation of gasification and bed heating into 2 different vessels, as combustion is not present in the gasifier reactor. This setup is also called dual bed gasification because it requires two separate beds and consists of one shared bed circulating between the two vessels. This procedure results in a lower content of CO_2 produced and no requirement for oxygen feed, in addition to increased receptivity of steam injection, in comparison to self-supporting systems. Dual fluidized bed systems require a combustion chamber, which in retrofitting adaptation requires the same pressure as the gasifier, and a higher temperature to compensate for losses through heating. Attaching a boiler or riser as a combustion chamber is the basic principle in DFB systems, for example, shown in 20 MW GoBiGas chemical plant (Thunman et al., 2018) and the 0.1 MW plant in Vienna (Wilk et al., 2011), that primarily utilizes the reject from the gasification process.

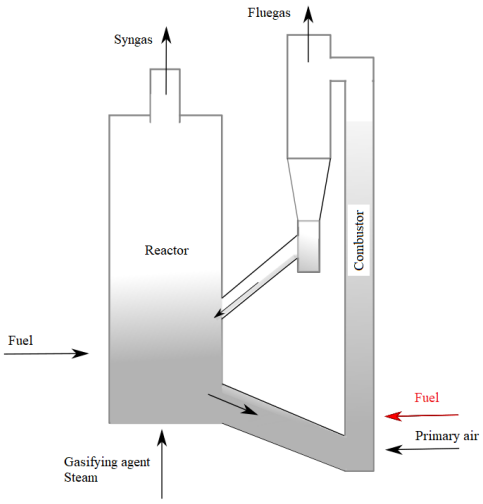

Figure 8: Dual bed gasification, with black arrows indicating conventional material flows, and the red one is added for retrofitting of the existing boiler.

A recent development has shown that dual feeding systems are efficient, meaning that fuel feed to both the gasifier and combustion chamber from separate streams is a possible configuration as shown in Figure 8. In Sweden, Chalmers has developed a test facility retrofitting a gasifier 2-4 MW to an existing boiler, thus utilizing two separate fuels. The configuration allows the boiler section to produce the normal products heat, power, and simultaneously heat the gasifier bed material (Lundberg, 2018). The configuration has been shown to obtain nearly nitrogen-free and low tar-content gas, with the most efficient combination consisting of a fast fluidized riser as the combustion reactor with BFB as the gasifier reactor. The dynamic of the catalyst material is also an alternative to increasing the desired function of the DFB. A reason to add catalyst material is, by sorption-enhanced reforming with CaO, to initiate selective transport of CO2 in the form of CaCO3. The functionality of this process is determined by the place of calcination, as gasifier temperature is required to be in the interval of 600-700℃ to initiate carbonation, and combustion in the interval 830-930℃ to calcinate the catalyst material and release CO2 (Fuchs et al., 2019).

Even though DFB is one of the reviewed technologies that show the most comparability to the current situation at Stockholm Exergi, the main drawback is that in comparison to the other reviewed gasifier systems, that have been commercial since the mid-late 1900s, the method of combining gasifier is not classified as mature.

2.3.5 Solid fuels

In this study, solid fuels in existing production are utilized as fuel to gasification plants for the respective facilities. Utilizing the same fuel as boiler feed helps in estimating the fuel content, due to real-time information, in addition to preventing the requirement of alternating any permit or treatment of ongoing production.

In the facility *Hgdalen*, municipal solid waste and industry residue are the primary fuels, that are sorted and handled to an average particle length of $5 - 100$ mm. In Table 4 it can be observed that the content of the fuel is dominated by carbon and hydrogen.

Table 4: Average composition of fuel to gasifier and boiler in Högdalen

Element	**wt**	**C**	**H**	**O**	**N**	**ash**	**S**
Volume fraction (%)	27	37.5	6.2	41.4	0.7	13.7	0.5

MSW with altering carbon content and size over 0.5 mm is not suitable for entrained flow gasifiers, so the fixed- or fluidized-bed is the technology fit for this type of fuel.

Forestry residues are used in the facility *Brista* and are of varying size, mostly consisting of carbon and oxygen, with an inherently low trace of sulfur and ash, though the ash content is presumably increasing in the future because of a higher blend of bark. The granular size of the fuel is 5-70 mm and is preheated before combustion.

Table 5: Average composition of fuel to gasifier and boiler in Brista

Element	**wt**	**C**	**H**	**O**	**N**	**ash**	**S**
Volume fraction (%)	50	49	7.7	39.9	1.2	2.2	0

Forestry-derived fuel as presented in Table 5 has a relatively constant and high content of carbon in comparison to MSW, which makes it fit for more sensitive gasifying methods and the potential of a higher hydrogen yield after steam reforming, though due to the grain size fixed- or fluidized bed configuration is the only option for the gasification if no alteration of current grind process is made. Note that the sulfur content in biomass is rounded from 0.02 to 0 in Table 5.

2.4 Systems related to hydrogen utilization

Hydrogen, as mentioned in section 1, has the potential to serve as energy storage to support the grid through fuel cells. Fuel cells work similarly to electrolyzers, but in reverse, and dispatch power when hydrogen is consumed. The power that fuel cells generate can then be utilized in order to sell on the electricity market when the demand for power peaks.

The current electricity market in Sweden offers delegation of frequency balancing responsibility. Balancing deficit and excess power in the grid is essential to uphold the frequency in the net. These support services generally have a higher price per MW delivered than producing basic electricity to the net. The reason behind the compensation is because of the demand to uphold frequency, with criteria for each service and regulating effect shown in Table 6.

Table 6: List of support services and criteria.

Parameter	FFR	FCR-N	FCR-D up	FCR-D down	aFRR	mFRR
Symmetrical	No	Yes	No	No	No	No
Min. ordersize	0.1 MW	0.1 MW	0.1 MW	0.1 MW	1 MW	10 MW
Activation	Automatic	Automatic	Automatic	Automatic	Manual	Automatic
Act. time 100%	within 0.7-1.3s	within 3min	within 30s	within 30s	within 5min	within 15min
Act. time 63%	-	within 60s	-	-	-	-
Act. time 50%	-	-	within 5s	within 5s	-	-
Least amount	varying	240 MW	to 580 MW	to 560 MW	140 MW	0 MW
Durability	30-5s	1h	20min	20min	1h	1h
Pricing by:						
Compensation	Capacity	Cap/Energy	Capacity	Capacity	Cap/Energy	Energy
Trade type	Margin	Pay as bid	Pay as bid	Pay as bid	Margin	Margin

Note that the symmetrical services require both delivery and reception of power. In this thesis, the assumption is made that the least amount and minimal order size is planned to be lowered in the future to increase the flexibility of the grid (Min order size = 0.1 MW). Additional elaboration about the planned change is discussed in Section 6.4.

Using hydrogen as a reserve has benefits regarding the scaling of available power reserve in comparison to battery storage, which is only limited by available storage space and an installed capacity of fuel cells. If the fuel cell is coupled to a type of capacitor that regulates the output voltage, the system can deliver power in accordance with the set criteria, if scaling of utility is in line with the minimal order volume. In addition, energy taxes are deductible for the energy that is stored and sent back to the grid, creating a flexible definition of the stored energy volumes in both hydrogen and battery.

In Table 6 the economic compensation and trade types for each support service are listed. *Capacity* in this matter indicates that the pricing of the support service is based upon the available capacity of the reserve during the specific hour, and *Energy* is based on the amount of energy transferred to the grid during the specific hour. *Trade type* tells if the price for the activated volume of the reserve is then compensated further by a preset market margin or if the price is defined by auction bidding price. In conclusion, this means that services are compensated firstly by initial power available, and then additional income is generated by the time of activated reserve that is priced similarly to standard market pricing.

The main difference between support services can be classified by timing, for example, the FCR services relieve the load of the grid for a longer duration at lower volumes. aFRR and mFRR have larger and more intermittent load curves for supporting large deficits in the grid. FFR is intermittent and requires lower power support compared to other services, only to balance out frequency deviations in smaller intervals. This creates different values for each service towards liable operators, as less intermittent and longer activation time can be suitable for turbine-derived power, and shorter intermittent frequency deviations, for providers utilizing battery storage. (Esett-Oy., 2022) (SVK, 2022)

Regarding the estimation of activation time for the various services, it can be referred to as the average frequency drop during the year, as the large frequency drops ($Hz < 49.8$ *or* $Hz => 50.2$) representing aFRR and mFRR measured in a span during the year 2015 to 2020. Low frequency drops, ($50.1 > Hz > 49.9; \neq 50.0$) is representing FCR and FFR during the same time period. From previous studies, the expected activation time during this span can be approximated to 1-2 seconds for FCR and FFR, not including the actual activation of the reserve. The approximation of active time for aFRR and mFRR is concluded to be 6.95 seconds with the same presumptions for actual reserve utilization, although this time is expected to increase when the Swedish energy production implements wind and solar to replace stable power production (Fingrid., 2021).

2.5 Systems related to byproducts of hydrogen production

Byproducts from electrolysis and steam reforming can be of interest when calculating the economical performance of each plant. Stockholm Exergi has a particular interest in these byproducts since they could be integrated with the existing product portfolio. A flow sheet of the planned layout can be observed in Figure 9,

and water re-circulation is left out for illustrative purposes.

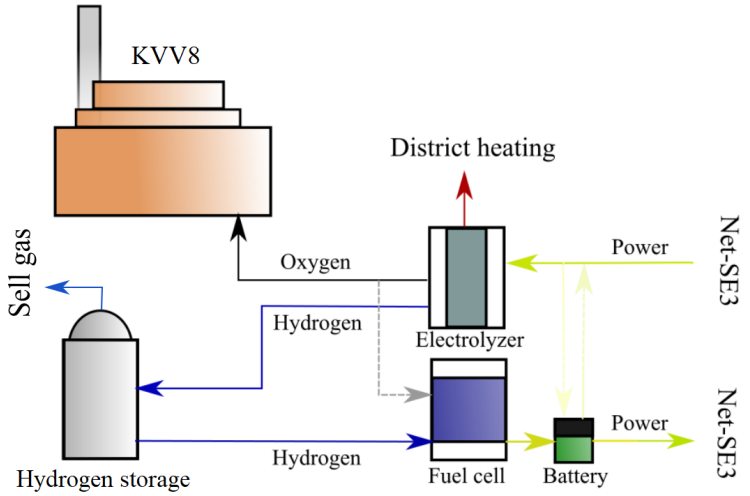

Figure 9: Flowchart of the hydrogen production platform, with major material flows and related facility of integration.

This configuration shows the implementation of hydrogen storage with electrolysis adjacent to KVV8, to increase hydrogen distribution, pipelines or the current gas grid could be upgraded to connect with customers or other facilities producing hydrogen to increase the reliability of the reserve. The overall structure of the power-to-gas system is following conventional design with only the utilization of excess heat and supplied oxygen as a non-conventional application of byproducts (Kopp et al., 2017),

2.5.1 District heating

When producing hydrogen by either gasification or electrolysis, system energy losses in the form of heat are inevitable. To cost-efficiently produce hydrogen, these losses require to be identified and evaluated, as potential utilization of district heating. In this study, only heat sources capable of delivering heat over 70℃ in a DH subsystem will be considered, in combination with the criteria of supplying heat with more than 1000 disposable hours annually.

To create valid economic and technical models, for the district heating system, an analysis of the present year can quantify the set of high/low demand hours. In Stockholm, the daily average is presented in Figure 10.

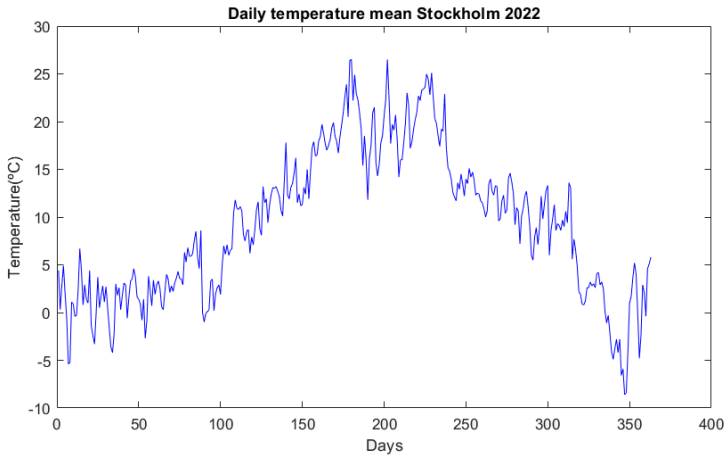

Figure 10: Ambient temperature means in Stockholm during the year 2022.

The assumptions are made that amount of high and low demand hours generate revenue, whilst no revenue is generated during days when the temperature is above 10℃. In Table 7, the amount of demand hours during high

and low demand is presented for the proposed plants. During 2022, a total of 4560 hours had a temperature under 10℃.

Table 7: District heating, valuable time.

Demand	**hours**
High	2280
Low	2280
None	4226

It is worth noting that the district heating for gasification and the boilers have a different system, as demand for the boiler are varying on an hourly basis, whereas the gasifiers have 3 price ranges similar to the electrolyzer since it is running on 3 different loads. The load for the electrolyzer depends on the electricity market and does not have a planned preset of working hours that depends on district heating. Though the load of the existing boilers are depending on district heating demand, the gasifiers are not bound to this production behavior, albeit the primary product of gasification is hydrogen production and not district heating or electricity. This creates a different preset for the gasification, as it only shuts down during maintenance or shut down of the connected boiler.

Table 8: Working hours of a stand-alone gasifier.

Load	**hours**
100 %	4320
90 %	4200
0 %	266

The load of which the stand-alone gasifiers operate is shown in Table 8, and the load is adjusted to prevent overexertion of the system during periods when there is low demand for district heating.

2.5.2 Oxygen utilization

Oxygen is a byproduct of electrolysis and can be recirculated to fuel cells or sold depending on the value of oxygen. Historically the oxygen from electrolysis has no exceptional value since transportation cost and criteria of purity override the income from selling the oxygen to external actors. In recent studies, the utilization of injecting oxygen in adjacent processes has been shown to theoretically increase the value of oxygen. An example relevant to the case of Stockholm Exergi is oxyfuel purposes, in order to increase efficiency or even out temperature sinks, and is seen as a potential source of revenue if hydrogen production is adjacent to a combined heat and power plant (Tibbelin et al., 2022).
For increasing the price for oxygen as a byproduct of hydrogen production, it is also of interest to study the impact of oxygen in a boiler with CCS, since increasing the oxygen levels decreases the amount of nitrogen in the flue gas, thus creating a more efficient separation of the carbon dioxide.
Potassium carbonate solutions are widely used as gas purification and have shown potential in CO_2 absorption from power plants flue gas (Mumford et al., 2011). Figure 11 shows the process of the carbon capture model used in an existing plant, which is based on an adsorption and desorption step. The input flue gas is initially fed into the absorber, in a counter-current to the amine solvent for absorption of CO_2. The gas is then detached from the main solvent by adding heat to the desorber, or alternatively by decreasing pressure. The solvent is regenerated in a loop, decreasing the material used for capturing. The CO_2 is then compressed and treated before transportation from the facility.

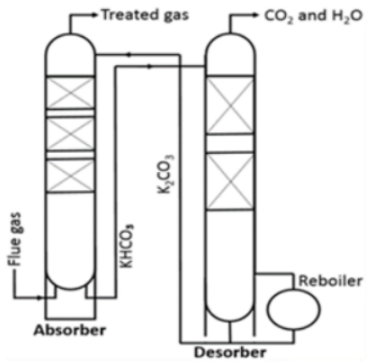

Figure 11: Simplified flow diagram of the CCS process applied to flue gasses derived from KVV8 (Exergi, 2023a).

To increase the efficiency of this process, the mass of the flue gas can be decreased and the temperature of the amine blend increased slightly, depending on kinetic acceleration in the adsorbent, thus creating a smaller equipment size and lower capital investment costs. This finalizes the background related to the value of oxygen supply in the proximity of CHP installations.

2.5.3 CCU

When producing hydrogen through the method of steam reforming or water gas shift, the majority of the mass flow is converted to carbon dioxide, that depending on process pressure and separating process can reach purity grades of >90% before refining the process gas (Lin et al., 2014). If additional cleaning steps follow and the process pressure stays over 18 bar until storage, only the external cooler and expansion step is required to supply liquefied carbon dioxide to be sold as a chemical product. The selling price of this carbon dioxide from bio-derived fuels is expected to reach 2000-2500 SEK/tonne, as some deviations can occur depending on the content of fossil-derived fuel, though it is expected to reach the same price in the future (Singh & Tan, 2023).

2.6 Sustainability

In regards to sustainability, this project can make a relevant impact on innovation (SDG 9), responsible consumption, and production (SDG 12). In addition to SDG9 and SDG12, climate action (SDG 13) can also be considered as relevant. The motivation for innovation is connected to the development of functional hydrogen production systems, that in the current stage have not reached complete maturity. Responsible consumption, production, and climate action are motivated through synergy between preventing energy losses via storage in the shape of chemical energy, thus reducing both energy production and efficient consumption by balancing out the grid power supply. The connection of hydrogen production with climate action is by opening possibilities of replacing transport fuels and industrial chemicals derived from fossil fuels, to net zero or CO_2 negative hydrogen.

In the current situation (2023), an increase in hydrogen production is one of the EU's main strategies to reach 2050 climate goals (Nyqvist & Sillén, 2023). The reasoning behind this statement is because of the versatility of hydrogen and its applications, as an economical and environmentally sustainable fuel source. To estimate hydrogen's official value as an alternate source in the energy mix, an approach of estimating this is by verifying said sustainability on the eligibility of subsidies; in other words, quantify the social, environmental, and economical benefits expected by the authority by measuring the amount of economical support the production can achieve.

2.6.1 European delegation act

As the topic of electrofuels becomes more relevant, the European Commission has developed a methodology to ensure that the means of production for renewable liquid and gaseous transport fuels are derived from renewable sources, thus promote to the financial benefit of renewable deployment. As per definition renewable transport fuels are the collective meaning for fuels deriving from non-biological origin and recycled carbon fuels.
If the produced fuel can be classified as renewable, it could lead to a major tax reduction from electricity for powering the electrolysis or in tax relief from accumulated income from sold gas. In Sweden, there is no tax for creating hydrogen and a complete tax deduction for hydrogen used to supply the grid. This is because

taxing the same energy twice from both production and storage is not viable, though it is expected that the tax relief for electrolysis will be following the European regulation once the act is set in place. The first mention of promoting renewable electricity, for the production of renewable is followed by a set of criteria. The primary criteria explain the electricity classification in regard to the production of fuels.

1. The producer may count electricity as fully renewable if the origin is located in a bidding zone as the share of renewable electricity exceed approximately 90%. The same also applies to zones having a lower average emission rate of 65 gCO2eq/KWh.

2. In addition to (1), the origin of the electricity must be directly derived from renewable sources, utilizing PPA or similar systems. An exception is renewable energy derived from biomass, as it is not accepted as fully renewable by the commission.

3. The fuel producer must report the evidence for utilizing fully renewable electricity in accordance with (1) and (2) annually on the initial implementation of this act; after the initialization, reports proving production connection on an hourly basis are required to fulfill these criteria.

It is mentioned that, in accordance with acts 3 a and b in the delegation act, electricity is seen as fully renewable if created in support of balancing while in a bidding zone complying with (1). Elaboration on the delegated act, calculating greenhouse gas criteria, can potentially promote continued use of recycled carbon fuels as in favor of counting CO_2 from municipal solid waste if captured, as zero or negative through calculating emissions from the bidding zone. This is contradicted in the supplementing Directive (EU) 2018/2001 Section 6, with the uncertainty of the upcoming delegation regarding biomass or recycled carbon fuels. For the production of renewable transport fuels, this delegation will decide how the future framework of hydrogen production and circular economy will be designed (European-Commission, 2023).

In this study, we can conclude that hydrogen production from electrolysis will be seen as fully renewable since the relevant bidding zone (SE3) has historically <40 g/KWh emission rate all hours during the year. This act does not promote hydrogen derived from solid fuels and considers electrolysis as the sole option to produce hydrogen in a sustainable matter.

2.6.2 Economy and subsidies

Subsidies for different projects can promote the implementation of hydrogen production by minimizing capital investment costs (CAPEX). A product of the EU hydrogen incentive is by assigning over 10 billion euros under the Recovery and Resilience Facility and 1 Billion Euros to the EU innovation fund for supporting hydrogen innovation. In Sweden, there are three major subsidies that are relevant and can apply to the production of hydrogen production or other relevant technology for reducing climate impact. These subsidies are an incentive on providing new solutions to benefit a certain cause.

Industriklivet: Subsidies that can help fund research, environmental studies, and new technologies that have not been fully commercialized and support the net zero emission goal or negative emissions. The size of the funding often resides between 20-44%, with higher shares for lower investment costs and an average initial project investment CAPEX of 2-70 million SEK. The limit of total funding from this asset is set by the EU. (Energimyndigheten, 2023a)

Klimatklivet: The climate initiative can fund 30-70% of the total investment, which has the highest funding share amongst corporations and an upper limit of 210 million SEK before it is instead handed by the commission, resulting in a lower rate of approval. Recycling of fossil fuels and carbon-based MSW fuel is of interest in this case with CCS/U, albeit it promotes the largest reduction of avoided CO_2 per Sek (Naturvårdsverket, 2023).

Energimyndigheten pilot och demo: This is a subsidy given to projects with a minimum initial investment of 7 million SEK and a threshold coverage limit of 25% for larger corporations. The classification of larger companies is made by the EU, so the increase or decrease of subsidy is decided by the commission. The cause of the funding has no limitation on technology as long as it is experimental and relevant (Energimyndigheten, 2023b).

In addition to the subsidies, the EU tax-directory and Swedish legislation of energy (LSE,1994:1776) state in chapter 11 paragraph 9 that, the entitlement of tax deductions are obtained by the producer that uses electricity for chemical reduction or processes based on electrolysis. So the deduction on taxed electricity is given

for the electrolysis process itself, and not for the surrounding equipment (Skatteverket, 2023).

From this, it can be concluded that the attitude of the authorities towards hydrogen innovation is positive, and is seen as a major part of the upcoming goal of net zero emission, as long as the emissions are captured. A general benefit can be allocated for renewable hydrogen production with connections to electrolysis and larger-scale investments as the main promotion for environmental sustainability.

3 Theory

In this section, only the theoretical aspects that are directly connected to the processes are presented and not to the elements that are trivial or can be performed with the help of general knowledge of physics, except in descriptive parts of the model layout.

3.1 Calculation of thermodynamic performance and energy balance

This chapter is giving an overview of the main equations and definitions used to determine the thermodynamic performance of the plants introduced in Section 4. The basic mass balance is calculated by applying the assumptions of steady mass flows in and out of a given control volume and is described by Equation 15.

$$0 = \sum \dot{m}_{in} - \sum \dot{m}_{out}. \tag{15}$$

The balance of the associated flows of energy and the other energy flows in and out of the control volume is presented in Equation 16.

$$\frac{\mathrm{d}E}{\mathrm{d}t} = \sum_i \dot{m}_i(h_i + e_{a,i}) + \sum_j \dot{Q}_j + \sum_k P_k. \tag{16}$$

The specific enthalpy h_i is calculated following the 4th-grade polynomial for the case of gas containing presented elements in Equation 17.

$$h_i = R\left[b_1 T + b_2\frac{T^2}{2} + b_3\frac{T^3}{3} + b_4\frac{T^4}{4}\right]. \tag{17}$$

In the plant, an internal balance of energy and mass calculation of total processes follow the Equation 18. The energy balance is based on the assumption of stationary conditions, no accumulation of energy inside the plant control volume, and negligible contribution of kinetic and potential energy terms $e_{a,i}$.

$$0 = \sum_i \dot{m}_i h_i + \sum_j \dot{Q}_j + \sum_k P_k. \tag{18}$$

In the calculation of electrical or heat output from the steam cycle, the Equation s 15 and 18 are applied, together with physical influence over the system. In the case of power production from fuel cells, the output follows the same method.

The theoretical indicator to describe plant energy conversion performance is efficiency. The energy input is converted to heat, electricity, or chemical product, and the efficiency of each product is measured through calculation.
The common principle is adhering to the definition of efficiency as the ratio of power output to energy input as described in Equation 19.

$$\eta = \frac{Q, P_{out}}{Qfuel}. \tag{19}$$

The energy fed into the plant can be present in the state of solid fuel or as electricity, depending on the type of plant, for example, the energy P_{fuel} is bound to the solid fuel, thus corresponding to the power input. The overall assumption is that incoming fuel or water entering the system has the same temperature as ambient T_0, which renders the energy difference equal to 0, with the exception of the return water of district heating feed to the electrolyzer heat exchanger. The thermal energy of input is the primary value determining incoming Q_{fuel}, and is defined as the lower heating value $H_{biomass}$ multiplied by the mass flow of fuel m_{fuel}. The energy input of electricity to the electrolyzer is not defined by thermal energy, and utilizes the product of current A and voltage V.

The efficiency with respect to a particular output i (district heating, chemical energy associated with a fuel, electricity) is defined as the energy content of that output divided by the input energy used to generate it as shown in Equation 20.

$$\eta_i = \frac{Q_i}{Q_{fuel}}. \tag{20}$$

Overall efficiency, is the summation of the output heat and electrical power, as expressed in Equation 21.

$$\eta_{overall} = \frac{\sum_i (P_{el,net} + \sum Q_i)}{\sum_{g,b} Q_{fuel}}. \tag{21}$$

The total efficiency η_{Total}, is the summation of output heat and electrical power including chemically stored energy, and is calculated with the mass flow of chemical product converted to energy by its lower heating value (David, 1967).

3.2 Gasification and combustion

In this section, theory connected to the mathematical modeling of production methods based on gasification and incineration is presented.

3.2.1 Gasification

The gasification process is mathematically designed to simulate a realistic output from the devolatilization and formation of gas, thus giving results eligible for application.
Utilizing different gasifier reactors, i.e. methods of gasification, will however create the need for varying complexity of theoretical models to achieve the desired simulation of the process. The target is to create a model producing syngas, with the account of char conversion (and geometry if possible), to investigate internal performance. The char conversion of BFB gasification is also required to predict the performance of energy exchange between the boiler and gasifier. In addition to the prediction requirement, the gasifiers obtain uncertainties dependent on the method, as theory is adapted to fit the expected uncertainty of model output.

The BFB gasifier and integrated BFB gasifier are based on mathematical calculations of high complexity, in relation to the other methods, utilizing kinetic and non-kinetic equations with influence from geometric parameters. In Figure 12 the semi-kinetic calculative process is illustrated, presenting the main sections of the BFB gasifier and boiler interplay. This process is also applied to BFB gasifier without integration into the boiler, as the only adaption required is the conservation of mass reject from the gasifier and removal of boiler criterion.
The initial step in the semi-kinetic model is to calculate gasification and volatile combustion without consideration of kinetics. The products from primary decomposition are then inserted to generate conditions simulating the process of water-gas shift and char gasification in the bed. The next step is then representing the WGS of syngas inside freeboard space, and total generated product gas from rector (Tanaka et al., 2015).

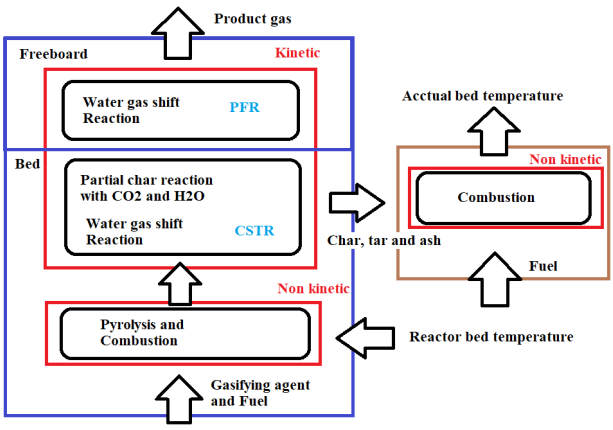

Figure 12: Calculating process for the semi-kinetic model, with combustion path for a connected boiler.

This method is based on previous adaptations of mathematical gasification models and includes the char residence time to stabilize bed volume, tar reject, and the effect of diffusion efficiency (Gómez-Barea & Leckner, 2013) (Kramb et al., 2014).

The FB and EF gasifier mathematical model is based on stoichiometry with a low amount of kinetic emergence in comparison to the BFB calculation. The EF gasification theoretic model is limited and has no relation to physical geometry or char conversion.

The general reaction for gasification is by definition a thermochemical process that converts material fuels into a gaseous state. It involves heating the fuel in an oxygen-starved environment, which suppresses combustion reactions and triggers the formation of molecules conserving initial heating value. The gasification includes several stages, namely pyrolysis, oxidation, reduction, and reforming, as the conversion from solid to gas can be expressed with the stoichiometric expression 22.

$$\begin{aligned} \dot{m_{BM}}(\alpha C + \beta H + \gamma O + \delta N + \epsilon H_2O) + \frac{\dot{m}_{OX}}{M_{OX}}(x_{O2}O2 + x_{N_2}N_2 + x_{CO_2}CO_2 + x_{H_2O}H_2O) \\ \rightarrow aN2 + bH2 + cCO + dCO_2 + eH_2O + fCH_4. \end{aligned} \tag{22}$$

The process starts with feeding fuel to a gasifier in the absence of oxygen leading to thermal decomposition if heated to over 250-300 ℃, called pyrolysis. In the oxidation stage, air or oxygen is introduced into the system leading to partial combustion of fuel and converting C and CO to CO_2. The water-gas, water-gas-shift, Bouduard, and Fischer-Tropsch reactions then create the composition of output gas, as kinetics determine the conversion rate of molecules. The general expression for the calculation of the kinetics is the Arrhenius equation, which is the base of applied kinetics and is described as Equation 23.

$$K = A\,exp(\frac{-E}{RT_{reactor}}). \tag{23}$$

In the equation, A is a predetermined constant, E is the activation energy and T is the reactor temperature. The water-gas reaction is based on water and oxygen bound in the solid, in addition to excess steam and oxygen, to form CO and H_2. The excess oxygen ratio, λ_{ER}, is calculated with Equation 24 and is also required to reach the target reactor temperature by partial combustion of the solid fuels.

$$\lambda_{ER} = \frac{O_{2,input}}{C_{dry,fuel} + 0.25H_{dry,fuel} - 0.5O_{dry,fuel}}. \tag{24}$$

To produce syngas with maximum heating value, both air excess and the addition of steam are required to be configured, in order to fit the production method.

3.2.2 Semi-Kinetic calculation

The semi-kinetic calculation, representative of the BFB process, is first initiated by the gasification process, as an instant conversion of the solids is assumed. This particular calculation is non-kinetic and resides at the base of the gasifier, utilizing empirical theory. In the application, the yield of CH_4 is not calculated and is instead estimated to be 7.639% of product gas to constrain the reaction balance. The char yield derived from gasification is also estimated utilizing the algebraic expression in Equation 25 (Campoy et al., 2009)

$$\dot{m}_{char,0} = \frac{\dot{m}_{b,daf}}{100}(-15.03 + 50.58(\tfrac{T-273}{500}) - 18.09(\tfrac{T-273}{500})^2). \tag{25}$$

After calculating char and product gas output from the initial gasifier stage, the balanced output from calculating reactions occurring in the circulating stirred tank reactor (CSTR) can be expressed as Equation 26.

$$\dot{\Gamma}_{i,out} = \dot{\Gamma}_{i,in} + \sum v_{i,j} r_j V. \tag{26}$$

In order to calculate the product out of Equation 26, the sum of input species and volume of bed is accounted for by first applying the intrinsic conversion rate of CO_2. The conversion rate is presented in Equation 27, and the state i is representative of H_2O or CO_2 for each species. In calculation porous rate of species is predetermined constant, as $X_{porous,i} = 0.5$, and k_i derived from the Arrhenius equation.

$$\frac{dX_i}{dt} = k_i \frac{p_i^{n_i}(1-(1-X_{porous,i}^{-1})X)(log(1-(X_{porous,i}^{-1})X))^{2/3}}{(1+log(X_{porous,i}))}. \tag{27}$$

This rate is then used to calculate the average char conversion rate: $C + H2O = CO + H2$, $C + CO2 = 2CO$, of the CSTR stage as described in Equation 28.

$$X = X_{H_2O} + X_{CO_2}. \tag{28}$$

Here X_i is the product of intrinsic conversion rate and effective factor $\eta_{diffusion}$. The shape and size of the particle decide the effective factor, albeit expressed as Equation 29 for spherical geometries.

$$\eta_{diffusion} = \frac{1}{M_T}(\frac{1}{\tanh 3M_T} - \frac{1}{3M_T}). \tag{29}$$

The Thiele modulus, M_T, is descriptive of the ratio between diffusion and reaction rates connected to the porosity of particle surface while maintaining no limitations in mass transfer ability. The dimensionless modulus is calculated through Equation 30.

$$M_T = \frac{d_{char}}{3}\sqrt{\frac{(n+1)A^m C_{A,surf}^{m-1}}{2R_{eff}}}. \tag{30}$$

Here, the effective diffusivity, D_{eff}, can be explained as the effectiveness of transportation through the specific catalyst structure matrix and is defined as Equation 31 in this particular case utilizing the effective diffusivity to solve Thiele modulus. The pore is touristy is represented by τ, ϵ, the char porosity, with D_{bulk} and $D_{knudsen}$ as standing for diffusivity of bulk gas mixture and Knudsen diffusion, respectively.

$$D_{eff} = \frac{\epsilon/\tau}{\frac{1}{R_{bulk}} + \frac{1}{R_{knudsen}}}. \tag{31}$$

Knudsen diffusivity derives from the occurrence when pore diameter compared with the mean free path of gaseous particles is in disproportion ($>> 1$) and is expressed by Equation 32,

$$D_{knudsen} = \frac{2}{3} r_p \sqrt{\frac{8RT}{\pi,\ M_A}} \tag{32}$$

as the average pore radius can be approximated by Equation 33

$$r_{pore} = \frac{2\epsilon}{\rho_{char} S_{char}}, \quad and \quad \epsilon = 1 - (1 - X_{porous,i})(1 - X). \tag{33}$$

In the calculation of gas diffusivity utilized in internal mass diffusion prediction, the molecular diffusion can be accounted for utilizing the binary bulk diffusivity. The R_{bulk} is calculated with the account of the interaction between solid and gas state, with the Stefan-Maxwell Equation 34,

$$D_{bulk} = \frac{D_{bulk,0}}{\nabla \mu_r} \tag{34}$$

as $D_{bulk,0}$ is defined via expression 35,

$$D_{bulk,0} = \frac{\nabla \mu_r'}{\sum_{i=1(i\neq A)} \frac{v_i}{v_A}\left(\frac{1}{D_{gamma}(x_i - x_A \frac{v_i}{v_A})}\right)} \tag{35}$$

and differential operator 36.

$$\nabla \mu_r' = 1 - x_a \sum_{i=1} \frac{v_i}{v_A}. \tag{36}$$

The binary molecular diffusivity, D_γ, is the expression derived from using the correlation of Fuller–Schettler–Giddings, representing the diffusivity of species H_2O and CO_2 to gas composition (Fuller et al., 1966).

$$D_\gamma = \frac{3.3 \times 10^{-11}\, T^{1.75} \sqrt{\frac{1}{M_A} + \frac{1}{M_B}}}{p_{total}((\sum v_A)^{1/3} + (\sum v_B)^{1/3})}. \tag{37}$$

In this equation, overall pressure is represented by p_{total} and $\sum v_i$ stand for the diffusion volume.

With the diffusion effective factor defined, the average char rate is calculated, thus the reaction balance of conversion is applied with WGSR illustrated in Appendix 1.2. Kinetic application of WGSR in the CSTR bed is commonly expressed by Equation 38,

$$r_{wgsr} = K_{wgsr}(c_{CO}c_{H_2O} - \frac{c_{CO_2}c_{H_2}}{Ke}). \tag{38}$$

and K_{wgsr} is defined by the Arrhenius Equation, with constants listed in Appendix B2.

In order to calculate the volume of char and void properties, the bed volume V_{bed} and void fraction of bed ϵ_{bed} are estimated through input data and reactor scaling. The method of scaling accounting for devolatilization and horizontal dispersion is illustrated in Appendix 1.4. The char volume V_{char} is calculated with Equation 39,

$$V_{char} = V_{bed}\,(1 - \epsilon_{bed}) - V_{bm}. \tag{39}$$

with the volume of bed material V_{bm}, bed volume, and void fraction, which is estimated by using Equation 40 (P. et al., 1978).

$$\epsilon_{bed} = 1 - \frac{1}{f_{bex}}(1 - \epsilon_{bed,0}). \tag{40}$$

Bed expansion factor, f_{bex}, is a value indexing the rising of bed following the vector v_{0f} in Figure 13. Superficial velocity v_0, minimum fluidization velocity v_{mf}, together with the mass of quartz bed density ρ_{bm} and average quartz grain diameter d_{bm}, generate the bed expansion factor 41.

$$f_{bex} = 1 + \frac{14.31(u_0 - u_{mf})^{0.738} d_{bm}^{1.006}\, \rho_{bm}^{0.376}}{\rho_{bm}^{0.126} u_{mf}^{0.937}}. \tag{41}$$

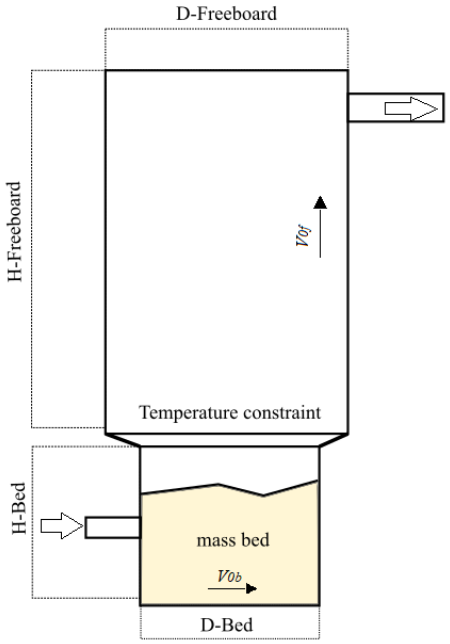

Figure 13: Schematic of a BFB reactor, with parameters indicating the dimensions of the freeboard and bed utilized for void and volume calculation. Vectors illustrating expansion and fluidization are not representative of the actual direction of movement,

The superficial velocity is calculated utilizing the modified Ergun Equation 42, accounting for the internal hydrodynamics of bed movement (JR., 1986).

$$v_{mf} = Re_{bm,mf}(\frac{v0_g}{d_{bm}\rho_g}), \quad and \quad Re_{bm,mf} = \sqrt{28.7^2 + 0.0408\,Ar} - 28.7. \tag{42}$$

The particle Archimedes number representing the relations of gravitational forces, sizing, mass difference, and viscosity is calculated with Equation 43,

$$A_r = 9.80665\,O_2^3\rho_g\frac{Q_{gas} - \rho_g}{v0_g}. \tag{43}$$

and the specific density of gas flow ρ_g is utilized for the calculation of bed expansion with Equation 44. It should be noted that the stationary void fraction was assumed to be 0.4, assuming that the gas viscosity is kept constant to the predetermined reactor temperature.

$$\rho_g = \frac{p_a}{RT}\dot{n}_g. \tag{44}$$

The mass of char out is calculated with Equation 45 as the fixed input of carbon from pyrolysis, while the transformation of tar and ash is bypassed to continue in the combustion chamber or gasifier reject.

$$\frac{dm_{char}}{dt} = \frac{dm_{char,0}}{dt} - \frac{n_{ash}}{dt}M_{ash}. \tag{45}$$

equation 46 summarizes the CSTR mass flow of char out of the bed, ending the mathematical model for the bed.

$$\dot{\Gamma}_{char,out} = (1 - X)\dot{\Gamma}_{char,in}. \tag{46}$$

The next stage in the gasifier is the freeboard, as the mass balance is calculated through the assumption of a plug flow reactor (PFR) process, that accounts for the particle residence time in the reactor dependent on volume. In the freeboard, the primary reaction is the WGSR that utilizes the same method presented for the CSTR, but with time as the critical factor of output and no involvement of solid formations of char is considered to occur. To determine the output of product gas, the total concentration (c_i) is calculated as presented in Equation 47, in utilizing empirical relations of the gas constant, temperature, and reactor pressure:

$$c_i = \frac{p_{freeboard}}{R(T - 80)} \cdot 10^{-2} \tag{47}$$

Gas entering the freeboard is assumed to be 80K lower than in the bed due to heat losses in the bed and distance from the combustion center. In order to calculate the spacial residence time, the molar flow of specie $\dot{n}_{in}$ and the freeboard volume $V_{freeboard}$, are inserted in Equation 48, generating the conditions required for the matrices in Appendix B20.

$$t_{space} = \frac{V_{freeboard}}{(\frac{\dot{n}_{in}}{c_i})}. \tag{48}$$

The final mass-energy balance of reactor input and output is defined by Equation 49 following the principle of mass conversion,

$$\eta_{adiabatic}\, Q_b + \Upsilon_{gas} - Q_{L,mc} = Q_{syn} + \Upsilon_{syn} + Q_{char} + \Upsilon_{char}. \tag{49}$$

as enthalpy, latent heat, and specific capacity of the gas mixture are expressed according to, Equation 50 for each state of mass flow.

$$\Upsilon_i = \dot{m}_i \int C_{P_i} dT. \tag{50}$$

This concludes the theory applied for the calculation defining the production of syngas from BFB gasification using the semi-kinetic model.

3.2.3 Single course-Kinetic calculation

The theory applied for the calculation of FB and EF gasification is not the same as for the BFB gasification. The fundamental gasification reaction in Appendix 1.1 applies to all gasification models in an initial state, as the calculation of WGS equilibrium for FB and EF is expressed with K_{eq} derived from the Arrhenius expression. In the theoretic calculation of EF gasification, no account for geometry or char conversion is made. The modification deviating from the universal gasification calculation is the account of increased losses during partial oxidation in the reactor, which is estimated to 10 %, representing the mass reject subtracted from the product gas mass flow during the quench. The FB gasification calculation modification builds on the PFR approach assuming 1-D calculations.

In the FB gasifier, a dynamic 1-D mathematical model estimation of the char gasification is applied with no radial parameters, thus Equation 51 is the base expression for the differential volume. The initial assumption is made that N_2 and CH_4 can be seen as inert in the bed reaction, and that tar is negligible in the reaction residing above the bed.

$$\frac{dM_{char}}{dt} + \frac{\partial \dot{m}_{char}}{\partial x} = \dot{\Gamma}_{char}. \tag{51}$$

Conversion of gas, expressed in Equation 52, and char chemical balance then support the Law of conservation of mass, as described in Equation 15, and the process can be isolated as such to estimate the char reactivity in reactor bed.

$$\frac{\partial \dot{m}_{gas}}{\partial x} = \dot{\Gamma}_{gas} = -\dot{\Gamma}_{char}. \tag{52}$$

Through defining the heterogeneous reactions, overall char reactivity can be expressed as Equation 53, as the product is explained as the relation between concentration and overall rate coefficient, resulting in the maximum intrinsic conversion rate $X(t)$, and volatilization of material after time t (Laurendeal, 1978). Temperature, content in gas, pressure, catalyst, and porosity affect $X(t)$ as observed in Equation 53.

$$X'(t) = -\frac{1}{m}\frac{dm}{dt} = \frac{1}{1-X}\frac{dX}{dt}. \tag{53}$$

Char rate during conversion of material can be expressed with Equation 54.

$$X \equiv \frac{m_0 - m}{m_0}. \tag{54}$$

If kinetics are unaffected by conversion, predicting the overall particle reactivity depending on time is possible. Reactivity models for char gasification and combustion are built on diffusion, profile, and char characteristics as previously mentioned in the semi-kinetic calculation, as the equilibrium factor r and structural function dependent on conversion $f(x)$ can be expressed as the product of particle and the particle reactivity, or vice versa through Equation 55.

$$X'(t) = \sum R_i\, f(X). \tag{55}$$

The equilibrium factors D_i are the sum of D_{H_2O} and D_{CO_2}, with the factor representing concentration profile between H_2/H_2O and CO/CO_2. In the Equation 56, the global intrinsic conversion rate is calculated by the

analogy of heterogeneous factor R_{H_2O},

$$D_{H_2O} = \frac{k_{1,fw} p_{H_2O}}{1 + \frac{k_{1,fw}}{k_3} p_{H_2O} + \frac{k_{1,bw}}{k_3} p_{H_2}}. \tag{56}$$

and similar D_{CO_2} is solved, by substituting H_2O with CO_2 and H_2 with CO. Both the expressions are based on Langmuir–Hinshelwood kinetics, modified to fit the particular model, with A and E defined in Appendix B1, together with also adaptation with the partial pressure of p_i species (M et al., 2000). The updated expression after replacement should then be equal to the mass conversion rate differential observed in Equation 57,

$$(D_{H_2O} + D_{CO_2}) f(X) - \frac{1}{m_{char}} \dot{\Gamma}_{char} = 0 \tag{57}$$

as alternative reaction rate is described through the diffusion interaction between char and gas, expressed by Equation 58 with total diffusivity D_i .

$$D_i = \frac{(D_{H_2O} + R_{CO_2}) D_\gamma, i}{(R_{H_2O} + R_{CO_2}) + D_\gamma, i}. \tag{58}$$

The rate is dependent on internal movement instead of partial pressure, and D_γ, i is given by the Equation 59.

$$D_\gamma, i = \sum \frac{B_i \, Sh}{d_p}. \tag{59}$$

In the Equation, B_i is the reaction-diffusion coefficient calculated as the product of r_i/d_i. Variable Sh stands for the dimensional Sherwood-Schmidt number, defined by Equation 60, representing the relatively low-pressure condition and friction due to a non-fluidized state. Reynolds number is approximated with the same method as in the semi-kinetic model.

$$Sh = 0.9(2 + 0.6 Re^{0.6} Sc^{1/3}), \quad and \quad Sc = \frac{\nu_{0g}}{\rho_g \, c_i}. \tag{60}$$

The structural profile $f(x)$ is connected with the bottom of the gasifier, or bed of the two-stage downdraft gasifier, obtaining a dry state with partial pressure for H_2 greater than 0.2 atm. The structure is defined by polynomial 61 and is an alternative method for determining surface area and changes of cathylic active species.

$$f(X) = 32.17X^6 - 57.17X^5 + 46.10X^4 - 16.04X^3 + 2.92X^2 + 0.297X + 0.529. \tag{61}$$

The height of the char bed is correlated with the char surface activation rate throughout the bed and is illustrated in the dimension calculation through scaling of the gasifier in Appendix 1.4. A model including trivial effect conversion ratio is based on a continuously operated reactor as non-converted char, meaning condition assuming steady-state properties, is calculated and transported downwards during the gasification reactor presented in Figure 14.

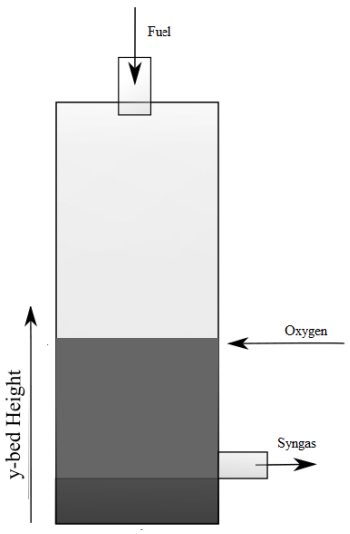

Figure 14: Schematic of a FB reactor, with the height of bed consisting of char, tar, and ash is parameterized by height y.

Utilizing ash content as an indication of conversion, assuming the ash is inert, the char conversion rate can be determined by the amount of ash accumulation during gasification. The conversion rate can then be expressed as Equation 62 with the calculation of the initial ash content $C_{ash,0}$ and current ash content C_{ash}.

$$X = 1 - \frac{C_{ash,0}}{C_{ash}}. \tag{62}$$

The ash content in the gasifier is calculated with Equation 63,

$$C_{ash} = \frac{m_{ash}}{m_{char}}, \quad and \quad C_{ash,0} = \frac{m_{ash,0}}{m_{char,0}}. \tag{63}$$

as the mass flow of char, m_{char}, is calculated utilizing the finite difference expressed as Equation 64. The ash content of char can be calculated with the initial and mass balance of ash, with a density of particles required for calculating mass flows.

$$\frac{dM_{ash}}{dt} + \frac{\partial \dot{m}_{ash}}{\partial x} = 0. \tag{64}$$

In the estimation of ash, the assumed content to calculate the molar weight and density of the initial state is 40% Potassium, 40% Calcium, and 20% Magnesium. Please note that this composition is not derived from the actual content and is only a guess to estimate initial ash mass flow. Utilizing the porous particle model, with no account for size variation in transportation, the particle can be assumed to have a reaction occurring over the whole particle as described in Equation 65, as the conversion rate is determining the decreasing density (Gøbel et al., 2007),

$$\rho(X) = \rho_0(1 - X). \tag{65}$$

as the shrinking particle method assumes reaction on particle surface in Equation 66. The $m_{char,0}$ is calculated with Equation 25 as in the semi-kinetic model.

$$\rho(X) = \rho_0. \tag{66}$$

In theory, this is applied to both biomass and MSW, as the estimated conversion rate is dependent on the porosity of fuel with initial carbon and ash content.

3.2.4 WGS reactor

The reformation of molecules from H_2O and CO to H_2 and CO_2 occurring in the WGS reactor in order to control the syngas composition is the primary function of this unit. The reaction for this process is exothermic, meaning it releases heat as it occurs. The kinetics are explained according to Le Chatelier's principle of shifting equilibrium, as the absorption of heat initiates the chemical reaction. Other than heat and pressure, the catalyst material is a determinant of recovery or acceleration of the shifting reaction. In order to estimate the reaction rate, a micro-kinetic model of the elementary reaction through the catalyst surface is utilized. For temperatures under 750 K, the reaction catalyst is based on $Cu/ZnO/Al_2O_3$ for low-pressure systems. The WGS primary kinetic reaction is Equation 67, which is an adaptation of the Arrhenius expression.

$$K_{tr} = exp(\frac{4577.8}{T} - 4.33). \tag{67}$$

The mathematical model of the WGS reactor consists of 2 high-temperature reactors, called $HT1$ and $HT2$. Reactor HT1 operates in temperatures between 500-750K, HT2 between 600 - 750K.

To account for void fraction, effective diffusivity inside catalyst pores, and thermal conductivity, the specific catalyst dynamics can be described by Equation 68 as an approximate relationship of reactions.

$$r_{wgs*} = d_{cat}\,(1-\theta)\,k_{r,l}\,p^2(C_{CO}C_{H_2O} - \frac{C_{CO_2}C_{H_2}}{K_{tr}}). \tag{68}$$

In the expression, d_{cat} stands for the mass density of solid catalyst, and C_x is the vapor mole fraction of species in near atmospheric pressure (II & Barton, 2009). In the case of a pressurized vessel, a model including the partial pressure of each species is applied replacing the vapor molar fraction for FeO catalysts. In industrial applications, the pressure increase has a scale-up relation as presented in Figure 15. The Equation 69 is representative of pressure correlation for both HT and LT catalysts,

$$F_{pressure} = p^{0.5-\frac{p}{250}}. \tag{69}$$

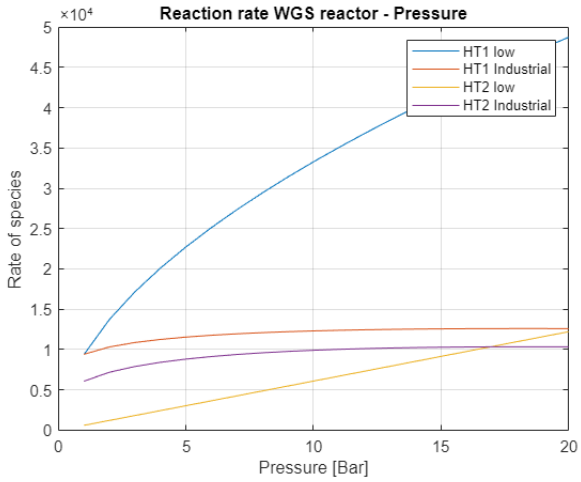

Figure 15: Representation of the catalyst pressure effect on conversion rate according to mathematical expression.

as the theoretical principle accounting for the high-pressure catalyst is expressed by Equation 70.

$$r_{wgs*} = d_{cat}\,(1-\theta)\,F_{pressure}\,k_{ht,12}\,C_{CO}^{n}C_{H_2O}^{m}C_{CO_2}^{p}C_{H_2}^{q}\,(C_{CO}C_{H_2O} - \frac{C_{CO_2}C_{H_2}}{C_{CO}C_{H_2O}K_{tr}}). \tag{70}$$

In industrial scale pressure application, the constants n, m, p, q adapt to the increased pressure through $n = n(0.5 - \frac{p}{250})$ for individual molecular pressure or vapor mole fraction, depending on high or low-temperature catalyst.

3.2.5 Combustion and Boiler

Combustion is related to both partial oxidation in the gasifier and boiler performance. In the boiler, combustion controls the state of flue gas output, heat to steam cycle, and air blower. The theoretical combustion reaction is calculated with the stoichiometric Equation 71, expressing the reaction balance.

$$\begin{aligned}\dot{m}_{fuel}(\alpha C + \beta H + \gamma O + \delta N + \epsilon H_2O) + \dot{m}_{air}\lambda_{ER}(0.21O_2 + 0.79N_2)\\ \rightarrow \dot{m}_{fluegas}(aO_2 + bN_2 + cCO + dCO_2 + eH_2O).\end{aligned} \tag{71}$$

Application of gas combustion follows the same theory, with the exception of gas composition on the left side instead of solid composition, as gas reacts with oxygen generating the exothermic reaction. The stoichiometric matrix for the applied reaction is illustrated in Appendix 1.3. The mathematical model takes into account the process of combusting the fuel with an excess of air intake, to represent physical operation. Variable λ_{ER} describes the excess ratio of atmospheric air feed to the process for completing combustion subtracting the amount of oxygen residing in the solid material. Air is fed into the combustion and brought to boiler pressure with the air blower utilizing the ideal gas law expressed in Equation 106, additionally, γ_a express the heat capacity ratio of air and performance based on the isentropic efficiency of compression (Paraschiv et al., 2020). In the boiler, mass, energy, and mole balances determine the combustion chamber's internal state described by Equation 72, thus the output of energy recoverable for the flue gas condensers.

$$Q_{flueGas} = \eta_{comb}(Q_{fuel} + Q_{oxidizer}). \tag{72}$$

Please note that the flue gas condensers connected to the steam cycle are dependent on internal flow conditions and particle transfer moving inside the boiler. Not all heat from the solid fuel is transferred to condensers, and the efficiency and radiation losses are preset to estimated values listed in Appendix 1.8.2. The mathematical model is also constrained since the condenser is not able to transfer heat if the temperature falls below the temperature for saturated steam at a specific pressure. The updated state of gas leaving the condenser obtains lower temperature and energy content than before heat exchange.

3.3 Electrolysis

In this section, fundamental theory related to the calculation of stack performance and process flows will be explained. Theory related to heat recovery of stacks is found in Appendix 1.5

3.3.1 AEL

The alkaline electrolyzer cell is based on electrochemical theory, which builds on the fundamental potential and product of an independent cell. To initiate the electrolysis, and thus the dissociation of water molecules, an oxidation reaction occurs on the anode side, while a reduction occurs on the cathode side. The reaction is achieved by applying the change in Gibbs free energy ΔG, thus calculating the electromotive force for the reversible electrochemical process (J_{rev}) as expressed in Equation 73. This process is enthalpy dependent, and change in energy includes the thermal irreversible effect equal to the endothermic dissipation of the reaction.

$$J_{rev} = \frac{\Delta G}{zF}, \quad (\Delta G = \Delta H - T\Delta S.) \tag{73}$$

In standard application number of electrons transferred z, is equal to 2. Faraday's constant F is approximately 96.485 C/mol and represents the amount of electric charge per mole of electrons involved in an electrochemical reaction. In the AEL cell the molar output can be calculated with Equation 74 representing the cathode,

$$n_{H_2} = \eta_{faraday} \frac{1}{zF}. \tag{74}$$

and equation 75 representing the output of anode,

$$n_{O_2} = n_{H_2} \frac{1}{2}. \tag{75}$$

and multiplying total cell current $i_{cell,tot}$ the mass flow from the cell is obtained following Equation 76. Multiplying the product with the number of cells is equal to the stack theoretical mass flow.

$$n_i \, i_{cell,tot} = \dot{m}_i. \tag{76}$$

To measure cell performance, the potential increase of achieving the reaction is required to be calculated, as the loss of energy is correlated to the difference between the reversible voltage and applied cell voltage. The loss of energy is dispersed in the form of thermal energy and can be calculated utilizing the summarized potential in Equation 77. The cell overpotential is calculated as the summation of ohmic potential J_{ohm}, activation potential J_{act}, and open circuit voltage J_{ocv} increase derived from internal resistances.

$$J_{cell} = J_{ocv} + J_{act} + J_{ohm}. \tag{77}$$

In addition to the potential increase from reaction kinetics in electrodes by activated complex, the electrode catalyst activity is connected to the activation voltage. The expression of the activation overpotential and current density i_0 can be described by the Butler-Volmer expression 78. The presented equation calculates the exchange current density, which expresses the energy distribution over a certain area (Schnuelle et al., 2020).

$$i_0 = i_{0,ref} e^{\frac{-E_{act}}{R}(\frac{1}{T} - \frac{1}{T_{ref}})}. \tag{78}$$

The activation and ohmic overpotentials are calculated differently for AEL and PEM cells, as per current density relation to activation kinetics. In the calculation of AEL cell overpotential, Equation 79 is utilized, as Θ represents the bubble factor. In Appendix 1.6 the difference by time cycle degradation effect on cell potential is explained.

$$J_{cell} = J_{ocv} + (r_1 + r_2(T_{cell} + \Theta))i + s_1 log_{10}((\xi_1 + \frac{\xi_2}{T_{cell}} + (\frac{\xi_3}{T_{cell}})^2)i + 1). \tag{79}$$

J_{ocv} can be calculated with Nernst Equation 80, which describes the state of current absent reactions dependency on the activity of present gas, in addition to reversible voltage.

$$J_{ocv} = J_{rev} + \frac{RT}{2F} ln(\frac{p_{H_2}\sqrt{p_{O_2}}}{p_{H_2O}}). \tag{80}$$

In accordance with open circuit voltage and with the thermal dependency on Gibbs free energy, the reversible voltage dependency on thermal effect is expressed in Equation 81.

$$J_{rev} = 1.5184 - 1.5421 \times 10^{-3} \, (T_{cell}) + 9.526 \times 10^{-5} \, (T_{cell}) \, ln((T_{cell})) + 9.84 \times 10^{-8} (T_{cell})^2. \tag{81}$$

The partial pressure of the cathodic and anode cell space is calculated in accordance to Equation 82, as i expresses the cathode or anode and the respective flow of oxygen or hydrogen, R represents the universal gas constant and is equal to 8.314 J/molK, and T_{cell} the operational temperature of the cell.

$$p_i = RT_{cell} \frac{n_i}{V_i}. \tag{82}$$

On the membrane surface, bubbles propagate during the process and reduce the active surface area onto which the electrolyte can split the molecules, thus leading to a lower exchange rate (Abdin et al., 2017). The effect can be described as a resistance factor and thus contribute to the overpotential. The impact is estimated utilizing a resistance factor for the catalyst cell in application with bubble factor Θ, calculated via Equation 83.

$$\Theta = (-97.25 + 182\frac{T}{T_{ref}} - 84(\frac{T}{T_{ref}})^2)(\frac{i}{i_{lim}})^{0.3}. \tag{83}$$

Overpotential by the concentration of electrolyte is not included in this as it is estimated to be negligible.
In order to finalize the model output, the independent cell current and area are combined with a series of cells, resulting in a stack. The combined output describes total power demand after theoretical losses in terms of overpotential, expressed as Equation 84. This method is applied to the mass flow of product gas since the accumulated molar flow from the Faradic Equation output increases flow dependent on total cell current and the number of cells.

$$P_{stack} = N_{cells}(J_{cell} i_{cell} A_{cell}) \quad and \quad i_{cell,tot} = i_{cell} A_{cell}. \tag{84}$$

The power consumption on the surrounding system adds to stack performance calculation, thus overall power requirement is calculated in Equation 85, as P_{stack} is the power requirement of cells including internal resistance.

$$P_{consumption} = \sum_i P_{compressors} + \sum_i P_{pumps} + P_{stack}. \tag{85}$$

Utilizing the total power consumption of the system and the theoretical reversible process, a hydrogen efficiency can be determined with expression 86,

$$\eta_{AEL} = \frac{P_{electrolysis}}{P_{consumption}}. \tag{86}$$

as the energy used for electrolysis is expressed as the product of reversible potential in Equation 87.

$$P_{electrolysis} = J_{rev} i_{cell} N_c A_{cell}. \tag{87}$$

The produced hydrogen and district heating can then be combined to express the overall efficiency of the electrolyzer system.

3.3.2 PEM

The modeling of the PEM electrolyzer cell is utilizing the same fundamental electrochemical theory as the AEL, but with a different adaptation of the Faradic model, and can be calculated with Equation 88 and 89 utilizing the Faradic efficiency $\eta_{faraday}$ equal to 0.99. $\eta_{faraday}$ is applied on the cathode operation,

$$n_{H_2,c} = \frac{1}{zF}\eta_{faraday}. \tag{88}$$

$$n_{O_2,c} = \frac{1}{2zF}(1 - \eta_{faraday}). \tag{89}$$

then in the opposite way in the anode, which is described by Equation 90 and 91.

$$n_{H_2,a} = \frac{1}{zF}(1 - \eta_{faraday}). \tag{90}$$

$$n_{O_2,a} = \frac{1}{2zF}\eta_{faraday}. \tag{91}$$

Since the activation is dependent on pressure and product gas reaching saturated conditions, the molar flow of product gas from the cathode is explained by Equation 92. It should be noted that the internal pressure follows fundamental thermodynamic laws, meaning p_{H_2O} is also temperature dependent.

$$n_{H_2} = \frac{p_{H_2} - p_{H_2O}}{p_{H_2O}}\, i_{cell}\, A_{cell}\, N_c(n_{O_2,c} + n_{H_2,c}). \tag{92}$$

The product flow from anode n_{O_2} follows the same method as presented in 92 but with the change of H_2 to O_2. As the product flow of mass is achieved by the addition of activation energy, the activation potential relation to current can be described by 93. The temperature T_{cell} is different for the PEM model and is listed in Appendix B1. $\dot{m} = \dot{n_x} M$ generates the mass flow in terms of grams per second from molar flow, through the Faradic model

as previously explained in theory. For oxidation reactions exceeding zero activation potential, the Butler-Volmer equation for adjusted cell current density(i_j) can be rejected.

$$i_j = i_{0,i}(exp(\frac{-\alpha z F}{RT_{cell}}\eta) - exp(\frac{(1-\alpha)zF}{RT_{cell}}\eta)). \tag{93}$$

In the calculation of J_{cell} the same approach is done as Equation 77, i.e. the sum of potential interference and internal resistance is equivalent to the cell voltage. The activation can be defined as the sum of J_{act}, with the dimensionless charge transfer coefficients α_i for cathode and anode using Tafel Equation 94. The charge transfer is the result of Butler-Volmer relations, thus the coefficient represents the fraction of electrostatic potential energy and reduction rate in the affected electrode reaction.

$$J_{act} = \sum_{i=a,c} \frac{RT_i}{\alpha_i z F} ln(\frac{i}{i_{0,i}}). \tag{94}$$

Ohmic overpotential is calculated with the account of ionic resistance from the proton conduction membrane between electrodes, resulting in ohmic resistance R_{ohm}, by utilizing Equation 95 (Yigit & Selamet, 2016).

$$U_{ohm} = i_{cell} R_{ohm}. \tag{95}$$

The conductivity σ_{cell} is expressed as the semi-empirical relationship in Equation 96, derived from an Arrhenius type expression. The relationship varies dependent on the membrane humidification of gas product reactants. In the relation, T_{ref} stands for the temperature used in reference calculation.

$$\sigma_{cell} = (0.005139\Xi - 0.00326)e^{1268(\frac{1}{303} - \frac{1}{T_{ref}})} \times 10^3. \tag{96}$$

The membrane hydration in the PEM cell is assumed to be the product of Equation 97, as β_{humid} is equal to 1 due to operation under 100% humidity.

$$\Xi = 0.043 + 17.81\beta_{humid} - 39.85\beta_{humid}^2 + 36\beta_{humid}^3. \tag{97}$$

Ohmic resistance is then calculated with Equation 96 and given constants, with negligible temperature dependence, via Equation 98.

$$R_{ohm} = \frac{t_m}{\sigma_{cell}} + \frac{2t_{cc}}{\sigma_{cc}} + \frac{4t_{bp}}{\sigma_{ti}}. \tag{98}$$

The contributing resistance from current collector R_{cc} and bipolar plating R_{bp} have a proportionally lower interference on ohmic potential since the material has suitable conductivity (Tiktak, 2019). The electrical conductivity of the current collector is material dependent and can vary dependent on the membrane porosity. The bipolar plates are dependent on flow distribution and cooling channel profile, as no current is applied (Schnuelle et al., 2020).
Other resistances contributing to overpotential, for example, Θ, are excluded. The bubble factor Θ is assumed to be negligible in PEM cells with accordance to increased pressure, which counteracts bubble propagation due to void collapsing.
The open circuit voltage J_{ocv} utilizes the Nernst Equation in similarity AEL theory, thus finalizing the internal cell overpotential.

3.3.3 PEMFC

The performance of the fuel cell is calculated in order to estimate fuel cell power output, and applies to the same Faradic model as presented in Section 3.3.2, except its calculated in reverse order as the molar flow output is instead the required molar flow input.
For the fuel cell, a potential penalty is made for the resulting voltage, as increased performance corresponds to decreased potential resistance as described in expression 99. The diffusion voltage decrease $J_{diffusion}$, is the adaptation of J_{ohm}, but accounting for the surface diffusivity, electrode active area, and concentration loss Ψ_{con}. A similar method as presented in Section 3.3.2, is applied to activation and open circuit potential (Um et al., 2000).

$$J_{cell} = J_{ocv} - J_{act} - J_{diffusion} - \Psi_{con}. \tag{99}$$

The ohmic resistance is not accounting the current collector of the cell membrane material, as only the membrane conductivity and thickness are calculated and described in Equation 100. In order to account for diffusivity, pure electrical resistance, and platinum loading, a constant value is applied representing the average penalty.

This method does not follow empirical examples, and should thus be calculated specifically for the utilized membrane material (Edwards & Demuren, 2019).

$$J_{diffusion} = i_{cell}(0.0979 + \frac{t_m}{\sigma_{cell}}). \tag{100}$$

The concentration loss Ψ_{con} represents the reactant's mass transfer limit, affecting maximal output. This transfer is due to the ability of mass transfer being reduced, thus concentrations of oxygen and hydrogen reaching current demands at higher values. The supply of reactants is then given a maximum limit when the cell is no longer increasing current density efficiently. The concentration loss can be expressed as Equation 101 and does not affect efficiency under peak conditions (Saeed & Warkozek, 2015) (Um et al., 2000).

$$\Psi_{con} = -Real(\frac{RT}{zF} ln(1 - \frac{i_{cell}}{i_{lim}})). \tag{101}$$

With concentration and material losses, the updated value of fuel cell voltage J_{cell} is calculated. The power output of the stack is determined by total voltage output J and stack current I, as the stack voltage is the product of the coupled cells in series, thus described as $N_c J_{cell} = J$. The stack power output is calculated with Equation 102, excluding the energy losses from equipment consumption.

$$P_{stack} = J\, I. \tag{102}$$

In the fuel cell stack, the consumption is only from supporting utility ($P_{consumtion} = P_{utility}$), which consists of pumps for conveying water and creating sufficient back pressure enough to not flood the cell, additionally to the cooling circuit pump.

$$P_{output} = P_{stack} - P_{utility}. \tag{103}$$

The utility consumption can increase if the stack is disconnected from pure oxygen supply and atmospheric air is utilized, as a compressor is inserted to increase internal air pressure.

3.4 Major equipment

This section describes the fundamental theory utilized for equipment in process modeling, with a brief introduction to the application.

3.4.1 Steam cycle and Turbo-machinery

in a plant to generate electricity and heat, the boiler is connected to a steam cycle. The main components found in all steam cycle calculations are a steam turbine, heat exchangers, condensers, pumps, a deaerator, and a steam drum. The mathematical model, while retaining all the main components, differs in its layout. For example, amount of turbines, district heating condensers, or process piping design can vary and is configured for each specific steam cycle. A general flow diagram of how a cycle is calculated is presented in Figure 16.

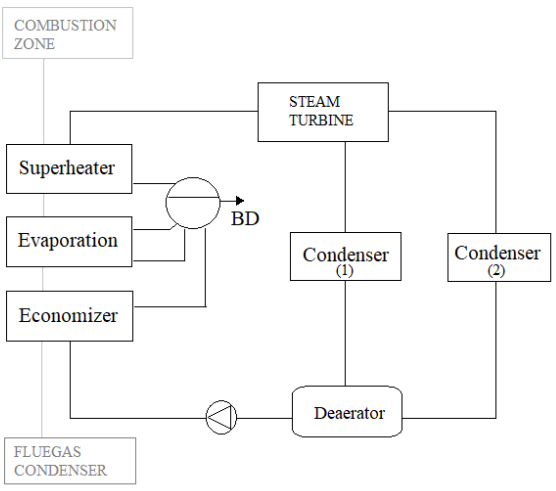

Figure 16: Graphical representation of how the general setup of the mathematical model is designed. This, however, is only a simplified representation and is configured to fit the specific plant model.

The calculation process in all the equipment is based on mass energy balance, and changes in specific enthalpy decide the next state of the steam, liquid or vapor. The state includes the variables mass, pressure, composition, temperature, heating value, enthalpy, entropy, and vapor fraction. The energy and mass balance equations can be applied, with the heat generated by combustion making the steam reach the preset cycle conditions and enter the steam turbine, whereas the exit conditions of the steam turbine stage are calculated with the isotropic efficiency as presented in Equation Equation 104. To achieve the specific enthalpy of the output h_2, the steam expands to the same pressure as the theoretical output enthalpy h_{2is}. In the expression, the specific enthalpy of the input h_1 represents the initial stage.

$$h_2 = h_1 - (h_1 - h_{2is})\eta_{s,ST} \tag{104}$$

Applying theoretical calculations directly, with values representing actual mass flow but without information on flow relation between condensers 1 and 2, is not a feasible model. In order to apply the mass and energy balance for the steam turbine, the condenser 1 is calculated by using the district heating demand Q_{DH}, as described in Equation 105, thus a minimum amount of mass flow $\dot{m}_{DH}$ can be updated in next iteration.

$$Q_{DH} = \dot{m}_{DH}(h_{out} - h_{in}). \tag{105}$$

The state and output of condenser 2, representing cooling water, are altered to fit the steam cycle iteration that is based on the bisection method. After the deaerator, and mixing of incoming saturated water at minimum temperature, steam reconfigured is fed back to the steam generator heat package consisting of an economizer, evaporator, and superheater, which cool down the boiler flue gas and generate heat.

Pumps and compressors exist in all mathematical models, with input parameters deciding the desired state of output after pump or compression. The updated state is calculated by applying the pressure and thus the increase of the temperature of gas. In Equation 106 the outlet temperature is calculated through compression of an ideal gas, as the thermal capacity and temperature define the enthalpy of outgoing gas.

$$T_2 = T_1 + \frac{T_1}{\eta_{s,AB}} \left[\left(\frac{p_2}{p_1} \right)^{\frac{\gamma_a - 1}{\gamma_a}} - 1 \right]. \tag{106}$$

In the water pump, the steam Table is utilized to calculate the outgoing enthalpy, which originates from mathematical linear approximations (M. Holmgren, 2023). The power consumption is then expressed as the change of inlet and outlet-specific enthalpy.

$$P_{equipment} = \eta_{mech}\dot{m}(h_2 - h_1). \tag{107}$$

Calculating the generation of electricity through steam turbines follow a similar approach as the compressor, with the difference in specific enthalpy deciding output mechanical power. The generated power can then be calculated by multiplying the product with generator efficiency η_{gen}.

3.4.2 Purification and cleaning

The primary objective of syngas cleaning is to remove contaminants such as tar, particulate matter, sulfur compounds, and heavy metals from the gas stream. These impurities can cause corrosion in downstream equipment and reduce the efficiency of processes. To calculate the impact of pollutants on the product syngas from the gasification stage, the S, C, and O molecular structures are assumed to follow the balance reaction 108,

$$H_2 + S \rightarrow H_2S. \tag{108}$$

and balance reaction 109 describing hydrolysis stage.

$$COS + H_2O \rightarrow H_2S + CO_2. \tag{109}$$

In the calculation sulfur separation follows the balance reaction, giving a content penalty for hydrogen in gas depending on the size of sulfur exiting the gasifier. Sulfur is completely removed from energy and mass balance during cleaning, thus no other penalty except power, temperature drop, and hydrogen content is calculated during this step which is connected to the wet scrubbing.
In the cleaning steps, heavy tars or large particles leaving the gasifier island are not calculated, and they are assumed to be removed in the cyclone or bag filter before entering the next process. For cases requiring conditioning of the gas, mathematical models for cleaning, separation, or purification are not executed, except

for sulfur removal, and basic stoichiometry is applied. Instead, pressure and temperature are adjusted to meet the conditions through a specific state of the product gas. For example, increasing temperature and pressure to x and b, respectively, give the recovery rate of z for a chosen cathylic base, thus creating the new state of product gas as described in Equation 110.

$$z = process(x, b). \tag{110}$$

A similar approach is applied to the case of electrolysis process models, including energy penalty for water purification.
Details on requirements for each component are found in Appendix 2.1.1, and certain conditions need to be fulfilled, for reaching a passable purity grade in order to assume the pollutant is completely removed from downstream calculations.

3.4.3 Heat exchangers

Heat exchange between streams is described by applied thermodynamics, as various calculation methods are utilized to solve the state of output streams from the heat exchanger. The selection of the method is dependent on the complexity of flows or how the heat will be transferred. The initial method for solving the outgoing temperature of streams in a HEX is the Epsilon NTU method, with the main heat equation, expressed as Equation 111.

$$Q_{trans} = U\ A\ (T_{hot,in} - T_{hot,out}) \tag{111}$$

The transfer coefficient U and tube area describes the conditions of the tube heat exchanger (DeWitt, 2006). To calculate the effectiveness of the heat exchanger through the NTU method, the first step is to define the stream thermal mass capacity value ϑ, as in Equation 112 and 113.

$$\vartheta_{hot} = \dot{m}_{hot}\ c_{p,hot} \tag{112}$$

$$\vartheta_{cold} = \dot{m}_{cold}\ c_{p,cold} \tag{113}$$

A function for finding the lower and higher values, ϑ_{min} and ϑ_{max}, is applied to evaluate the streams shared constant ϑ_r with Equation 114. Equipment-specific parameters define the NTU number with Equation 115.

$$\vartheta_r = \frac{\vartheta_{min}}{\vartheta_{max}} \tag{114}$$

$$NTU = \frac{UA}{\vartheta_{min}} \tag{115}$$

The NTU number is utilized to generate the effectiveness of the heat exchanger, depending on the selected type of tube heat exchanger and flow configuration.

$$\eta_\epsilon = \frac{1 - exp(-NTU(1 + \vartheta_r))}{1 + \vartheta_r} \tag{116}$$

Equation 116 represents the effectiveness of the parallel flow of streams inside the heat exchanger, and Equations 117 and 118 for counter-flow movement (Equation 117 is valid for ϑ_r equal to 1, Equation 118 otherwise).

$$\eta_\epsilon = \frac{NTU}{1 + NTU} \tag{117}$$

$$\eta_\epsilon = \frac{1 - exp(-NTU(1 - \vartheta_r))}{1 - \vartheta_r exp(-NTU, (1 - \vartheta_r))} \tag{118}$$

After defining the effectiveness, the heat transfer for the stream is calculated as described in Equation 119 to obtain the amount of heat transferred.

$$Q = \eta_\epsilon\ \vartheta_{min}(T_{varm,in} - T_{kall,in}) \tag{119}$$

Through Q, the temperature of outgoing streams can be calculated as Equation 120 for the heating medium, and Equation 121 for the heated medium. This also applies to cooling.

$$T_{hot,uot} = T_{hot,in} - \frac{Q}{\vartheta_{hot}} \tag{120}$$

$$T_{cold,uot} = T_{cold,in} - \frac{Q}{\vartheta_{cold}} \tag{121}$$

This calculation can be applied for any flowing medium, that is, if the drag or turbulence inside equipment can be approximated.

3.5 Economy

In this section theories regarding investment cost, economic performance indicators, and system benchmarking are presented.

3.5.1 Economical performance

In order to calculate the economic state of the plants, it is required that the necessary investment costs are mapped, as this lays the foundation for the financial feasibility. Only components that are assumed to have a high relative cost are treated in the calculations. In the case when data derives from a facility of a different scale than the one applied in the current model, equipment cost is dimensioned according to Equation 122 to generate a price estimate C for the component,

$$C = C_0(\frac{s}{s_0})^f \tag{122}$$

and C_0 is the reference cost. Variables s and s_0 are the dimension value of the plant, additionally the dimension value of the reference, respectively, f is the scaling exponent, which is the factor determining equipment sizing effect on price. In order to approximate the cost for equipment having values documented before the current time, the exchange rate proportional to the year 2023 is accounted for.

$$C_{estimated} = C_{historic}\, \iota_i. \tag{123}$$

Equation 123 presents the formula used to determine the current investment cost of components. The inflation-weighted constant ι_i, is generated by comparing present and historic change rates. To determine net present value, the net cash flow NCF is calculated, which is descriptive of gross income subtracting the expenses of the facility, which is presented in Equation 124. C_{OPEX} and C_{CAPEX} describe the annual operating cost and the capital investment cost.

$$NCF = C_{income} - C_{OPEX} - C_{CAPEX}. \tag{124}$$

Net cash flow that accounts for the annual discount rate calculated through a similar method as the tax from gross income is suppressed due to the discount rate. Please note that equations also include the current year from starting the payment plan, as income and OPEX increase annually due to inflation. The net present value (NPV) is calculated according to Equation 125 and is a value that defines the economic performance of the facility by translating future income and expenses into the present value. A value of NPV > 0 is considered a profitable and positive result. Calculating NPV, year 0 is the initial time of investment and constant production is assumed unless otherwise stated.

$$NPV = \sum_{Z=0}^{Z} \frac{NCF_Z}{1 + DR^Z}. \tag{125}$$

In the equation, DR denotes the discount rate and Z is defined as the current period. The investment cost, CAPEX, of the facility, and income are the fundamental values calculating economic performance. An alternative method of measuring the economic performance of the facility can is determined by calculating the payback time (PBT). The period of payback is calculated as the number of periods required to achieve a NPV equal to 0 and represents the time required to pay off the facility's investment cost. A shorter payback time is reached, indicates the time required, and generates a decreased time for the facility to be economically beneficial. Another economic indicator is the internal rate of return, IRR, which is the expected annual return on the investment to assure a NPV equal to 0 after a specific time. The metric IRR takes into account the time value of money and is calculated through each period. A value of IRR is obtained by iterative calculations of Equation 126.

$$0 = NPV = \frac{NCF_z}{(1 + IRR)^z}, \tag{126}$$

3.5.2 Benchmarking

When calculating the economic and physical relation into a converged model, the theory of utilizing the variable market over time to benchmark economic performance is executed mathematically. To set the initial parameter determining the overall annual activity for the electrolyzer and fuel cell, a threshold is applied for activating the equipment, consuming or producing electricity depending on the spot price. The flat rate modulation is used for this particular system that stops the production of hydrogen after a certain threshold and is a simplified application similar to those derived from documented cases in literature (Nguyen et al., 2019a). In Equation 127, the fixed price $Fixed_e$ represents the threshold, producing a time vector $\vec{t_1}$ with hours of hydrogen production.

$$\vec{t_1} = f(Fixed_e < spotprice(t)), \quad and \quad t = 1\, or\, 0. \tag{127}$$

The time vector has a length equal to the number of hours during the year, with activation indicated with values 1, and 0 if the equipment is shut down. The time vector can be expressed as Equation 128.

$$\vec{t_1} = \begin{bmatrix} x1 \\ x2 \\ .. \\ xn \end{bmatrix}, \quad and \quad \sum_{8760}^{1} \vec{t_1} = 8760\, max. \tag{128}$$

The vector describing the activation of the fuel cell or electrolyzer during balancing, either by receiving power in the electrolyzer or output power to the grid, is not set by any threshold for nominal spot price activation. The activation is instead based on the specific support service price and demanded volume, while only providing the balancing service during a limited time on the specific hour, observed in Equation 129.

$$\vec{S}(t) = \nabla f(P_{volume}(t) < Fixed_{cap}). \tag{129}$$

Due to the uncertainty of the actual time span and when the activation of the reserve is required during the biding hour, 1 service per hour is applied and a selection process between services is initiated to achieve maximum economical performance. In selection, the prediction of actual activation time length is dependent on volume, and volume demands over a certain threshold render slightly longer balancing time than the anticipated average, or shorter for volumes under the fuel cell capacity. Equation 130 express the method by which the activation time length is scaled after the demanded volume, and δ_{S_i} is the time scale factor that is limited. The scale factor's critical value is set so that the estimated activation time can not be higher than the quadratic product of average balancing time.

$$\Lambda(t_2) = \vec{S_t}\vec{t}_{S_i} t_{avg} \quad and \quad \vec{t}_{S_i} = \frac{\vec{P}_{volume}(t)}{P_{S_i}} \quad and \quad t_{S_i} \notin \vec{t}_{S_i} > t_{avg}. \tag{130}$$

The actual activation time is then calculated as the product of each activated service (Ω_i) and weighted activation time,Λ_i, during the specific hour, as expressed in Equation 131.

$$\vec{t_2} = \sum_i \vec{\Omega_i}\vec{\Lambda_i}. \tag{131}$$

Variable i represents the support services. In Appendix 1.1 the economical calculation and utilization of activation time of support services are illustrated. The activated service times Ω_i are the price and volume optimized vector of support service selection and output the time when balancing is active, as presented in Equation 132. Accordingly, $S_{p,i}$ represents the product of the price and volume of a specific service.

$$\vec{\Omega_i}(S_{p,o}, S_{p,b}, S_{p,c}, ...) = \begin{bmatrix} S_{p,o} > S_{p,b} & S_{p,o} > S_{p,c} & ... \\ S_{p,b} > S_{p,o} & S_{p,b} > S_{p,c} & ... \\ S_{p,c} > S_{p,b} & S_{p,c} > S_{p,b} & ... \\ ... & ... & ... \end{bmatrix}. \tag{132}$$

The updated activation time of support services is then subtracted from the production time and added to avoid an accumulation of time exceeding the feasible amount. The total actual activation time is then quantified as t_{tot} or activation time vector $\vec{t_{tot}}$, calculated with Equation 133.

$$\sum \vec{t_{tot}} = \sum_{8786} (\vec{t_1} - \vec{t_1}\vec{t_2}) + \sum_{8760} \vec{t_2}. \tag{133}$$

The output time vector $\vec{t_{tot}}$ is the total time in second resolution, and the specific hour of basic power production is not distributed entirely, as the support service only requires a fraction of the nominal activation hour. The

same equation is applied in the case of fuel cell activation, as the fixed threshold for fuel cell activation is calculated as Equation 134, and Y is a configurable variable that logically should be set as the efficiency of the fuel cell (although this is not fixed and can be changed to test economical equity to the model).

$$Fixed_{FC} = \frac{Fixed_e}{Y}. \tag{134}$$

In determining the specific hours when the fuel cell or electrolyzer is active, the threshold is based on a factor $Fixed_{FC}$, as the factor is required to be greater than the threshold $Fixed_e$ to generate economically beneficial results, thus creating time vectors with positive integers not exceeding 1 as described in Equation 135.

$$\vec{x_0} = \vec{t_{tot,FC}}, \quad and \quad 0 \leq \sum t_{tot,FC} \leq 1. \tag{135}$$

In balancing the hydrogen storage and exchange, $\vec{t_3}$ is the vector representing the time when hydrogen is extracted out of the system, with DM as the total annual demand distributed on the sum of $\vec{t_3}$. Equation 136 expresses the consumption of hydrogen, from selling the gas as a product.

$$\vec{\omega} = \vec{t_3}\, DM. \tag{136}$$

The dynamic performance of the cell is measured by the accumulated time under sub-optimal operation and nominal operation, signified by the change in electrolyzer or fuel cell load. The overall production penalty for the accumulation of ramping time and production flux is calculated in Equation 137 as $\eta_{production}$ and will thus affect the production of gas.

$$\eta_{production} = \frac{\vec{t}_{P,optimal}}{\vec{t}_{P,optimal} + \vec{t}_{P,sub}}. \tag{137}$$

In order to simulate the dynamic storage, time operators change to the activity of each parameter $x = \frac{activity \times t}{P_{indicate}}$ and are multiplied with the production of hydrogen to simulate the active exchange of gas between fuel cell, electrolyzer and sell of gas.

$$\hat{\phi} = \dot{m}_{H2,E}(\eta_{production}\, \vec{x}_{tot} + \vec{x}_{0*}) - \vec{\omega} - \dot{m}_{H2,FC}\, \vec{x}_0. \tag{138}$$

x_{0*} represents the power received from the balancing grid, meaning the non-nominal production of hydrogen. The vector representing the exchange of accumulated hydrogen $\hat{\phi}$ is added to the initial amount of hydrogen in storage $Storage_{initial}$ to prevent the exchange of hydrogen if no hydrogen is available in storage. The cumulative sum of the product in Equation 139 is then the mathematical representation of storage dynamics.

$$Storage <= \hat{\phi} + Storage_{initial} \tag{139}$$

In terms of byproducts, the district heating is dispersed momentarily and is not assumed to accumulate. The calculation of oxygen supply is based on the same main line equation as hydrogen but with no initial storage and constant consumption of supply.

The reliability of product supply is based on the availability of the plant, the general formula being presented in Equation 140, as the time during partial load and full load is represented by t_{acive}.

$$a = \frac{t_{active}}{t_{active,tot} + t_{off}}. \tag{140}$$

In order to numerically estimate the probability ζ of each outcome, utilization of each specific plant is combined in the manner of $p(a) = a$, as seen in Equation 141 representing the probability of capacity supply.

$$\zeta = p(a1)\, p(a3)\, p(a3) \,..\, p(an). \tag{141}$$

The probability of no availability, or the change of state, off, for the specific plant's availability is calculated as the inverted nominator for each case $p(1 - a)$, thus is utilized instead of activation, creating several possible combinations of such equations describing the probable outcome.

4 Method

In this section, overall methods for solving the research end goal, are described, also a review of material is briefly discussed under Section 4.1.4.

4.1 Method description

The overall method in this work is to create simulations through programming in MATLAB2021b that performs the calculations mentioned in the theory section, while literature studies and mapping of existing and design processes to fit plant layout form the basis for how the content is computed. To calculate the dynamic activity between fuel cells, energy storage, and hydrogen production, a model is created through programming in the calculation tool, as the facilities work to deliver electricity, support services, district heating, and hydrogen. To determine the economic performance of the plants and benchmark results, calculations and programming in Excel are executed, which are activity-based from determining technical performances.

4.1.1 Matlab 2021b

To simulate a calculation model of the plant, mathematical programming is utilized in order to freely customize reactions and processes in the simulation, whilst maintaining computation times to a moderate level. The tool that has been used is MATLAB, which is a programming and numerical calculation platform that provides the opportunity to analyze data, develop algorithms and create models. The process models for the facilities are based on built-up concepts gathered from literature and by having their physical processes translated into mathematical code. The numerical tool can additionally print a graphical representation of the result that contributes to analyzing the results. The tool MATLAB also includes software called Simulink that provides support with computation of control systems to test models in live iteration, for example, to measure fuel cell ramping performance (*MATLAB version 9.7 R2021b*, 2022).

4.1.2 Aspen plus 10V

Aspen is a flowsheet tool that can with given values calculate basic chemical reactions and mass energy balances. In this thesis, Aspen will only be used as an extension to calculate the effect on CCS during oxyfuel combustion in KVV8. Aspen can be used for most of the calculations about the gasification processes as well to verify less advanced steps outside the gasification process but is not used due to the complexity of the kinetics and the long computation time.

4.1.3 Approximation methods in computation

In order to generate plausible flows in the model that do not depend on the direct order of the physical modeling, some streams need to adapt themselves to match the continuous equations of the model. For example, the distribution of steam cycle condenser mass flows, requires downstream flows to adjust for function replicating the real-life plant when district heating demand and heat added to the system alters. The Newton method is in this thesis applied for the gasification computation, for example, to renew the flow of downstream syngas from the freeboard or the rate of char conversion and thus the particle mass-flux out of the reactor. The method is called the Newton method or the Newton-Rahpson method and is a root-finding algorithm that, through iterative calculations approximates and solves an equation (Raphson, 1697). The bi-section method is utilized in computation to solve mass, energy, and temperature flow rates. The advantage of using this approach is that the convergence is guaranteed and the error can be controlled, as the fitting for numerical calculations that have infinite solutions. On the other hand, in some cases, it cannot find the root, and convergence may be slow especially depending on precision (R. & D., 1985).

4.1.4 Data collection

A basic prerequisite for the model created to be considered physically applicable is that the location and existing structure support the integration of new technology. In those cases gasification is considered applicable, field surveys have been carried out in consultation with a plant expert to take measurements and connection points where the new reactor unit can be connected. In order to make correct simulations, process drawings, and operating data are treated to determine the parameters of the steam cycle, fluidized bed, size, and quality of

the fuel raw material.

For the market research and the electrolyzer, historical data strings are collected on electricity prices, support services, and heating demand of current periods. The data is reviewed and compared with collected data from the RISE department for hydrogen, in order to assess the credibility of the material. The data collected to estimate the oxygen value is linked to the internal performance of the co-generation plant located in the vicinity of the electrolyzers, as operating data under varying amounts of oxygen is analyzed to link the energy consumption of downstream applications.

Information not derived from existing systems or facilities, for example, the density of bed material, is taken from literature and applied only if two or more sources exist that can verify the value, which then proves that empirical material is followed.

4.2 Program: Technical performance

To apply the theory for each individual case, the calculation tool is used by defining the input data, which is then processed and generates a string of output data.

4.2.1 Main script: Plant modeling

The structure of the script, representing designed process plant models, is made up of several sub-scripts and functions which are then called in the main program to calculate a result sending it back to the main script. Input data is required to start the calculation, which means defining the parameters of the various components, the states of the processes, and external factors such as outdoor temperature and heating demand. With this input, the various sub-scripts are called in order and finally calculate, using mass-energy balance, the result of the plant's performance. In each subscript, a process is calculated, for example, chemical reactions or compressing gas utilizing known theory. The output flow of the respective process is given by updated temperature, mass, composition, vapor fraction, enthalpy, state of energy, and pressure. Other outputs of these functions or subscripts are computed separately, for example, the power consumption of the specific component or reject material flows. In combustion processes, air separation units, and gasification functions of relatively shallow complexity, the mass is undefined and only expressed in a number between 0 and 1 that represents the proportion of fuel or air. This is because the amount of fuel is calculated depending on the consumption of the boiler and the boiler or reactor to achieve the target temperature. The oxidation point from the combustion is then used to recalculate the mass in the gasification section, the iteration is performed and a new quantity of biomass with updated parameters goes through the process once more, in iteration, to output the final mass balance. Steam cycle, char conversion, gasification, and combustion are processes that require iterative calculations, that are solved by approximation. The approximation methods are central for the scripts to function and are defined by either the Newton method or the bi-section method to update the correct dimensions of steam flows, oxidation, conversion time, or mass fluxes in general until a steady state is reached.

In the gasification script, the theory is used to calculate gasification syngas flow and mass flow of char by the semi-kinetic model, or kinetic models with single course complexity. After all process stages are calculated the final result is presented, which is descriptive of the plant's technical performance. Losses in the model are calculated or predetermined. Assumptions are that pipes are completely isolated and no heat is lost due to transport between stages, only internal. No components except the heat exchanger have U value, since the transition of heat losses out of the model is limited to radiation loss of the boilers and electrolysis unit.

The scripts for the electrolysis are based on the same premise with only structural differences and overall lower complexity. In this type of script, the cell performance is initially calculated, which then is translated to the demand and output of a single stack. Fuel in this case represents the electricity demand and water, instead of solid fuels, air, and steam for the combustion or gasification. If there is any outcome in a process or called function that violates fundamental physical laws, for example, a sum of composition shares below 100 %, the computation is stopped. Even too low fuel flows during combustion, temperatures, or deficit of oxygen, generate an error code stopping the computation.

4.2.2 Program: Support services and activity

To calculate the activation together with the performance of the electrolysis and fuel cell platform, called Ägir 1, a threshold is required on which the cell or stack is active. This threshold is set by iterative calculation in the

program when the economic profit of the whole plant is at its peak, as described in Section 3.5.2. The program is calculating the process in steps, by initially determining the current market that is given, and outputs the total activation time. Activation is the input for functions representing the specific clusters of electrolyzers and fuel cells. The functions for the technical equipment are split into two modes to simulate the ramping of each stack, which operates at different loads during the start of activation. The second stage in the program optimizes and selects support services for electrolyzers based on volume and compensation pricing. The same process is applied to support services up for fuel cell activation, taking also into account the price of the general spot market, thus resulting in the most cost-effective distribution of balancing reserve. The third step synthesizes the information computed by each production method, thus calculating accumulated production and consumption of the hydrogen, with a preset of an initial state of the storage. Please note that the storage is simulated because of problems that can occur with the support services and basic use of power-to-gas-to-power service from the fuel cell. The target of the analysis is to balance the gas in the storage while continuously also selling the gas and providing support services to the grid. In the case of auto-balancing, iterations are then applied to balance the storage with the help of minimizing hydrogen production and stop of the gas-to-power basic service. A simplified description of the algorithm process is presented in Figure 17. During the peaks when supply over-exceeds the capacity threshold, hydrogen is assumed to be stored externally from the continuous selling of hydrogen. Another balancing is made by trial and error until peak conditions can be identified. After the balancing of each parameter is made, a primary economical estimation is executed. Additionally, the byproducts water and oxygen re-circulation are calculated, to decrease operational cost if not the function with atmospheric compressor is used. No fitting of the phase of the grid is accounted for mathematically in the program, since a battery is included in the cluster, and evens out frequency or reactive displacement.

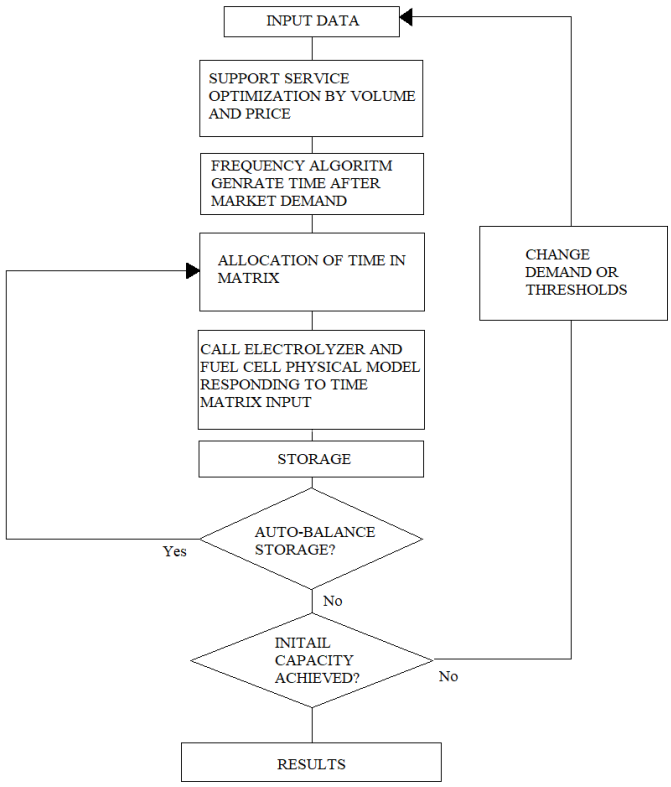

Figure 17: Flowchart of the benchmark algorithm utilized to optimize services and activation with hydrogen production.

The gasification script is similar script as the Ägir 1 platform in the initial state, but with activation based on load without any interference from the spot market or support services, since hydrogen is the primary product of the gasification. The script also shares the same method with storage but with only selling hydrogen as a consuming service. no second resolution is applied since there is no need for applying high-resolution simulation.

The combined gasification, fuel cell, and electrolyzer scripts calculate the combined performance of the system, as fuel cell size can be increased to deliver a larger portion of service, or hydrogen can be sold in larger volumes in an attempt to satisfy future demand. The methodology of this is the same as previous methods and

the facilities work independently except in the generation of supplied hydrogen or district heating.

4.3 Value of oxygen

When calculating the value of oxygen from electrolysis, the varying performance of the adjacent CHP and post-combustion CCS is working as a metric. The method of calculating the impact of oxygen enhancing the air input consists in initially computing the flue-gas composition, mass, and boiler temperature change dependent on the added parts of oxygen in the inlet air. This is designed with the same base as the boiler and gasification program. The data strings gathered from the calculation are then inserted in the Aspen model, obtained from Stockholms Exergi's own model, as presented in Figure 18. By simulating the updated data, the performance can be measured, thus supporting the estimation of a reduced operation or investment cost for the future installation of BECCS in Värtahamnen.

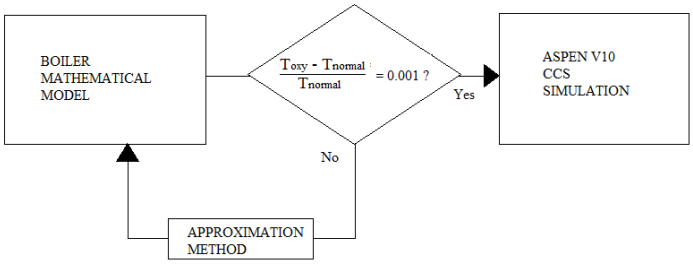

Figure 18: Iterative process of the CCS performance calculation.

To simulate realistic values, an iterative process is required to optimize boiler temperature, by recirculating the flue gas downstream back to the combustion, thus cooling the combustion process to nominal working temperature and controlling oxygen content in emission from the stack. In order to retrieve usable results, a normal run is executed and compared to real process flows.

4.4 Proposed models

To analyze the possibilities of regional scale integration of hydrogen production, a screening of the alternatives is established to determine results in the following proposed models. The basis for the decision is the location and opportunities for the technology, which is illustrated in Appendix 1.1. By investigating the current layout of the plants and opportunities for integration and replacement of current boilers, process models of the new systems need to be mapped in order to execute any type of simulation. The proposed models consist of four types of gasifiers and one type of electrolysis-based platform. All models have hydrogen as the main product, with the exception of the electrolysis platform, which delivers of balancing grid as a shared main product.

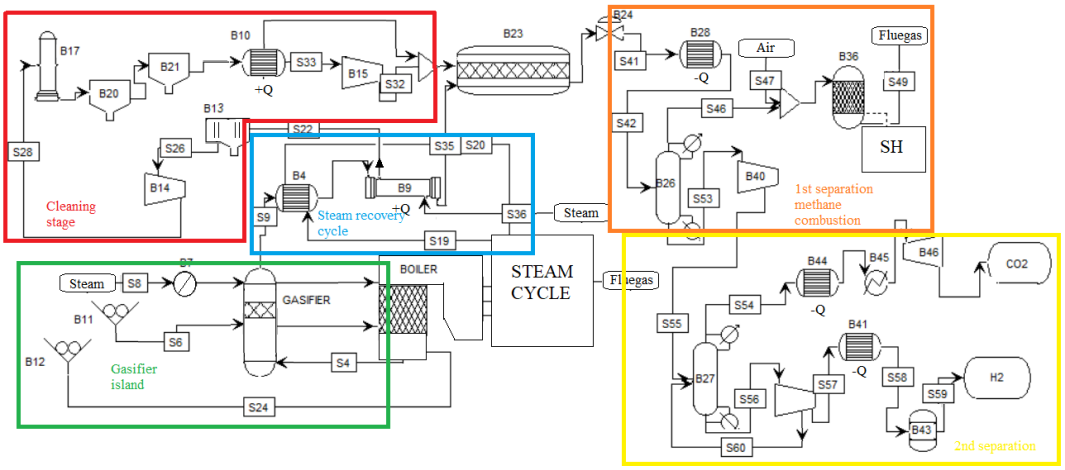

Figure 19: Process flow diagram of the proposed integrated gasifier system, named Idun 1a. The boiler process and the steam cycle are illustrated as a box, of the existing plant, thus is not shown due to confidentiality.

In Figure 19 a process model is presented, showing how the Equation based mathematical simulation is structured, and all the equipment pictured is calculated in steps based on the integrated gasification model. A list containing of all the suggested process models, operational parameters, and calculation results can be observed in Appendix 2. In the Figure beginning with the gasifier island, the gasification reactor is present and connected by circulating bed material (S4), heating of steam (B7) through central HEX, and grinding of solid fuel (B11). In the steam recovery cycle, syngas cooling (B4) and heat transmission (B9) in a shell and tube heat exchanger are present to produce high-pressure steam to the existing steam cycle for downstream applications. In the next stage after cooling, the syngas is fed through the bag filters (B13) and conveyed with a fan (B14) or expanded before entering the cleaning stage. The cleaning stage consists of scrubbers (B17) and other equipment indexing the separation points (B20, B21). The cleaning process is illustrated further in Appendix 2.1.1. In the cleaning stage, condensing of water and compression of dry syngas are made to match the operation state for water gas shift reactors (B23). The condensed water is utilized for the water gas shift after internal pressure is equal to the dry syngas and is then mixed.
In the 1st separation stage, CH_4 and leftover CO are separated (B26) and combusted (B36) with atmospheric air. The heat generated by the reject gas combustion is utilized as a complementary source of heat to the heat exchange cluster (SH). Note that the CH_4 is not vital for creating high-pressure steam in this particular case. The labels called *Steam* are descriptive of the input of low-pressure steam or water since they represent the material flow and not the inlet state. In the calculation, these types of flows are at ambient temperature and at atmospheric pressure. After the 1st separation stage, the 2nd separation stage is calculated, as syngas is purified by PSA (B27), a process resulting in separate material flows of CO_2 and H_2. The CO_2 is cooled after the separation, cooled (B44) to atmospheric temperature, and then subcooled (B45) with cooling utility to the desired temperature, before expansion (B46) of the gas. The product of the CO2 is then stored as a liquid and ready for transportation. The H_2 stream is then compressed to 30 bar, cooled in a heat exchanger (B41), and passed through a last purification (B43) step before entering the storage as a final product. Condensers and heat exchangers have the same visuals in this flow sheet, with $+ - Q$ indicating if the step requires heat or output heat to the central heat exchange cluster (SH). The excess heat from the cluster is utilized in for district heating applications, combined with the accumulation of high-temperature condensed water throughout the process.

The facilities of which the different gasification systems are investigated are *Högdalenverket* and *Bristaverket*. After Consultation with the management at Stockholm Exergi, boiler P6 at Högdalen and B1 at Brista were suggested as suitable for integration, while boiler P3 at Högdalen is the only boiler relevant to be replaced completely. For strategic purposes, the gasifiers have a maximum limit for the dimension when being integrated into the boilers. In Figure 20 and 21, an illustration of the placement of the proposed gasifier integrated with the respective boiler is shown.

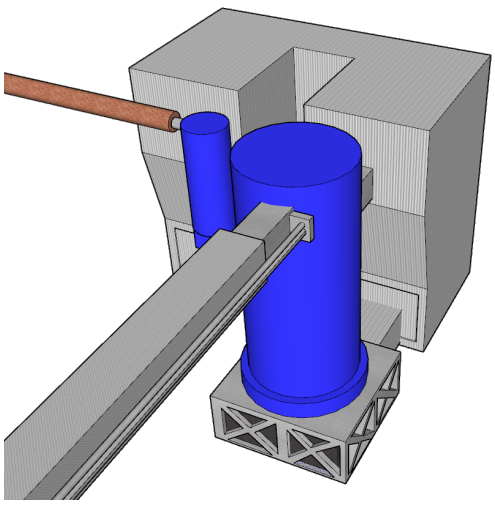

Figure 20: Gasifier for system Idun 1a, connected to the boiler sand trap called intrex, with the connection in the upper freeboard surface for circulation of remaining particles. To the right of the gasification reactor a smaller cylinder is placed which represents the feed separation of heavy particles residing in the synthetic gas, leaving the gasification stage.

It should be noted that the figures presented are made only for illustration purposes for placement strategy, and do not represent the complete system.

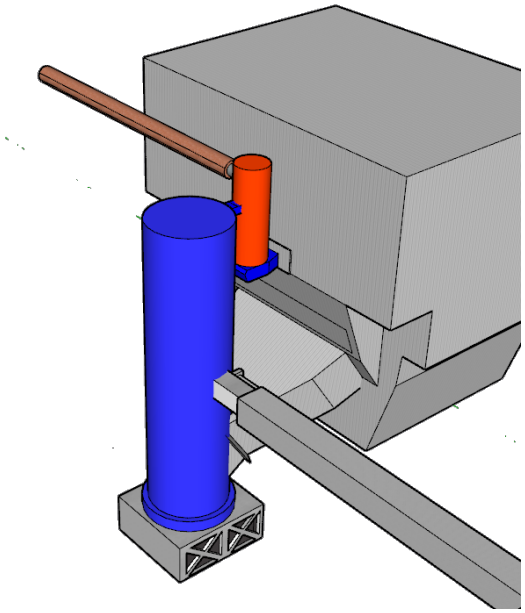

Figure 21: Gasifier Idun 1b, connected to the boiler sand trap called intrex, and connection in the upper freeboard surface for circulation of remaining particles. To the left of the gasification reactor a smaller cylinder is placed which then represents the feed separation of heavy particles residing in the synthetic gas, leaving the gasification stage.

In Figure 22 a process diagram of the AEL stack for the electrolysis platform is presented, the representation does not include the fuel cell or surrounding equipment connected to oxygen or hydrogen utilization. This process is based on the suggested design by literature (Sánchez et al., 2020), with the only difference located within the cooling circuit (Sakas, 2021). Water is assumed to have been passing the purification de-ionization stage before entering the simulated process, and is applied with the premise of an energy penalty to the process simulation.

To initiate the process, the inlet water is pumped (B3) into the H_2 separation chamber, followed by agitation (B2) with electrolyte and water. The water is not to be preheated, since compression of the pumped water and re-circulation of condensation, heats the water over the operating temperature. In the agitation and mixing, water from O_2 and H_2 separation (B, E) is included. The product gases from the electrolysis product then pass the purification and de-watering stage, as demisting and drying of the H_2 is executed before sequential compression (B12, B1) and heat exchange (B10) of the H_2 is made to recover sensible heat for the cooling circuit. The oxygen is separated from water, with no additional purification. The product gasses are then stored at 30 bar for H_2 and 20 bar for the O_2 by-product.

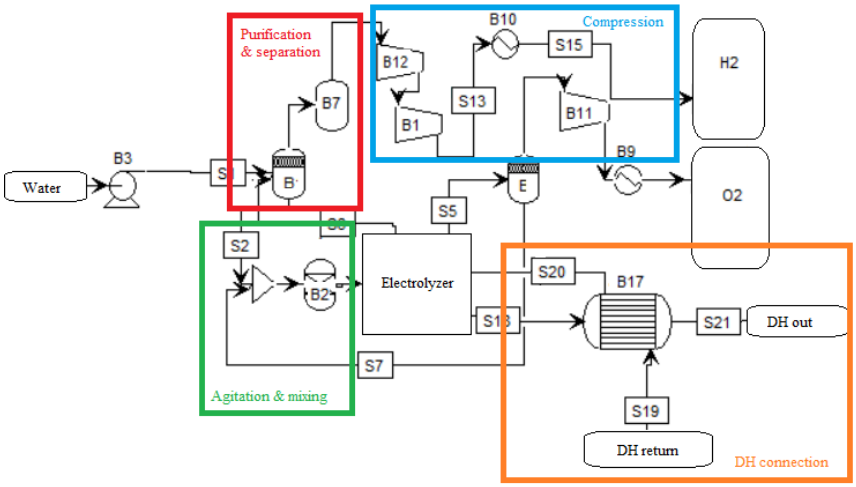

Figure 22: AEL electrolyzer process model, connected to district heating.

The electrolysis cooling system and internal coolant feed pump are coupled to the central district heat exchanger (B17), and return water from the district heating is heated by the coolant water from the electrolysis platform (Burrin et al., 2021). This completes the proposed model for the AEL stack. The PEM stack layout is assumed to work similarly to this process, with an exemption of equipment related to the increased pressure surrounding the electrolysis.

In order to simplify the documentation of the proposed models, different names are assigned to each system as presented in Table 9. Each gasifier model is scaled to fit the environment, with the available space as the only constant, since the fuel feed rate is assumed to be continuously saturated.

Table 9: List of the proposed hydrogen production facilities.

Facility	Idun 1a	Idun 1b	Idun 2a	Idun 2b	Idun 2c	Ägir 1
Main technology	DBFB	DBFB	CFB	EF	Downdraft FB	AEL/PEM
Input capacity (MW)	72	23	45	49	10	5.1
Location	Högdalen	Brista	Högdalen	Högdalen	Högdalen	Värtan
Replacing Boiler	No	No	P3	P3	P3	No
Connected Boiler	P6	B1	No	No	No	P8

Multiple systems replace the P3 boiler in the Table because the names a,b, and c stand for the alternative of Idun 2 configuration. This thesis includes the evaluation of technologies listed as the most cost-efficient alternative for this kind of replacement, meaning that only one of the gasification technologies will be selected as a final proposition and not altogether replace the P3 boiler.

4.5 Market study

The analysis method of the benchmark is by analyzing historical market data within the span ranging from 2017-2022 to apprehend relevant information. Moreover, the utilization of mean values for historical counterparts in the study is set to a minimum to achieve realism in the economic and performance output. For example, the market preset for each string of volume utilize the respective string of active pricing as seen in Figure 23.

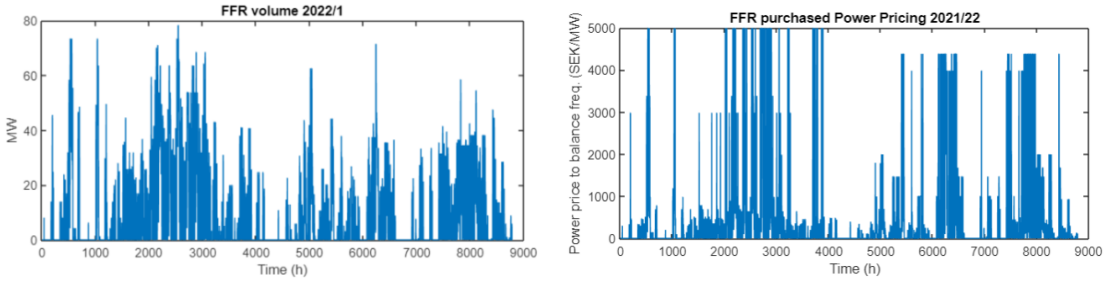

Figure 23: Example of data string containing demanded volume and market price for capacity compensation over the year 2021-2022.

The execution of all models is activity based with the assumption of working loads for the gasifier since it is not entirely controlled by the boiler load. The price for fuel is derived from a quarterly analysis of historical data of market value presented in Appendix B12.

In the case of an information gap for economic data, especially regarding data on support services, the demand and pricing are observed to share some linear similarity and can be replicated. For example in Figure 24 this connection can be observed for most services, according to data collated from sources Mimer, 2023 Nordpool, 2023. Combining this with the historical demand such data can then be calculated to generate a weighted value for the missing data set. Forecasting data for future cash flows of support services to generate possible scenarios is also investigated and is illustrated in Appendix 1.3.

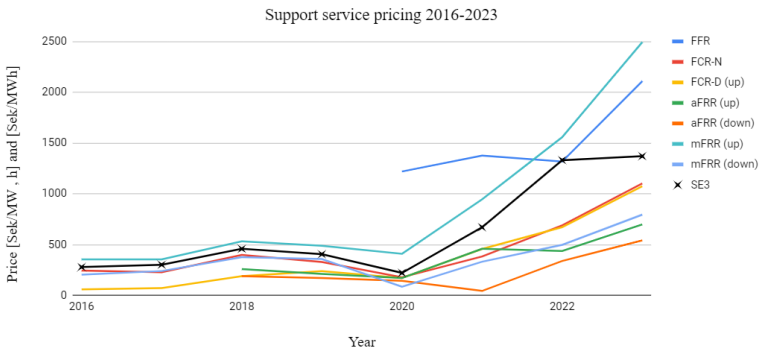

Figure 24: Diagram representing the historic price change of support services, with the price, indexed for both capacity- and energy compensation. Year 2023 is augmented, partly estimated from literature SVK, 2023a

In the selection process of support services, cost optimization for deciding a combination of services without depleting or creating an imbalance in the storage supply is required, thus enabling the provision of minimal volume requirement for each service. Different combinations are tested with an active optimization of services for the ones that are expected to initiate at the same time range, auto-selecting the most cost-efficient support service at the specific hour. In this calculation, support service is prioritized before the basic sale of power when the second pricing of power is less than the compensation price.
All the tests generate different types of income from sold excess gas and gas utilized for balancing the net, with the expectancy of volatile results due to less or no taxation of gas with balancing, while basic power-gas-to-power can create several endpoints in the economic calculations.

5 Results

The result section is split into three main parts, beginning with the technological performances of proposed plants, followed by economical performance and investment analysis under Section 5.2. The investment analysis and benchmark are then elaborated in Section 1.7.2, since the volatility of the result regarding electrolyzers requires an additional basis for determining economic feasibility.

5.1 Independent technical performances

This section focuses on results from the process model simulations, and presents the technical performance of each proposed model independently, including selected information regarding technical equipment performance. All values are rounded up to the nearest integer before decimal.

5.1.1 Electrolyzers plant models

AEL From calculating the cell performance, the optimal conditions for the cell can be evaluated with the constraints of the physical application. The constraints for achieving higher temperature is depending on the durability of the cell, as the nominal temperature for an AEL cell is 80℃, and is not expected to exceed this limit. In application, a specific current density is assigned from equipment information, In Appendix 1.1 the input data for the cell can be observed. Over-potential is directly correlated to performance since every voltage increase over the reversible voltage (J_{rev}) increases the amount of energy loss in the form of heat. The result of the cell potential difference of temperature and bubbling factor can be presented in Figure 25, as the potential increases with the decrease of operational temperature. Through testing the bubbling factor and temperatures combined, it can be concluded that the bubbling factor and temperature render a slightly increased potential than if the bubbling factor is excluded. The temperature and bubble propagation effect on potential correspond to previous research with an insignificant margin of error (Hoedemakers, 2021) (Vogt, 2023) (Abdin et al., 2017) (Schnuelle et al., 2020).

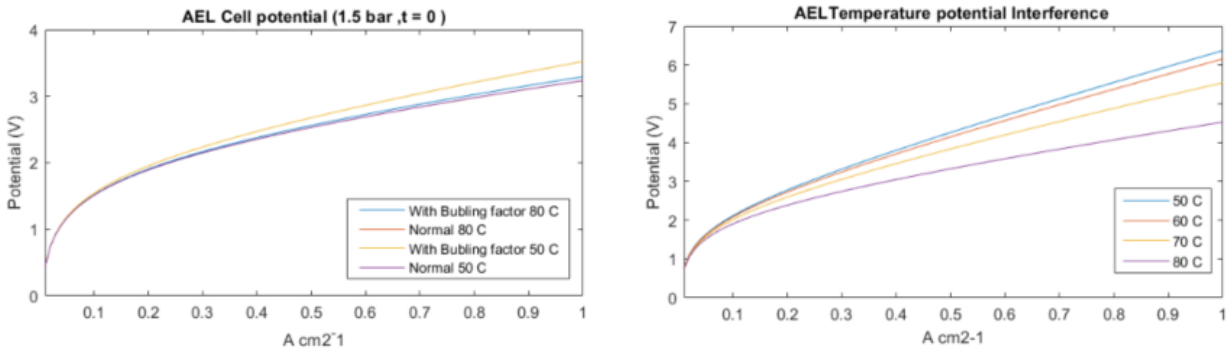

Figure 25: Diagram illustrative of the AEL cell performance. The cell performance change, dependent only on the bubbling factor and temperature offset, is presented to the left. The performance including all interference with potential is presented to the right.

The cell potential for AEL electrolysis has documented flux of efficiency dependent on activation time and can be utilized when planning activation. The research suggests that the propagation of degrading factors has an effect on short-term cycle times, thus the performance of the cell is affected as presented in Figure 26, and is non-linear. The detailed reasoning is not investigated in this thesis but is considered in the strategic analysis since the result is not verified through source and is a mathematical curve approximation made for illustrative basis (Weiß et al., 2019). This effect does not apply to the receiving and compliance with the technological internal ramp behavior of the cell, which is concluded not to interfere with the performance of a capacitor is present or during nominal frequency (Tuinema et al., 2020).

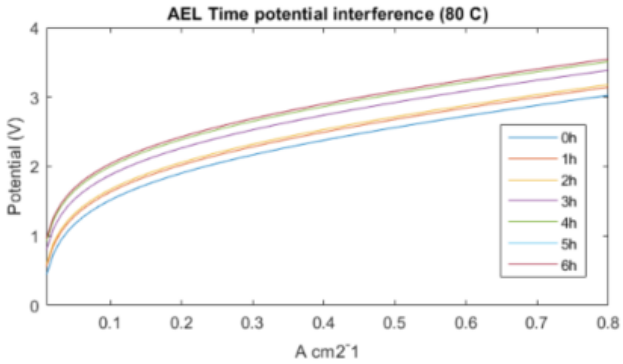

Figure 26: Result of mathematical curve fitting for the activation times effect on cell potential.

The production of district heating from the excess heat in the system is based on coolant and cooling circuit performance. Figure 27 shows the results based on different flow configurations.

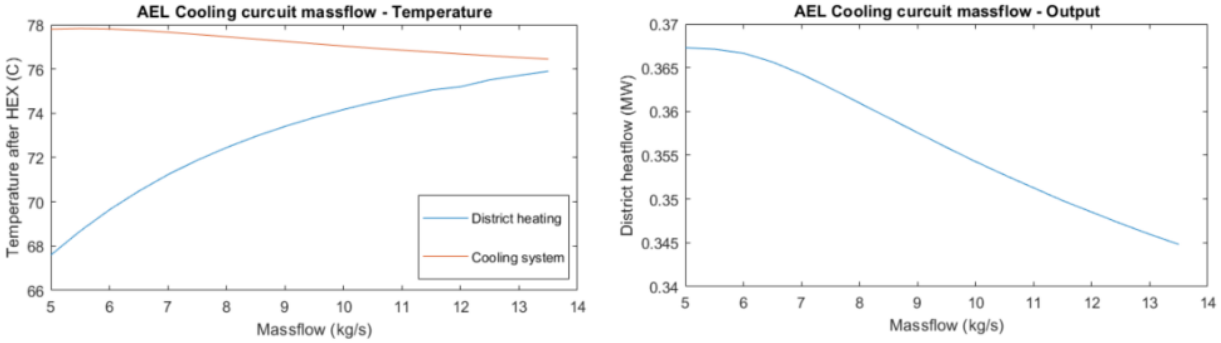

Figure 27: In the left diagram, the circuit cooling temperature and output district heating temperature is illustrated, additionally with total output performance to the right.

In Table 10 the calculated performance of the stack, cluster, and other performance-related parameters are presented. This simulation assumes isothermal conditions for all utilities except for the electrolyzer stack. The mass flow at hydrogen output is not the pure product, thus 0.1% of it is water and tells the summarized weight of the outgoing stream.

Table 10: Electrolyzer for Ägir 1 platform, AEL stack and cluster performance.

Parameter	Value	Unit
Massflow Input/output		
Water feed	110.2	kg/h
H_2 output	22.2	kg/h
$O2$ output	88.0	kg/h
District heating		
Supplied capacity	288.0	kW
Return temperature	60	℃
Output temperature	74	℃
Power consumption		
Utility Cleaning	99.7	kW
Utility Compressors	94.1	kW
Utility Pumps	4.6	kW
AEL Electrolyzer	944.7	kW
Total consumption	1044.4	kW
Hydrogen efficiency	70.7	%
District heat effeciency	25.0	%
Total effeciency	95.7	%
AEL Cluster 5.1 MW:		
No. Stacks	5	st
Connection	Parallel	-
Coupled input Voltage	3096	V
Coupled input Current	1500	A

The simulation result of other parameters that can be relevant for performance, is allocated in Appendix 2.

PEM The result from calculating the performance of the PEM electrolyzer stack indicates that the temperature is not as intricate for achieving workload potential, in comparison to AEL cells. In Figure 28 the temperature effect on cell potential is presented. The simulation result in regard to temperature interference of cell performance correlates with previous research (Schnuelle et al., 2020). In the case of PEM, it is assumed that pressure is high enough to prevent any type of void propagation in the fluid, thus decreasing the number of variables that affect PEM final performance.

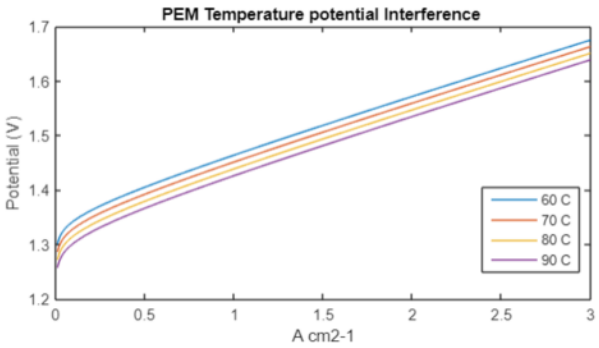

Figure 28

In Figure 29 the dynamic between cooling and outlet temperature is shown. The result from temperature and recovered heat differs from the AEL stack, because of the difference in heat transfer ability and size of the cooling medium.

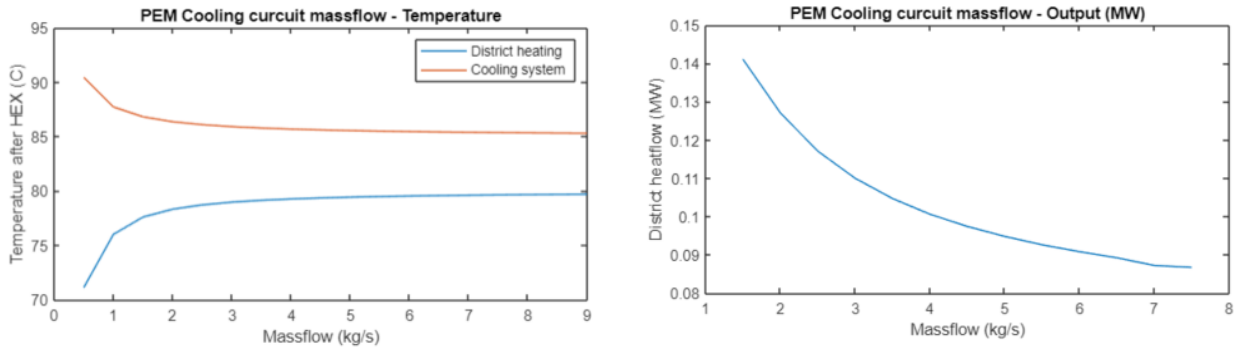

Figure 29: In the left diagram, the circuit cooling temperature and output district heating temperature is illustrated, additionally with total output performance to the right.

In Table 11 the calculated performance of the stack, cluster, and other performance-related parameters are presented. This simulation assumes isothermal conditions for all utilities except for the electrolyzer stack.

Table 11: Electrolyzer for Ägir 1 platform, PEM stack, and cluster performance.

Parameter	Value	Unit
Massflow Input/output		
Water feed	11.7	kg/h
H_2 output	2.4	kg/h
$O2$ output	10	kg/h
District heating		
Supplied capacity	32	kW
Return temperature	60	℃
Output temperature	83	℃
Power consumption		
Utility Cleaning	0.2	kW
Utility Compressors	0.9	kW
Utility Pumps	1	kW
PEM Electrolyzer	112.2	kW
Total consumption	114.4	kW
Hydrogen efficiency	71.1	%
District heat efficiency	28.0	%
Total efficiency	99.1	%
PEM Cluster 5.1 MW:		
No. Stacks	45	st
Connection	Parallel	-
Coupled Voltage	140.3	V
Coupled Current	3599	A

As presented in Table 11, the fuel stack size is smaller in comparison to the AEL stack, and requires more electrolyzers to achieve the same capacity, though larger pieces exist and are not bound to this exact size.

PEMFC The approach to measuring fuel cell performance is similar to the AEL and PEM, achieving optimal conditions by investigating temperature and current density, though with the negative potential as a penalty of decreased efficiency. Different temperatures are not presented, since PEM and PEMFC share the same method of proton transportation, and thus have a similar effect on the cell. In addition, the operational temperature is fixed to 70℃ to fit the intermittent utilization of the fuel cell. In Figure 30 the potential and power output of the PEMFC are shown.

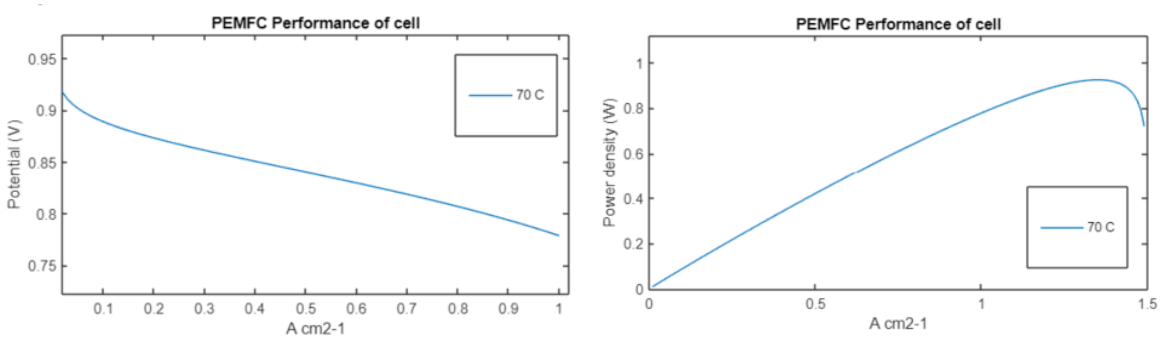

Figure 30: To the left, the potential difference over current density is shown for nominal temperature, and to the right, the power output of current density

In this simulation, two configurations of oxygen supply were executed. The first configuration is with the supply by an external 6-bar compressor to feed atmospheric air to the fuel cell, and the second configuration is the re-circulation of oxygen derived from the electrolyzer. The result in Table 12 presents the fuel cell stack with the second configuration.

Table 12: Fuel cell for Ägir 1 platform, PEMFC stack, and cluster performance.

Parameter	Value	Unit
Massflow Input/output		
Water output	18.7	kg/h
H_2 input	5.4	kg/h
$O2$ input	13	kg/h
Power consumption		
Utility total consumption (O_2 recirc.)	1.5	kW
Power output	98.1	kW
Hydrogen efficiency	55	%
PEMFC Cluster 3.7 MW:		
No. Stacks	56	st
Connection	Parallel/Series	-
Coupled Voltage	2237	V
Coupled Current	1674	A
Air excess ratio	1.05	-

The fuel cell performance is based on calculations with the configuration of the stack so it resembles commercially available fuel cells ($FCM400$ and $PGS100$), which have an output capacity range from 0.015 - 0.325MW, and a maximum coolant temperature of approximately 80 ℃ (2030, 2023) (Group, 2023). The air excess in the fuel cell is detrimental to cell performance, but is necessary to achieve quick response times for the internal reactions, which require higher ratios if atmospheric configurations are applied. The output voltage and current of the cluster are specific to this setup, as stacks are connected 14 in series with 4 in parallel, that is altered to fit battery properties.

5.1.2 Gasification plant models

When addressing the performance of gasification and steam reforming, the system output can primarily be derived from the gasifier reactor fuel conversion efficiency. In Figure 31 the steam to biomass (S/B), temperature and oxygen excess ratio can be observed according to simulation results. This representation does not assess the air deficit for combustion.

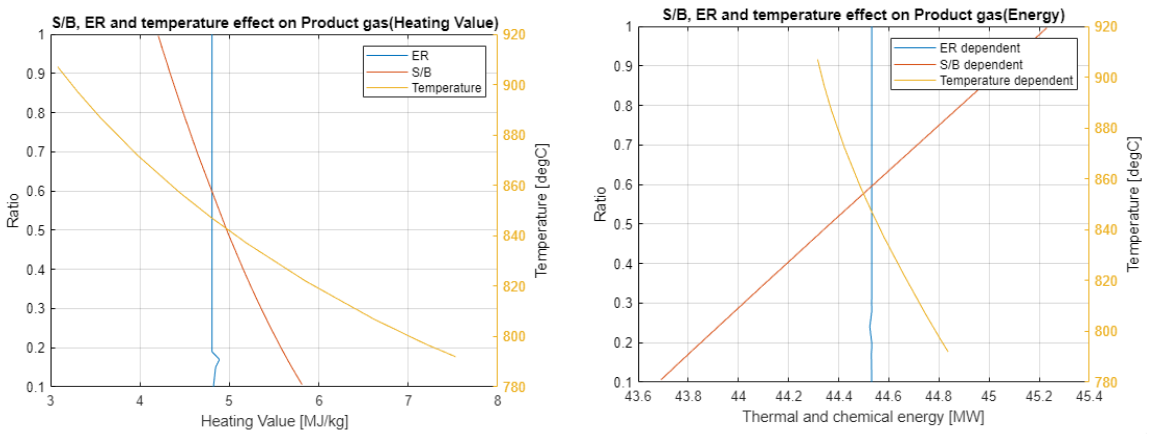

Figure 31: Result of general gasifier simulation. With the total product gas heating value presented on the right, and the achieved output energy on the right

As observed in Figure 31 and 32 the oxygen excess ratio has little or no effect on product gas since the partial oxidation process is completed to achieve a target temperature and is programmed not to combust any other material beyond this point, giving a distorted output on the actual impact in real life application. In Figure 32 the H_2 content of product gas is decreasing mainly because of the added steam, and is not representative of dry gas content.

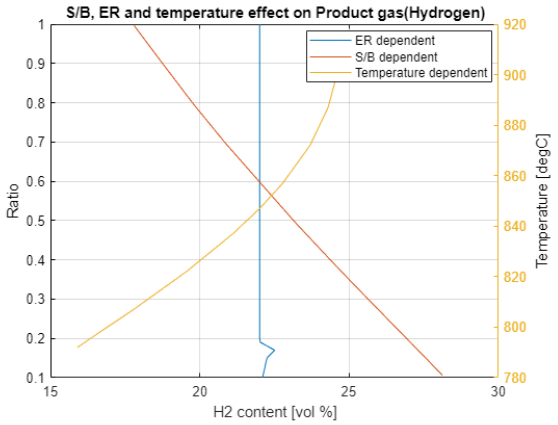

Figure 32: Result of general gasifier simulation of H2 content in product gas(wet).

To modify the performance of the gasifier reactor, the residence time of particles has an impact on product gas content since the reaction rate cannot if there is not enough time for the reaction to occur.
The time of reaction for the gas conversion, excluding solids, is commonly measured as the particle residence time in freeboard space, and the gas molecules reform to reactant species such as H_2, CO, or CH_4. The conversion and time profile of the semi-kinetic calculations in the freeboard of the gasifier reactor is presented in Figure 33. In this particular case, the steam-to-biomass or fuel ratio is exceeding the feasible amount and should not be interpreted as applicable to all gasifiers. The freeboard temperature is set to a temperature 80 K lower than the reactor bed temperature.

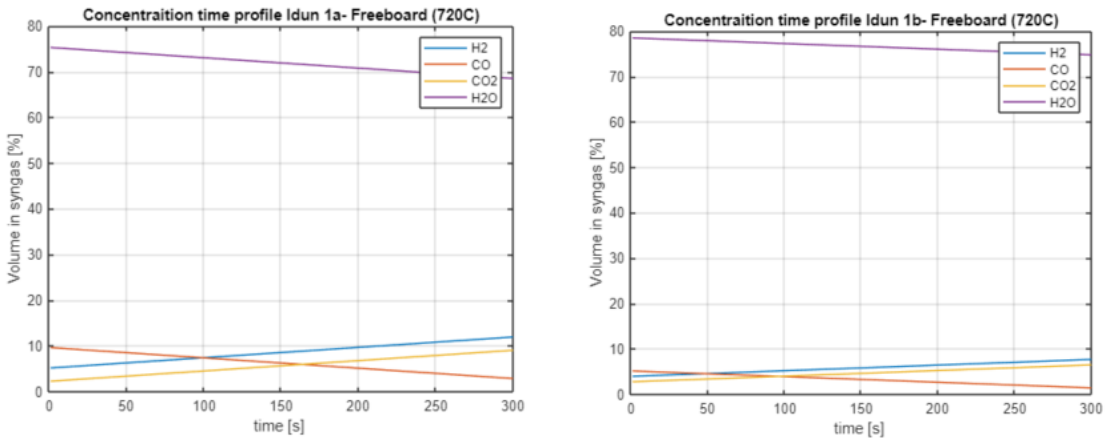

Figure 33: Freeboard time profile for BFB gasifiers in Idun 1a and 1b.

To increase the reaction rate or residence time of particles, freeboard volume or reactor pressure can be increased. The increase of volume induces a longer residence time for the particles, before exiting the gasifier. The internal pressure of the gasifier does not actually increase residence time, but will rather increase the reaction rate, thus it can be translated to longer residence time since the rate decreases the volume required to achieve an equal amount of gas conversion. In Figure 34 the pressure and volumes impact on gas conversion time in freeboard space is presented.

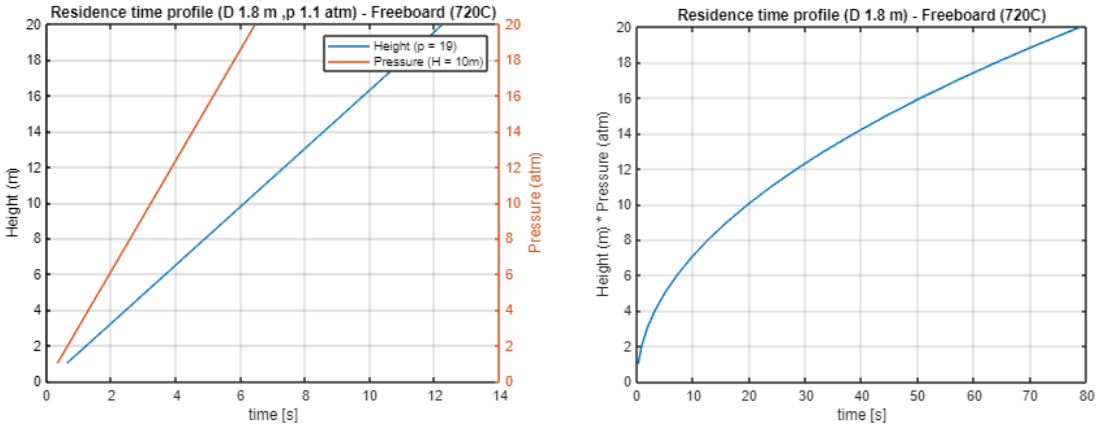

Figure 34: Particle residence time impact, with height and pressure separate on the right, and combined impact on time on the right.

In steam reforming, the performance is set by the catalyst material and recovery efficiency of the water gas shift reactor. If hydrogen is not recovered, this can be cycled in order to be subjected to significant losses. To measure the reactor performance and impact of pressure and temperature, the amount of time to reach the recovery limit can be seen as an alternative indicator of catalyst effectiveness. In Figure 35, two catalysts for water gas shift reactors utilized in calculation and their effect by temperature are presented.

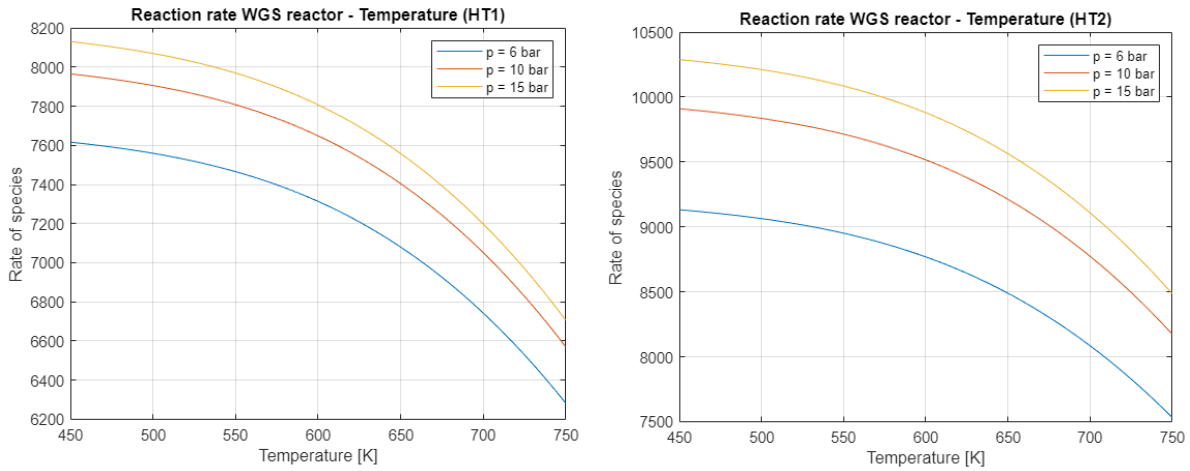

Figure 35: To the right, the results of the first high-temperature reactor and its effect on various parameters are presented, with the secondary reactor to the left.

In order to determine the reaction time span, and if the reaction is within a rational range of operation, an approximation of the conversion rate for the syngas leaving the cleaning stage in Idun 1a is presented in Figure 36. This representation is not entirely correct since it shows a 5 times slower conversion time than of experimental models found in literature, though the relative difference regarding affection by temperature and pressure is still valid. Details about the reactor's technical information are illustrated in Appendix 2.1.

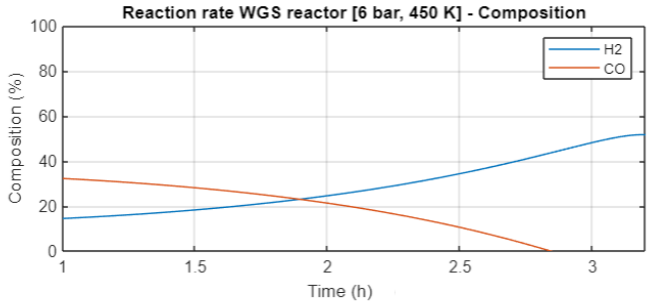

Figure 36: Modified Water gas shift reactor results from the theoretical model.(HT1)

In comparison to previous reaction rate, if the temperature and pressure are increased marginally, this results in a shorter conversion time with pressure as the accelerating variable and temperature increase as a negative by-product of the increased molecular pressure. Figure 37 shows an example of the case when increased pressure is introduced, obtaining a slightly shorter time than the low-pressure example.
In order to reach optimal process condition to reduce cycling, the inlet syngas requires high pressure and stable temperature stream not exceeding 323 °C. Please note that this result is component specific for validating feasibility, and can be changed to fit with other catalysts in order to optimize the process model for real-life applications.

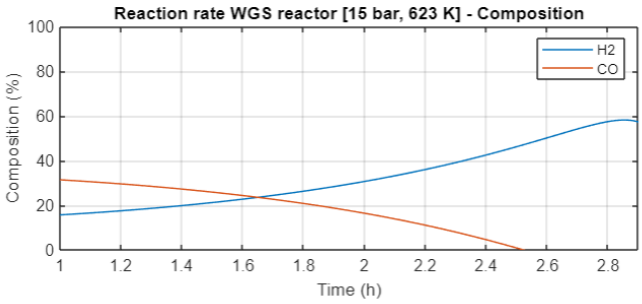

Figure 37: Modified Water gas shift reactor results from the theoretical model, with an increase in temperature and pressure.(HT1)

In the integration method of gasifier reactors, the performance of the boiler is analyzed to validate the feasibility and hydrogen production efficiency. The exchange of energy-dense materials and heat between the gasifier and boiler needs to be equal in order to function, otherwise, a higher amount of transferred energy from the gasifier would benefit the boiler energy balance. The effect on boiler performance is the potential penalty in temperature and energy transferred to the steam cycle since the bed material is circulated and utilized to heat gasifier fuel to reactor temperature. The incineration of char and tar from the gasification process in the boiler combustion chamber is then meant to counteract this energy and temperature penalty to not affect boiler efficiency. In Figure 38 the composite curve of heat transfer for the boilers retrofitted with a gasifier is presented.

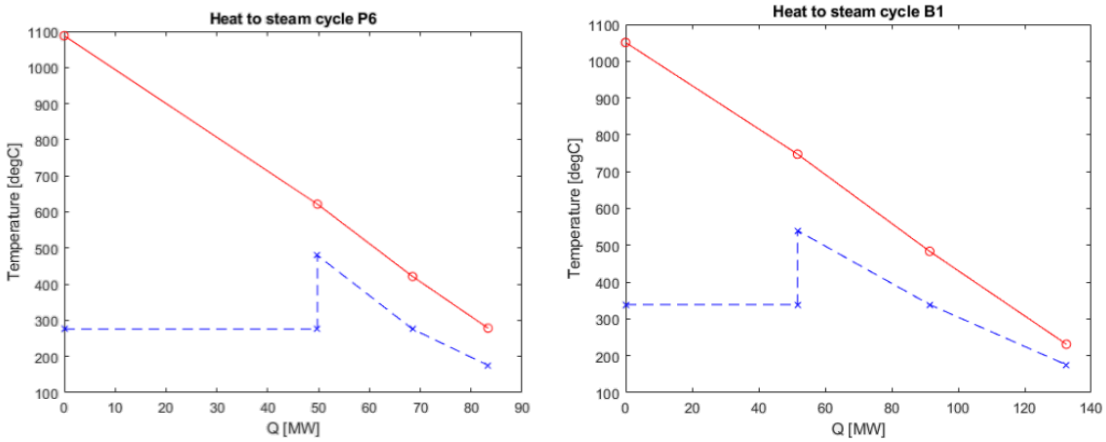

Figure 38: Composite curve over the heat generation from the boilers after retrofitting the gasifiers to the system, with the graph to the left representing the Idun 1a at Högdalen(P6). To the left, Idun 2a implementation in Brista(B1) is presented.

In this calculation, the FGR to achieve a target combustion temperature around 850 ℃, is not calculated, thus the output of the system is only required to match system output without an integrated gasifier. The difference between nominal operation and integration in the simulation is negligible, as only a decrease of temperature and slightly increased efficiency of boiler combustion are determined. Theoretical bed temperature reached is 1087.8 ℃ for boiler P6 and 1050.9 ℃ with integrated gasifier without FGR. These temperatures can be compared with 1142.6 ℃ and 1069.7 ℃ without integration and no FGR. Additional to the decrease of FGR, the air input to the boiler is required to increase 10% for P6 and 2% for B1 to incinerate reject material from the gasification. When implementing the gasifier, heat from the syngas cooling provides additional steam heating by increasing the mass flow of the retrofitted steam cycle. The additional steam input from syngas cooling is constrained to not be below steam cycle temperature and pressure. The initial settings of the steam cycle presented in Table 13 is then altered by the input of external steam input before the turbine generates additional electricity.

Table 13: Fixed parameters for the steam cycle model.

Parameter	P6	B1	P3
Steam cycle max. Temperature (℃)	480	540	377
Steam cycle max. Pressure (Bar)	40	144	34
Steam cycle max. mass flow (kg/s)	32	50	2

DBFB [Idun 1a] The performance of hydrogen production by retrofitting existing boiler P6 with a gasifier is presented in Table 14, as initial values are descriptive of the separate processes of gasification and hydrogen production. The value connecting the performance of the boiler output is the char flux and represents the minimum amount of heat recovered by char incineration. The nexus char transfer is required to exceed this amount otherwise the simulation stops, thus the performance of the boiler will be affected by the heating of bed material inside the gasifier. The result also includes the dimensions of the reactor, since the volume and mass of bed material are related to conversion rate and fuel input.

Table 14: Performance of proposed model Idun 1a.

Parameter	Value	Unit
MSW Fuel input	72	MW
Gasifying agent massflow	12.1	kg/s
Q_{bed} / **Minimum char flux**	5.7	MW
Internal consumption:		
Cleaning utility	0.3	MW
Compressors	5.4	MW
Subcooler and misc.	0.2	MW
Heat flow:		
Recovered heat DH	33.1	MW
Hydrogen produced	28.3	MW
Efficiency:		
Hydrogen efficiency	39.3	%
DH efficiency	46	%
Gasifier reactor dimensions:		
Diameter-Bed ∅	1.43	m
Height-Bed	6.2	m
Diameter-Freeboard ∅	2.2	m
Height-Freeboard	9.1	m
Bed material mass	1785	kg

To measure the performance of Idun 1a and Idun 1b, the boiler's efficiency is required to be equivalent to or higher than the current state. Presented in Table15 is the updated values for the CHP plant from the integration of the gasifier system. Efficiencies include added char and tar rejection from gasification streams.

Table 15: Performance parameters, results retrofitted boiler P6 related to Idun 1a.

Parameter	Value	Unit
MSW Fuel input	91.3	MW
ST power output	28.2	MW
Internal power consumption:		
Utility (Fans and SC pumps)	0.2	MW
Net power output	28	MW
Heat condensation recovery	26.3	MW
Electrical efficiency	27.9	%
District heating efficiency	92	%
Overall efficiency	119.9	%

The combined output of the gasifier and boiler is presented in Table 16, additional to the overall performance of heat and electricity is summarized.

Table 16: Performance parameters, based on the combined result of the gasifier and boiler-related to Idun 1a.

Parameter	Value	Unit
Total electrical efficiency	13,6	%
Total DH efficiency	76,8	%
Total overall efficiency	107,7	%

DBFB [Idun 1b] In the proposed integration model Idun 1b, similar conditions are applied as in the case of Idun 1a, as Idun 1b has a smaller geometry in comparison to the previous model, due to space utilization issues in the facility. The results of system performance are presented in Table 17. In the heat allocation within the system, the heat deriving from gasification and downstream synthesis processing is utilized.

Table 17: Performance of proposed model Idun 1b.

Parameter	Value	Unit
Biomass Fuel input	23,3	MW
Gasifying agent massflow	5.16	kg/s
Q_{bed} / **Minimum char flux**	3.1	MW
Internal consumption:		
Cleaning utility	0.1	MW
Compressors	2.2	MW
Subcooler and misc.	0.1	MW
Heat flow:		
Recovered heat DH	6.3	MW
Hydrogen produced	8.9	MW
Efficiency:		
Hydrogen efficiency	38.3	%
DH efficiency	27	%
Gasifier reactor dimensions:		
Diameter-Bed ⌀	0.8	m
Height-Bed	7.2	m
Diameter-Freeboard ⌀	1.4	m
Height-Freeboard	7.8	m
Bed material mass	870	kg

The updated values for the CHP plant from the integration of the gasifier are presented in Table 18. The efficiency of the CHP plant, in the case of Idun 1b and the case of Idun 1a, is near the current performance. Please note that the efficiency does not break any thermodynamic laws, since the lower heating value is utilized as a reference with the maximum recovery of flue gas condensation down to approximately 36 ℃, which is a common feature in Scandinavian CHP plants according to interview (Dahlen, 2023).

Table 18: Performance parameters, results retrofitted boiler B1, related to Idun 1b.

Parameter	Value	Unit
Biomass Fuel input	120	MW
ST power output	43.2	MW
Internal power consumption:		
Utility (Fans and SC pumps)	0.1	MW
Net power output	43.1	MW
Heat condensation recovery	35.1	MW
Electrical efficiency	35.9	%
District heating efficiency	92.5	%
Overall efficiency	128.5	%

In Table 19 the total performance of Idun 1b and B1 combined output is presented. The main difference in performance compared to Idun 1a is the increased energy required to heat the bed impacting the overall efficiency. The increase of required heating can be explained by the thermal capacity difference of fuel (MSW: 1.387 kJ/kg K - Grot: 2.3 kJ/kg K), non-linear dimensioning of the reactor and moisture content (BERNARDO et al., 2012) (Radmanović et al., 2012).

Table 19: Performance parameters, based on the combined result of gasifier and boiler, related to Idun 1b.

Parameter	Value	Unit
Total electrical efficiency	28.4	%
Total DH efficiency	110.7	%
Total overall efficiency	116.5	%

Designing the process models, and the optimization of streams has an effect on the overall performance since,

avoiding unnecessary heating and cooling equipment, the plant's net electricity consumption is reduced. The target of all process model designs is to achieve a process that is self-sustaining and in addition to utilize the remaining excess heat for district heating applications. In Figure 39 there is a graphical representation of the results after synoptic optimizing the streams with pinch analysis, including heating equipment. The integration of Idun 1a and Idun 1b does not require any major heating equipment affecting energy balance significantly and only utilizes external cooling utility for subcooling of compressed CO2 before expansion.

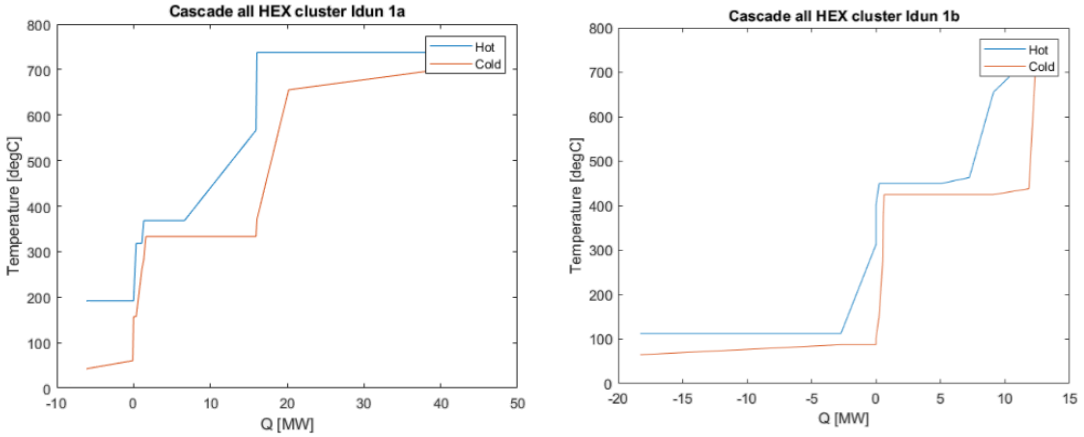

Figure 39: Composite curve diagrams representing process streams after gasifier, not including subcooling of separated CO2.

CFB The process model named Idun 2 is integrated with the current steam cycle related to boiler P3 and district heating, replacing the entire boiler. During process modeling, it can be determined that the EF and FB gasifier do not carry enough energy in the product gas to heat the existing steam cycle. The conditions presented in Table 13 can not be satisfied, since the minimum mass flow of steam is not compatible with the available heat. The only configuration relevant for replacing P3 is configuration Idun 2a, which can carry relatively more significant amounts of energy due to the possibility of gasifying solid fuels with the addition of steam. In Table 20 the performance of Idun 2a stand-alone gasifier is presented, as an ASU is required for internally combusting material supplying heat to handle and reach reactor temperature.

Table 20: Performance of proposed model Idun 2a.

Parameter	Value	Unit
MSW Fuel input	45	MW
Steam massflow	1.7	kg/s
Oxygen mass flow (95% purity)	0.9	kg/s
Internal consumption:		
Cleaning utility	0.2	MW
Compressors	0.8	MW
Heater	0.4	MW
Subcooler and misc.	0.2	MW
Cyclone	0.2	MW
ASU	0.7	MW
ST output	1.2	MW
Heat flow:		
Recovered heat DH	23.2	MW
Hydrogen produced	16.8	MW
Efficiency:		
Hydrogen efficiency	39.3	%
DH efficiency	51.6	%
Electrical efficiency	-0	%
Overall efficiency	86	%
Gasifier reactor dimensions:		
Diameter-Bed ∅	1	m
Height-Bed	5	m
Diameter-Freeboard ∅	1.6	m
Height-Freeboard	7.2	m
Bed material mass	1050	kg

Since the product from gasification is not bound to heat steam for generation purposes, using instead chemically latent energy, heat recovered from the gasification is not enough to create a net positive result for electricity generation, though low-value heat is produced in excess and is possible to recover for district heating utilization. In Figure 40 a composite curve diagram over the process flow streams is presented.

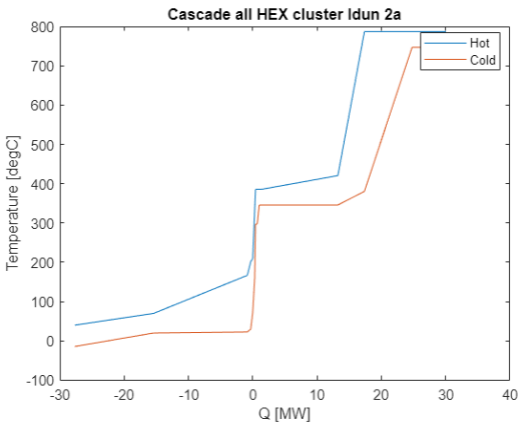

Figure 40: Composite curve diagram for Idun 2a, not including subcooling of separated CO2.

EF In Idun 2b the gasification setup is made to be dry in order to incinerate and gasify at a relatively high rate. This process also is assumed to require a higher flow of oxidizer material stream. In calculation, the dimensions of the gasifier are not required thanks to the theoretical model for EF gasification.

Table 21: Performance proposed model Idun 2b.

Parameter	Value	Unit
Biomass Fuel input	49.2	MW
Oxygen mass flow (95% purity)	1.6	kg/s
Internal consumption:		
Cleaning utility	0.1	MW
Compressors	0.9	MW
ASU	1.4	MW
Pre-treatment of fuel	0.9	MW
Heater	0.8	MW
Subcooler and misc.	0.1	MW
Heat flow:		
Recovered heat DH	22.5	MW
Total heat allocation	6.4	MW
Hydrogen produced	20.1	MW
Efficiency:		
Hydrogen efficiency	40.9	%
DH efficiency	45.7	%
Electrical efficiency	-8.5	%
Overall efficiency	78.1	%

Notable is that sub-cooler demand does not change linearly with the size of the process, and is affected by pressure and temperature of incoming material stream, also including other consuming devices. "Miscellaneous" in subcooling includes the cooling fan, control, and mechanical expansion of CO_2 stream.
In Figure 41 the resulting composite curve after synoptic optimization of the process flow is presented. The particular model requires heating units, that are included in the presented diagram.

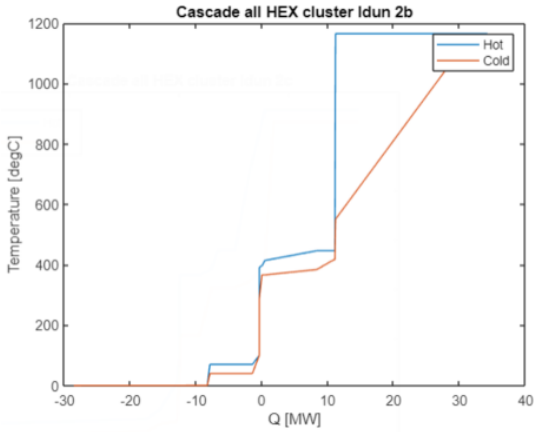

Figure 41: Composite curve diagram for Idun 2b, not including subcooling of separated CO2.

FB Idun 2c is the Fixed Bed gasifier configuration and is limited by size. The 9.9 MW gasification reactor is equivalent in size to the previous gasifiers and is not receptive to installations exceeding this amount, thus efficient utilization of space is not possible. The result from the simulation is presented in Table 22. With the low-kinetic theoretical model, reactor bed height can be gathered from calculations.

Table 22: Performance proposed model Idun 2c.

Parameter	Value	Unit
MSW Fuel input	9,9	MW
Oxygen mass flow (95% purity)	0.2	kg/s
Internal consumption:		
Cleaning utility	0.2	MW
Compressors	0.6	MW
ASU	0.2	MW
Subcooler and misc.	0	MW
Heat flow:		
Recovered heat DH	5	MW
Total heat allocation	0.3	MW
Hydrogen produced	4.2	MW
Efficiency:		
Hydrogen efficiency	42.9	%
DH efficiency	50.9	%
Electrical efficiency	-10.1	%
Overall efficiency	83.7	%
Gasifier reactor dimensions:		
Height-Bed min.	4.5	m

Figure 42 presenst the composite curve for Idun 2c process model. In this configuration, large pressure equipment is required for synthesis applications and conditioning before entering the WGS reactor step. Heating units are included in the composite curve diagram.

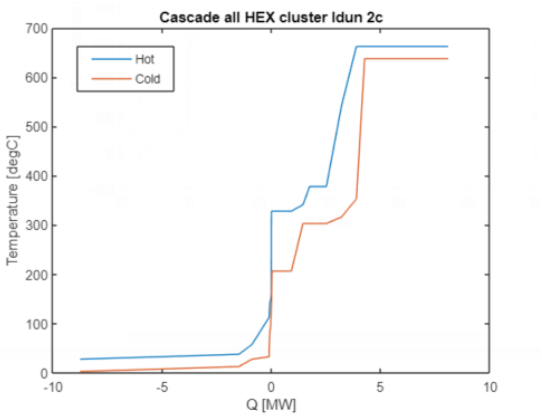

Figure 42: Composite curve diagram for Idun 2c, not including subcooling of separated CO2.

With the introduction of heaters and cooler units, the low-temperature heat derived from the downstream process can be recovered for district heating purposes.

From this point, analytic utilizing Idun 2b and 2c will be limited, because of the lack of competitiveness from a technological performance standpoint.

5.2 Benchmarking

In this section, the economic performance and measurement of product opportunities are identified and presented. Additionally, results with relevance for investment or other information that can be applied to strategic planning integrating the proposed models for hydrogen production are listed in sub-sections. The intricacy of storage and supply of products is analyzed, and availability is relevant to determining possible strengths or weaknesses regarding the system feasibility of integration.

5.2.1 Economical performance

In order to evaluate the economic performance of the proposed models, a market study of the consumption, delivery, and utilization of other services is introduced. The difference between the gasifier- and electrolysis-based production systems is the consumption of product. When measuring the economical performance of gasification-based systems, the price volatility of solid fuel is the key factor in the same way as the price of electricity for electrolysis-based production. The price for solid fuel is evaluated in Appendix 1.6, and the spot price of electricity with support service pricing is continuously discussed throughout the current and the following sections.

The Ägir 1 platform utilizes the spot price to produce hydrogen via electrolyzer and produce electricity from stored gas via the fuel cell. The electrolyzer activates when the spot price is under a set threshold, while the fuel cell activates when over a set threshold. In Figure 43 the activation of each technology can be observed over the year 2022, as accumulated hours in the active production set define the annual production.

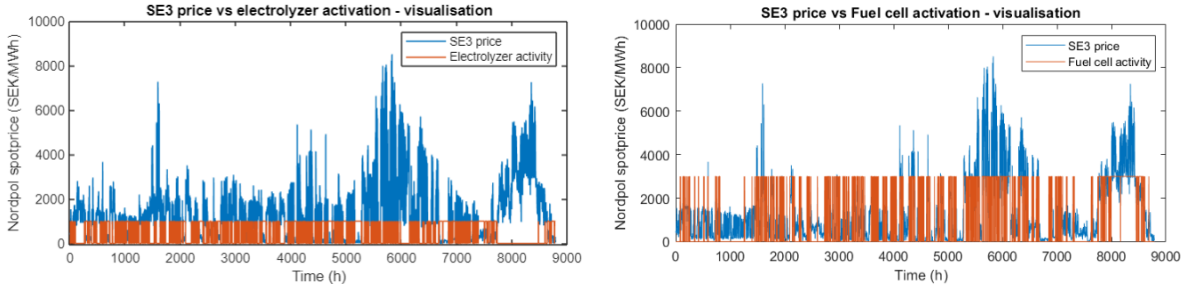

Figure 43: The left diagram represents the electrolyzer activity, and to the right, fuel cell activity for the year 2022.

To calculate the cash flows of Ägir 1 the benchmark script is required. The result is generated by the input of historical data for electricity prices and support services from previous years, which are then acclimated to the algorithm to output the economic result of investigated plant. In the algorithm, initial activation of the electrolyzer is accounted for in terms of internal ramping, which renders the electrolyzer less efficient during *Cold start* than in continuous activation. A graphical representation of the internal ramping effect on the AEL electrolyzer efficiency is observed in Figure 44, which normalizes to $Load = 1$ after a preset internal ramping time. The amount of production hours is calculated with the incorporation of support service consumption and production, as the accumulated activation time for the electrolyzer is 3682 hours 1250 seconds and 3646 h 2569 seconds for the fuel cell during the year 2022. The result of activation time is executed with the presumption of storage flexibility, which is the basic configuration of this plant and is explained further in Section 5.2.2.

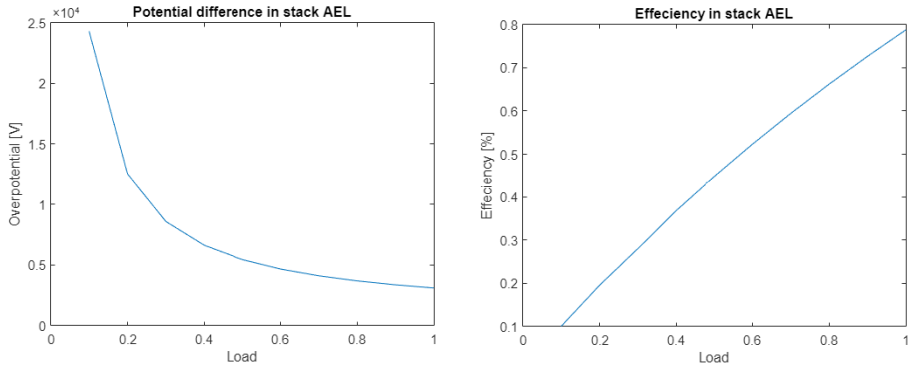

Figure 44: In the diagram to the right, the overpotential of the electrolyzer stack is presented, and the load = 1 is the nominal target that is reached after a specific time. To the left, the total efficiency of the stack is presented

Notable is that activation time for both PEM and AEL is equal to each other, as production efficiency with full load production hours is the main difference between the techniques. In the case of utilizing PEM, the annual production efficiency of hydrogen production is dependent on internal ramping and is calculated to be 99.11% during the year 2022, while it is 97.68%, for the AEL.

Production of oxygen as a by-product is specific for electrolysis and follows a similar pattern of hydrogen production. In calculations, the oxygen produced by the electrolyzer is utilized in the adjacent CHP in order to minimize the operation costs of CCS and fuel consumption, in addition to generating income based on savings from fuel utilization. The excess oxygen is also used in fuel cells for controlling efficient operation. The value of the oxygen for utilization in KVV8 is estimated approximately to 0.9 SEK/kg according to Appendix 2.3.4. In Figure 45 the annual excess supply of oxygen is presented after utilization in fuel cell operation and a constant supply of 86 kg/h to KVV8 from the AEL electrolyzer.

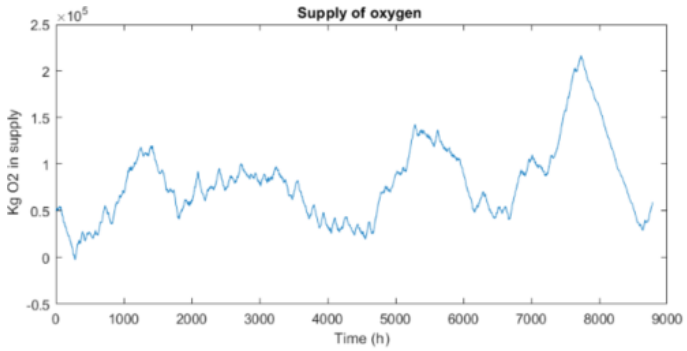

Figure 45: Annual excess supply of oxygen produced from Ägir 1 (AEL)

In the benchmark of all hydrogen production, the byproduct of heat is also accounted for in combination with annual activity. The byproduct of all hydrogen production is district heating, assuming that output temperatures ranging from 70-120 ℃ of all mass flows are considered valuable for district heating applications. The annual supply from each plant is presented in Figure 46 and 47.
Thermal ramping efficiency of 90% is added to the district heating output of Ägir 1 plant, in addition to the internal ramping efficiency rendering additional penalties for this system in comparison to the gasifier plants, as no lagging or internal ramping is accounted for. The gasification-based plants have, instead of internal ramping, a seasonal production rate, as the plant is operating at 90% capacity or is shut down completely during periods of low or no district heating demand. This production rate is also applied to hydrogen and electricity production.

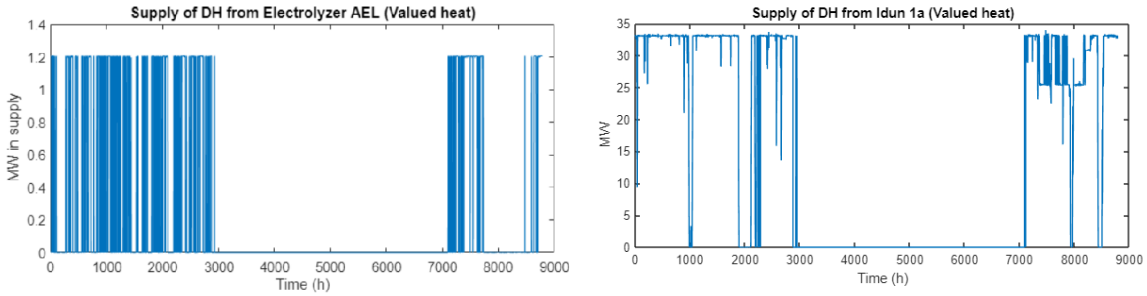

Figure 46: In the left diagram, the annual output of DH from electrolyzer activation in Ägir 1 is presented, and in the right diagram, the output of DH from Idun 1a is presented.

In Figure 46 and 47 the interval between the hours 3000 to 7000 shows a value of district heating equal to 0, i.e. it is assumed that there is no demand for district heating when outside temperature is above 10 degrees, and no income is generated by district heating. Idun 1a or 1b are interconnected to boilers, that are constrained to the primary product of district heating, rendering the amount of active hours during the year lower than stand-alone systems.

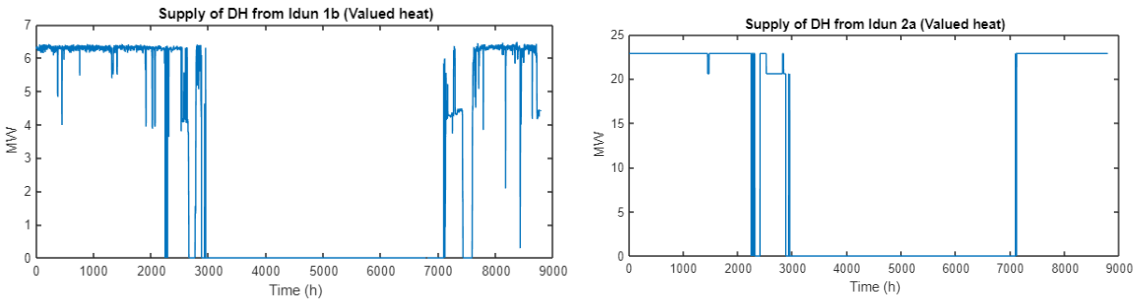

Figure 47: In the left diagram, the annual output of DH from Idun 1b respectively Idun 2a to the right.

Activity results from Idun 2b and 2c are not graphically represented since the curve will have a similar appearance to the district heating supply of 2a and share the same active time of 8520 h annually, with approximately 4600 hours supplying valuable district heating.

In Table 23 the summation of economic operation cost and investment for the different proposed models is presented. Calculating the economic performance includes taxes, net provider fees, and other costs related to the operation. A list of the values utilized and other related economical parameters can be located in Appendix 1.4. Figures representing the response activation for support services are presented in Appendix 1.1.

Table 23: List of Capital investment cost and operational expenditures based on the facility.

Parameter	Idun 1a	Idun 1b	Idun 2a	Idun 2b	Idun 2c	Ägir 1 (AEL)	Ägir 1 (PEM)	Unit
CAPEX	958.7	463.7	628.4	1505.4	302.7	131.6	137.6	MSEK
OPEX	-59.9	33	-38.7	112	-3.6	12.5	12.6	MSEK

The OPEX for Idun 1a, 2a, and 2c is negative because income from handling MSW exceeds the cost of other operational expenses. In Table 24 the final indicators of economic performance are presented, accounting tax. Income from byproducts and hydrogen production is included, as the price of hydrogen is fixed at 30 SEK/kg. Additional income from support services is also included for the Ägir 1 platform. The included support services are: FFR-up, FCR-D-up, aFRR-up, mFRR-up, aFRR-down, and mFRR-down, excluding FCR-N and FCR-D(down) due to lack of data.

Table 24: List of economical performance indicators based on facility, including construction time for NPV and IRR.

Parameter	Idun 1a	Idun 1b	Idun 2a	Idun 2b	Idun 2c	Ägir 1 (AEL)	Ägir 1 (PEM)	Unit
PBT	1.9	7.2	1.5	8.4	5.1	1.5	1.6	Years
NPV	5831.1	356.3	4087.6	731.6	281.8	667.4	655.7	MSEK
IRR	50	16	53	14	19	48	47	%

Please note that certificates are not included, since the certificate system from renewable energy is under liquidation. From 2022 onward new power plants will not be entitled to the benefits of certificate income, Power-to-gas-to-power (PtGtP) is not affected by this factor since it is not eligible for certificates prior to the transition. It is also worth noting that NPV for Ägir 1 includes the replacement of electrolyzer components, which occurs after lifetime expectancy is reached.

This result only presents the standard operation of the electrolyzer, and other alternatives that are considered relevant, are instigated in Section 1.7.2. Additional results, such as subsidies or other factors that can alter the economic feasibility are included and are presented in Section 1.7.

5.2.2 Storage and Supply

The benchmark script is designed so the initial amount of hydrogen at the beginning of the year should be equal to the amount stored at the end of the year, and so that it does not reach a state of deficit in the storage. This

balancing is done semi-automatically and requires a threshold of hydrogen production and GtP production. In Figure 48 the accumulation of hydrogen is presented, after activation of balancing, PtG, and basic sale of hydrogen to fuel stations. If support service trade is active, the storage is also required to always have at least 109.85 kg in reserve to uphold reserve responsibility of 1 MW during 1-hour continuous operation. The amount required varies among services and is considered when balancing storage.

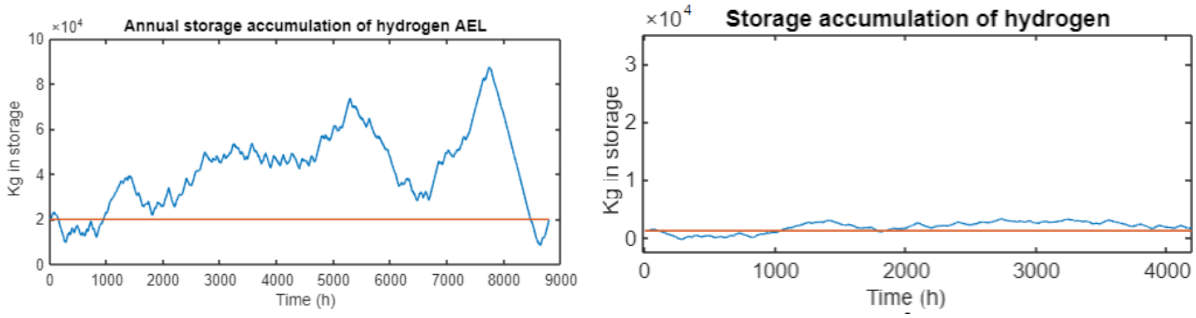

Figure 48: Dynamic storage is presented in the left diagram, respectively balanced storage to the right, for Ägir 1 during 2022. The orange line indicates the initial capacity of hydrogen in its current state(30 bar) in a 35000 cubic tank.

In the case presented, overshooting of the storage initial limit is allowed. If balancing is introduced to this and no overshooting is allowed, the penalty can be significant to the economic feasibility, when down-regulation of GtP activation can negatively impact the revenue of cash flow to approximately 19-36% and 14.5% of income generated from sold hydrogen, since production of hydrogen is limited. The majority of income is based on sold power during peak demand hours, this has an overall effect of net income reduction of up to 17% if balanced. Figure 48 graphically represent the balanced storage when minor overshooting is allowed, in order to fit the algorithm computation method, and has negligible effect on plant economy. The mentioned case of both balanced and overshooting is applied to the year 2022, deviations may occur based on the year of interest. The daily consumption is set to dispatch hydrogen to the fuel station 12 hours a day during the daytime, this volatility has no considerable effect on the current configuration but can be optimized with storage if the fuel cell is eliminated. In 1.7.2 alternative production methods are shown to have an effect on the required storage capacity in the electrolyzer platform Ägir 1.

Storage of hydrogen produced by gasification is not applied in this study, thus the hydrogen is assumed to enter the distribution chain directly. The supply of hydrogen can be directly connected to the activity of the gasifier in a distribution network. Annual activity of proposed gasification plants that produce hydrogen are presented in Figure 49 and 50. In Idun 1a, approximately 853.2 kg/h of hydrogen is produced during the 7954 hours when the plant is active. In the Idun 1b plant the flow is 252 kg/h during the 4640 hours when the gasifier is operational.

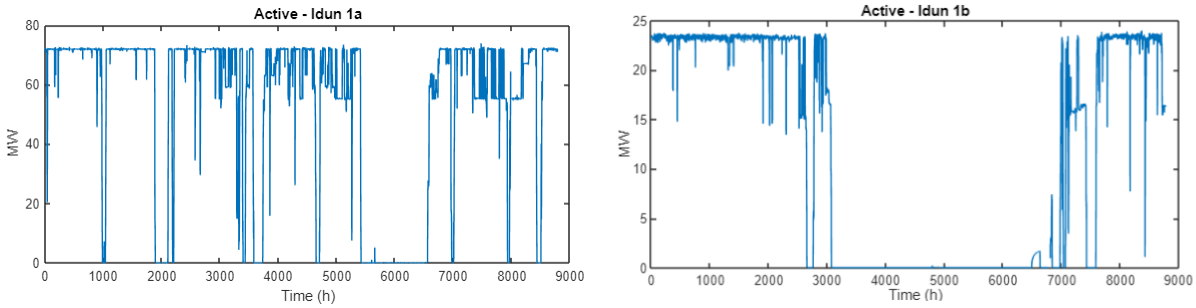

Figure 49: Left diagram presents annual load over time for gasifier Idun 1a, respectively Idun 1b to right. The activation and hydrogen production is directly synchronized.

The amount of hydrogen delivered to the distribution network for plant Idun 2a is 504 kg/h during peak loads, or 1080 kg/h during partial loads, and is supplied 8520 hours annually. The time, when the gasifier is not operational, is selected as an assumption of required maintenance hours. Idun 1a and 1b share maintenance hours with the connected boiler, based on data from previous operations.

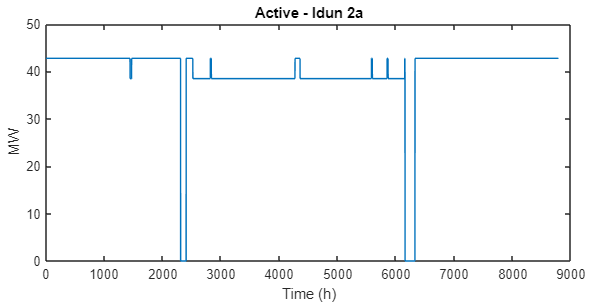

Figure 50: Diagram presenting the annual load of Idun 2a, as the production of hydrogen is directly synchronized.

To quantify mass flow, the Tables in 5.1 present the output of 100% load. The factor to convert energy to mass flow is 120 MJ/kg, which is the lower heating value of hydrogen. The amount of hours with hydrogen supply for Idun 1a is 6818, 4631 for Idun 1b, and 8520 hours for Idun 2a. Combined annual production of all gasifier systems reaches peak mass flow at 1672.7 kg/h whereas minimum mass flow is 0 kg/h. Minimum system production can be counteracted with the selection of maintenance hours for Idun 2a and updated minimum results in 504 kg/h.

5.2.3 Reliability

When implementing a new system on a large scale level supplying products on an inconsistent basis during the year, it is suitable to quantify the probability of production flows in order to estimate the system's reliability. In this particular case, district heating and hydrogen are the main products from the plants that are essential for sustaining infrastructure, climate, and overall health for customers. In Table 25, the capacity and availability ζ are described for each facility producing hydrogen and district heating.

Table 25: Availability annually for all proposed plant models with data from 2022.

Facility	ζ_{H_2}**(100%)**	ζ_{DH}**(100%)**	ζ_{H_2}**(90%)**	ζ_{H_2}**(90%)**	ζ_{H_2}**(Off)**	ζ_{DH}**(Off)**
Idun 1a	95.3	99	N/A	N/A	4.7	1
Idun 1b	52.8	94.35	N/A	N/A	47.2	5.7
Idun 2a	56.9	99	40.1	0	3	1
Ägir 1	41.9	46.4	N/A	N/A	58.1	53.6

The assumption is made that district heating availability is only based on activation during the period when demand exists. The interval length of this period is approximately 4000 to 4600 consecutive hours annually and is based on the amount of time as district heating reaches a certain value. Base case AEL is utilized as the capacity source from Ägir 1, though calculations are made with a PEM electrolyzer. The factor of 1.099 can be used on the delivery of hydrogen to create similar results for the PEM-based platform, since it has a slightly increased production during internal ramping, thus longer availability of full production. Regarding the oversize case Ägir 2 platform, a similar method can be applied to achieve proportional output for the plant.

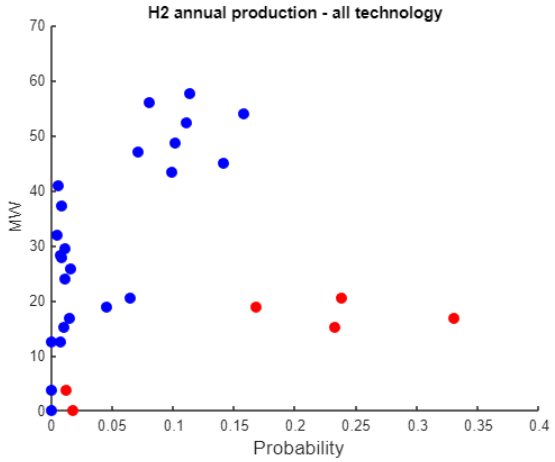

Figure 51: Reliability of hydrogen production with the probability of different total capacities. Red and blue colors indicate mature respectively non-mature technology.

Note that the platform of Ägir 1 is behaving differently depending on the year since the production of hydrogen is directly dependent on the electricity market. In appendix 1.0.1 a list of reliability key numbers is presented for historical values.

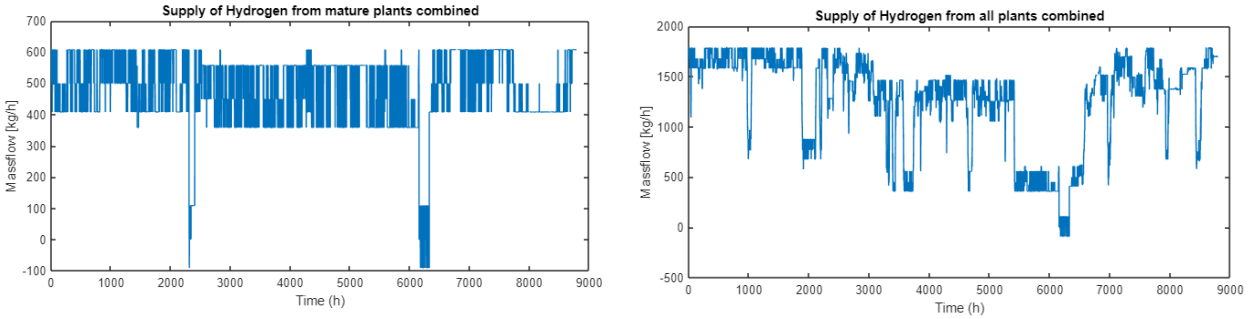

Figure 52: Diagrams presented show the output of hydrogen over time, with mature only technology (Stand alone gasifier Idun 2a and Electrolysis) to the left, and all investigated plants (excluding Idun 2b and 2c) to the right.

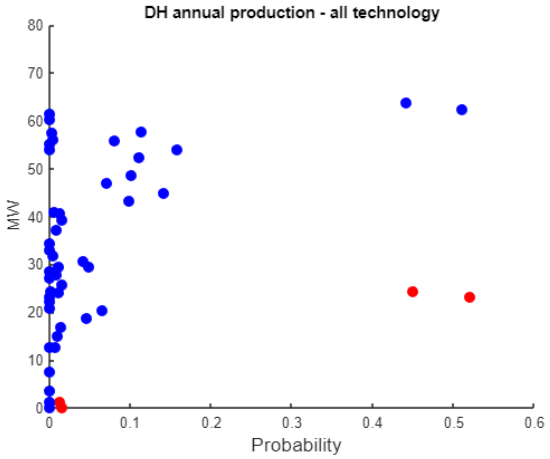

Figure 53: Reliability of district heating supply during demand season, as red and blue colors indicate mature respectively non-mature technology.

The information used for the reliability analysis can be found in Appendix 1.0.1, and different operation scenarios are presented.

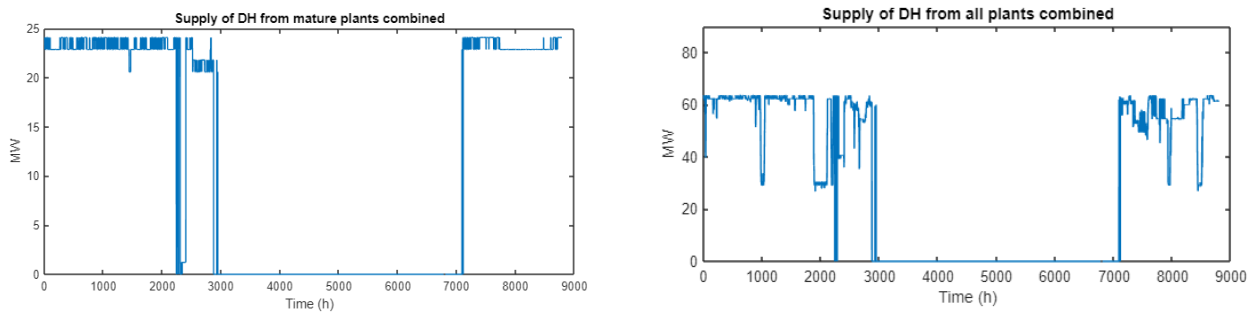

Figure 54: Diagrams presented show the output of district heating over time, with mature-only technology (Stand alone gasifier Idun 2a and Electrolysis) to the left, and all investigated plants to the right. The output during times when district heating obtains no value is not presented in diagrams.

The values presented only represent the probability of specific capacity output and not the probability of exceeding a given production capacity. In the case of cumulative capacity, the probability of non-zero hydrogen production is 99.37% for all plants combined and 98.7% for the combination of mature technology. The probability of supplying over 13.3 MW (400 kg/h) is 79.54% annually for mature technology, and 90.85% combined. Supplying over 50 MW (1500 kg/h) of hydrogen is only applied to the case of all plants combined, and is available 40.39% of the time.

5.2.4 Alternative operation Ägir 1

Due to the volatility of electrolyzer plant results depending on external factors, this segment will explore alternative configurations of the plant and other external factors affecting the economical feasibility and performance of the plant. Synopsis from the case study for each operation is presented in Appendix 1.7.2, with the results from benchmarking in 26.

Table 26: Varying economic performance indicators based on the operation mode of Ägir 1.

Operation	PPA	PPA*	PPA, no FC	Oversize	Sleep mode	Unit
PBT	1.7	1.8	1.5	1.9	1.5	Years
NPV	403.9	322.5	156.5	661.2	602.3	MSEK
IRR	34.7	30	28	37	45	%

The name is based on the modified technical aspects in the platform, e.g. *PPA* stands for fixed electricity price determined by a PPA contract. Changing the technical configuration of the plant or fixing the price will change the results to various degree, depending on the mode of operation.

6 Discussion

In this section method, technical aspects, and economy will be discussed, regarding both results and other information connected to the study of hydrogen integration in Stockholm.

6.1 Method

The reasoning behind the utilization of mathematical programming to calculate the process flows and chemical reactions is that complex kinetics and processes can be freely expanded. Using code in Matlab to compute mass and energy balance and chemical reactions is also estimated to be able to cut computation time as iterations can be designed to fit the process.
The main argument for applying different theoretical complexity for gasifier calculation is to utilize simpler modeling for processes that are too complex in order to simulate the reactions properly, thus generating the best results. In the BFB geometric consideration is required since it is utilized in proximity to existing equipment and thus is constrained by available space in the plant. In the calculation of the potential for electrolyzers and fuel cell, the factors that are most significant for the potential difference specific to the technology is accounted for. For example, calculating the bubbling factor or diffusivity in all technologies would be excessive, so it is limited to only AEL because the physical impact from other trivial variables is more significant for the PEM or PEMFC. Dynamics in models with the use of numerical simulation is the most common method of approach in combination with verification of experimental results to determine the performance of all the technologies (Ramos et al., 2019). It can be concluded that, comparing the results of other methods the difference is insignificant in relation to economic results, even if the applied physical theory differentiates between the models. Uncertainties regarding residential behavior of char occurrence can be determined through literature, (Lewin et al., 2020) in FB and (Ramos et al., 2019) in BFB. Bed dynamics for non-bed-based technologies (EF) are not considered.
Please note that, in mass and energy balances and system output, the LHV of hydrogen is utilized.

6.2 Technical aspects

Regarding subject to technical performance and feasibility of proposed models, most of the uncertainty lies in the application of integrating a gasifier to an existing boiler. The integration requires that the boiler incinerates enough solid fuels enabling the combustion of char and tar rejected from gasification, which will heat the quartz bed. It could be argued whether the incineration of the reject will impact the boiler negatively or positively, as the reject could lead to higher combustion temperature or leaner incineration. The risk of sintering could also increase with the rise of tar and char content in bed material, as the active surface of bed material decreases. The solution to counteract some of these issues is by utilizing the H_2S rejected from cleaning of syngas in order to stop corrosive and other negative impacts on the superheated package inside the boiler. Increasing bed volume and riser height can be a solution for the possible impact on the particle active surface inside the boiler.

In all gasifier models, the resident profile of char, tar, and other reactions, are in the theory located on different levels of the gasifier through consensus of previous examples, when the reactor concentration profile is calculated through the Eulerian method with computational fluid dynamics Wu et al., 2018. In the dual fluidized bed, the behavior of particle flows and concentration profile is concluded with the same approach H. Liu et al., 2015, enabling the assumption of not reaching particle overflow between the combustion chamber and gasifier. It is also shown that cyclone operation may not be required for the DFB gasifier.

In regards to geometry, the difference between the BFB and FB is that the FB results in a larger geometry in order to increase active surface or height, which leads to sufficient residence time, when simulating the same mass of syngas exiting the gasifier as in the other models. The behavior of non-symmetric devolatilization and heat distribution renders the calculation of geometry, required in terms of volume, difficult in comparison to the BFB gasifier as symmetric conditions can be assumed in the bed. This makes the application of a numerical model based on height more reliable, but still not as reliable compared to the FB or EF calculation. Addressing proper diffusivity models accounts for bed gasification only utilizing CO/CO_2 and H_20/H_2 due to avoiding unnecessary complexity and somewhat accurate model output. To compensate for all the uncertainties of the gasifier-based system, conservative calculations are applied, and lower efficiencies, enhanced conversion to inert molecules in purification, together with separation generate an overall minimum technical performance of the system.
In retrospect, utilizing the method in Appendix 1.4 could have given a slight error in the gasifier geometry of MSW, as a longer residence time could have been set to ensure appropriate modeling for drying, devolatilization,

and char burnout. Oxygen concentration affects the bed temperature distribution and decreases the superficial velocity in the bed, in the normal calculation, of bed connection to dispersion coefficient, and thus was set a minimum to match the concentration of 40% oxygen flow rate in gasifying agent mix. According to this, this would not be a correct usage in the integrated gasifier, thus modification was made to replicate the steam partial fluidization agent for the gasifier reactor. It should also be stated that the scale-up method, utilizing a reference gasifier, has deviation in bed mass and fuel, which also can increase the uncertainty of the model related to internal drag and flow calculations.

The formation of CH_4 during gasification could be used for steam reforming, rather than being combusted, as done in the current configuration. Please note that the process does not have enough CH_4 for steam reforming via the ATR process, albeit the process would consume too much of the CH_4 to heat steam while simultaneously being resource efficient. In the separation of CH_4 and CO, there is an uncertainty of recovery rate and area usage, since membrane techniques can be quite large in comparison to alternative separation methods. The question is if the membrane technology can be seen as a viable alternative to cut power loss of operation. In the integrated gasifier system, it is calculated that the available H_2S used for boiler application results in reject mass flows less than 6.3 g/s for Idun 1b and 157.5 g/s for Idun 1a. The estimated reject flow from other gasifiers follows the same proportion dependent on fuel composition and solid fuel consumption. Chemical products that are not considered in the calculation are N_2 from ASU, as the rejected N_2 from Idun 2a results in 2270 g/s. The N_2 could be of use if chemical products in the form of HCN could be utilized to regulate any in-house boiler that has integrated gasification or ammonia production, though the utilization has not been researched enough to give any specific estimation of system effects. In regards to chemical purification, the assumption is made that CO_2 is purified from the resident contaminants to a certain degree. Further research is needed to determine the penalty of CO_2 purification. The final product is calculated in order to reach a transportable state at 15 bar and -25 ℃ with no account of contaminants.

Emphasis should be made that heat exchange and optimization between streams is required since catalytic processes are sensitive to temperature, and just cooling the stream would jeopardize the technical or economical feasibility of the facility. Please note that increasing temperature in downstream applications from the gasifier can have negative effects on catalyst conversion rate, though this is applied to the synthesizing of product gas (WGS reactor) at medium to low-temperature water gas shifting in all models.

In this thesis the assumption is made that grid can be supported by existing batteries as a capacitor, though it is proven in the literature that sells of base power are possible if a transformer and frequency controller is added (Um et al., 2000). The phase and frequency are adjusted to fit the grid through the batteries, consecutive time lagging will not affect the delivery of power significantly if distributed through lithium-ion batteries that last longer and will be able to catch up when large volumes are required for extensive time, (Alshehri et al., 2019).

Integrating a heat pump to increase output temperature from electrolyzers is excluded in this thesis because integration is too expensive in an over-complicate system for the investigated scale of facility (Kalmykov et al., 2022) (F. Jonsson & Miljanovic, 2022).

Regarding by-products of electrolysis, the maximum temperature of cooling water depends on membrane durability. Changing materials of the membrane may increase resistance to temperature change several degrees higher than the current configuration. It should be noted that the output temperature of the water could be lower in actual application depending on whether an additional HEX cycle is required, and by the equipment's sensitivity to fluctuating cooling temperature. In the outtake of sensible heat in the electrolyzer platform, it is assumed that cooling of gas between compressing stages can be made without cooling of the actual compressor, or if the compressor cooling circuit can be configured freely within reasonable temperatures. In this thesis, the evaluation of the system applies the condition that the heat recovered from the fuel cell in Ägir 1 platform has insufficient potential for district heating distribution due to intermittent utilization and relatively low operating temperatures.

In the computation of oxyfuel, the model was verified by comparing the operation and flows of the actual plant. According to simulation results, all flows in normal operation with flue gas recycling, have an overall error of 99.5% compared to the real plant. The flows calculated are the flue gas, flue gas re-circulation, inlet air, solid fuel, and steam cycle flows. Regarding the FCR the condensate level is constrained and held to 5.3% according to literature (Gustafsson et al., 2021) complementing the supplied data surrounding the boiler.
It should be noted that retrofitting oxyfuel to the facility with connection to CCS requires the proportional dimensions of the adsorber and desorber to achieve the optimal result. For this particular case, the main compressor work can be lowered by 40%, meaning 60% of its original value. In order for the lower volume of gas to be processed in the stripper, a lower pressure can be set to achieve full contact with the solvent film. Loading

and concentration are also factors to be considered when accelerating the process. In retrospect, the saving from the amount of CO_2 for the process should have been measured, since the significant increase of partial pressure for the CO_2 can result in a better uptake, thus a more efficient process. Parallel coupling of two compressors, instead of installing one compressor, can have benefits when varying the mass flow and increasing the mass flow tolerance. External factors, such as FGR fan and inner wall structure, are not required to be adapted for this boiler assuming that the oxygen in inlet air does not exceed 43% in oxyfuel application. In addition to further investigating the properties of oxyfuel combustion in retrofit application with an intermittent feed of oxygen, the time transition between a steady state in the boiler from air to oxygen enhancement should be considered. Planning the release of oxygen or installing an accumulator tank is preferred to make the boiler combustion and power control as efficient as possible since an uneven run of the boiler decreases the efficiency. The transition to a steady state can approximately take up to 30 minutes, although reverting to the original run is much faster. This, of course, depends on the boiler and technical potential for adaptation to the plant. (Jia et al., 2013).

6.3 Economic feasibility

Regarding the economy of gasifier plants using MSW, it can be observed that the cash flows are robust compared to other production methods. For example, if the income from CO_2 is removed from Idun 1a, the NPV will be 3458.4 MSEK with an IRR of 37%, still giving a positive result. If removing income from both CO_2 and district heating, an NPV of 1885.3 MSEK with an IRR of 26% is obtained. This economic robustness can be derived from continuous income during the year from hydrogen, chemically fixing the price to the price of hydrogen during all periods of the year, combined with income from MSW disposal. The economic robustness of such an investment could arguably be higher than a normal CHP plant, as seasons and electricity prices determine the economic robustness. Observing the case of Idun 1b, it can be concluded that the economic stability depends mostly on fuel pricing, and if removing income from CO_2 the plant NPV will be -217.7 MSEK with an IRR of 0%, only having a positive return of 7% counting with a margined discount. The economical savings of fuel and other benefits from the integration of the gasifier with the boiler are not accounted for in the plant cash flow calculation.

It can be observed from economic results that the NPV is high for the CAPEX-intensive plants. This is because of the relatively large cash flows that generate more extreme values for the plants. In comparing the profitability between low and high CAPEX plants, the IRR is a more suitable benchmark, since it calculates the maximum possibility of return. A factor affecting the NPV is how the cash flow is calculated, and that can differ depending on the method. When calculating the cash flow the construction years have a negative value, since there is no income. In this calculation, the presumption is made that the cash flow during the initial construction is the CAPEX divided by the number of years with no income. If the cash flow is not divided this has a major impact on the return rate, since it in all cases is decreasing to slightly under 50% of its original value and NPV decreases with around 20%.
In the tables presented in Appendix 1.4, it can be observed that the indirect cost added to equipment is lower, this is explained by the lower implementation and construction site cost for gasifiers, since permits and structure exist, due to the gasifier either replacing a boiler or integrated without requiring any expansion of the plant itself. The cost of labor, steam piping, and to some extent, related machinery is also reduced for a retrofit in an existing facility. Reinvestment costs are only accounted for in Ägir 1 and are assumed to be 30% of the initial CAPEX, though it is estimated to occur only once in the 25-year period. Observing the result with or without the reinvestment of the electrolyzer, the effect on performance indicators is low.
The economy of each plant is activity-based, thus increased active hours generate more profit for the investment. This means that the integrated gasifiers that are connected to boilers that have more available time will result in better financial output, and for the electrolyzer platform the spot price and activity threshold set the activity for the plant, thus it depends on external factors. In the case of stand-alone gasifiers, the activity can be scheduled and configured to generate the highest possible profit for the plant, since it is not affected by the volatility of the electric market or boiler activity.
Addressing economic feasibility, a way of benchmarking is increasing the CAPEX extreme values, pushing the financial aspect to its limit. When increasing the plant CAPEX to 4 times its original value, the plants still generating positive results are Ägir 1 in normal operation, Idun 2a, and Idun 1a. Comparing the gasifier technologies it can be concluded that Idun 2a is the most profitable and cost-efficient alternative, while Ägir 1, consisting of AEL electrolyzer and PEM fuel cell, is the most cost-efficient option. For the Ägir 1 platform, the alternative configuration is less cost-efficient, with the *sleep mode* configuration as the second most profitable followed by the oversize, though it should be noted that the configuration without fuel cell and PPA contract, results in a competitive payback time yet with less IRR and NPV compared to the other alternatives.

Uncertainty of income for the Ägir 1 plant can be connected to the income of support services. For exam-

ple, the aFRR exponentially increases and has a potential income differential of approximately 20 million SEK during the years 2021 to 2022. Utilizing results from 2022 could overestimate economic performance, thus utilizing an average is more suitable for actual calculations alternatively following the market analysis in Appendix 1.2. According to the study investigating the risk connected to the volatility of capacity and energy prices in appendix 1.3, it seems that there is no sign of significant influence as the demand for reserve will rise. The projected cases all promote an overall increase of compensation, even in case of low prices the demanded volume will still rise and thus the amount of auctioned volumes. The increased amount of auctioned hours will increase income from obtaining available reserves. Please note that local reserves probably will be more efficient than connecting to stem-grid, due to preventing time lag for reserve. This effect on price is most probably negligible, but still notable. Also, it should be noted that Case 2 in the forecast is based on that the spot price market will decrease due to renewables, but with the benefit of instead increasing compensation, which causes investment in balance reserve economically favorable even though OPEX is high. To conclude, the result from alternating the cash flows based on projection is presented in Table B16, as all forecasts indicate positive values for the plant economy. This result also shows that the uncertainty of the market and volatility of forecast cases create economically beneficial balances for the plant. When implemented in a real case scenario, the possibility of not winning all the bids should be accounted for, especially if the competitors in the market of reserves expand.

PPAs are contracts written by power producers that alternatively offer renewable energy at a fixed price so that the customer can take benefit of securing electricity price in addition to controlling and cutting their impact on realized emissions. In the case of electrofuels, there are plans to have several tax-related benefits within the EU if the electricity used can be traced with PPA or other methods. Depending on which tax reductions can be made, this will have significance to the plant economy. At the time of writing, the energy tax was increased from 36 to 45 SEK/MWh, but considering the result of sensitivity analysis, this increase will have no significant effect on plant economy, still making the normal operation the most cost-effective configuration of the Ägir 1 plants. The overall effect on tax is suppressed, since the assumption is made that no tax is applied to income from the balancing services and basic sale of power, since power sold back to the grid fall under the legislation of energy storage. The income from oxygen is not taxable either, since it is utilized internally to boost the efficiency of KVV8 and BECCS process.

In alternative operation when the Ägir 1 platform consists of both fuel cell and PPA pricing, there is a possibility of utilizing the fuel cell without base sell of Gas-to-Power application, thus only offering balancing with support services. With this configuration, it can be observed that only utilizing the fuel cell for support services will not alter storage significantly, since the total annual activation time is approximately 10 hours and 1080 seconds during the year 2022. A graphical representation of the simulation is given in Appendix 1.7.2, and the required volume of an 800 m3 silo is enough to handle the maximum capacity at 30 bar. At the current price of storage and fuel cell, it is the least economical solution since the fuel cell can not be utilized to its fullest, causing its investment to be ineffective as the other alternatives. Both configurations not selling base power can have other beneficial usages, as they can regulate storage at overproduction of hydrogen and also work as a backup generator, increasing its functional value. Change in PPA price also has a significant impact on how competitive the operations are in comparison to normal operation, and the plant economy changes as described in Table B15 depending on agreed pricing.

All alternative operations are more profitable in proportion to economic recession, except the one with PPA and no fuel cell. Without a fuel cell, the system also is more sensitive to change according to analysis, so fixing the operational costs is essential for the economical feasibility of the configuration. The alternative has the lowest documented IRR of all alternatives, but still with a relatively low PBT, which indicates that the configuration can be seen as more stable but less profitable in the long run as NPV diminishes in proportion to the other alternatives.

6.4 Strategic analysis

Due to the relatively high mass flow of hydrogen originating from gasifiers, conventional storage is not a suitable option. The alternative to handle large-scale production is by utilization of sealed caverns or direct distribution. Since the utilization of cavern spaces are an arguable alternative for implementation in a city environment, the method of direct distribution is a more secure method of approach. To implement a large-scale market of hydrogen, intercity distribution with pipeline should be considered due to the low cost of transportation and preventing supply bottlenecks in terms of traffic. Because of the current transition, international trade can be executed by shipping to for example Germany and Japan, as upcoming demand increases by the day (Bloomberg, 2020).
In this study, there is no account for legislation and permits for hydrogen storage, nor costs related to imple-

mentation surrounding storage. Even though the storage aspect is uncertain, the overall reasoning has been made that the space is finite and should not be allocated on a large scale at Värtahamnen due to explosion hazards.

Through calculating the reliability of annual hydrogen and district heating production found in Appendix 1.0.1, the mature technology is able to supply district heating at least 97% of the time required, and 45% of the time at full capacity. Of course, since the Idun 2a operates interdependently, supply can be secured 100% of the time if maintenance is scheduled appropriately. In regards to district heating supply from the mix of all technologies, the supply can be secured for almost 100% of the time, of which 44% at full capacity. The same pattern of availability can be transferred to hydrogen production, but with a larger distribution during the year, since it assumed that availability of district heating is 0 when there is no demand. The mix of all technologies will make the hydrogen supply of the system volatile during the summer period, due to shut down of boilers, thus making the hydrogen supply less stable for the integrated gasifiers.

Opportunities of producing hydrogen at Värtahamnen with the plans of building CCS are increasing the reliability of the storage for carbon capture. If transportation of compressed carbon dioxide is scarce, hydrogen and carbon dioxide synthesis could act as a temporary solution thus ensuring a stable capture rate from the plant. The synthesis will create methanol, a common grade chemical that is easier to dispose of and sells than carbon dioxide, and, though the reaction requires energy to start, it could still be beneficial to be not entirely dependent on external factors. Moreover, the value of utilizing oxygen for oxyfuel purposes in KVV8 can be seen as a valuable asset, as the option of utilizing oxygen for fuel cell applications can be questionable. The benefits of recirculating oxygen to fuel cell is uncertain, thus the value of lowered nitrogen dilution is not accounted for in this thesis. Promoting hydrogen and CCS production as sustainable due to oxygen utilization is an additional argument in order to apply for grants supporting the initial investment.
Producing hydrogen proximate to existing CHP with a gas turbine could also open the potential for increasing the capacity or energy compensation, due to increased maximum output, meaning a gas turbine can increase the volume of delivered momentary power to the grid. Combustion utilization also has other benefits, e.g., better control of incineration properties and lower emissions, though with the drawback of higher internal temperatures in blade connection. Also, utilizing gas turbines for support service purposes is limited to services allowing longer response times in comparison to fuel cells or batteries.

Regarding the application of an electrolyzer and fuel cell, it is recommended to install a fuel cell with less capacity than the electrolyzer to prevent hydrogen storage from being depleted due to over-consumption. Oversizing the fuel cell in general also risks that the installed capacity is excessive in proportion to balance volume demand, thus the dimension was set to <4 MW in this thesis, in order to utilize full potential during most of the year. Balancing the fuel cell and electrolyzer proportion is important for cost-efficient use.

When setting the activation price threshold it is important to acknowledge the benefits of having a stable source of income versus unpredictable income from support services, thus the hydrogen demand as fuel is constant relative to imbalances in the net. A higher threshold can then be set to increase the share of income from hydrogen sold as gas. Implementing a nominal activation of the electrolyzer at a certain load, while not controlled by this price threshold, has the same effect since the production rate will be constant, this however has a significant impact on plant NCF.

With the introduction of a support service market system *MARI*, and 15 minutes bidding span instead of an hourly basis will be implemented, the income of support services is prone to change (SVK, 2023b). The argument for this change is that prices of support services will be higher with the open market and increase of the price cap. Factors that could change the price negatively can be that more actors lead to more competition and the requirement of accepting lower bids. If the spot price is lowered due to a more open market, this will increase the cost efficiency of the electrolyzer, since operations can be lower, but decrease the cost efficiency of the fuel cell.

Uncertainty regarding the implementation of gasification is considered too low in comparison to electrolysis since the system is less reliant on external factors. The factors that are connected to uncertainty are internal factors such as if the initial investment is larger than expected or purification issues. Since gasification and related processes are difficult to map entirely in the time span of this thesis, the actual cost of the system or subsystems are uncertain. It should also be noted that gasifier reactor prices can differ greatly, as most reports state the price of the system around the reactor as the actual price for a reactor, and the price for just the reactor shell is not documented. The argument for exchanging old incineration boilers to gasification reactors, as electricity is not the primary product, derives from the reasoning that it is more efficient and produces fewer

emissions than combustion of fossil fuels or biomass, but primarily for the reason of creating syngas that can be applied for a variety of purposes including power production. This makes it a versatile technology that can be applied in different industries and not just for hydrogen production (Nohlgren et al., 2014),

The sensitivity curve presented in Figure 55, benchmarking the most profitable versions of gasification and electrolysis platforms, indicates the IRR for extreme cases with and without subsidies. The result shows that the technology with the most potential for proportional profit is the electrolysis platform Ägir 1 if the CAPEX is reduced. The Idun 2a gasification platform seems to be the most stable, and subsidies barely affect the outcome because of the scale of cash flows. In this analysis, the electricity price and compensation prices are accounted for simultaneously in the Ägir 1 calculation, respectively the fuel and CO_2 price in Idun 2a.

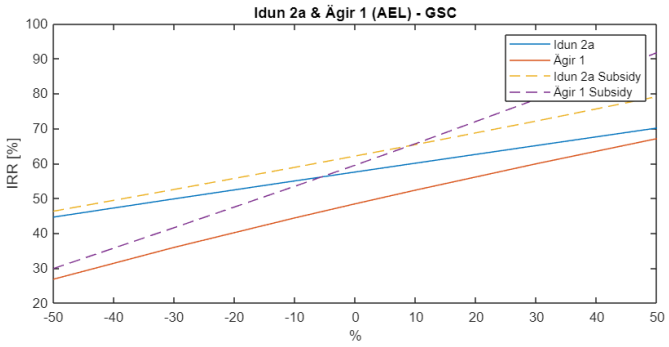

Figure 55: Sensitivity analysis of the most profitable versions of gasification and electrolysis. In the graph the subsidies from secured investment coverage from Industriklivet, additionally volatile income and cost variables are accounted for.

Arguably the most economically strategic investment would be the gasifier platform if subsidies cannot be secured and aggressive changes in the market are not expected to occur. In the case of market volatility is expected to increase, the Ägir 1 platform seems to be the strategic choice.

In terms of emissions and sustainability, the plants are considered not to contribute to any environmentally negative effect, since hydrogen produced from electricity is derived from renewable sources in the current zone. The gasification plants can be observed as CO_2 negative or neutral, since the CO_2 is stored and sold for utilization, promoting a circular economy for residual waste or capturing CO_2 from biomass. The only emission from gasification is from the combustion of CH_4, which is not captured in the proposed models. The emission from combustion is considered as negligible as it could be avoided with a smaller installation of capture or oxyfuel application.
The combination of all plants produces approximately 406 GWh of hydrogen annually and thus has the ability to replace 9.4% of the demand for heavy transport fuel in the Stockholm region. If the alternative of PPA is utilized without the sale of base electricity, the system could potentially cover up to 10.1% of the demand, also reducing the carbon footprint of transport.

The economic result from all plants is shown to be positive, so it can be questioned why there has not been yet any similar projects or investment. The explanation could reside in the fact that the calculations are wrong, but more probable is that the technology is more efficient than before and that now an actual demand exists. The demand will create infrastructure, making the gas more cost-efficient to distribute and store, since storage and distribution of hydrogen could lead to considerable expenses. Regarding electrolysis, the lifetime of electrolyzers has also increased in the past years, and with the introduction of renewable energy, compensation prices have increased significantly. Computational modeling and digital tools have also accelerated research regarding both gasification and electrolysis, increasing the advancement pace within the innovation and reliability of the technology.

7 Conclusion

The integration of hydrogen production in Stockholm is mapped and utilizes the strategic placement of each plant in combination with current production. In the CHP facilities, Högdalen and Brista the possibility of retrofitting gasifiers is concluded to be theoretically possible, also accounting for available space adjacent to the boiler. Integrating the gasifiers will affect net electrical output negatively, but with a significant increase

in district heating output from the facility. The replacement of boiler P3 to a gasifier is also possible, but restricting the steam flow to fit heat output from the gasifier. In Värtahamnen, the proposition is made to place electrolyzers that can provide district heating and chemical products locally. The design of the process and simulation prove that the plants are possible without any major setback for the surrounding system except in terms of electricity consumption.
According to results and strategical analysis, the gasifiers require pipeline or transport of gas from the facility immediately, since a very large space is required to store the gas. For the electrolyzer platform, all operations indicate that storage is possible, but show the requirement of storage at least for operations with PPA and restricted utilization of fuel cells.

All proposed plants are compatible with the district heating system, as return water can be heated to 100-120 ℃ for the gasification systems, and 74-82 ℃ with the connection of an electrolyzer. The plants that can offer the most stable supply of district heating are the gasifier systems, as the electrolyzers are unstable except for the operation with PPA. Similar results are obtained regarding gas supply reliability.

Investigating the value of oxygen by-product, it can be concluded that the alternative savings of avoiding an ASU and fuel savings are 0.9 SEK/kg. Determining this price requires that the oxygen input is beneficial to the integration with BECCS, without major re-investment in the current plant. The simulation proves that savings can be possible with oxygen input, thus verifying the value of oxygen. In terms of other byproducts, heat, and CO_2 can be recoverable for district heating and sold as chemical products at market value, respectively.

Calculating the economic performance of each plant, results show positive indicators for both gasifiers and electrolyzer platforms. It can be concluded that the gasifier replacing the P3 boiler called Idun 2 is the most profitable of all technologies using CFB configuration. The gasifier system has an NPV of 4165.8 MSEK in normal operation, and electrolyzer Ägir 1 has an NPV of 667.4 MSEK. A comparison of operation modes in Ägir 1 shows that the normal configuration is the most cost-effective, while the operation utilizing PPA and no fuel cell is the least cost-effective. Regarding gasifiers, EF and FB as replacements for P3 are the least economically beneficial alternatives. According to sensitivity analysis, all plants can be self-sustained economically, without subsidies. The analysis shows that most configurations are economically stable, as hydrogen price impact on electrolyzer in normal operation economy, can be considered almost negligible. Additionally, tax and other fees result in minimal interference in relation to the cost of electricity and amortization.

The strategic analysis result indicates that the reliability of the gasifier outperforms the electrolyzers in terms of the availability of district heating and product gas. This changes depending on the configuration of the electrolyzer, as PPA alternatives supply products continuously over the year. From the analysis, it is determined that the placement of the electrolyzer platform in Värtahamnen could provide system benefits, supporting the turbine and synthesis of chemicals with hydrogen. In the aspect of gasification, the utilization of chemical byproducts from cleaning, separation, and the ability to handle unwanted polymers can be positive for the overall operation of the facility. The strategic and sensitivity analysis results indicate that an unstable spot market or reserve trading will not affect the plant economy in any critical matter for the electrolysis platform. For the gasification plant, the uncertainty of income based on fuel prices and CO_2 trading is critical only for some of the plants, as the economic stability of Idun 2a and 1a is the highest of all technologies, and Idun 2a is the highest of the mature technology.

Regarding storage and infrastructure, the electrolysis platform is a relatively stable option, generating an amount of hydrogen suitable for intercity storage, especially if basic power is sold from GtP application. Storage does not destabilize if only balancing services are offered. Gasification-derived scale seems to be suitable only if the grid is large enough to handle the outgoing quantity. Intercity storage for hydrogen production from gasification is not suitable, especially not for the integrated gasifiers, as the intermittent operation will lead to the requirement for large-scale accumulation to distribute contracted amounts of hydrogen evenly throughout the year. This means that investing in electrolysis is the most feasible choice before the integration of hydrogen infrastructure, with gasification as the second step after high demand from customers is secured to handle the quantities produced.

Regarding progress in the energy transition and CCS, the fuel derived from Biogen sources can be assumed as carbon negative, while recycling of MSW is seen as net zero. Both electrolyzer and gasification of MSW are not actively capturing any CO_2, but leading to indirect reduction of fossil fuel utilized in industry or transport sector.

References

2030, T. (2023, April 16). Teco marine fuel cell system. Retrieved April 16, 2023, from https://teco2030.no/solutions/teco-marine-fuel-cell/

Abdin, Z., Webb, C., Mac, E., & Gray, A. (2017). Modelling and simulation of an alkaline electrolyser cell. *Energy Vol 138*, 316–331.

Alshehri, F., Suárez, V. G., Torres, J. L. R., Perilla, A., & van der Meijden, M. (2019). Modelling and evaluation of pem hydrogen technologies for frequency ancillary services in future multi-energy sustainable power systems. *Heliyon Vol 5(4)*, e01396.

Aromada, S. A., Eldrup, N. H., Normann, F., & Øi, L. E. (2020). Techno-economic assessment of different heat exchangers for co2 capture. *Energies Vol 13(23)*, 6315.

Baltrusaitis, J., & Luyben, W. L. (2015). Methane conversion to syngas for gas-to-liquids (gtl): Is sustainable co2 reuse via dry methane reforming (dmr) cost competitive with smr and atr processes? *CS Sustainable Chemical Engineering vol 3(9)*, 2100–2111.

Baraj, E., Ciahotný, K., & Hlinčík, T. (2022). Advanced catalysts for the water gas shift reaction. *Crystals Vol 12(4)*.

Battelle. (2016). Manufacturing cost analysis of pem fuel cell systems for 5- and 10-kw backup power applications. *Battelle Memorial Institute*, 16–48.

BERNARDO, M., LAPA, N., GONÇALVES, M., MENDES, B., PINTO, F., FONSECA, I., & LOPES, H. (2012). *Characterization and potential applications of chars from the pyrolysis of polymeric residues* (tech. rep.). Universidade Nova de Lisboa, Laboratório Nacional de Energia e Geologia,Universidade Nova de Lisboa.

Bloomberg. (2020). Hydrogen economy outlook key messages, 1–14.

Bouillon, P.-A., Hennes, S., & Mahieux, C. (2009). Eco2: Post-combustion or oxyfuel–a comparison between coal power plants with integrated co2 capture. *Energy Procedia Vol 1(1)*, 4015–4022.

Burrin, D., Roy, S., Roskilly, A. P., & Smallbone, A. (2021). A combined heat and green hydrogen (chh) generator integrated with a heat network. *Energy Conversion and Management Vol 246*, 114686.

Campoy, M., Gómez-Barea, A., Vidal, F. B., & Ollero, P. (2009). Air–steam gasification of biomass in a fluidised bed: Process optimisation by enriched air. *Fuel Processing Technology Vol 90(5)*, 677–685.

Campoy, M., Gómez-Barea, A., Villanueva, A. L., & Ollero, P. (2008). Air–steam gasification of biomass in a fluidized bed under simulated autothermal and adiabatic conditions. *Industrial Engineering Chem. Res Vol 47(16)*, 5957–5965.

Cau, G., Tola, V., Ferrara, F., Porcu, A., & Pettinau, A. (2018). Co2-free coal-fired power generation by partial oxy-fuel and post-combustion co2 capture: Techno-economic analysis. *Fuel Vol 214*, 423–435.

Chi, J., & Yu, H. (2018). *Water electrolysis based on renewable energy for hydrogen production* (tech. rep.). Chinese Academy of Sciences.

Christensen, A. (2020). Assessment of hydrogen production costs from electrolysis: United states and europe. *International Council on Clean Transportation*, 1–73.

Cormos, C.-C. (2016). Oxy-combustion of coal, lignite and biomass: A techno-economic analysis for a large scale carbon capture and storage (ccs) project in romania. *Fuel Vol 169*, 50–57.

Craig, K. R., & Mann, M. K. (1996). Cost and performance analysis of biomass-based integrated gasification combined-cycle (bigcc) power systems. *NREL*, 26–32.

Dahlen, E. (2023, February 10). Stockholm exergi.

David, H. (1967). *Basic principles and calculations in chemical engineering, 2 ed.* Prentice Hall.

DeWitt, D. P. (2006). Fundamentals of heat and mass transfer. *6th edition,* 658–660.

Du, Z., Zhai, J., Guo, X., Xiong, Y., Su, W., & He, G. (2021). A review of hydrogen purification technologies for fuel cell vehicles. *Catalysts for Sustainable Hydrogen Production: Preparation, Applications and Process Integration Vol 11(3)*.

Edwards, R. L., & Demuren, A. (2019). Interface model of pem fuel cell membrane steady-state behavior. *International Journal of Energy and Environmental Engineering Vol 10*, 85–106.

Ellevio. (2023, February 26). *Elnätspriser företag*. Retrieved February 26, 2023, from https://www.ellevio.se/foretag/om-er-el/forsta-er-elnatskostnad/ert-pris/

Energimyndigheten. (2023a, April 6). *Industriklivet*. Retrieved April 6, 2023, from https://www.energimyndigheten.se/forskning-och-innovation/forskning/industri/industriklivet/

Energimyndigheten. (2023b, April 6). *Större pilot och demonstrationsprojekt för energi- och klimatomställning*. Retrieved April 6, 2023, from https://www.energimyndigheten.se/utlysningar/storre-pilot-och-demonstrationsprojekt-for-energi--och-klimatomstallning/

Energimyndigheten. (2023c, February 22). *Trädbränsle-, torv- och avfallspriser*. Retrieved February 22, 2023, from https://www.energimyndigheten.se/statistik/den-officiella-statistiken/statistikprodukter/tradbransle--och-torvpriser/?currentTab=1

Esett-Oy. (2022). Nordisk balansavräkning – handbok. *Instruktioner och regler för marknadsaktörer*.

European-Commission. (2023, April 6). *Questions and answers on the eu delegated acts on renewable hydrogen*. Retrieved April 6, 2023, from https://ec.europa.eu/commission/presscorner/detail/en/qanda_23_595

Exergi, S. (2023a, March 9). *How it works*. Retrieved March 9, 2023, from https://beccs.se/cdr/how-it-works/

Exergi, S. (2023b, May 11). *Minusutsläpp via koldioxidinfångning*. Retrieved May 11, 2023, from https://www.stockholmexergi.se/minusutslapp/

Fingrid. (2021). Frequency quality analysis 2020. *Fingrid*.

Fuchs, J., Schmid, J. C., Müller, S., & Hofbauer, H. (2019). Dual fluidized bed gasification of biomass with selective carbon dioxide removal and limestone as bed material, a review. *Renewable and Sustainable Energy Reviews Vol 107*, 212–231.

Fuller, E. N., Schettler, P. D., & Giddings, J. C. (1966). New method for prediction of binary gas-phase diffusion coefficients. *Industrial and engineering chemistry vol 58(5)*, 18–27.

Gallandat, N., Romanowicz, K., & Züttel, A. (2017). An analytical model for the electrolyser performance derived from materials parameter. *Journal of Power and Energy Engineering Vol 5(10)*, 34–49.

Gil, F. S. C. (2016). *Downdraft gasifier modeling* (tech. rep.). Universidad Eafit, Medellin.

Glicksman, L. R., Hyre, M. R., & Farrelll, P. A. (1994). *Dynamic similarity in fluidization* (tech. rep.). Massachusetts Institute of Technology, Cambridge.

Gøbel, B., Henriksen, U., Jensen, T. K., Qvale, B., & Houbak, N. (2007). The development of a computer model for a fixed bed gasifier and its use for optimization and control. *Bioresource Technology Vol 98(10)*, 2043–2052.

Gómez-Barea, A., & Leckner, B. (2013). Estimation of gas composition and char conversion in a fluidized bed biomass gasifier. *Fuel Vol 107*, 419–431.

Gong, X. (2014). Pilot-scale comparison investigation of different entrained-flow gasification technologies and prediction on industrial-scale gasification performance. *Fuel*, 37–44.

Group, P. C. (2023, April 16). Power generation system 100. Retrieved April 16, 2023, from https://powercellgroup.com/product/power-generation-system-100/

Gustafsson, K., Sadegh-Vazairi, R., Grönkvist, S., Levihn, F., & Sundberg, C. (2021). Beccs with combined heat and power: Assessing the energy penalty. *International Journal of Greenhouse Gas Control vol 110*, 103434.

Hamadeh, H., Toor, S. Y., Douglas, P. L., Sarathy, M., Dibble, R. W., & Croiset, E. (2020). Techno-economic analysis of pressurized oxy-fuel combustion of petroleum coke. *Energies Vol 13(13)*, 3463.

Hanak, D. P., Powell, D., & Manovic, V. (2017). Techno-economic analysis of oxy-combustion coal-fired power plant with cryogenic oxygen storage. *Applied Energy Vol 191*, 193–203.

Hannula, I., & Kurkela. (2013). *Liquid transportation fuels via large-scale fluidised-bed gasification of lignocellulosic biomass* (tech. rep.). VTT Technical Research Centre of Finland.

Heden, A., & Saleh., M. (2021). Implementation of oxyfuel combustion in a waste incineration chp plant. *Mälardalen university*, 264–273.

Hoedemakers, I. (2021). *Study of the bubble behavior in alkaline water electrolysis* (tech. rep.). Eindhoven University of Technology.

Holmgren, K. M. (2015). Investment cost estimates for gasificationbased biofuel production systems. *IVL Swedish Environmental Research Institute*, 11–15.

Holmgren, M. (2023, April 24). *X steam, thermodynamic properties of water and steam*. Retrieved April 24, 2023, from https://se.mathworks.com/matlabcentral/fileexchange/9817-x-steam-thermodynamic-properties-of-water-and-steam

Hruška, M., Variny, M., Haydary, J., & andJán Janošovský. (2020). Sulfur recovery from syngas in pulp mills with integrated black liquor gasification. *Forests Vol 11(11)*.

Hu, Y., Li, X., Li, H., & Yan, J. (2013). Peak and off-peak operations of the air separation unit in oxy-coal combustion power generation systems. *Energies Vol 112*, 747–754.

II, T. A. A., & Barton, P. I. (2009). A dynamic two-dimensional heterogeneous model for water gas shift reactors. *International Journal of Hydrogen Energy Vol 34(21)*, 8877–8891.

Incropera, F. P. (2017). *Principles of heat and mass transfer*. John Wiley Sons Inc.

Jansen, D., van Selow, E., Cobden, P., Manzolini, G., Macchi, E., Gazzani, M., Blom, R., Henriksen, P. P., Beavis, R., & Wright, A. (2013). Sewgs technology is now ready for scale-up. *Energy Procedia Vol 37*, 2265–2273.

Ji, M., & Wang, J. (2021). *Review and comparison of various hydrogen production methods based on costs and life cycle impact assessment indicators* (tech. rep.). Hydrogen Energy Publications LLC. Published by Elsevier Ltd.

Jia, L., McCalden, D., Tan, Y., Wu, Y., He, I., Symmonds, R., & Anthony, E. (2013). Commissioning of a 0.8 mwth cfbc for oxy-fuel combustion. *Commissioning of a 0.8 MWth CFBC for oxy-fuel combustion Vol 7*.

Jonsson, A., & Mässgård, H. (2021). *An Industrial Perspective on Ultrapure Water Production for Electrolysis* (tech. rep.). Royal institute of technology.

Jonsson, F., & Miljanovic, A. (2022). *Utalization of waste heat from hydrogen production* (tech. rep.). Mälardalen University.

JR., G. (1986). Fluid beds as chemical reactors. *Gas Fluidization Technology*, 285–339.

Kalmykov, K., Anikina, I., Kolbantseva, D., Trescheva, M., Treschev, D., Kalyutik, A., Aleshina, A., & andIaroslav Vladimirov. (2022). Use of heat pumps in the hydrogen production cycle at thermal power plants. *Sustainability Vol 14(13)*.

Khanipour, M., Mirvakili, A., Bakhtyari, A., Farniaei, M., & Rahimpour, M. R. (2017). Enhancement of synthesis gas and methanol production by flare gas recovery utilizing a membrane based separation process. *Fuel Processing Technology Vol 166*, 186–201.

Khavidak, S. S., Pallarès, D., Normann, F., Johnsson, F., & Ylä-Outinen, V. (2015). Heat transfer in a 4–mwth circulating fluidized bed furnace operated under oxy-fired and air-fired conditions: Modeling and measurements. *International Journal of Greenhouse Gas Control Vol 37*, 264–273.

Kopp, M., Coleman, D., Stiller, C., Scheffer, K., Aichinger, J., & Scheppat, B. (2017). Energiepark mainz: Technical and economic analysis of the worldwide largest power-to-gas plant with pem electrolysis. *International Journal of Hydrogen Energy Vol 42(19)*, 13311–13320.

Kramb, J., Konttinen, J., Gómez-Barea, A., Moilanen, A., & Umeki, K. (2014). Modeling biomass char gasification kinetics for improving prediction of carbon conversion in a fluidized bed gasifier. *Fuel Vol 12*, 107–115.

Laboratory, N. R. E. (2006). Equipment design and cost estimation for small modular biomass systems, synthesis gas cleanup, and oxygen separation equipment. *Task 2: Gas Cleanup Design and Cost Estimates, Wood Feedstock*, 59–65.

Laurendeal, N. (1978). Heterogeneous kinetics of coal char gasification and combustion. *Energy combustion science vol 4(4)*, 221–270.

Leckner, B., Szentannai, P., & c, F. W. (2011). Scale-up of fluidized-bed combustion – a review. *Fuel Vol 90(10)*, 2951–2964.

Lee, S. J., Kim, S. H., Kang, K. H., Yoo, Y. D., & Yun, Y. (2007). Development of a pilot-scale acid gas removal system for coal syngas. *Korean Journal of Chemical Engineering Vol 24*, 1128–1132.

LeValley, T. L., Richard, A. R., & Fan, M. (2014). The progress in water gas shift and steam reforming hydrogen production technologies – a review. *International Journal of Hydrogen Energy Vol 39(30)*, 16983–17000.

Lewin, C. S., de Aguiar Martins, A. R. F., & Pradelle, F. (2020). Modelling, simulation and optimization of a solid residues downdraft gasifier: Application to the co-gasification of municipal solid waste and sugarcane bagasse. *Energy vol 210*, 118498.

Li, M., Rao, A. D., & Samuelsen, G. S. (2012). Performance and costs of advanced sustainable central power plants with ccs and h2 co-production. *Applied Energy vol 91(1)*, 43–50.

Li, P., Wang, Z., Qiao, Z., Liu, Y., Cao, X., Li, W., Wang, J., & Wang, S. (2015). Recent developments in membranes for efficient hydrogen purification. *Journal of Membrane Science Vol 495*, 130–168.

Lian, Z., Wang, Y., Zhang, X., Yusuf, A., Famiyeh, L., Murindababisha, D., Jin, H., Liu, Y., He, J., Wang, Y., Yang, G., & Sun, Y. (2021). Hydrogen production by fluidized bed reactors:a quantitative perspective using the supervised machinelearning approach. *MDPI Vol 4(3)*, 6–10.

Lin, H., He, Z., Sun, Z., Vu, J., Ng, A., Mohammed, M., Kniep, J., Merkel, T. C., Wu, T., & Lambrecht, R. C. (2014). Co2-selective membranes for hydrogen production and co2 capture – part i: Membrane development. *Journal of Membrane Science Vol 457*, 149–161.

Lindborg, J. (2023). Syrgasens potentiella värde och möjligheter. *HyCoGen P107879-7*, 1–14.

Liu, D., & Chen, X. (2010). Lateral solids dispersion coefficient in large-scale fluidized beds. combustion and flame. *Combustion and Flame Vol 157(11)*, 2116–2124.

Liu, H., J., R., Cattolica, Seiser, R., & Liao, C.-h. (2015). Three-dimensional full-loop simulation of a dual fluidized-bed biomass gasifier. *Applied Energy Vol 160*, 489–501.

López, R., Fernández, C., Martínez, O., & Sánchez, M. (2016). Techno-economic analysis of a 15 mw corn-rape oxy-combustion power plant. *Fuel Processing Technology Vol 154*, 296–304.

Lundberg, L. (2018). *Solid Fuel Conversion in Dual Fluidized Bed Gasification , Modelling and Experiments* (tech. rep.). Chalmers university of technology.

Lupion, M., Alvarez, I., Otero, P., Kuivalainen, R., Lantto, J., Hotta, A., & Hack, H. (2013). 30 mwth ciuden oxy-cfb boiler - first experiences. *Energy Procedia Vol 37*, 6179–6188.

M, B., Benny, G., Henriksen, R. H., Birk, U., E., H. J., & H., S. L. (2000). Steam gasification of wood char and the effect of hydrogen inhibition on the chemical kinetics. *Progress in Thermochemical Biomass Conversion*.

Machhammer, O., Bode, A., & Hormuth, W. (2016). Financial and ecological evaluation of hydrogen production processes on large scale. *Chemical engineering technology Vol 39(6)*, 1185–1193.

Matlab version 9.7 r2021b. (2022). The Mathworks, Inc. Natick, Massachusetts.

Mesfun, S., Anderson, J.-O., Umeki, K., & Toffolo, A. (2016). Integrated sng production in a typical nordic sawmill. *Energies Vol 9(5)*, 333.

Miljöförvaltningen. (2023, February 16). *Volym levererad fordonsgas*. Retrieved February 16, 2023, from https://miljobarometern.stockholm.se/trafik/miljobilar-och-fornyelsebara-branslen/volym-levererad-fordonsgas/

Mimer. (2023, March 26). *Market data*. Retrieved March 26, 2023, from https://mimer.svk.se/PrimaryRegulation/PrimaryRegulationIndex

Morselli, N., Parenti, M., Puglia, M., & Tartarini, P. (2019). Use of fabric filters for syngas dry filtration in small-scale gasification power systems. *AIP Conference Proceedings Vol 2191(1)*.

Mumford, K. A., Smith, K. H., Anderson, C. J., Shen, S., Tao, W., Suryaputradinata, Y. A., Quyn, D. M., Qader, A., Hooper, B., Innocenzi, R. A., & Kentish, S. E. (2011). Post-combustion capture of co2: Results from the solvent absorption capture plant at hazelwood power station using potassium carbonate solvent. *Energy Fuel Vol 26(1)*, 138–146.

Naturvårdsverket. (2023, April 6). *Klimatklivets samlade resultat*. Retrieved April 6, 2023, from https://www.naturvardsverket.se/amnesomraden/klimatomstallningen/klimatklivet/resultat-for-klimatklivet/

NETL. (2023, March 29). *Syngas contaminant removal and conditioning*. Retrieved March 29, 2023, from https://netl.doe.gov/research/coal/energy-systems/gasification/gasifipedia/cleanup

NETL. (2010). Bituminous coal and natural gas to electricity. *Cost and Performance Baseline for Fossil Energy Plants Vol 1*, 153–154.

Nguyen, T., Abdin, Z., Holm, T., & Mérida, W. (2019a). Grid-connected hydrogen production via large-scale water electrolysis. *Energy Conversion and Management Vol 200*, 112108.

Nguyen, T., Abdin, Z., Holm, T., & Mérida, W. (2019b). Grid-connected hydrogen production via large-scale water electrolysis. *Energy Conversion and Management Vol 200*, 112108.

Nohlgren, I., Svärd, S. H., Jansson, M., & Rodin, J. (2014). El från nya och framtida anläggningar 2014. *Elforsk rapport 14:40*, 50–165.

Nordio, M., Wassie, S. A., Annaland, M. V. S., Tanaka, D. A. P., Sole, J. L. V., & Gallucci, F. (2021). Techno-economic evaluation on a hybrid technology for low hydrogen concentration separation and purification from natural gas grid. *International Journal of Hydrogen Energy Vol 46(45)*, 23417–23435.

Nordpool. (2023, April 26). *Market data*. Retrieved April 26, 2023, from https://www.nordpoolgroup.com/en/Market-data1/#/nordic/table

Nyqvist, J., & Sillén, M. (2023, April 3). *Värdekedjor för grön vätgas i stockholms län*. Retrieved April 3, 2023, from https://www.storsthlm.se/media/d2jdipy4/v%C3%A4rdekejor-f%C3%B6r-gr%C3%B6n-v%C3%A4tgas-i-stockholms-l%C3%A4n-f%C3%B6rstudie-energikontoret-storsthlm.pdf

P., B. S., B., S., & A., T. (1978). Fluidization correlations for coal gasification materials minimum fluidization velocity and fluidized bed expansion ratio. *IAIChE Symp Ser Vol 74(176)*, 176–186.

Pallarès, D., & Johnsson, F. (2006). A novel technique for particle tracking in cold 2-dimensional fluidized beds—simulating fuel dispersion. *Chemical Engineering Science Vol 61(8)*, 2710–2720.

Paraschiv, L. S., Serban, A., & Paraschiv, S. (2020). Calculation of combustion air required for burning solid fuels (coal / biomass / solid waste) and analysis of flue gas composition. *Energy Reports Vol 6(3)*, 36–45.

Pettinau, A., Ferrara, F., Tola, V., & Cau, G. (2017). Techno-economic comparison between different technologies for co2-free power generation from coal. *Applied Energy Vol 193*, 426–439.

R., B., & D., F. (1985). *2.1 the bisection algorithm 3rd ed.* PWS.

Radmanović, K., Đukić, I., & Pervan, S. (2012). *Specific Heat Capacityof Wood* (tech. rep.). University of Zagreb,University of Zagreb.

Ramos, A., Monteiro, E., & Rouboa, A. (2019). Numerical approaches and comprehensive models for gasification process: A review. *Renewable and Sustainable Energy Reviews Vol 110*, 188–206.

Raphson, J. (1697). *Analysis aequationum universalis 2nd ed.* Thomas Bradyll.

Reyes, Á. (2023, April 7). *Balance of plant of an electrolyser (incl. product files)*. Retrieved April 7, 2023, from https://synerhy.com/en/2022/02/balance-of-plant-bop-of-an-electrolyser/

Ribeiro, A. M., Grande, C. A., Lopes, F. V., Loureiro, J. M., & Rodrigues, A. E. (2008). A parametric study of layered bed psa for hydrogen purification. *Chemical Engineering Science Vol 63(21)*, 5258–5273.

Rudra, S., & Tesfagaber, Y. K. (2019). Future district heating plant integrated with municipal solid waste (msw) gasification for hydrogen production. *Energy Vol 180*, 881–892.

Saeed, W., & Warkozek, G. (2015). Modeling and analysis of renewable pem fuel cell system. *Energy Procedia Vol 74*, 87–101.

Sakas, G. (2021). Dynamic energy and mass balance model for an industrial alkaline water electrolyzer plant process. *International Journal of Hydrogen Energy*, 4328–4345.

Sánchez, M., Amores, E., Abad, D., Rodríguez, L., & Clemente-Jul, C. (2020). Aspen plus model of an alkaline electrolysis system for hydrogen production. *International Journal of Hydrogen Energy Vol 45(7)*, 3916–3929.

Schmidt, O., Gambhir, A., Staffell, I., Hawkes, A., Nelson, J., & Few, S. (2017). Future cost and performance of water electrolysis:an expert elicitation study. *International Journal of Hydrogen Energy Volume 42(52)*, 30470–30492.

Schnuelle, C., Wassermann, T., Fuhrlaender, D., & Zondervan, E. (2020). Dynamic hydrogen production from pv & wind direct electricity supply – modeling and techno-economic assessment. *International Journal of Hydrogen Energy Vol 45(55)*, 29938–29952.

Sharifiana, S., Asasian-Kolura, N., & Harasekb, M. (2019). Process simulation of syngas purification by gas permeation application. *Chemical engineering transactions Vol 76*.

Singh, J., & Tan, T. (2023, April 16). *Carbon offsets price may rise 3,000% by 2029 under tighter rules*. Retrieved April 16, 2023, from https://www.bloomberg.com/professional/blog/carbon-offsets-price-may-rise-3000-by-2029-under-tighter-rules/

Sjölin, K., & Holmgren, E. (2019). *A Proton Exchange Membrane and Solid Oxide Fuel Cell comparison* (tech. rep.). Department of Mechanics and Maritime Sciences Chalmers University of Technology.

Skatteverket. (2023, April 6). *Skatt på el*. Retrieved April 6, 2023, from https://skatteverket.se/foretag/skatterochavdrag/punktskatter/energiskatter/skattpael.4.15532c7b1442f256bae5e4c.html

Solli, K.-A., Thapa, R. K., & Moldestad, B. M. E. (2016). Screening of kinetic rate equations for gasification simulation models, 105–112.

Stanger, R., Wall, T., Spörl, R., Paneru, M., Grathwohl, S., Weidmann, M., Scheffknecht, G., McDonald, D., Myöhänen, K., Ritvanen, J., Rahiala, S., Hyppänen, T., Mletzko, J., Kather, A., & f, S. S. (2015). Oxyfuel combustion for co2 capture in power plants. *International Journal of Greenhouse Gas Control Vol 40*, 55–125.

SVK. (2023a, March 16). *Marknaden för stödtjänster*. Retrieved March 16, 2023, from https://www.svk.se/press-och-nyheter/press/marknaden-for-stodtjanster-till-kraftsystemet-vaxer-kraftigt---3292104/

SVK. (2023b, May 10). *Systemutvecklingsplan 2022–2031*. Retrieved May 10, 2023, from https://www.svk.se/siteassets/om-oss/rapporter/2021/svk_systemutvecklingsplan_2022-2031.pdf

SVK. (2023c, April 17). *Systemutvecklingsplan 2022–2031*. Retrieved April 17, 2023, from https://www.svk.se/siteassets/om-oss/rapporter/2021/svk_systemutvecklingsplan_2022-2031.pdf

SVK. (2022). Handel med och prissättning av reserver.

Tanaka, Y., Mesfun, S., Umeki, K., Toffolo, A., Tamaura, Y., & Yoshikawa, K. (2015). Thermodynamic performance of a hybrid power generation system using biomass gasification and concentrated solar thermal processes. *Applied Energy Vol 160*, 664–672.

Thunman, H., Gustavsson, C., Larsson, A., Gunnarsson, I., & Tengberg, F. (2018). Economic assessment of advanced biofuel production via gasification using cost data from the gobigas plant. *Energy Science & Engineering Vol 7(1)*.

Tibbelin, A., Lindborg, J., Fürdös, A. N., & Forsström, E. (2022). Vätgasproduktion för ellagring efter elnätsnytta och affärsmodeller. *RISE Research Institutes of Sweden*, (47590-1), 1–102.

Tiktak, W. (2019). *Heat management of pem electrolysis, a study on the potential of excess heat from medium to large scale pem electrolyisis and the performance analysis of a dedicated cooling system* (tech. rep.). Delft University of Technology.

Tuinema, B. W., Adabi, M. E., Ayivor, P. K. S., Suárez, V. G., Liu, L., Perilla, A., Ahmad, Z., Torres, J. L. R., van der Meijden, M. A., & Palensky, P. (2020). *Modelling of Large-Size Electrolysers for Real-Time Simulation and Study of the Possibility of Frequency Support by Electrolysers* (tech. rep.). Delft University of Technology.

Um, S., Wang, C. Y., & Chen, K. S. (2000). Computational fluid dynamics modeling of proton exchange membrane fuel cells. *Electrochemchal Society Vol 147(12)*, 4485–4493.

Valente, A., Iribarren, D., & Dufour, J. (2020). Prospective carbon footprint comparison of hydrogen options. *Science of The Total Environment Vol 728*, 138212.

Vogt, U. (2023, April 6). *Novel developments in alkaline water electrolysis*. Retrieved April 6, 2023, from https://www.elygrid.com/wp-content/uploads/2021/07/event_8th-international-symposium-hydrogen-and-energy.pdf

Vu, T. T., Lim, Y.-I., Song, D., Mun, T.-Y., Moon, J.-H., Sun, D., Hwang, Y.-T., Lee, J.-G., & Park, Y. C. (2020). Techno-economic analysis of ultra-supercritical power plants using air- and oxy-combustion circulating fluidized bed with and without co2 capture. *Energy Vol 194*, 116855.

Weerachanchai, P., Horio, M., & Tangsathitkulchai, C. (2008). Effects of gasifying conditions and bed materials on fluidized bed steam gasification of wood biomass. *Bioresource Technology Vol 100(3)*, 1419–1427.

Weiß, A., Siebel, A., Bernt, M., Shen, T.-H., Tileli, V., & Gasteiger, H. A. (2019). Impact of intermittent operation on lifetime and performance of a pem water electrolyzer. *Electrochem. Soc. Vol 166 F487*, 487.

Wilk, V., Kitzler, H., Koppatz, S., Pfeifer, C., & Hofbauer, H. (2011). Gasification of waste wood and bark in a dual fluidized bed steam gasifier. *Biomass Conversion and Biorefinery Vol 1*, 91–97.

Williams, R., & Kaffka, S. (2015). *Public Interest Energy Research (PIER) Program* (tech. rep.). California Biomass Collaborative, University of California, Davis.
Woolcock, P. J., & Brown., R. C. (2013). A review of cleaning technologies for biomass-derived syngas. *Biomass and Bioenergy Vol 52*, 54–84.
Wu, Y., Liu, D., Ma, J., & Chen, X. (2018). Effects of gas-solid drag model on eulerian-eulerian cfd simulation of coal combustion in a circulating fluidized bed. *Powder Technology Vol 324*, 48–61.
Xing, T. L. L. H. (2008). *Statistical models and methods for financial markets*. Springer.
Yigit, T., & Selamet, O. F. (2016). Mathematical modeling and dynamic simulink simulation of high-pressure pem electrolyzer system. *International Journal of Hydrogen Energy*, 13901–13914.

Appendix A

1 Calculation abbreviation

1.1 Algebraic solution to gasification

By calculating the required oxygen O_{in} dependent on fuel, an initial value is determined, which is utilized to solve the reaction formula 22 with six equations that are defined as the following matrice:

$$C_{IN} = c + d + f \tag{B1}$$
$$H_{IN} = 2b + 2e + 4f \tag{B2}$$
$$O_{IN} = c + 2d + e \tag{B3}$$
$$N_{IN} = 2a \tag{B4}$$
$$K_{eq} = \frac{b \cdot d}{c \cdot e} \tag{B5}$$
$$A_{mc} = \frac{f}{c} \tag{B6}$$

The Equations are then utilized to solve the variable a. The remaining expressions can be rearranged to form a quadratic equation, with only variable c left unsolved. The expression for the quadratic formula is $A \cdot c^2 + B \cdot c + C = 0$. This algebraic approach is to calculate the stoichiometric reactions and constants relevant to gasifier output. The setup of algebraic Equations together with reaction variables is used to solve the problem as presented:

$$A = 1 + 5A_{mc} + 4A_{mc}^2 - K_{eq}(1 + 2A_{mc}) \tag{B7}$$
$$B = C_{IN}(2K_{eq} - 3 - A_{mc}) + H_{IN}(-\tfrac{1}{2} - \tfrac{1}{2}A_{mc}) + O_{IN}(1 + A_{mc} - K_{eq}) \tag{B8}$$
$$C = C_{IN}(2C_{IN} + \tfrac{1}{2}H_{IN} - O_{IN}) \tag{B9}$$

By solving the quadratic equation, two solutions are obtained for the variable c. Testing the result, only positive solutions determine the value for all variables a-f. In the case, one of the solutions is resulting in a negative number, the solution of variable c can be rejected. Updated values are written as Equation Matrice:

$$a = \tfrac{1}{2}N_{IN} \tag{B10}$$
$$b = \tfrac{1}{2}H_{IN} - O_{IN} + 2C_{IN} - c(1 + 4A_{mc}) \tag{B11}$$
$$d = C_{IN} - c(1 + A_{mc}) \tag{B12}$$
$$e = O_{IN} - 2C_{IN} + c(1 + 2A_{mc}) \tag{B13}$$
$$f = c \cdot A_{mc} \tag{B14}$$

Solution of the Equation system, thus estimation of outgoing composition can be defined inserted in the general expression for gasification, Equation 22, with the mass flow of solid fuel, oxygen, and steam.

1.2 Solution for conversion rate

Water gas shift reaction, the atomic balance of CSTR conversion presented in Matrices B15. CH_4, O_2, and N_2 are not affected through the process.

$$H_{2_{out}} = H_{2_{in}} + X_{H_2O} + r_{wgsr} \tag{B15}$$
$$CO_{out} = CO_{in} + 2X_{CO_2} + X_{H_2O} - r_{wgsr} \tag{B16}$$
$$CO_{2_{out}} = CO_{2_{in}} - X_{CO_2} + r_{wgsr} \tag{B17}$$
$$H_2O_{out} = H_2O_{in} - X_{H_2O} - r_{wgsr} \tag{B18}$$
$$\tag{B19}$$

Water gas shift reaction, of atomic balance in freeboard space. Assuming PFR, calculation presented in matrix B20 represent the reaction, CH_4, O_2 and N_2 are not affected through the process.

$$H_{2_{out}} = H_{2_{in}} + r_{wgsr} t_{space} \tag{B20}$$
$$CO_{out} = CO_{in} - r_{wgsr} t_{space} \tag{B21}$$
$$CO_{2_{out}} = CO_{2_{in}} + r_{wgsr} t_{space} \tag{B22}$$
$$H_2O_{out} = H_2O_{in} - r_{wgsr} t_{space} \tag{B23}$$
$$\tag{B24}$$

This method also applies to downstream equipment shifting steam and carbon monoxide but with a reaction rate dependent on the catalyst and a set resident time to accelerate the process.

1.3 Algebraic solution to combustion

Stoichiometric balance is calculated using the minimum molar flow rate of each gas, as the flow of oxygen $\dot{m}_{combustion}$ are from oxidizer output, shown in reaction:

$$O2_{out} = \dot{m}_{combustion} - \dot{m}_{stochiometry} \tag{B25}$$
$$N2_{out} = \dot{m}_{stochiometry} \tfrac{1}{2} N_{IN} + (\tfrac{N_{ox}}{O_{ox}}) \dot{m}_{combustion} \tag{B26}$$
$$H2_{out} = 0 \tag{B27}$$
$$CO_{out} = 0 \tag{B28}$$
$$CO2_{out} = C_{IN} \dot{m}_{stochiometry} + \tfrac{CO2_{ox}}{O_{ox}} \dot{m}_{combustion} \tag{B29}$$
$$H2O_{out} = (\tfrac{1}{2} H_{IN} + H_2O_{IN}) \dot{m}_{stochiometry} + \tfrac{H_2O_{ox}}{O_{ox}} \dot{m}_{combustion} \tag{B30}$$
$$CH4_{out} = 0 \tag{B31}$$
$$\tag{B32}$$

then recompile the updated composition of flue gas.

1.4 Dimensions of gasifier

The primary method of scaling the BFB gasifier is by adhering to the *The Damköhler criterion* from solving the fluid dynamic conditions and char dispersion found in literature (Leckner et al., 2011). The account of gas movement in vertical and horizontal directions through the reactor to describe diffusion or chemical reaction rate in terms of dimensionless ratio is called the Damköhler number. Through Equation B33 this number is determined, as $t_{transport}$ is the particle radial transportation time, and $t_{reaction}$ is the time of reaction for the devolatilization.

$$Da = \frac{t_{transport}}{t_{reaction}}. \tag{B33}$$

The criterion for assuming that the fuel is fully dispersed in the bottom of the reactor and that the devolatilization of all fuel is complete, the Damköhler number requires to be lower than 1. In this model, the same time of reaction is set for temperatures ranging from 750 to 850 °C according to reference study (Tanaka et al., 2015), and the minimum time of 54 was used to describe the near complete devolatilization the fuel (Campoy et al.,

2008). In order to scale the gasifier depending on radial dispersion or geometry d_{bed} and dispersion coefficient D_h, can be solved by the Einstein expression in Equation B34.

$$t_{trans} = \frac{d_{bed}^2}{2D_h}. \tag{B34}$$

The dispersion coefficient is taken from literature (Pallarès & Johnsson, 2006), as catalyst bed material is weighted to global dispersion values and superficial velocity u_0. Horizontal geometry and particle trace, also affect the coefficient and thus scaling is made as a function, as the dimension is not linear (D. Liu & Chen, 2010), and can be calculated as for example with Equation B35, to obtain the updated value of bed diameter depending on biomass feed $\dot{m}_{fuel}$ and reference width d_{ref}.

$$d_{bed} = \sqrt{\dot{m}_{fuel}\, 0.4452}. \tag{B35}$$

If the mathematical approximation of geometry input, does not satisfy the earlier stated conditions, values need to be configured to complete calculations. In accordance with the previously mentioned criteria, the proportion between the bed and freeboard needs to be configured so that the reaction rate is similar to reference experiments. The dimensionless numbers determining the proportion is derived from fluid-dynamic correlations, as the full set of these values are calculated at a common approach of modeling, as Glicksman presents it (Glicksman et al., 1994), through expressions B36.

$$\frac{v_o \rho_g d_{bm}}{\mu_g}, \frac{v_0^2}{gD}, \frac{\rho_g}{\rho_{bm}}, \frac{D}{H}, \frac{d_{bm}}{D}. \tag{B36}$$

In the single-course kinetic calculation of fixed bed, an alternative method of setting the structure geometry, not including trivial effects, is by determining the geometry of the gasifier without the Damkhöler number, thus not accounting for the dispersion of fuel. To calculate the molar flow depending on height can be rearranged by calculating the structural active surface A_j, from the void factor inside the reactor with Equation B37(Gil, 2016).

$$\frac{\partial n_j}{\partial y} = \sum_j D_i A_j(y). \tag{B37}$$

The method of predetermined geometry does not include varied states of the structure profile and is thus rejected to calculate the molar flow. Method when trivial effects on conversion rate without the influence of CH_4, is utilized. Applying the reactivity of the char and particle model, in Equation B39, the active area of solids,A_s, can be calculated with rearrangement of expression B38.

$$\frac{\partial n_{char}}{\partial y} = A_s \sum (D_i \rho_0\,). \tag{B38}$$

The volume and active surface are then defined by Equation B39, as reactor diameter d_t, is constant and height y varies dependent on the porous particle model reaching maximum reactivity rate. Figure 14 displays the geometry for the fixed bed gasifier.

$$V_{bed} = \pi(\frac{d_t}{2})y, \quad and \quad A_s = (1 - \epsilon_{bed})A. \tag{B39}$$

To calculate void fraction for the FB gasifier, Equation B40 as the active surface is derived from species volume in the gasifier. The particle diameter d_p can be related to $f(X)$ in stationary conditions when $X = 0$.

$$\epsilon_{bed} = 0.38 + 0.073 \left[1 + \frac{(\frac{d_t}{d_p} - 2)^2}{(\frac{d_t}{d_p})^2} \right]. \tag{B40}$$

The height is determined, with Equation 55, as the exchange of structural profile generates the volume differential for the rate of species entering and leaving the gasifier.

1.5 Mass and heat transfer models for electrolyzers

Calculating the technological performance of the electrolysis stack, utilization of heat, and utility is required, to estimate the overall technological efficiency. In this calculation, it is notable that the different theoretical material flows are adapted to suit a realistic output by applying mechanical, recovery, and electrical efficiency to the mathematical model. For example, in calculating the mass flow of water required for the desired configuration of the stack that is expressed by the relation: $\dot{m}_{O2} + \dot{m}_{H2} = \dot{m}_{H2O}$, the theoretical mass flow of water is divided by $\eta_{recovery}$, to update flow for water pump and mass transfer equation.

1.5.1 Heat recovery AEL

The main Equation B41 is describing the thermodynamic balance of the system, expressed as the useful heat Q_{useful} that is also equal to the cooling demand of the stack Q_{cool}.

$$Q_{useful} = Q_{gen} - Q_{loss} - Q_{Heating} + Q_{sensible}. \tag{B41}$$

The sensible heat in this process is expressed by B42, and represents the cooling of compressed gas. The heat transferred from the compressed gas is assumed to be in direct connection to the electrolyzer cooling circuit but is not representative of how an actual cooling system is designed. Here the thermal capacity of gas C_p, is adapted to the composition of gas at ambient temperature, without any adaptation to linear differential solutions.

$$Q_{sensible} = \dot{m}_{H_2} C_{p,H_2}(T_{H_2} - T_{stack}) + \dot{m}_{O_2} C_{p,O_2}(T_{O_2} - T_{stack}). \tag{B42}$$

In order to account for thermal losses from the stack to the surrounding environment, the loss is calculated with expression B43. The heat loss is dependent on stack active surface area A_{stack}, in combination with the radiation h_r and the convective h_C, heat transfer coefficient determining heat acclimation to ambient temperature T_a.

$$Q_{loss} = A_{stack}(h_c + h_r)(T_{stack} - T_a). \tag{B43}$$

The radiation conductivity is expressed as B44, as ε_{rad} is the emittance of stack material and σ_b represents the Boltzmann constant.

$$h_r = \sigma_b \varepsilon_{rad}(T_{stack})^3. \tag{B44}$$

To calculate the convective heat transfer coefficient, the stack can be assumed to operate on the ground surrounded by atmospheric air. The suitable method for ambient conditions is applying a low-velocity convection problem, as both buoyancy and natural air flow is accounted for in the Nusselt Equation B45. For ambient conditions of slow-moving air, the ratio between momentum diffusivity and thermal diffusion can be approximately defined with Prandt's number $Pr = 0.72$. In relation to buoyancy-driven flow and effect of viscosity, Raleigh number Ra_d, is applied as gravity around the cylindrical shape is the major drive for convection, thus is approximated to $Ra_d = 2.19 \cdot 10^5$ in accordance to empirical theory (Incropera, 2017).

$$Nu = \frac{(0.6 + (0.387 Ra_d^{1/6}))}{(1 + (\frac{0.559}{Pr})^{9/16})^{8/27}}. \tag{B45}$$

The vertical profile can in this case be set to $d_1 = 2d$, and k the conduction of steel with minor insulation, thus calculating the convective coefficient with expression B46.

$$h_c = \frac{Nu\, k}{d_1}. \tag{B46}$$

The heat exchange from inlet water and agitation after the water feed pump is defined by Equation B47, when the heat dispatch is based on the mixed electrolyte KOH and water as the transfer medium. The inlet temperature T_{inlett} of fluid is required to reach operational temperature, as the lye is cooled due to inlet temperature increase from pump compression,

$$Q_{Heat} = \dot{m}_{H_2O}(C_{p,KOH}\chi_{KOH} + (1 - \chi_{KOH})C_{p,w})(T_{stack} - T_{inlett}). \tag{B47}$$

The primary cooling system that the utilization of excess heat is based on, is the heat generated from losses due to overpotential in cell Q_{gen}.

$$Q_{gen} = N_c\, i\, A_{cell}(J_{cell} - J_{rev}). \tag{B48}$$

The transfer between the cooling circuit and heat exchange of return water from district heating resulting in output temperature of $T_{dh,out}$, is calculated with the NTU method. In the AEL cooling circuit, a maximum temperature difference from heat returning water after heat exchange is set to 6 ℃, though it is possible to increase temperature difference dependent on equipment thresholds. The general expression for the output capacity of district heating is via Equation B49.

$$Q_{DHw} = \dot{m}_w C_{p,w}(T_{dh,out} - T_{dh,in}) \tag{B49}$$

1.5.2 Heat recovery PEM

To calculate the performance of district heating output from the PEM electrolyzer stack, the same method as AEL can be applied to calculate the useful heat Q_{useful} , with changes in the uptake of sensible heat and heat

losses to the surrounding environment. The changes to sensible heat are because of uncertainties regarding hydrogen temperature, only utilizing the heat dissipated from the oxygen outlet since the hydrogen stream is not recirculated for heat exchange. The updated equation of recoverable sensible heat can be expressed as Equation B50.

$$Q_{sensible} = \dot{m}_{O_2} C_{p,O_2} (T_{O_2} - T_{stack}). \tag{B50}$$

The changes applied to heat losses from a cubical stack instead of cylindrical, are calculated via empirical theory, with the radiation coefficient B51.

$$h_r = 4\sigma_b \varepsilon_{rad} (T_{stack})^3. \tag{B51}$$

Calculating the convective heat transfer coefficient, the stack is assumed to operate on the ground surrounded by atmospheric air. The method for ambient conditions applies low-velocity convection conditions when both buoyancy and forced air flow is accounted for in the Nusselt Equation B52. For ambient conditions of slow-moving air at 0.2 m/s, the ratio between momentum diffusivity and thermal diffusion is approximately defined with Prandt's number $Pr = 0.72$. In accountancy to internal and viscous forces, the Reynolds number is applied. The application of Reynolds is suitable, because of the flow rate condition of air surrounding the stack, thus creating a laminar flow of $Re_L \approx 5 \times 10^4$. Reynolds and Prandt generate the average Nusselt number with Equation B52.

$$Nu = 0.66 Re^{0.675} Pr^{1/3}. \tag{B52}$$

In order to then calculate the convective transfer coefficient h_c, Equation B53 is applied, which is dependent on the characteristic length instead of profile diameter, as in the thermodynamic calculations for an AEL stack. The characteristic length is expressed as the surface area $L_1 = \sqrt{H}$ as described in literature (Tiktak, 2019).

$$h_c = \frac{Nu\, k}{L_1}. \tag{B53}$$

1.6 Mathematical curve fitting of cycling degradation

In the case of cycling, the following assumptions are made to modify the potential according to the fit degradation curve;

$$J_{cell} = J_{ocv} + (r_1 + r_2(T_{cell} + \beta_{bubble}\Theta))i + s_1 log_{10}((\xi_1 + \frac{\xi_2}{T_{cell}} + (\frac{\xi_3}{T_{cell}})^2)i + 1) - V_{dec}. \tag{B54}$$

In this time form, t defines the number of hours from initial activation.

$$J_{dec} = \frac{t_{activation^{0.3}}}{3.1} + 2t_{activation} e^{(t^{0.8}_{activation}(2.1 - t_{activation}))}. \tag{B55}$$

This assumption is not to be applied in the benchmarking model, since is not a confirmed result, and is rejected as it is not derived from empirical theory and only to illustrate the possible influence of time from experiment data.

Appendix B

1 Economy

1.1 Support service market

The figures below present the activity during the balance reserve operation, for the base scenario. Note that the volume is set in Megawatt, thus the amount of delivered MW per hour is accumulated during the hour. This does not however mean that capacity compensation will be paid for the delivered amount, and only for the max capacity of a Fuel cell(3.66 MW) or Electrolyzer(5.1 MW). Compensation for actual delivered volume is paid according to B1 or example B2.

$$Income_{tot} = P(0)\, C_{Capacitycompensation} + P(t_i)\, C_{Energycompensation}. \tag{B1}$$

This equation is only utilized for services that offer both kinds of compensation. If only one compensation is offered, the same equation works if the variable for the compensation type that is not offered is removed.

$$Income_{tot} = 3.66\, C_{Capacitycompensation} + \frac{6.95}{3600}\, C_{Energycompensation}. \tag{B2}$$

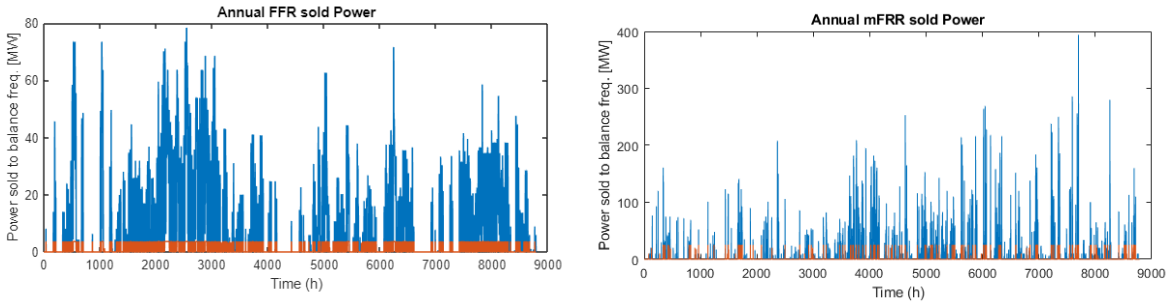

Figure B1: The demanded volume of support service market is represented by the color blue, as actual activity response by the Fuel cell is represented by the color orange.

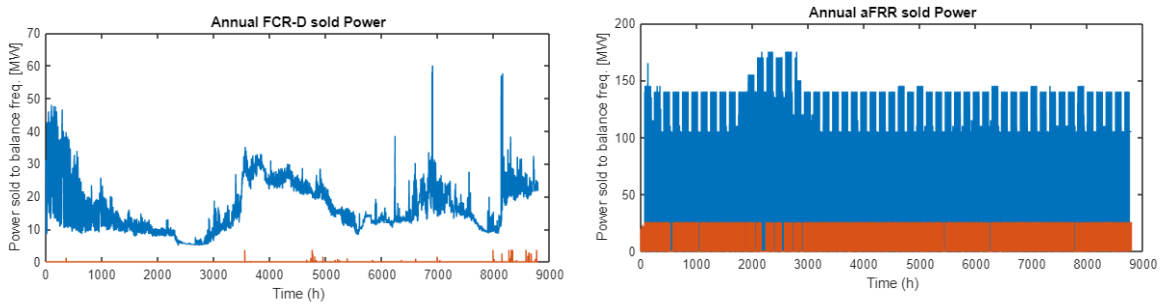

Figure B2: The demanded volume of support service market is represented by the color blue, as actual activity response by the Fuel cell is represented by the color orange.

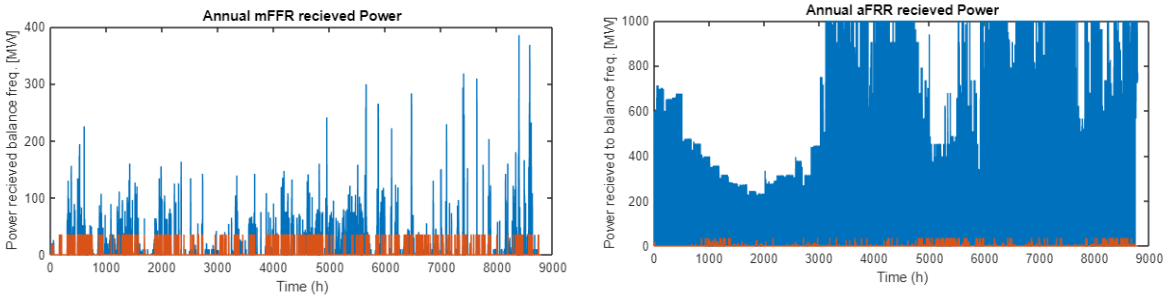

Figure B3: The demanded volume of support service market is represented by the color blue, as actual activity response by the Fuel cell is represented by the color orange

1.2 Market study

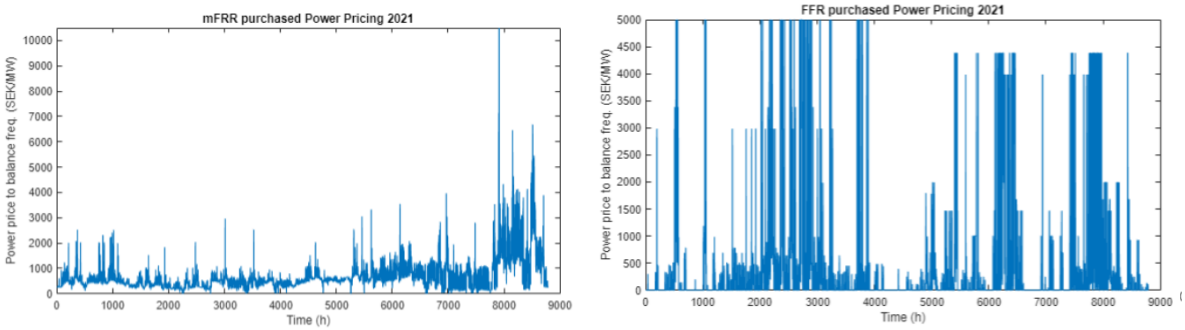

Figure B4: Support services pricing of historic data.

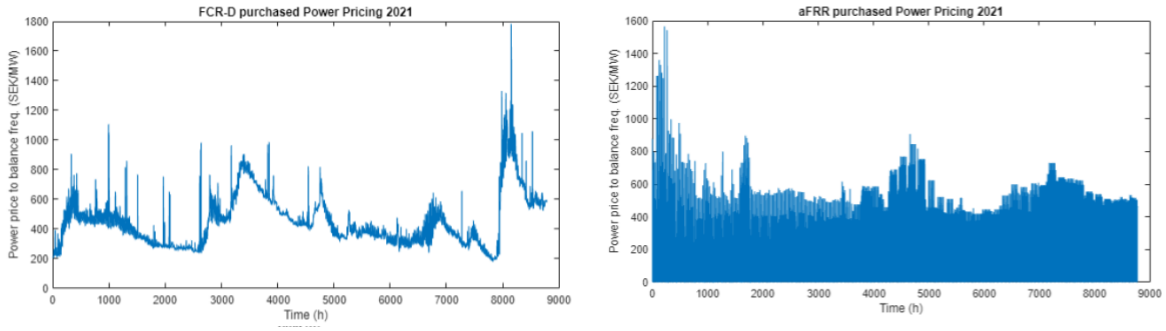

Figure B5: Support services pricing of historic data.

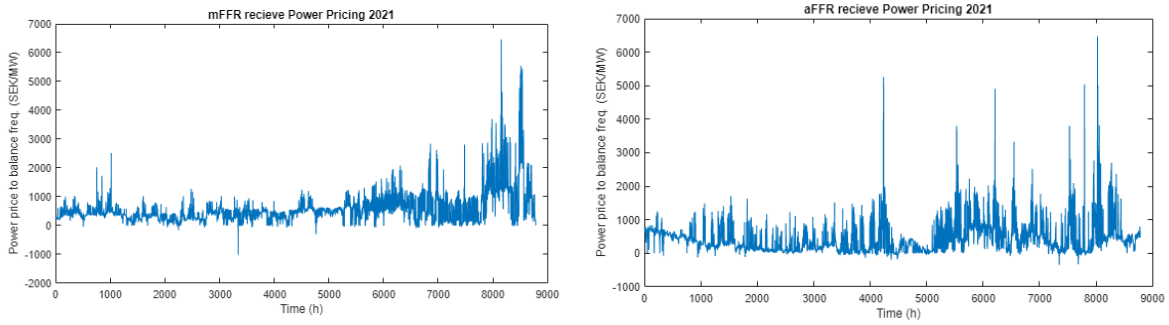

Figure B6: Support services pricing of historic data.

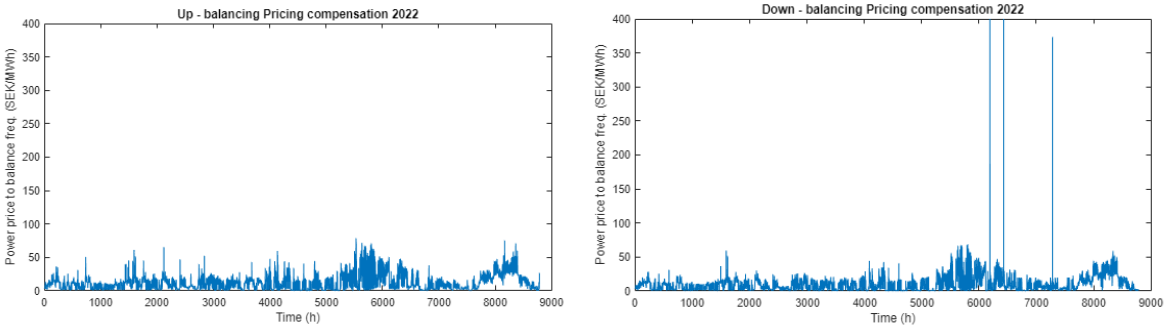

Figure B7: Support services data on compensation for activated reserve (Energy margin compensation).

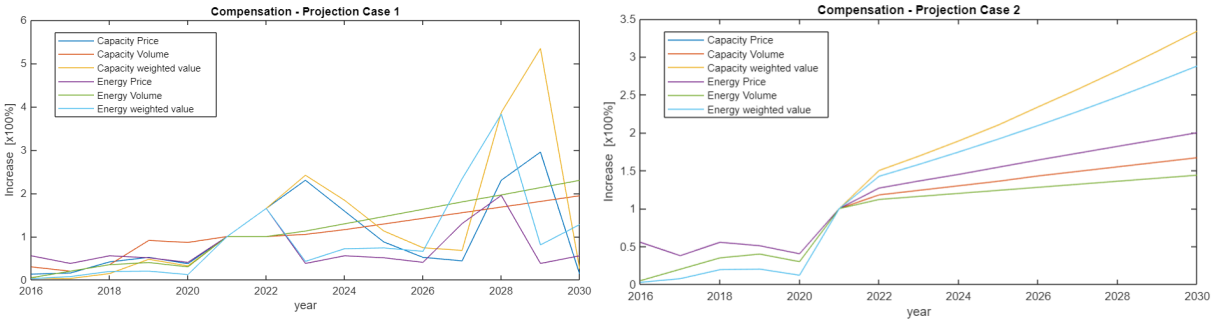

Figure B8: The prediction regarding the energy and capacity market, as volume and prices are weighted towards a shared constant. Increase describes the values proportional to the year 2021.

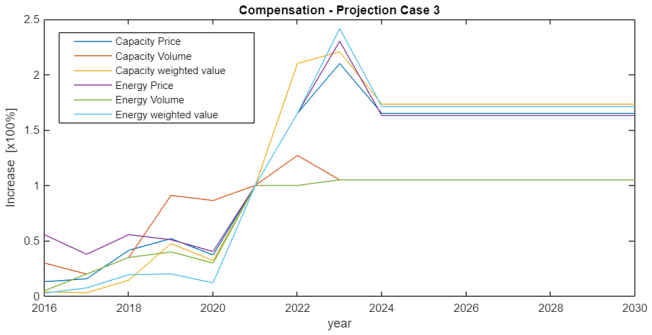

Figure B9: The Prediction regarding the energy and capacity market, as volume and prices are weighted towards a shared constant. Increase describes the values proportional to the year 2021.

1.3 Comments on future market prediction

In regards to predicting the future market, volumes, and prices, data is analyzed to forge several weighted constant vectors f_x, for each projected year. By using the weighted set of numbers gathered from a combination of forecast data, these numbers can then generate a projection for the year $Year_i$ using the formula in B3, to predict future pricing.

$$\vec{C}_{price} = \frac{\vec{S}(t)}{f_x} \tag{B3}$$

To validate the prediction values f_x a test on support service capacity compensation for 2021 was executed, utilizing the product of the previous amount of volume and price demand. The projected result was concluded to deviate approximately 9-8% from the actual price in 2021. The validation is arguably rejected since it the future price of electricity is not possible to predict with any kind of certainty. As this prediction works for the span of 2021 and 2022 for an annual average, it cannot predict on hourly-based resolution, thus is suitable for sensitive analytical applications.
In projection Case 1, the forecast data is randomly generated following patterns of previous years to achieve a type of reference value. The peak of years 2028-2029 is not depicting an actual phase but conjures approximately with the implementation of the hydrogen transition in the North of Sweden. Projection is presented in Figure B9.

In projection 2, the prediction is based on linear regression, as data from interviews and planned transitions in the energy system, is quantified with a simplified regression model following empirical theory from literature (Xing, 2008). To note is that the values are translated from the increased amount of volume demand and bandwidth of power peaks. The reason behind power peak increased bandwidth or time, is that the mass of rotation is expected to increase rendering the energy system more volatile, and with significantly larger max and minimum deficit or excess power that requires balancing. Projection is presented in Figure B8.

In projection case 3, the prediction of coming years is estimated to be constant, which results in the most conservative of the cases presented and is based on the least aggressive modification of SVKs prediction of

support service prices in the future, as the consensus is that the curve will decrease and flatten to the year 2025 (SVK, 2023c). Projection is presented in Figure B9

1.4 Economy related parameters

Table B1: CAPEX related assumptions for gasifiers.

Parameter	Value	Unit
Direct costs;		
Process piping	3	% of total major equipment costs
Instrumentation	2	% of total major equipment costs
Electrical facilities	2	% of total major equipment costs
Buildings	0	% of total major equipment costs
Foundations	0	% of total major equipment costs
Site preparation	3	% of total major equipment costs
Indirect costs;		
Engineering	10	% of total costs

Table B2: CAPEX related assumptions for Ägir 1.

Parameter	Value	Unit
Direct costs;		
Process piping	3	% of total major equipment costs
Instrumentation	2	% of total major equipment costs
Electrical facilities	2	% of total major equipment costs
Buildings	5	% of total major equipment costs
Foundations	1	% of total major equipment costs
Site preparation	3	% of total major equipment costs
Indirect costs;		
Engineering	10	% of total costs
Permits/Inspections	5	% of total costs

Table B3: Assumptions and recorded rates for economical calculations. Certificate of origin and energy tax only applies to Ägir 1 calculation.

Parameter	Value	Unit
DH period price, Apr-Oct	288.8	SEK/MWh
DH period price, Nov-Mar	738.8	SEK/MWh
Retail price H_2	30	SEK/kg
Retail price CO_2	2	SEK/kg
Retail price O_2	0.9	SEK/kg
Water cost	11.3	SEK/tonne
Ash disposal	500	SEK/tonne
Technical lifetime (BFB)	25	years
Technical lifetime (EF)	25	years
Technical lifetime (FB)	20	years
Technical lifetime (AEL)	19.7	years
Technical lifetime (PEM/FC)	10.5	years
Construction time Ägir 1	2	years
Construction time Idun 1 and 2	3	years
Corporate tax	25	%
Energy tax	36	SEK/MWh
Discount rate	8	%
Inflation rate	2	%
Variable maintenance cost	10	SEK/MWh
Certificate of origin cost	100	SEK/MWh
PPA cost incl. Certificate of origin	527.3	SEK/MWh

Table B4: Net specific fees for transmission point Värtan, not including tax (Ellevio, 2023).

Parameter	Value	Unit
Net fee variable	2.5	SEK/MWh
Power fee variable	2.2	SEK/MWh
Replacement fee	2.1	SEK/MWh
Net fee fixed	62000	SEK, year
Power fee fixed	352000	SEK/MW ,year

1.5 Component cost

Table B5: Cost of major components Idun 1a.

Equipment	Scale exponent	Cost	Unit	Source
WGS reactor	1	72	MSEK	(Laboratory, 2006)
Compressors	0.62	83.9	MSEK	(Laboratory, 2006)
Heat exchangers	0.59	61.5	MSEK	(Laboratory, 2006)
Fabric filtering system	1	0.9	MSEK	(K. M. Holmgren, 2015)
Solid fuel handling	1	3.6	MSEK	(Mesfun et al., 2016)
Gasifier reactor	0.72	180.9	MSEK	(Mesfun et al., 2016)
Scrubber	1	11.3	MSEK	(Laboratory, 2006)
PSA system	0.67	105.9	MSEK	(M. Li et al., 2012)
Membrane separator AHF	0.67	13.8	MSEK	(Nordio et al., 2021)
AGR system	1	150.45	MSEK	(Hannula & Kurkela, 2013)
Hydrolosis unit	0.67	13.3	MSEK	(NETL, 2010)
Active carbon unit	0.67	3.1	MSEK	(NETL, 2010)
Membrane separator MFI/CMS	1	0.7	MSEK	(K. M. Holmgren, 2015)
Amine unit	0.67	90.9	MSEK	(Laboratory, 2006)
Methane combustion boiler	0.67	15	MSEK	(Baltrusaitis & Luyben, 2015)

Table B6: Cost of major components Idun 1b.

Equipment	Scale exponent	Cost	Unit	Source
WGS reactor	1	21.1	MSEK	(Laboratory, 2006)
Compressors	0.62	48.1	MSEK	(Laboratory, 2006)
Heat exchangers	0.59	46.4	MSEK	(Laboratory, 2006)
Fabric filtering system	1	0.9	MSEK	(K. M. Holmgren, 2015)
Solid fuel handling	1	1.6	MSEK	(Mesfun et al., 2016)
Gasifier reactor	0.72	74.8	MSEK	(Mesfun et al., 2016)
Scrubber	1	5.4	MSEK	(Laboratory, 2006)
PSA system	0.67	66.6	MSEK	(M. Li et al., 2012)
Membrane separator AHF	0.67	6.8	MSEK	(Nordio et al., 2021)
AGR system	1	44.2	MSEK	(Hannula & Kurkela, 2013)
Hydrolosis unit	0.67	3.9	MSEK	(NETL, 2010)
Active carbon unit	0.67	0.9	MSEK	(NETL, 2010)
Membrane separator MFI/CMS	1	0.2	MSEK	(K. M. Holmgren, 2015)
Amine unit	0.67	55.4	MSEK	(Laboratory, 2006)
Methane combustion boiler	0.67	7	MSEK	(Baltrusaitis & Luyben, 2015)

Table B7: Cost of major components Idun 2a.

Equipment	Scale exponent	Cost	Unit	Source
WGS reactor	1	42.6	MSEK	(Laboratory, 2006)
Compressors	0.62	25	MSEK	(Laboratory, 2006)
Heat exchangers	0.59	30.3	MSEK	(Laboratory, 2006)
Fabric filtering system	1	0.5	MSEK	(K. M. Holmgren, 2015)
Solid fuel handling	1	1.5	MSEK	(Mesfun et al., 2016)
Gasifier reactor	0.72	124.1	MSEK	(Mesfun et al., 2016)
Scrubber	1	3.4	MSEK	(Laboratory, 2006)
PSA system	0.67	23.1	M MSEK	(M. Li et al., 2012)
Membrane separator AHF	0.67	11.24	MSEK	(Nordio et al., 2021)
ASU	0.75	92.7	MSEK	(Nordio et al., 2021)
AGR system	1	89.1	MSEK	(Hannula & Kurkela, 2013)
Hydrolosis unit	0.67	7.9	MSEK	(NETL, 2010)
Active carbon unit	0.67	1.9	MSEK	(NETL, 2010)
Membrane separator MFI/CMS	1	0.4	MSEK	(K. M. Holmgren, 2015)
Cyclone	0.67	4.1	MSEK	(Laboratory, 2006)
Amine unit	0.67	40.6	MSEK	(Laboratory, 2006)
Methane combustion boiler	0.67	7.3	MSEK	(Baltrusaitis & Luyben, 2015)

Table B8: Cost of major components Idun 2b.

Equipment	Scale exponent	Cost	Unit	Source
WGS reactor	1	46.4	MSEK	(Laboratory, 2006)
Compressors	0.62	23.9	MSEK	(Laboratory, 2006)
Heat exchangers	0.59	34.5	MSEK	(Laboratory, 2006)
Fabric filtering system	1	0.6	MSEK	(K. M. Holmgren, 2015)
Solid fuel handling	1	10.6	MSEK	(Mesfun et al., 2016)
Gasifier reactor	0.7	727.5	MSEK	(Mesfun et al., 2016)
Scrubber	1	2.9	MSEK	(Laboratory, 2006)
PSA system	0.67	41.8	MSEK	(M. Li et al., 2012)
Membrane separator AHF	0.67	14.5	MSEK	(Nordio et al., 2021)
ASU	0.75	150.7	MSEK	(Nordio et al., 2021)
AGR system	1	97	MSEK	(Hannula & Kurkela, 2013)
Hydrolosis unit	0.67	8.6	MSEK	(NETL, 2010)
Active carbon unit	0.67	2	MSEK	(NETL, 2010)
Membrane separator MFI/CMS	1	0.4	MSEK	(K. M. Holmgren, 2015)
Amine unit	0.67	36.6	MSEK	(Laboratory, 2006)
Methane combustion boiler	0.67	13	MSEK	(Baltrusaitis & Luyben, 2015)

Table B9: Cost of major components Idun 2c.

Equipment	Scale exponent	Cost	Unit	Source
WGS reactor	1	9.4	MSEK	(Laboratory, 2006)
Compressors	0.62	27.2	MSEK	(Laboratory, 2006)
Heat exchangers	0.59	12.5	MSEK	(Laboratory, 2006)
Fabric filtering system	1	0.1	MSEK	(K. M. Holmgren, 2015)
Solid fuel handling	1	0.6	MSEK	(Mesfun et al., 2016)
Gasifier reactor	0.72	87.6	MSEK	(Mesfun et al., 2016)
Scrubber	1	0.6	M MSEK	(Laboratory, 2006)
PSA system	0.67	25.5	MSEK	(M. Li et al., 2012)
Membrane separator AHF	0.67	3.7	MSEK	(Nordio et al., 2021)
ASU	0.75	36.4	MSEK	(Nordio et al., 2021)
AGR system	1	19.7	MSEK	(Hannula & Kurkela, 2013)
Hydrolosis unit	0.67	1.7	MSEK	(NETL, 2010)
Active carbon unit	0.67	0.4	MSEK	(NETL, 2010)
Membrane separator MFI/CMS	1	0.1	MSEK	(K. M. Holmgren, 2015)
Cyclone	0.67	1.25	MSEK	(Laboratory, 2006)
Amine unit	0.67	12.5	MSEK	(Laboratory, 2006)
Methane combustion boiler	0.67	4.4	MSEK	(Baltrusaitis & Luyben, 2015)

Table B10: Cost of major components Ägir 1 (AEL).

Equipment	Scale exponent	Cost	Unit	Source
Electrolyzers	0.95	49.6	MSEK	(Christensen, 2020)
Pumps	1	0.1	MSEK	(Hannula & Kurkela, 2013)
Compressors (HP)	0.67	1.5	MSEK	(Craig & Mann, 1996)
Storage	0.85	2.4	MSEK	(Nguyen et al., 2019b)
Oxygen piping	1	0.3	MSEK	-
Fuel cells	0.85	45.2	MSEK	(Battelle, 2016)
Battery	0.85	0	MSEK	-
Heat exchangers (CC)	0.95	0.1	MSEK	(Aromada et al., 2020)

Table B11: Cost of major components Ägir 1 (PEM).

Equipment	Scale exponent	Cost	Unit	Source
Electrolyzers	0.95	54.3	MSEK	Christensen, 2020
Pumps	1	0.1	MSEK	Hannula and Kurkela, 2013
Compressors (HP)	0.67	1.5	MSEK	(Craig & Mann, 1996)
Storage	0.85	2.4	MSEK	(Nguyen et al., 2019b)
Oxygen piping	1	0.3	MSEK	-
Fuel cells	0.85	45.2	MSEK	(Battelle, 2016)
Battery	0.85	0	MSEK	-
Heat exchangers (CC)	0.95	0.1	MSEK	(Aromada et al., 2020)

1.6 Fuel pricing matrix

Table B12: Fuel price index quarterly report(Energimyndigheten, 2023c). All values is in SEK/MWh except weighted numbers

Quarter	**Resdidential MSW**	**Industry MSW**	**Import MSW**	**Chipped Biomass**	**Residue Biomass**	**Recycled Biomass**
21a1	-156	-156	-163	199	173	100
21a2	-164	-172	-168	194	168	97
21a3	-171	-193	-202	184	153	98
21a4	-155	-149	-157	192	162	103
22a1	-176	-170	-156	192	161	103
22a2	-181	-168	-156	194	159	104
22a3	-177	-183	-173	211	172	130
Boiler	**Share**	**Share**	**Share**	**Share**	**Share**	**Share**
P6 feed	-	0.5	0.5	-	-	-
B1 feed	-	-	-	0.5	0.5	-
P3 feed	0.75	-	0.25	-	-	-

Table B13: Weighted solid fuel prices from TableB12, not including tax.

Type	Value	Unit
Fuel price Idun 1a/P6	-169	SEK/MWh
Fuel price Idun 1b/2b/B1	179.4	SEK/MWh
Fuel Price Idun 2a/2c/P3	-168.4	SEK/MWh

1.7 Sensitive analysis

In this section, different parameters will be altered to investigate the economic sensitivity of parameters. To note is that the subsidies sensitive analysis is based on receiving the minimum to maximum support, with the base of average subsidy.

1.7.1 Investment

Table B14: Sensitivity indicators for major economical variables Ägir 1 (AEL). The subsidy sensitivity starts at the average support percentage.

Change of input value (%)	-50	-30	-10	0	+10	+30	+50
				Payback time (years)			
CAPEX (Industriklivet)	1.4	1.3	1.2	1.2	1.2	1.1	1.0
CAPEX (Pilot och demo)	1.4	1.4	1.4	1.3	1.3	1.3	1.2
CAPEX 4x	-	-	-	6.1	-	-	-
Electricity Price	1.5	1.5	1.5	1.5	1.5	1.5	1.5
Compensation Price	2.1	1.8	1.6	1.5	1.5	1.3	1.2
Hydrogen Price	1.6	1.5	1.5	1.5	1.5	1.5	1.5
Tax and net fee	1.5	1.5	1.5	1.5	1.5	1.5	1.5
				Net present value (MSEK)			
CAPEX (Industriklivet)	684.4	691.2	697.9	701.3	704.7	711.5	718.3
CAPEX (Pilot och demo)	677.0	680.9	684.8	686.7	688.6	692.5	696.3
CAPEX 4x	-	-	-	204.3	-	-	-
Electricity Price	708.3	691.9	675.6	667.4	659.2	642.8	626.4
Compensation Price	420.3	519.1	618.0	667.4	716.8	815.6	914.5
Hydrogen Price	654.6	659.7	664.8	667.4	669.9	675.0	680.2
Tax and net fee	683.6	677.1	670.6	667.4	664.1	657.6	651.1
				Internal rate of return (%)			
CAPEX (Industriklivet)	53.4	55.6	58.1	59.5	60.9	63.9	67.3
CAPEX (Pilot och demo)	51.1	52.3	53.5	54.1	54.8	56.1	57.5
CAPEX 4x	-	-	-	12.4	-	-	-
Electricity Price	50.4	49.6	48.8	48.4	48.0	47.2	46.4
Compensation Price	35.6	40.9	45.9	48.4	50.8	55.6	60.2
Hydrogen Price	47.8	48.0	48.3	48.4	48.5	48.8	49.0
Tax and net fee	49.2	48.9	48.6	48.4	48.3	47.9	47.6

Table B15: Influence of PPA price on plant economy, for Ägir 1 (PPA without fuel cell).

Change of input value (%)	-50	-30	-10	0	+10	+30	+50
				PVQ (-)			
PPA Price	4.8	4.1	3.4	3	2.6	1.9	1.2
				Net present value (MSEK)			
PPA Price	286.8	234.7	182.5	156.5	130.4	78.3	26.1
				Internal rate of return (%)			
PPA Price	41.4	36.3	30.9	28.1	25.3	19.2	12.2

Table B16: Varying cash flows for Ägir 1 (AEL) dependent on forecasting models, from the time of deployment 2025, to 2030. Cash flows after this time span are constant and follow the weighted average.

Projection	Case 1	Case 2	Case 3	Constant - 2022	
PBT	1.5	1.3	1.7	1.5	Years
NPV	625.7	744	579.4	667.4	MSEK
IRR	45.9	57.4	48.8	48.4	%

Table B17: Sensitivity indicators for major economical variables Idun 1 a. The subsidy sensitivity starts at the average support percentage.

Change of input value (%)	-50	-30	-10	0	+10	+30	+50
	Payback time (years)						
CAPEX (Klimatklivet)	1.6	1.4	1.3	1.3	1.2	1.1	1.0
CAPEX (Industriklivet)	1.7	1.6	1.5	1.5	1.4	1.3	1.2
CAPEX (Pilot och demo)	1.7	1.7	1.7	1.6	1.6	1.6	1.5
CAPEX 4x	-	-	-	7.1	-	-	-
Fuel Costs	2.0	1.9	1.9	1.9	1.8	1.8	1.7
CO_2 Price	2.2	2.1	1.9	1.9	1.8	1.7	1.6
H_2 Price	2.2	2.0	1.9	1.9	1.8	1.7	1.6
DH recovery	2.1	2.0	1.9	1.9	1.8	1.7	1.7
	Net present value (MSEK)						
CAPEX (Klimatklivet)	6296.4	6234.4	6172.4	6141.3	6110.3	6048.3	5986.2
CAPEX (Industriklivet)	5936.1	5978.1	6020.1	6041.1	6062.1	6104.1	6146.1
CAPEX (Pilot och demo)	6010.1	5986.2	5962.4	5950.4	5938.5	5914.6	5890.8
CAPEX 4x	-	-	-	2967.5	-	-	-
Fuel Costs	5346.8	5540.5	5734.2	5831.1	5928.0	6121.7	6315.4
CO2 Price	4644.7	5119.3	5593.8	5831.1	6068.4	6542.9	7017.5
Hydrogen Price	4813.7	5220.7	5627.6	5831.1	6034.6	6441.5	6848.5
DH recovery	5044.6	5359.2	5673.8	5831.1	5988.4	6303.0	6617.6
	Internal rate of return (%)						
CAPEX (Klimatklivet)	78.2	72.6	67.8	65.7	63.7	60.1	57.0
CAPEX (Industriklivet)	54.7	56.6	58.7	59.8	60.9	63.3	66.0
CAPEX (Pilot och demo)	58.1	57.0	55.8	55.3	54.8	53.7	52.8
CAPEX 4x	-	-	-	16.3	-	-	-
Fuel Costs	47.9	48.9	49.9	50.4	50.9	51.9	52.9
CO2 Price	44.0	46.7	49.2	50.4	51.7	54.0	56.3
Hydrogen Price	45.0	47.2	49.4	50.4	51.5	53.5	55.5
DH recovery	46.2	48.0	49.6	50.4	51.3	52.9	54.4

Table B18: Sensitivity indicators for major economical variables Idun 1b. The subsidy sensitivity starts at the average support percentage.

Change of input value (%)	-50	-30	-10	0	+10	+30	+50
	Payback time (years)						
CAPEX (Klimatklivet)	6.0	5.6	5.1	4.9	4.6	4.2	3.7
CAPEX (Industriklivet)	6.4	6.1	5.8	5.6	5.5	5.1	4.8
CAPEX (Pilot och demo)	6.7	6.6	6.4	6.3	6.2	6.0	5.8
CAPEX 4x	-	-	-	24.4	-	-	-
Fuel Costs	6.5	6.7	7.0	7.2	7.4	7.7	8.1
CO2 Price	9.9	8.6	7.6	7.2	6.8	6.2	5.7
Hydrogen Price	9.2	8.3	7.5	7.2	6.9	6.4	5.9
DH recovery	8.1	7.7	7.4	7.2	7.0	6.7	6.5
	Net present value (MSEK)						
CAPEX (Klimatklivet)	421.3	451.3	481.4	496.4	511.4	541.4	571.4
CAPEX (Industriklivet)	397.1	417.4	437.7	447.9	458.0	478.4	498.7
CAPEX (Pilot och demo)	375.2	386.7	398.2	404.0	409.8	421.3	432.9
CAPEX 4x	-	-	-	-1038.9	-	-	-
Fuel Costs	443.4	404.5	365.7	346.3	326.9	288.1	249.3
CO2 Price	112.3	205.9	299.5	346.3	393.1	486.7	580.3
Hydrogen Price	159.3	234.1	308.9	346.3	383.7	458.5	533.3
DH recovery	250.4	288.7	327.1	346.3	365.5	403.9	442.3
	Internal rate of return (%)						
CAPEX (Klimatklivet)	19.1	20.5	22.2	23.1	24.1	26.4	29.1
CAPEX (Industriklivet)	18.0	18.9	19.8	20.3	20.9	22.0	23.3
CAPEX (Pilot och demo)	17.1	17.6	18.0	18.3	18.5	19.1	19.6
CAPEX 4x	-	-	-	-2	-	-	-
Fuel Costs	17.9	17.2	16.4	16.0	15.6	14.8	14.0
CO2 Price	10.9	13.1	15.1	16.0	17.0	18.8	20.5
Hydrogen Price	12.0	13.7	15.3	16.0	16.8	18.2	19.6
DH recovery	14.0	14.9	15.6	16.0	16.4	17.2	17.9

Table B19: Sensitivity indicators for major economical variables Idun 2a. The subsidy sensitivity starts at the average support percentage.

Change of input value (%)	-50	-30	-10	0	+10	+30	+50
	Payback time (years)						
CAPEX (Klimatklivet)	1.5	1.4	1.2	1.2	1.1	1.0	0.9
CAPEX (Industriklivet)	1.6	1.5	1.4	1.4	1.3	1.3	1.2
CAPEX (Pilot och demo)	1.6	1.6	1.6	1.5	1.5	1.5	1.4
CAPEX 4x	-	-	-	6.7	-	-	-
Fuel Costs	1.8	1.7	1.6	1.5	1.5	1.4	1.3
Electricity Price	1.6	1.6	1.6	1.5	1.5	1.5	1.4
CO2 Price	2.0	1.8	1.6	1.5	1.5	1.3	1.2
Hydrogen Price	1.9	1.7	1.6	1.5	1.5	1.4	1.3
DH recovery	1.9	1.7	1.6	1.5	1.5	1.4	1.3
	Net present value (MSEK)						
CAPEX (Klimatklivet)	4189.3	4230.0	4270.6	4291.0	4311.3	4352.0	4392.7
CAPEX (Industriklivet)	4156.4	4184.0	4211.5	4225.3	4239.0	4266.6	4294.1
CAPEX (Pilot och demo)	4126.7	4142.4	4158.0	4165.8	4173.7	4189.3	4204.9
CAPEX 4x	-	-	-	2210.5	-	-	-
Fuel Costs	3819.6	3958.1	4096.6	4165.8	4235.1	4373.6	4512.1
Electricity Price	4154.4	4159.0	4163.6	4165.8	4168.1	4172.7	4177.2
CO2 Price	3225.0	3601.3	3977.7	4165.8	4354.0	4730.3	5106.7
Hydrogen Price	3513.8	3774.6	4035.4	4165.8	4296.2	4557.0	4817.8
DH recovery	3520.8	3778.8	4036.8	4165.8	4294.8	4552.8	4810.8
	Internal rate of return (%)						
CAPEX (Klimatklivet)	59.2	62.5	66.2	68.2	70.4	75.3	81.1
CAPEX (Industriklivet)	56.9	58.8	61.0	62.1	63.3	65.8	68.5
CAPEX (Pilot och demo)	54.9	55.9	57.0	57.5	58.1	59.2	60.4
CAPEX 4x	-	-	-	17.3	-	-	-
Fuel Costs	52.4	54.4	56.5	57.5	58.6	60.8	63.0
Electricity Price	55.1	56.0	57.0	57.5	58.0	59.1	60.2
CO2 Price	47.4	51.4	55.5	57.5	59.6	63.6	67.8
Hydrogen Price	49.9	52.9	56.0	57.5	59.1	62.3	65.5
DH recovery	49.9	52.9	56.0	57.5	59.1	62.2	65.4

Table B20: Sensitivity indicators for major economical variables Idun 2b. The subsidy sensitivity starts at the average support percentage.

Change of input value (%)	-50	-30	-10	0	+10	+30	+50
	Payback time (years)						
CAPEX (Klimatklivet)	7.0	6.5	5.9	5.7	5.4	4.8	4.3
CAPEX (Industriklivet)	7.5	7.1	6.7	6.5	6.3	6.0	5.6
CAPEX (Pilot och demo)	7.8	7.6	7.4	7.3	7.2	7.0	6.8
CAPEX 4x	-	-	-	27.6	-	-	-
Fuel Costs	7.3	7.7	8.1	8.4	8.6	9.2	9.8
Electricity Price	7.3	7.7	8.1	8.4	8.6	9.2	9.8
CO2 Price	211.7	10.1	8.9	8.4	7.9	7.1	6.5
Hydrogen Price	11.9	10.2	8.9	8.4	7.9	7.1	6.4
DH recovery	9.5	9.0	8.6	8.4	8.2	7.8	7.4
	Net present value (MSEK)						
CAPEX (Klimatklivet)	975.1	1072.6	1170.0	1218.7	1267.4	1364.8	1462.3
CAPEX (Industriklivet)	896.4	962.4	1028.3	1061.3	1094.3	1160.2	1226.2
CAPEX (Pilot och demo)	825.2	862.7	900.2	918.9	937.7	975.1	1012.6
CAPEX 4x	-	-	-	-3765.0	-	-	-
Fuel Costs	1089.3	946.2	803.1	733.4	660.0	516.9	373.8
Electricity Price	910.7	839.8	768.8	733.4	697.9	627.0	556.1
CO2 Price	47.6	321.9	596.2	733.4	870.5	1144.8	1419.2
Hydrogen Price	18.3	304.4	590.4	733.4	876.4	1162.4	1448.4
DH recovery	438.1	556.2	674.3	733.4	792.4	910.5	1028.6
	Internal rate of return (%)						
CAPEX (Klimatklivet)	16.3	17.6	19.2	20.0	20.9	23.0	25.5
CAPEX (Industriklivet)	15.3	16.1	17.0	17.5	18.0	19.0	20.2
CAPEX (Pilot och demo) 14.5	14.9	15.3	15.6	15.8	16.3	16.8	
CAPEX 4x	-	-	-	-4.1	-	-	-
Fuel Costs	15.8	14.9	14.0	13.5	13.0	12.0	11.0
Electricity Price	14.7	14.2	13.8	13.5	13.3	12.8	12.3
CO2 Price	8.4	10.6	12.6	13.5	14.4	16.2	17.8
Hydrogen Price	8.2	10.5	12.5	13.5	14.5	16.3	18.0
DH recovery	11.5	12.3	13.1	13.5	13.9	14.7	15.4

Table B21: Sensitivity indicators for major economical variables Idun 2c. The subsidy sensitivity starts at the average support percentage.

Change of input value (%)	-50	-30	-10	0	+10	+30	+50
	Payback time (years)						
CAPEX (Klimatklivet)	4.9	4.6	4.2	4.0	3.8	3.5	3.1
CAPEX (Industriklivet)	5.2	5.0	4.7	4.6	4.5	4.2	4.0
CAPEX (Pilot och demo)	5.5	5.3	5.2	5.1	5.1	4.9	4.8
CAPEX 4x	-	-	-	19.7	-	-	-
Fuel Costs	6.1	5.7	5.3	5.1	5.0	4.6	4.4
Electricity Price	5.1	5.1	5.1	5.1	5.1	5.2	5.2
CO2 Price	6.4	5.9	5.4	5.1	4.9	4.5	4.2
Hydrogen Price	7.1	6.2	5.4	5.1	4.8	4.3	3.9
DH recovery	6.1	5.7	5.3	5.1	5.0	4.7	4.4
	Net present value (MSEK)						
CAPEX (Klimatklivet)	329.6	348.8	367.9	377.5	387.0	406.2	425.3
CAPEX (Industriklivet)	314.2	327.1	340.1	346.6	353.0	366.0	379.0
CAPEX (Pilot och demo)	300.2	307.6	314.9	318.6	322.3	329.6	337.0
CAPEX 4x	-	-	-	-601.3	-	-	-
Fuel Costs	240.3	271.6	302.9	318.6	334.3	365.6	397.0
Electricity Price	346.1	335.1	324.1	318.6	313.1	302.1	291.1
CO2 Price	208.5	252.5	296.6	318.6	340.6	384.7	428.8
Hydrogen Price	163.1	225.3	287.5	318.6	349.7	411.9	474.1
DH recovery	241.6	272.4	303.2	318.6	334.0	364.8	395.6
	Internal rate of return (%)						
CAPEX (Klimatklivet)	22.7	24.4	26.3	27.4	28.6	31.2	34.3
CAPEX (Industriklivet)	21.4	22.5	23.6	24.2	24.8	26.1	27.6
CAPEX (Pilot och demo)	20.4	20.9	21.5	21.8	22.1	22.7	23.3
CAPEX 4x	-	-	-	-1.9	-	-	-
Fuel Costs	18.3	19.7	21.1	21.8	22.5	23.9	25.4
Electricity Price	21.9	21.9	21.8	21.8	21.7	21.7	21.6
CO2 Price	17.1	19.0	20.8	21.8	22.7	24.6	26.5
Hydrogen Price	15.4	18.0	20.5	21.8	23.0	25.5	28.1
DH recovery	18.3	19.7	21.1	21.8	22.5	23.9	25.4

1.7.2 Alternative operations Ägir 1

7.2.4 A. Fixed operation cost (PPA)

In this configuration, the operational costs are fixed with a PPA. The PPA is a power producer agreement that is utilized to guarantee a fixed price for a specific time. Operation the Ägir 1 platform with the PPA instead of following the spot market pricing will make the activation constant, as presented in Figure B10. The introduction of PPA will not have any impact in fuel cell activation since it is connected to the grid, thus impact on production surplus in comparison to the standard configuration is low.

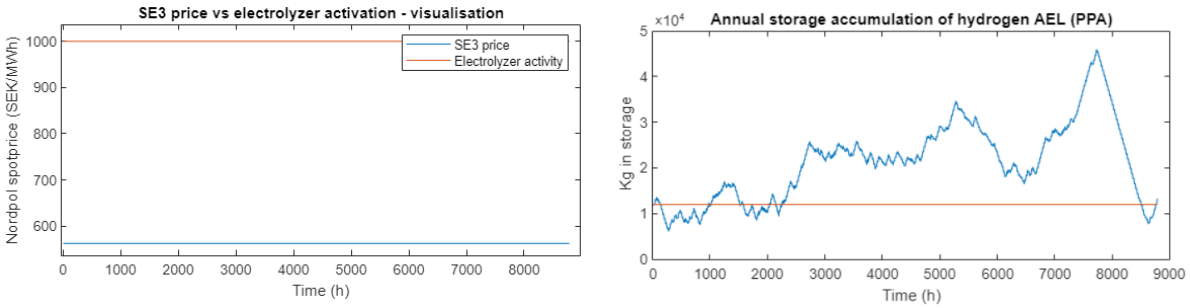

Figure B10: Diagram illustrating the effect the price have on electrolyzer activation to the left, and annual dynamic volumes of hydrogen in the right.

In Figure B11 the result from oxygen utilization and district heating output is observed. In comparison to the standard configuration, this scenario can supply district heating 4561 hours of the year and supply 332.6 kg/h oxygen at all times. The annual production quantity of hydrogen reaches 1.964 GWh with the current

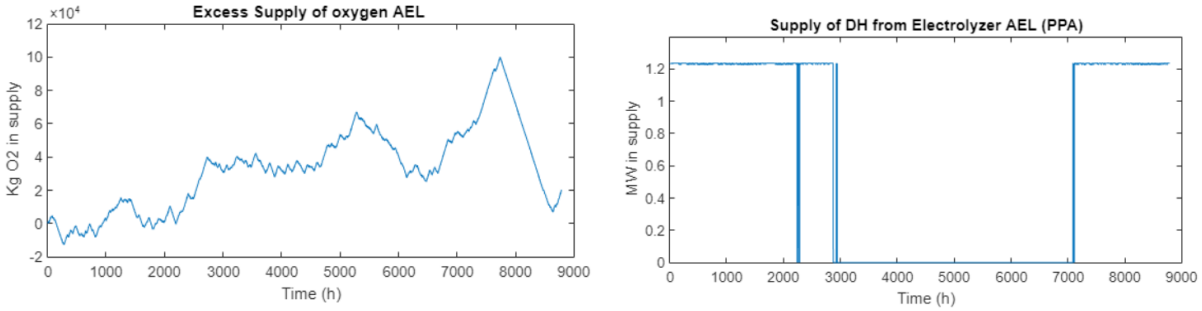

Figure B11: In the left diagram the excess supply of oxygen utilized for fuel cell activation is presented. The left diagram indicates the annual district heating capacity.

Including fuel cell operations give the ability of trading support services, it is also assumed that the electrolyzer can switch to balance down the grid, thus allocating contracted capacity to the spot market. In Table B23 the cash flow balance for the current scenario is presented, during the year 2022 is located in Appendix 1.6. Sensitivity analysis is presented in Figure B12.

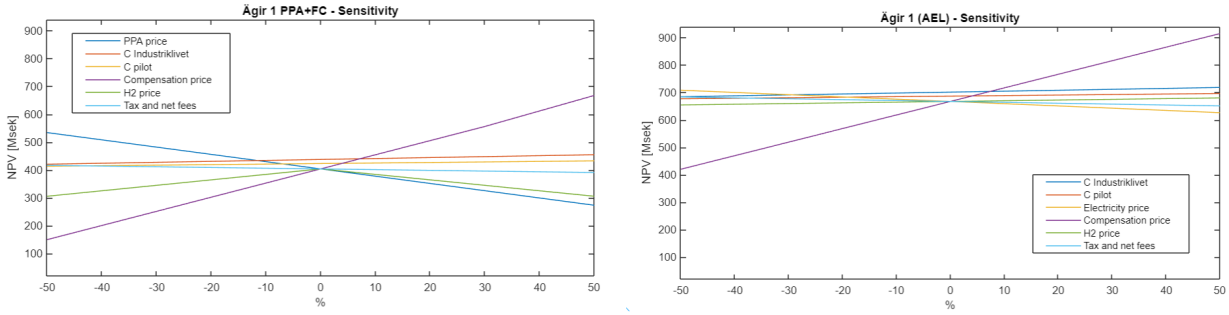

Figure B12: Sensitivity analysis of Ägir 1 with PPA to the left, and normal operation to the right.

7.2.4 B. Fixed operation cost (PPA) without fuel cell

In this scenario, the plant configuration is the same as the 7.2.4 A case and PPA is assigned for fixed operation, but without a fuel cell. The consumption of hydrogen is then only based on the daily consumption of the fuel distribution system. Production of hydrogen is then relatively constant and varies only by slight imbalances of support service activation. Figure B13 presents the current operational status of hydrogen storage. In this configuration dynamic storage capacity can be reduced up to 10 times less than in the standard scenario.

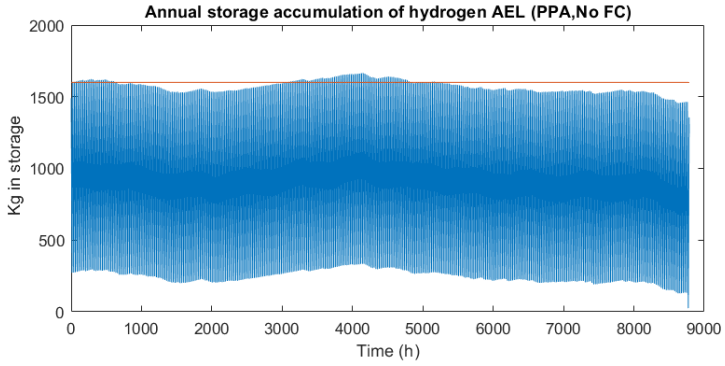

Figure B13: Diagram presenting the dynamic storage for the year 2022, without fuel cell and fixed electrolyzer operation.

Supply of district heating is equal to the case in Figure B11 and the plant reaches an annual production of 32.44 GWh annually with a supply of 439.2 kg/h oxygen to KVV8 continuously at all times. In Figure B14 it

can be observed that the production rate is not constant to electricity supply, and the cumulative losses from not utilizing the oxygen can lead to approximate losses of 1 tonne per year.

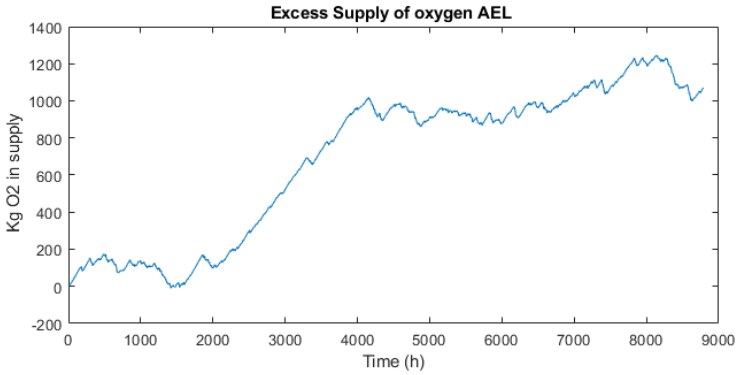

Figure B14: Diagram presenting the excess oxygen annually after KVV8 demand saturation, for year 2022.

The resulting impact the configuration has on plant economy is presented in Table B24, and the major cash flows of the operation are presented. Sensitivity analysis is observed in Figure B15.

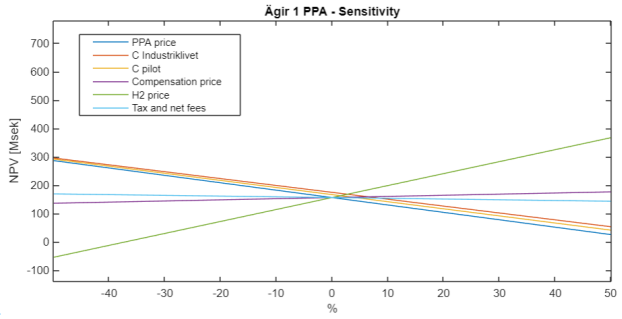

Figure B15: Sensitivity analysis of Ägir 1 with PPA and no fuel cell.

7.2.4 C. Oversize of electrolyzer capacity

In order to estimate the impact of fuel cell size in comparison to electrolyzer in economical performance, a simulation of Ägir 1 is made with double the amount of electrolyzer stacks. In Figure B16 it can be observed that no behavioral difference in periods as in the previous runs, with the only exemption of a larger quantity of hydrogen in surplus.

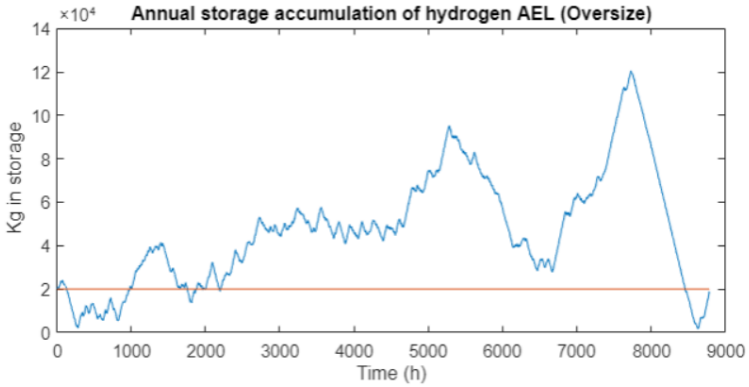

Figure B16: Diagram presenting the annual dynamic storage of hydrogen, during the year 2022.

Production rate reached 27.21 GWh/year, and 15.36 GWh sold hydrogen. The amount of oxygen continuously feed to KVV8 increases to 0.0726 kg/s from the standard mass flow of 0.0226 kg/s due to the fuel cell's proportional consumption. The updated NPV for this configuration is with major cash flows presented in Table B25. District heating supply and oxygen excess share the same appearance as the standard configuration, and

will not be shown since the only difference is that the supply is doubled. Sensitivity analysis is presented in Figure B17.

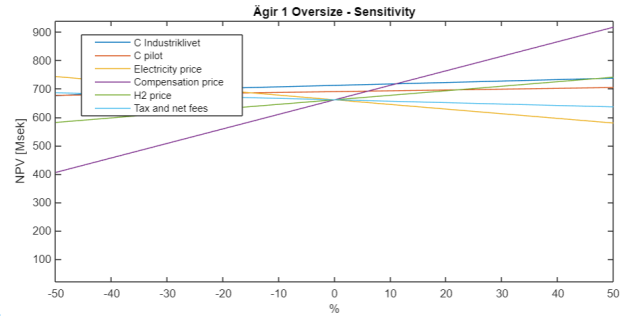

Figure B17: Sensitivity analysis of Oversize operation.

7.2.4 D. Electrolyzer continuous load - Sleep mode

The term sleeping mode is meaning that the electrolyzer is constantly activated at all times with a specific load. In this scenario the selected load is 20%, meaning that voltage is at constant max output but restrained current at a 20% of maximum load. This mode is initiated instead if the complete shutdown of the electrolyzer during hours when spot market prices exceed the threshold. In Figure B18 the activation of this mode is set, including activation imbalances.

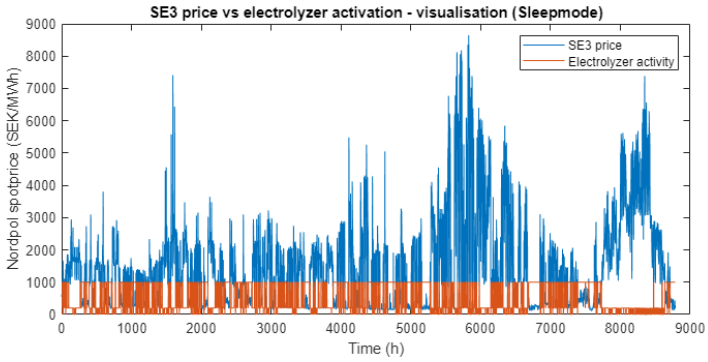

Figure B18: Annual activation for electrolyzer during sleep mode, for the year 2022.

In Figure B19 the results from utilizing nominal current at lower load instead of complete shutdown, indicate different behavior in district heating application than the standard configuration.

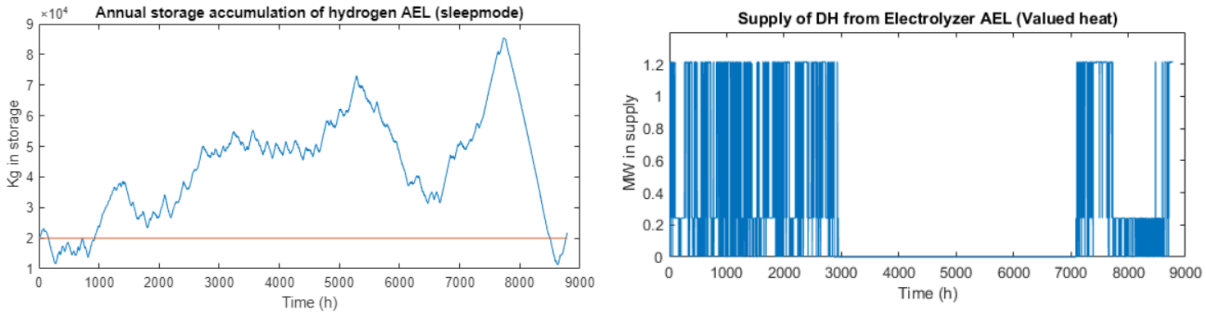

Figure B19: In the left diagram the excess supply of oxygen utilized for fuel cell activation is presented. The left diagram indicates the annual district heating capacity, for the year 2022.

The sub-optimal result from sleeping mode activation indicates a problem stabilizing thermal output up and down after activation. Oxygen supply results in 120.6 kg/h and follows a similar pattern as standard operation. The produced and sold hydrogen utilizing sleeping mode accumulates to 16.56 GWh respectively 5.495 GWh. Compared to other alternatives this configuration is exceeding the standard produced and sold hydrogen, which is 13.2 GWh respectively 2.23 GWh on an annual basis. In Table B26 the major cash flows for sleep mode operations is presented. Sensitivity analysis is observed in Figure B20.

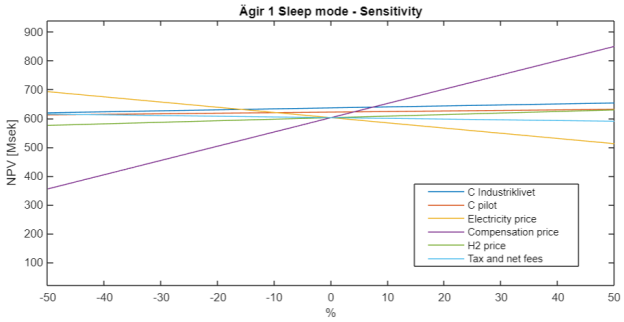

Figure B20: Sensitivity analysis of sleep mode operation.

7.2.4 A*. Fixed operation cost (PPA) with fuel cell, no base GtP.

In this scenario, the plant configuration is the same as the 7.2.4 A case and PPA is assigned for fixed operation, but without the sale of base power to the grid, meaning that the fuel cell only provides support services. Figure B21 presents the current operational status of hydrogen storage. In this configuration dynamic storage capacity can be reduced up to 10 times less than in the standard scenario and, thus the balancing does not affect storage in any significant matter.

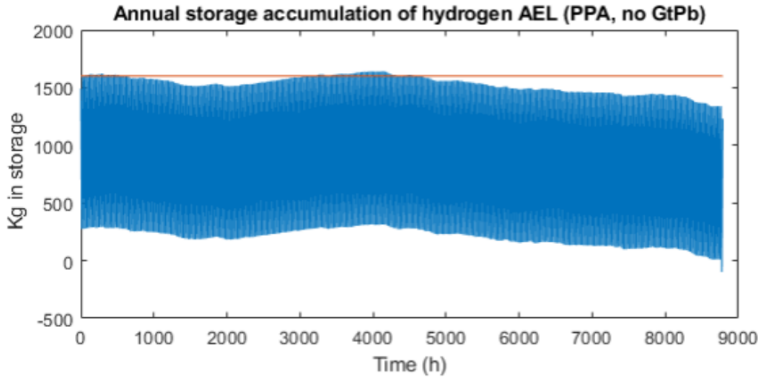

Figure B21: Diagram presenting the dynamic storage for the year 2022, with fuel cell only accounting for balancing of the grid and fixed electrolyzer operation.

The supply of district heating and oxygen is the same as the operation including the base sale of power. The resulting impact the configuration has on plant economy is presented in Table 7.2.4 A but and the basic sale of power.

1.8 Cash flow data

1.8.1 Diagrams cash flow

Diagrams presenting selected plants.

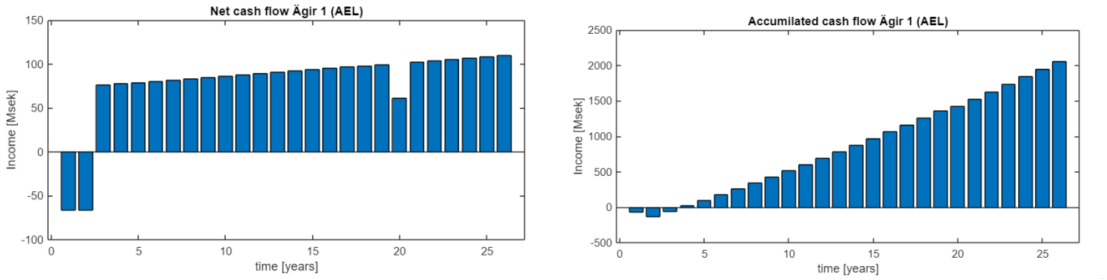

Figure B22: Cash flows for the year 2022 and forward, of AEL electrolyzer platform.

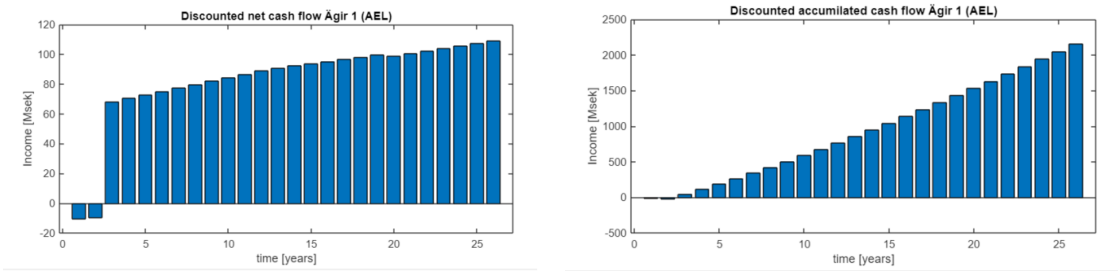

Figure B23: Cash flows for the year 2022 and forward, of AEL electrolyzer platform.

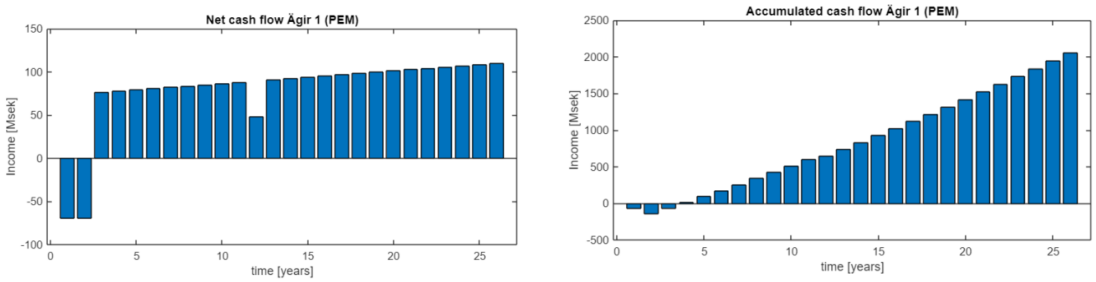

Figure B24: Cash flows for the year 2022 and forward, of PEM electrolyzer platform

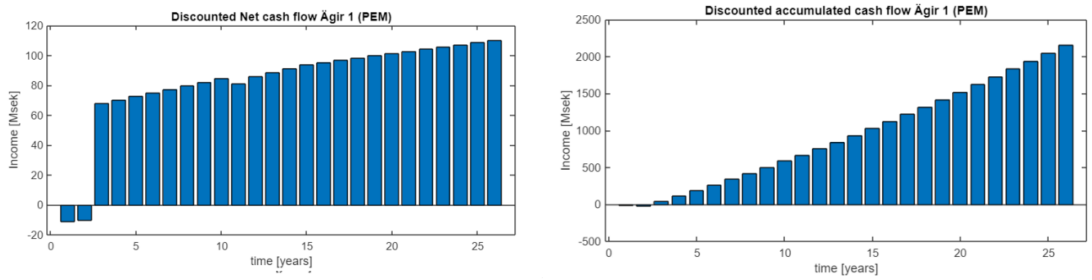

Figure B25: Cash flows for the year 2022 and forward, of PEM electrolyzer platform.

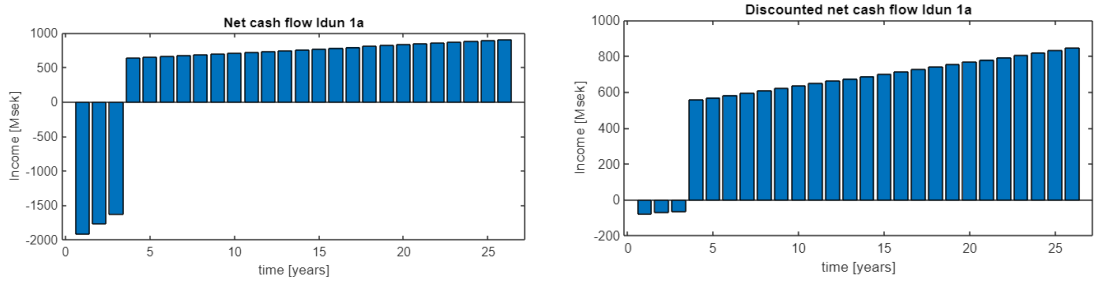

Figure B26: Cash flows for the year 2022 and forward, in the case of the integrated gasifier at Högdalen.

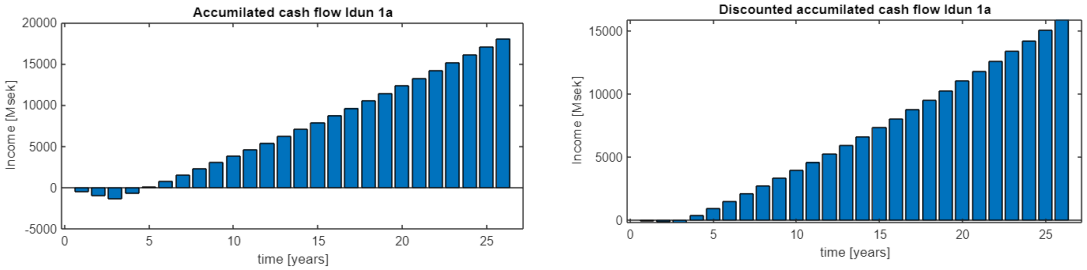

Figure B27: Cash flows for the year 2022 and forward, in the case of the integrated gasifier at Högdalen.

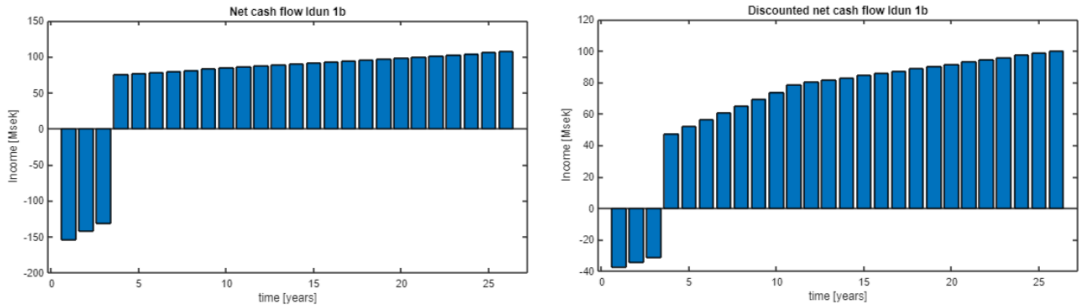

Figure B28: Cash flows for the year 2022 and forward, in the case of the integrated gasifier at Brista.

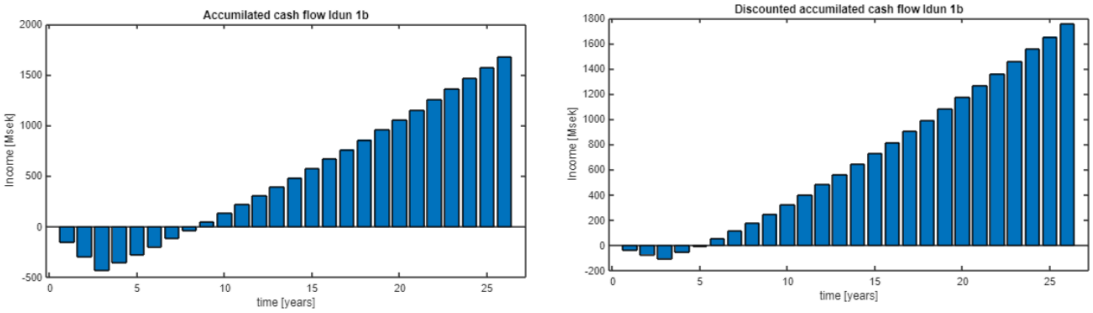

Figure B29: Cash flows for the year 2022 and forward, in the case of the integrated gasifier at Brista.

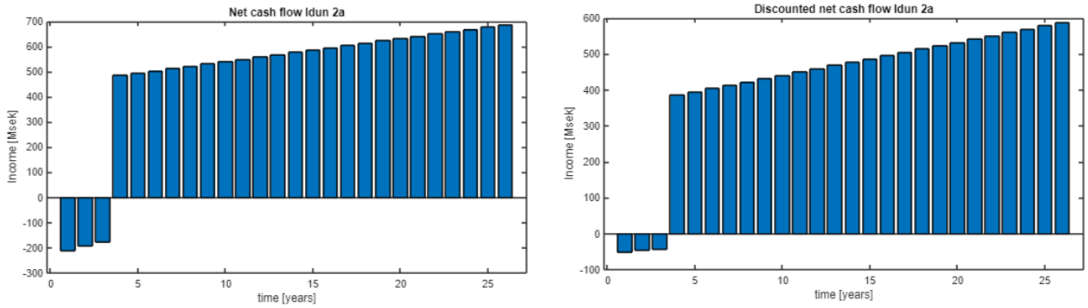

Figure B30: Cash flows for the year 2022 and forward, in the case of the stand-alone CFB gasifier at Högdalen.

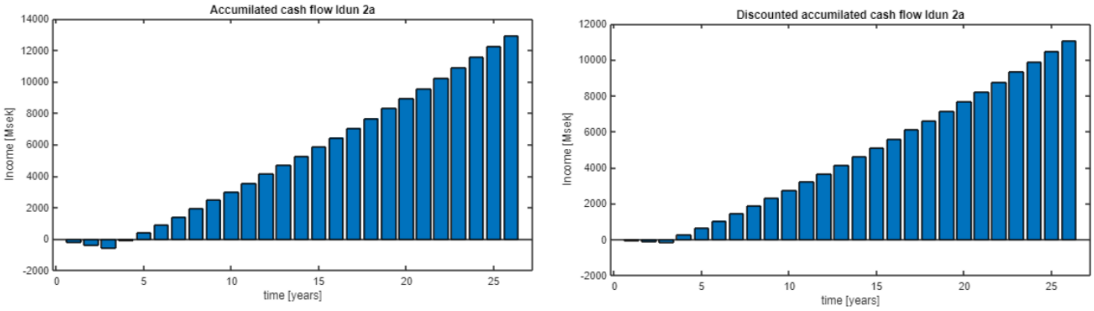

Figure B31: Cash flows for the year 2022 and forward, in the case of the stand-alone CFB gasifier at Högdalen.

1.8.2 Alternative cash flows

Table B22: **For reference**, Annual cash flows for base case Ägir 1 (AEL). Cost of operation, net fees and miscellaneous excluded from table.

Parameter	Value	Unit
Income basic sell of hydrogen	2.4	MSEK
Income support services up FFR	13.2	MSEK
Income support services up mFRR	1.7	MSEK
Income support services up aFRR	27.2	MSEK
Income support services up FCR-D	0.1	MSEK
Income support services down mFRR	1.6	MSEK
Income support services down aFRR	0.9	MSEK
Income basic sell of power	35.9	MSEK
Income from oxygen supply	0.7	MSEK
Income from district heating	1.2	MSEK
Cost water consumption	13.18	Ksek
Cost electricity consumption	7.6	MSEK

Table B23: Annual cash flows for the case with fixed operation cost and with fuel cell, the year 2022. **7.2.4 A**. Cost of operation, net fees, and miscellaneous are excluded from the table.

Parameter	Value	Unit
Income basic sell of hydrogen	2.4	MSEK
Income support services up FFR	13.2	MSEK
Income support services up mFRR	1.7	MSEK
Income support services up aFRR	27.2	MSEK
Income support services up FCR-D	0.1	MSEK
Income support services down mFRR	2.5	MSEK
Income support services down aFRR	1.2	MSEK
Income basic sell of power	7.8	MSEK
Income from oxygen supply	2.6	MSEK
Income from district heating	2.9	MSEK
Cost water consumption	46	Ksek
Cost electricity consumption	24.1	MSEK

Table B24: Annual cash flows for the case with fixed operation cost and without fuel cell **7.2.4 B**. Cost of operation, net fees, and miscellaneous are excluded from the table.

Parameter	Value	Unit
Income basic sell of hydrogen	38.9	MSEK
Income support services down mFRR	2.5	MSEK
Income support services down aFRR	1.2	MSEK
Income from oxygen supply	3.5	MSEK
Income from district heating	2.9	MSEK
Cost water consumption	59	Ksek
Cost electricity consumption	24.06	MSEK

Table B25: Annual cash flows for the case with double size of electrolyzer compared to standard case **7.2.4 C**, year 2022. Cost of operation, net fees, and miscellaneous are excluded from the table.

Parameter	Value	Unit
Income basic sell of hydrogen	14.72	MSEK
Income support services up FFR	13.2	MSEK
Income support services up mFRR	1.7	MSEK
Income support services up aFRR	27.2	MSEK
Income support services up FCR-D	0.1	MSEK
Income support services down mFRR	2.85	MSEK
Income support services down aFRR	1.21	MSEK
Income basic sell of power	35.93	MSEK
Income from oxygen supply	2.066	MSEK
Income from district heating	2.325	MSEK
Cost water consumption	37	Ksek
Cost electricity consumption	15.1	MSEK

Table B26: Annual cash flows for case with sleeping mode active **7.2.4 D**, year 2022. Cost of operation, net fees, and miscellaneous are excluded from the table.

Parameter	Value	Unit
Income basic sell of hydrogen	5	MSEK
Income support services up FFR	13.2	MSEK
Income support services up mFRR	1.7	MSEK
Income support services up aFRR	27.2	MSEK
Income support services up FCR-D	0.1	MSEK
Income support services down mFRR	1.6	MSEK
Income support services down aFRR	0.9	MSEK
Income basic sell of power	35.9	MSEK
Income from oxygen supply	1	MSEK
Income from district heating	1.4	MSEK
Cost water consumption	13.2	Ksek
Cost electricity consumption	16.7	MSEK

Appendix C

1 Processsimulations: Details

1.1 Constants Theory

Table B1: Fixed bed and Entrained flow gasification rate constants (M et al., 2000).

Index	Value	Unit
E_{1fw}	-199	kJ/mol
E_{1bw}	-146	kJ/mol
E_{1fc}	-214	kJ/mol
E_{1bc}	-284	kJ/mol
A_{1fw}	2	$10^7 \cdot s^{-1} bar^{-1}$
A_{1bw}	1.8	$10^6 \cdot s^{-1} bar^{-1}$
A_{1fc}	7.6	$10^7 \cdot s^{-1} bar^{-1}$
A_{1bc}	2.1	$10^12 \cdot s^{-1} bar^{-1}$
Pellet length	150	mm
d_p	50	μm
p_{H_2O}	0.1	bar_s
p_{H_2}	0.1	bar_s
p_{CO}	0.3	bar_s
p_{CO_2}	0.3	bar_s
E_{eq}	3966	kJ/mol
A_{eq}	26.5	$10^3 \cdot s^{-1} bar^{-1}$

Table B2: Fluidized bed gasification rate constants (Solli et al., 2016).

Index	Value	Unit
ρ_{char}	644.2	kg/m^3
d_{char}	4200	μm
ν_{gas}	4.5	$10^{-5} \cdot pas$
A_{CO_2}	3.1	$10^6 \cdot s^{-1} bar^{-1}$
E_{CO_2}	215	kJ/mol
n_{CO_2}	3.8	10^{-1}
A_{H_2O}	2.6	$10^8 \cdot s^{-1} bar^{-1}$
E_{H_2O}	237	kJ/mol
n_{H_20}	5.7	10^{-1}
A_e	26.5	$10^{-3} \cdots^{-1} bar^{-1}$
E_e	32.9	$\cdot 10^3$ kJ/mol
A_{rwgsr}	2.5	$10^5 \cdot s^{-1} bar^{-1}$
E_{rwgsr}	-138	$10^{-3} \cdot$ kJ/mol
$X_{Intrinsic}$	0.5	s^{-1}
S_{char}	2.5	$10^4 \cdot mm^2$
τ	4	-

Table B3: Theoretical constant used for the WGS reactor.

Index	Value	Unit
$A_{r,l}$	2.96	$10^5 \cdot s^{-1} bar^{-1}$
$E_{r,l}$	47.4	kJ/mol
$A_{ht,1}$	700	$s^{-1} bar^{-1}$
$E_{ht,1}$	-111	kJ/mol
$A_{ht,2}$	455.7	$10^{-2} \cdot s^{-1} bar^{-1}$
d_{cat}	5904	kg/m^3
θ	0.5	-
$n_{ht,1}$	1	-
$m_{ht,1}$	0	-
$p_{ht,1}$	-3.6	$\cdot 10^{-1}$
$q_{ht,1}$	-0.9	$\cdot 10^{-1}$
$n_{ht,2}$	0.9	-
$m_{ht,2}$	3.1	10^{-1}
$p_{ht,2}$	-15.6	10^{-2}
$q_{ht,2}$	-0.5	10^{-1}

Table B4: Theoretical constant used for potential AEL(1) , PEM(2), PEMFC(3), calculations (Um et al., 2000).

Index 1	**Value 1**	**Unit 1**	**Index 2**	**Value 2**	**Unit 2**	**Index 3**	**Value 3**	**Unit 3**
T_{cell}	353.2	K	T_{cell}	363.2	K	T_{cell}	343.2	K
T_{ref}	298	K	T_{ref}	318	K	T_{ref}	318	K
s_1	179.5	10^{-3}·V	$Load$	53.3	%	$Load$	1	-
s_2	0	V/K	p_{H_2O}	7	Bar	p_{O_2}	2.5	Bar
s_3	0	V/K	p_{H_2}	30	Bar	p_{H_2}	8	Bar
ξ_1	1017.1	$10^{-3} \cdot m^2/Amp$	t_m	125	μcm	t_m	126	μcm
ξ_2	842.4	$10^{-2} \cdot m^2 2/AmpK$	t_{cc}	0.1	cm	t_{cc}	0.1	cm
ξ_3	247.3	$m^2 2/AmpK^2$	t_{bp}	0.2	cm	t_{bp}	0.2	cm
r_1	80.5	$10^{-2} \cdot \Omega m^2$	σ_{ti}	150	s/cm	σ_{ti}	150	s/cm
r_2	-76.1	$10^{-8} \cdot \Omega m^2/K$	σ_{cc}	145	s/cm	σ_{cc}	200	s/cm
r_3	66.7	$10^{-3} \cdot \Omega m^2$	-	-	-	ER	1.2	-
i_{lim}	3	A/m^2	i_{lim}	1.5	A/m^2	i_{lim}	1.5	A/m^2
i_{cell}	0.4	A/m^2	i_{cell}	1.5	A/m^2	i_{cell}	1.4	A/m^2
vol_c	0.1	$10^1 \cdot cm^3$	$E_{act,a}$	90	kJ/mol	$E_{act,a}$	90	kJ/mol
vol_a	0.1	$10^1 \cdot cm^3$	$E_{act,c}$	30	kJ/mol	$E_{act,c}$	30	kJ/mol
E_{act}	90	kJ/mol	$\eta_{faraday}$	99	%	-	-	-
α_c	1.7	-	α_c	2	-	α_c	2	-
α_a	2	-	α_a	2	-	α_a	2	-

Table B5: Theoretical constants, physical AEL(1) , PEM(2), PEMFC(3).

Index 1	**Value 1**	**Unit 1**	**Index 2**	**Value 2**	**Unit 2**	**Index 3**	**Value 3**	**Unit 3**
A_{cell}	750	cm^2	A_{cell}	1000	cm^2	A_{cell}	352.2	cm^2
A_{surf}	19.8	m^2	A_{surf}	3	m^2	A_{surf}	1.8	m^2
d_{cell}	1.8	m	$Side$	0.5	m	$Side$	0.5	m
L_{stack}	7	m	L_{stack}	1	m	L_{stack}	0.6	m
N_{cells}	1985	–	N_{cells}	100	–	N_{cells}	299	–
k_{steel}	45	W/mK	k_{alloy}	22.5	W/mK	k_{sheet}	25	$10^{-2} \cdot W/mK$

Table B6: Overall theoretical constants for PEM, AEL, and PEMFC.

Index	Value	Unit
η_{isen}	70	%
η_{mech}	80	%
ε_{rad}	0.6	-
Ξ	14	-
T_{air}	20	°C
ν_{air}	1.5	μPas
v_{air}	0.2	m/s
$i_{0,a}$	1	mA
$i_{0,c}$	7.5	$10^1 \cdot mA$
$i_{0,ref}$	1	mA

2 Process design

Tables and diagrams related to individual plants are presented in this section. All equipment listed is used in the mathematical model.

2.1 Component details

Table B7: Pre-treatment of water before entering electrolysis.A. Jonsson and Mässgård, 2021

Equipment	Value	Unit
$\eta_{purification}$	90-99	%
Resistivity	17	$(m\Omega)$
Type	Reverse Osmosis/De-ionization	%
Power consumption	1534	Wh/m^3
TOC	$<$0.3	10^1·ppm

Table B8: Cleaning stage equipment (Hruška et al., 2020) (Woolcock & Brown., 2013) (Lee et al., 2007).

Equipment	Value	Unit
Scrubber $T_{operational}$	100	°C
Scrubber $p_{operational}$	>atm	Bar
Scrubber *retention*	H2s,HCL,NH3,HCN.Alkali,Tar	-
Scrubber $\eta_{purification}$	99 (50)	%
Scrubber type	absorber/gravimetric	-
Scrubber Material	Water	-
Mercury control filter $T_{operational}$	30-50	°C
Mercury control filter $p_{operational}$	62	Bar
Mercury control filter *retention*	Hg	-
Mercury control filter $\eta_{purification}$	90-95	%
Mercury control filter type	bed	-
Mercury control filter material	Active carbon	-
Hydrolysis unit $T_{operational}$	176-200	°C
Hydrolysis unit $p_{operational}$	9,89	Bar
Hydrolysis unit *retention*	COS	-
Hydrolysis unit $\eta_{purification}$	99	%
Hydrolysis unit type	catalyst	kW/kg
Hydrolysis unit material	Al	°C
AGR unit $T_{operational}$	40-120	°C
AGR unit $p_{operational}$	20	Bar
AGR unit *retention*	H2s,HCL(CO2)	-
AGR unit $\eta_{purification}$	99.2(25.3)	%
AGR unit type	absorber	-
AGR unit material	MDEA	-

Table B9: Pre-treatment particulate and ash cleaning units, no special conditions required (Morselli et al., 2019) (Woolcock & Brown., 2013).

Equipment	Removal efficiency	Unit
Cyclone	>90	%
Ceramic filter	>99.5	%
Bag filter	<50-60	%

Table B10: WGS reactor catalyst details(II & Barton, 2009) (Baraj et al., 2022).

Parameter	Value	Unit
WGS catalyst $T_{operational}$	177-500	°C
WGS catalyst $p_{operational}$	6-20	Bar
WGS catalyst *concersion*	H2/CO	-
WGS catalyst max $\eta_{conversion}$	95-96	%
WGS catalyst material HT1	FeO	-
WGS catalyst material HT2	FeCr	-
WGS bed material	SiO2	-

Table B11: Separation process CH4 (Sharifiana et al., 2019) (Khanipour et al., 2017).

Parameter	Value	Unit
Membrane $T_{operational}$	250	°C
Membrane $p_{operational}$	10	Bar
Membrane $separation$	CH_4, CO	-
Membrane $\eta_{purification}$	93-98	%
Membrane type	Asymmetric hollow fiber	-
Membrane Material	Polymer/zeolite	-
Membrane Permiance $CO_2, CO, H_2, CH_4, H20$	311.4, 12.8, 971.0, 12.4, 3348.2	$10^{-10} mol/sm2\,Pa$

Table B12: Separation process CO2 (Ribeiro et al., 2008)

Delprocess	Värde	Enhet
PSA $T_{operational}$	20	°C
PSA $p_{operational}$	7-10	Bar
PSA $retention$	CO2,trace molecules	-
PSA $\eta_{purification}$	98-99.99	%
PSA type	adsorption	-
PSA Material	AC and 5A Zeolite/silica gel	-
PSA Design	5 to 10-bed (alt 3-bed VSA)	-

Table B13: Final purification H2(Read comment section below*) (P. Li et al., 2015).

Delprocess	Värde	Enhet
Membrane $T_{operational}$	35-230	°C
Membrane $p_{operational}$	30	Bar
Membrane $retention$	H2*	-
Membrane $\eta_{purification}$	99.99	%
Membrane type	hollow fiber/MFI/CMS	-
Membrane material	Polymer/zeolite/carbon	-

2.1.1 Comments on cleaning and purification

Raw syngas leaving the heat recycling system is preconditioned through a rough filtering system and alternatively expanded before entering the cleaning stage, this is specific for low-temperature cleaning processes, which is the most common method for syngas treatment. Removal of unwanted sulfur, particulates, metals, chlorides, and other molecules is required before being handled in downstream synthesizing equipment for achieving fuel-grade hydrogen. Today's commercial moist-fed gasification processes, utilize quenching and scrubbing with water as the initial cleaning stage for the removal of fine particulates and char. Dry fed gasification system uses cyclones or ceramic filters before scrubbing. The scrubbing removes particulates, alkali, chloride, ammonia, char, and H_2S during this process. Approximately 10% of sulfur converts to COS in gasification, the rest bind into H_2S structures. The gas is then heated and fed to a hydrolysis unit for removal of COS in the form of H_2S. The rejected water from this process is then conveyed to a water treatment system since the water containment can be recovered for incineration or disposed of as wastewater. The recovered H_2S is then sieved and utilized and sprayed for preventing sintering in the boiler. All heat from each step due to pressure increase is recovered for processes that require slight heat procurement, rendering the cleaning systems main penalty in terms of electricity, for compressors. To note is that, in the model, all compressors are calculated as single units for modification factors. Mercury and trace elements, after the hydrolysis removed in a sulfide carbon bed filter, recover most of the heavy metals. The acid gas removal is made, using chemical or physical solvents, for example, MDEA and Rectisol. The mentioned methods have nexus in terms of work, and is primarily washed with a lean solvent in the absorption stage to remove all trace of sulfur, then sent to the regenerator to strip the material flow with low-pressure steam to remove captured sulfur to them be recovered in external processing(Claus sulfur recovery unit). During this process, CO_2 is also removed to a certain degree (NETL, 2023).
Critical values for contaminants reaching the WGS reactor is dependent on catalyst material, in some cases

catalyst are very durable and can act as a separation unit, thus utilizing excess sulfur to increase the reaction rate, together with rejection of char and heavy particulates. In the case mentioned, hydrolysis equipment is not required.

After the WGS section, the syngas that now are mainly compromised of H_2, CO_2, H_2O and $CH4$. The gas enters the 1st separation stage, which dries the gas, in addition to recovering the unused carbon monoxide and methane for flaring. This recovery is not only made to purify the syngas but also secure total heat balance internally, for heating input water, into steam if necessary. Before the methane separation, the syngas is flashed or condensed to remove any steam used during the water gas shift and recover both heat and water for streams entering the WGS reactor. Due to the significant size difference of the molecules $CO_2, H2$ and CO, CH_4, membrane technology is the most efficient separation method in this case but can be exchanged to PSA with the drawback of longer separation time and more use of power. Membrane performance is measured by the permeability of each molecule as molecules can have varying difficulty to penetrate the material, and obtaining equal or close to equal permeability between molecules renders poor separation. Syngas transported to the next stage is separated by PSA at low-to-medium pressure, to separate CO_2 with leftover trace elements and purified hydrogen in separate streams generating at least a recovery of 70-90%. Note that reject streams can be recycled and processed in iterations. When adjusting activated carbon length and increase of layered zeolite, the purification decrease and recovery rate increase, thus it can be beneficial to have lower purity and introduction off membrane for reaching higher fuel to hydrogen efficiency.
A membrane is often a cylinder filled with hollow tubes that have selectivity directly controlled by the temperature or pressure of inlet gas. These hydrogen purification processes are relatively simple in relation to conventional PSA but have other drawbacks depending on the type of membrane utilized. In this model, a CO_2 selective membrane is utilized since a H_2 selective membrane only reaches 95% purity at 30 bar(selectivity 11.8). while a CO_2 selective membrane can achieve 99.99% purity(selectivity 9.2) and H_2 selective membrane requires a selectivity of 368. The membrane is not bound to this type and is thus only recommended, since there are options that are dependent more on temperature change, rendering lower pressure requirements to reach similar purity. The change of membrane will however not change plant performance substantially if approximately the same inlet conditions are applicable for such installation (P. Li et al., 2015).
Overall the assumption is made that biomass and MSW as fuel require the same cleaning systems with only a reduction of recovery rate from syngas from gasification in cases when MSW is used as the primary fuel.

Contaminants in fuel can damage the fuel cell and are expected to be kept to a minimum during the hydrogen conversion of solid fuels. In Table B14 the requirements are shown for two universal standards for hydrogen fuel. In cases when the amount of contaminant is filled with (-), means that there is no actual limit, thus the content allowed is agreed upon with the customer.

Table B14: Requirements for impurity in hydrogen for utilization in fuel cells (Du et al., 2021)

Substance	**ISO 14687:2019 SAE J2719-202003**	**GB/T 3634.2-2011**	**Unit**
H2 purity	99.97	99.99	%
Non-Hydrogen gases	300	100	ppm
H20	5	10	ppm
Non-methane HC	2	-	ppm
Methane	100	10	ppm
O2	5	5	ppm
He	300	-	ppm
N2	300	60	ppm
Ar	300	-	ppm
CO2	2	5	ppm
CO	0.2	5	ppm
H2S	0.004	-	ppm
HCHO	0.2	-	ppm
HCOOH	0.2	-	ppm
NH3	0.1	-	ppm
Halides	0.05	-	ppm
Conc. particulate matter	1	-	mg/kg

Notable effects on cell is that the CO and CO_2 can damage the cell, in the form of catalyst poisoning. Halides

also damage the catalyst by the dissolution of the active material. Inert gases of nitrogen, argon, oxygen, and sulfides reduce the cell performance and do not actively destroy the material to the same extent as other contaminants.

2.2 Integrated gasifier

The global parameters set for all process models are set in Table B15. Critical steam fraction is 88% for steam cycles related to stand-alone gasifiers.

Table B15: Global parameters set in all process models related to gasification.

Parameter	value	Unit
Compressors: γ_a	1.39	%
Compressors: Electrical efficiency	95	%
Cleaning Equipment: Electrical efficiency	99	%
ST: Isentropic efficiency	89	%
ST: Generator efficiency	96	%
Water pumps: Isentropic efficiency	88	%
Water pumps: Electrical efficiency	95	%
Critical steam fraction	82-88	%
Fuel Boiler: Combustion efficiency	99	%
Methane B36: Combustion Efficiency	95.2	%
Boiler: Pressure loss	1	%
Boiler: Radiation γ_g	1.33	%
Fans: Isentropic efficiency	85	%
Fans: Electrical efficiency	95	%
Dryer: Efficiency	95	%
Gasifier: Insulation efficiency	99.67	%
Ambient: Temperature	15	°C

Results from simulations with parameters set from Table B18, B22 and B27 generate variable $DHcondenser$: $Temperature$ equal to 109.2℃.

2.2.1 Idun 1a Högdalen

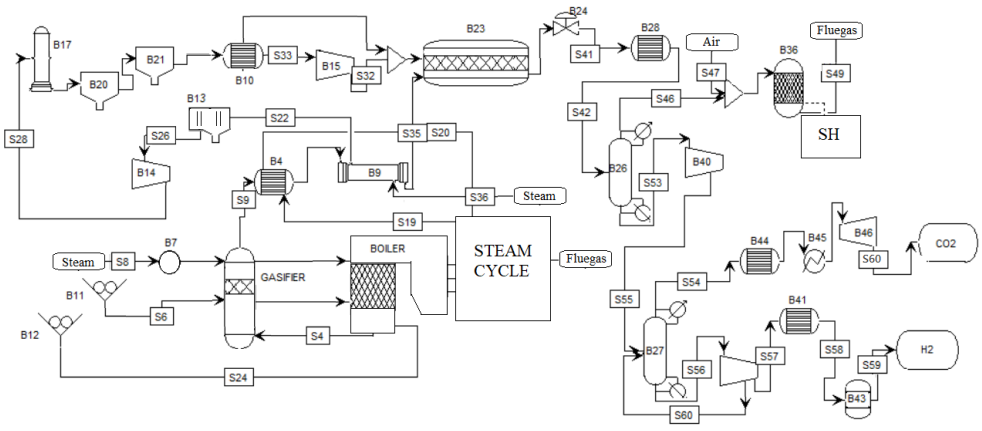

Figure B1: Process model flow of Idun 1a integrated gasifier with the subsystem.

The physical flows of selected nodes in the plant are presented in Table B16. Note that some equipment is displaced to the actual application due to simplicity, and is allocated so in order not to affect the total energy balance of the plant.

Table B16: Detail simulation flow results from unique streams, excluding contaminant content($S/H_2S/HCN$ etc.).

Material flow	**composition [O2 N2 H2 CO CO2 H20 CH4] % vol**	**T (K)**	**p (bar)**	$\dot{m}$ **(kg/s)**
S9	0 5.8358 5.3865 10.1030 2.1056 74.4458 2.1234	993	1.02	16.6
S28	0 20.3476 18.7810 35.2263 7.3417 10.9000 7.4035	373	2	5.5287
S33	0 1.2641 23.1023 43.7692 9.1221 13.5434 9.1990	447.3234	2	4.1865
B22	0 0.3091 5.6488 10.7021 2.2305 78.8602 2.2493	623.7	15.4358	15.27
S42	0 0.9180 43.0590 4.6836 33.8264 11.5013 6.0117	723	10	5.6634
S46	0 0 0 36.3544 0 0 63.6456	350.7	13.4358	0.5031
S53	0 1.1304 55.5692 0.0846 43.0678 0 0.1481	621.4	13.4358	4.5634
S56	0 1.9571 96.2095 0.1464 1.4913 0 0.1957	571.4	13.4350	0.4148
S60	0 0.1 0 0 99.9 0 0	248.15	15	4.148
S59	0 0 100 0 0 0 0	333	30.6886	0.2501

Table B17 presents the settings for the sub-processes. In regards to HEX, the primary exchanger for heat transfer to the steam cycle is presented. Note that, in the calculation, no computation is performed with regard to the number of tubes in the heat exchanger, instead it is calculated as a composite surface with the name *Tube area* and effective value depending on type.

Table B17: Miscellaneous optimization parameters.

Parameter	value	Unit
Primary HEX: HEX type	Parallel-flow	-
Primary HEX: Tube area	10	m^2
Primary HEX: Overall heat transfer coefficient (U)	6	kW/m^2K
Dryer: Temperature	0	°C
Dryer: Mass flow air	0	kg/s
Moisture content after drying	25	%
Methane B36: Mass flow air	14	kg/s

Table B18: Set parameters for steam cycle and general assumptions for the boiler.

Parameter	value	Unit
BDR	1	%
Pressure loss(Condenser-ST)	4	%
Number of ST	1	-
Overpressure feed pump	5	%
Deaerator: Pressure	9	bar
DH condenser: Pressure	1,4	bar
CW Condenser: Pressure	0,4	bar
Make up water: Temperature	200	°C
Make up water: Pressure	4	bar
Steam cycle Gasifier: Mass flow	4,2	kg/s

Table B19: Set parameters for the gasifier.

Parameter	value	Unit
Gasifier: Temperature	800	°C
Gasifier: Pressure	1,02	bar
Gasifier; Temperature drop	80	°C
Methane yield	7,64	%
λ_{ER}*	0.05	-
SB	0,8	-
Steam: Temperature	400	°C
Steam: Pressure	19	bar
O_2: Temperature	-	°C
O_2: Pressure	-	bar

In Table B19, the λ_{ER}* stands for the assumed air slip from the boiler, conveyed with the bed material re-circulation.

2.2.2 Idun 1b Brista

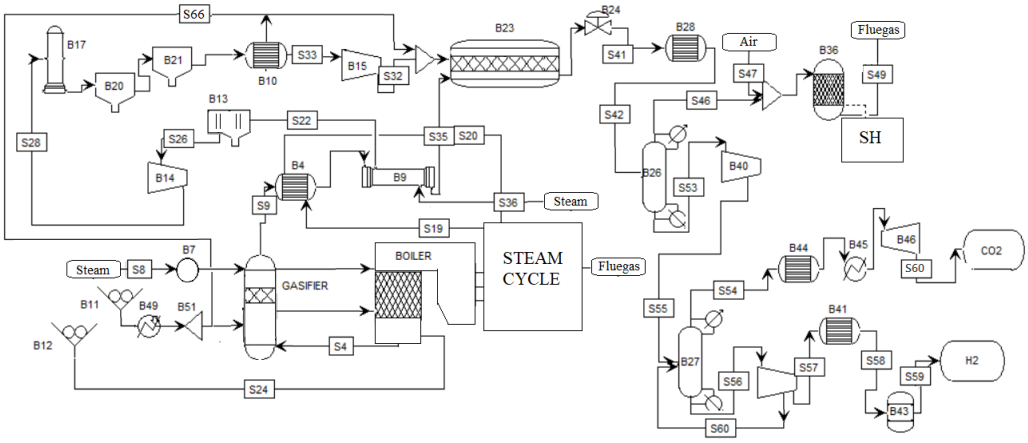

Figure B2: Process model flow of Idun 1b integrated gasifier with the subsystem.

Table B20: Detail simulation flow results from unique streams, excluding contaminant content($S/H_2S/HCN$ etc.).

Material flow	**composition [O2 N2 H2 CO CO2 H20 CH4] % vol**	**T (K)**	**p (bar)**	$\dot{m}$ **(kg/s)**
S9	0 7.6158 3.9335 5.0959 2.7509 78.4689 2.1351	993	1.02	8.2576
S28	0 31.5158 16.2775 21.0878 11.3837 10.9000 8.8353	373	1.1	2.4227
S32	0 2.2703 22.5135 30.3819 16.4009 15.7040 12.7294	447.4531	2	1.5548
B22	0 0.3869 3.8363 5.1771 2.7947 85.6358 2.1691	710.2590	18	7.8377
S42	0 2.0264 45.9914 1.2211 40.5355 0 10.2256	704.959	15.9	1.7154
S46	0 0 0 10.6676 0 0 89.3324	704.959	13.9	0.1515
S53	0 2.2824 51.8025 0.0275 45.6572 0 0.2304	704.9	15	1.5591
S56	0 4.1308 93.7537 0.0498 1.6526 0 0.4131	654.9590	13	0.1522
S60	0 0.1 0 0 99.9 0 0	248.15	15	1.4069
S59	0 0 100 0 0 0 0	333	30.7017	0.0746

Table B21: Miscellaneous optimization parameters.

Parameter	value	Unit
Primary HEX: HEX type	Parallel-flow	-
Primary HEX: Tube area	12	m^2
Primary HEX: Overall heat transfer coefficient (U)	6	kW/m^2K
Dryer: Temperature	81	°C
Moisture content after drying	30	%
Dryer; Efficiency	99	%
Dryer; Mass flow air	11	kg/s
Methane B36: Mass flow air	6	kg/s

Table B22: Set parameters for steam cycle and general assumptions for the boiler.

Parameter	value	Unit
BDR	1	%
Pressure loss(Condenser-ST)	3	%
Number of ST	2	-
Overpressure feed pump	5	%
Deaerator: Pressure	9	bar
DH condenser: Pressure	1,4	bar
CW Condenser: Pressure	0,4	bar
Make up water: Temperature	400	°C
Make up water: Pressure	4	bar
Steam cycle Gasifier: Mass flow	1,5	kg/s

Results from simulation with parameters set from Table B22, generate variable $DHcondenser : Temperature$ equal to 109℃.

Table B23: Set parameters for the gasifier.

Parameter	value	Unit
Gasifier: Temperature	800	°C
Gasifier: Pressure	1,02	bar
Gasifier; Temperature drop	80	°C
Methane yield	7,639	%
λ_{ER}*	0.05	-
SB	1,64	-
Steam: Temperature	300	°C
Steam: Pressure	19	bar
O_2: Temperature	-	°C
O_2: Pressure	-	bar

In Table B23, the λ_{ER}* stands for the assumed air slip from the boiler, conveyed with the bed material re-circulation.

2.3 Stand-alone gasifier

Table B24: Set parameters for the ASU. A booster compressor is only applied in pressurized reactors.

Parameter	value	Unit
Compressor: Isentropic efficiency	76,9	%
Compressor: Electrical efficiency	95	%
Main air Compression: Pressure	4,8	bar
Compression: Temperature	40	°C
Booster compressor: Pressure	19	bar
Expansion: Temperature	−185,0	°C

2.3.1 Idun 2a

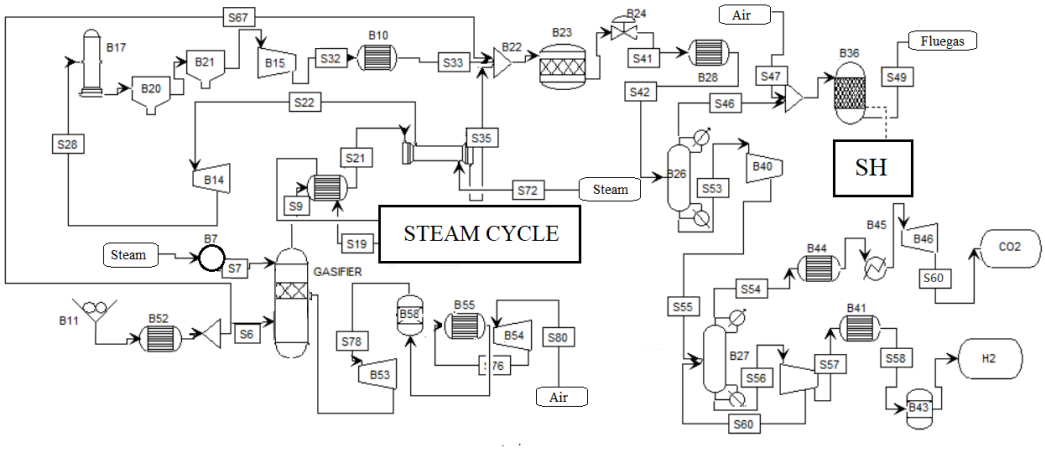

Figure B3: Process model flow of Idun 2a stand-alone gasifier with the subsystem.

Table B25: Detail simulation flow results from unique streams, excluding contaminant content($S/H_2S/HCN$ etc.).

Material flow	**composition [O2 N2 H2 CO CO2 H20 CH4] % vol**	**T (K)**	**p (bar)**	$\dot{m}$ **(kg/s)**
S9	0 9.3208 22.0031 9.6097 26.3038 28.9034 3.8591	1040	19.2	5.1914
S28	0 9.3208 22.0031 9.6097 26.3038 28.9034 3.8591	323	2.19	5.1914
S32	0 0.5126 23.9571 10.5688 28.9291 31.7881 4.2443	322.9762	18.19	4.6339
B22	0 0.3785 17.6920 7.8049 21.3637 49.6266 3.1344	638.8391	18.19	5.9339
S42	0 0.6588 43.6681 0.7055 50.0582 0 4.9094	636.539	16.0	3.83
S46	0 0 0 12.5647 0 0 87.4353	620.1391	13.8	0.1488
S53	0 0.6971 46.2109 0.0149 52.9731 0 0.1039	635.1391	14	3.6764
S56	0 1.4507 96.1683 0.0311 2.2048 0 0.1451	585.1391	12	0.2418
S60	0 0.1 0 0 99.9 0 0	248.15	15	3.43
S59	0 0 100 0 0 0 0	333	30.01	0.14

Table B26: Miscellaneous optimization parameters.

Parameter	value	Unit
Primary HEX: HEX type	Counter-flow	-
Primary HEX: Tube area	-	m^2
Primary HEX: Overall heat transfer coefficient (U)	-	w/m^2K
Dryer: Temperature	80,1	°C
Moisture content after drying	20	%
Dryer: Efficiency	99	%
Dryer: Mass flow air	14,2	kg/s
Methane B36: Mass flow air	11	kg/s

Table B27: Set parameters for the steam cycle.

Parameter	value	Unit
BDR	0,2	%
Pressure loss(Condenser-ST)	1	%
Number of ST	1	-
Overpressure feed pump	5	%
Deaerator: Pressure	4	bar
DH condenser: Pressure	1,4	bar

Table B28: Set parameters for the gasifier.

Parameter	value	Unit
Gasifier: Temperature	847	°C
Gasifier: Pressure	19,2	bar
Gasifier; Temperature drop	80	°C
Methane yield	7,64	%
λ_{ER}	0,28	-
SB	0,59	-
Steam: Temperature	>272	°C
Steam: Pressure	15	bar
O_2: Temperature	>100	°C
O_2: Pressure	19,2	bar

2.3.2 Idun 2b

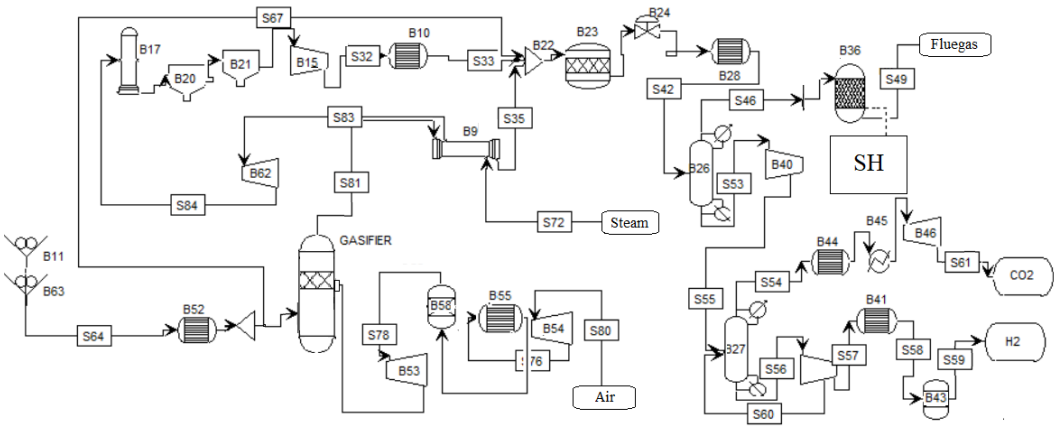

Figure B4: Process model flow of Idun 2b stand-alone gasifier with the subsystem.

Table B29: Detail simulation flow results from unique streams, excluding contaminant content($NO_x/S/H_2S/HCN$ etc.).

Material flow	**composition [O2 N2 H2 CO CO2 H20 CH4] % vol**	**T (K)**	**p (bar)**	$\dot{m}$ **(kg/s)**
S81	0 1.3539 23.8902 42.9095 12.1515 17.2920 2.4029	1423.15	19.19	4.0879
S84	0 1.6370 28.8850 51.8807 14.6920 0 2.9053	328.15	2.0	3.5019
S67,S35	0 0 0 0 0 100 0	743.9594	78.7068	2.3672
B22	0 0.8723 14.7761 27.6454 7.8288 47.3293 1.5481	729.1953	12.1	5.6941
S42	0 1.2273 46.6835 13.0022 36.9089 0 2.1782	726.3453	10.1	4.2473
S46	0 0 0 85.6513 0 0 14.3487	711.4953	8.099	0.7484
S53	0 1.4824 53.5690 0.3141 44.5818 0 0.0526	721.4950	12	3.4661
S56	0 2.6326 95.1336 0.5578 1.5835 0 0.0925	671.4953	9.9	0.3165
S60	0 0.1 0 0 99.9 0 0	248.15	15	3.1496
S59	0 0 100 0 0 0 0	333	30.0	0.1679

Table B30: Miscellaneous optimization parameters. Secondary HEX is the equipment for steam heating to the WGS reactor.

Parameter	value	Unit
Secondary HEX: HEX type	Counter-flow	-
Primary HEX: Tube area	30	m^2
Primary HEX: Overall heat transfer coefficient (U)	200	W/m^2K
Dryer: Temperature	105	°C
Moisture content after drying	6	%
Dryer; Efficiency	95	%
Dryer; Mass flow air	-	kg/s
Methane B36: Mass flow air	19,7	kg/s

Table B31: Set parameters for the gasifier.

Parameter	value	Unit
Gasifier:Temperature	1200	°C
Gasifier: Pressure	19	bar
Temperature drop	50	°C
Methane yield	5,6	%
λ_{ER}	0.38	-
SB	0	-
Steam: Temperature	-	°C
Steam: Pressure	-	bar
O_2: Temperature	40	°C
O_2: Pressure	2	bar

2.3.3 Idun 2c

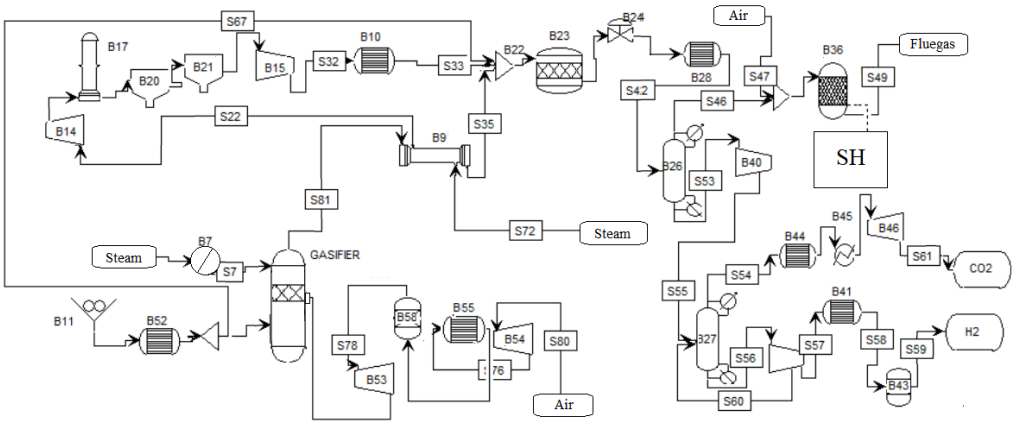

Figure B5: Process model flow of Idun 2c stand-alone gasifier with the subsystem. Anomaly in B27 in this process, as the heat from syngas is recovered for district heating application.

Table B32: Detail simulation flow results from unique streams, excluding contaminant content($S/H_2S/HCN$ etc.).

Material flow	**composition [O2 N2 H2 CO CO2 H20 CH4] % vol**	**T (K)**	**p (bar)**	$\dot{m}$ **(kg/s)**
S81	0 1.0870 38.1339 30.3554 13.8141 13.5742 3.0355	923.1500	1.02	0.7331
S22	0 1.2577 44.1232 35.1230 15.9838 0 3.5123	318.15	1.02	0.6367
B22	0 0.5384 18.7010 15.0367 6.8429 57.3772 1.5037	721.3050	16.11	1.4016
S42	0 1.0879 51.6659 16.5013 27.7067 0 3.0382	718.30	15.91	0.7058
S46	0 0 0 84.4511 0 0 15.5489	703.305	15.71	0.1837
S53	0 1.3900 62.7110 0.4217 35.3998 0 0.0776 0 0.0889	703.4550	15.71	0.5144
S56	0 2.1284 96.0242 0.6457 1.0841 0 0.1177	553.4162	15.61	0.0587
S59	0 0 100 0 0 0 0	333	30.0	0.0353

Table B33: Miscellaneous optimization parameters.

Parameter	value	Unit
Secondary HEX: HEX type	Counter-flow	-
Secondary HEX: Tube area	4	m^2
Secondary HEX: Overall heat transfer coefficient (U)	200	W/m^2K
Dryer: Temperature	105	°C
Moisture content after drying	6	%
Dryer; Efficiency	95	%
Dryer; Mass flow air	-	kg/s
Methane B23: Mass flow air	5	kg/s

Table B34: Set parameters for the gasifier.

Parameter	value	Unit
Gasifier: Temperature	750	°C
Gasifier: Pressure	1,01	bar
Temperature drop	-	°C
Methane yield	10	%
λ_{ER}	0.25	-
SB	0	-
Steam: Temperature	-	°C
Steam: Pressure	-	bar
O_2: Temperature	41	°C
O_2: Pressure	2	bar

2.3.4 Ägir 1 (Electrolysis stack)

Parameters that are connected to global equipment such as a compressor or feed water pumps are the same as for steam cycles, and will thus not be presented in the following tables.

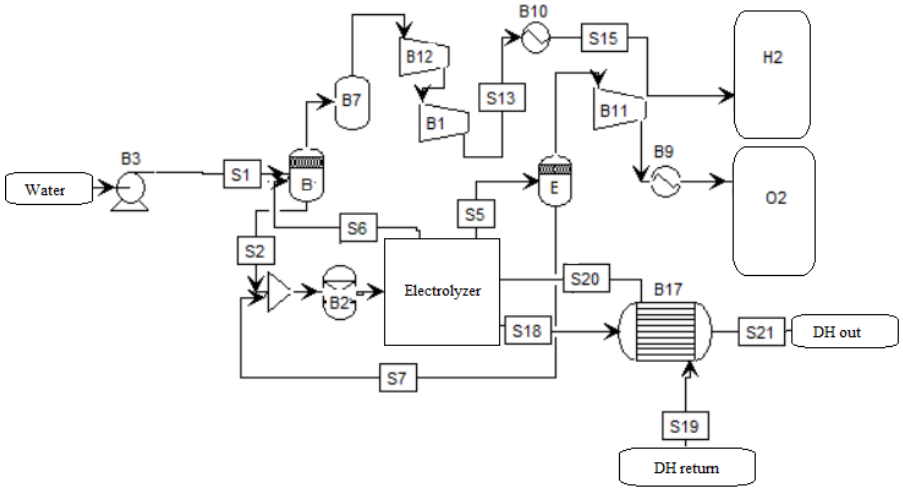

Figure B6: Schematic over the setup for AEL electrolyzer in Ägir 1.

Table B35: Detail simulation flow results from unique streams in AEL electrolyzer, excluding contaminant from lye and. (*) Indicate the accumulated temperature of gas if not cooled sequentially.

Material flow	**composition [O2 N2 H2 H20] % vol**	**T (K)**	**p (bar)**	$\dot{m}$ **(kg/s)**
S1	0 0 0 100	355.4542	1.4	0.0306
S18	0 0 0 100	353.15	1.2	12.5
S19	0 0 0 100	333.15	4.0	3.5
S20	0 0 0 100	349.1471	1.0	12.5
S21	0 0 0 100	348.5870	4	3.5
S13*	0 0 100 0	1131.5	30.0	0.0062
B11	100 0 0 0	918.4982	20.0	0.0244

Table B36: Set parameters for process concerning Ägir 1 (AEL).

Parameter	value	Unit
Cooling circuit: Temperature Δ max	6	°C
Cooling circuit: Mass flow	12.5	kg/s
Cooling circuit: Pressure	1.2	bar
Feed pressure: Pressure	1.4	bar
DH HEX: HEX Type	Counter-flow	-
DH HEX: Tube-Area	15.1	m^2
DH HEX: Overall heat transfer coefficient (U)	1400	W/m^{2}K
DH Return water: Temperature	60	°C
DH Return water: Mass flow	3.5	kg/s
DH Return water: Pressure	4	bar
KOH fraction	35	%
Separation tank: Pressure drop	0.2	bar

Results from simulation with parameters set from Table B36, generate variable $DH : Temperatureout$ equal to 74.2℃.

Table B37: Set parameters for process concerning Ägir 1 (PEM).

Parameter	value	Unit
Cooling circuit: Temperature Δ max	10	°C
Cooling circuit: Mass flow	2.7	kg/s
Cooling circuit: Pressure	1.2	bar
Feed pump pressure: Pressure	7	bar
DH HEX: HEX Type	Counter-flow	-
DH HEX: Tube-Area	3	m^2
DH HEX:Overall heat transfer coefficient (U)	1000	W/m^{2}K
DH Return water: Temperature	60	°C
DH Return water: Mass flow	0.5	kg/s
DH Return water: Pressure	4	bar
Separation tank: Pressure drop	0.3	bar

Results from simulation with parameters set from Table B37, generate variable $DH : Temperatureout$ equal to 81.9℃.

Appendix D

1 Oxygens impact on CCS

In this calculation, assumptions are made around the KVV8 boiler and carbon capture facility. An estimation from the boiler manufacturer is setting the initial boundary condition for the oxygen enrichment of inlet air to not exceed 43% of oxygen content before the boiler requires major modifications.

Table D1: Average composition of fuel to KVV8

Element	**wt**	**C**	**H**	**O**	**N**	**Ash**	**LHV**
Volume fraction (%)	47	51	5.8	38.2	0,9	4.1	20.4

Table D2: Operational presets for steam cycle and turbine

Parameter	value	Unit
BDR	1	%
Pressure loss SH-ST	1	%
Overpressure from pressure pump	16,5	%
ST: Isentropic efficiency	87	%
ST: Generator efficiency	96	%
Deaerator; Pressure	4	bar
DH condenser: Pressure	2	bar
CW condenser: Pressure	1.85	bar
Critical steam fraction	85	%
Water pump: Isentropic efficiency	88	%
Water pump: Mechanical efficiency	95	%
Make up water: Pressure	90	bar
Make up water: Temperature	560	°C
Steam: Mass flow	143	kg/s
Steam: Pressure	150,3	bar
Steam: Temperature	560	°C

Table D3: Operational presets for P8 subsystem.

Parameter	value	Unit
Combustion chamber: Pressure	1,01	bar
Combustion efficiency	99,5	%
FGR: Temperature	200	°C
Stack exit: Temperature	36	°C
Radiation loss of boiler heat accumulation	2	%

Table D4: Operation results of plant simulation.

Parameter	value	Unit
Combustion temperature	900,1	°C
SC heat	384,3	MW
DH condenser: Temperature	120,2	°C
Net electricity output	111,3	MW
Input fuel	399,4	MW
Efficiency system	95	%

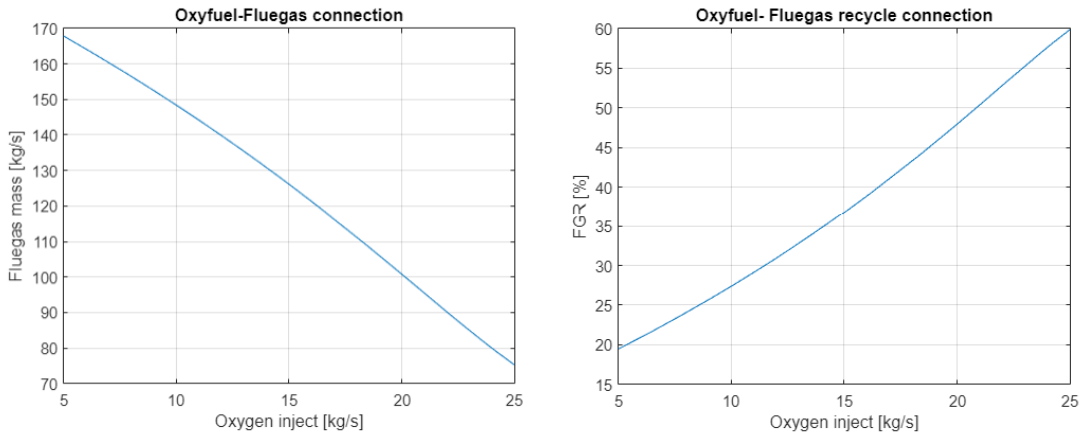

Figure D1: Oxygen injection effect on flue gas conditions.

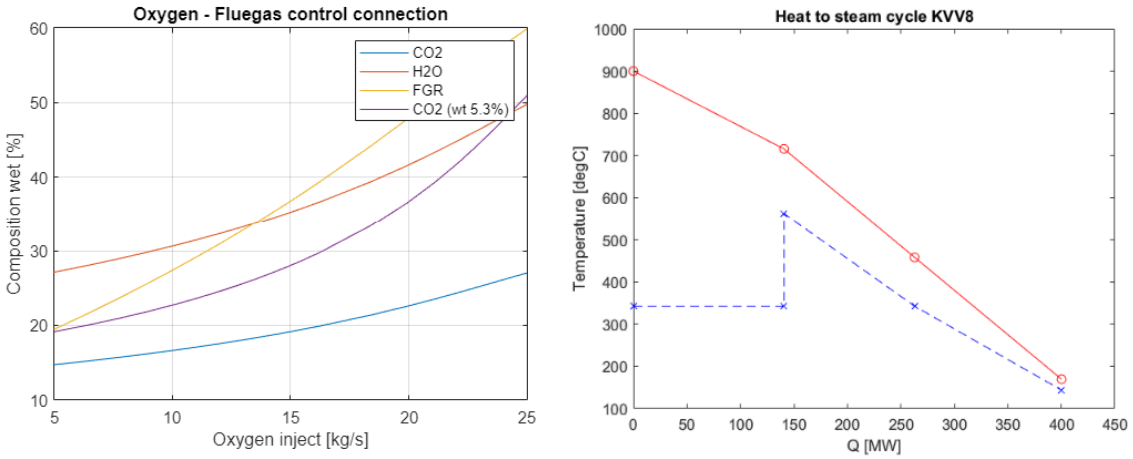

Figure D2: Flue gas content and composite curve of oxyfuel adaptation to KVV8. Points indicate the evaporator, economizer, and superheater.

1.1 Comments on Oxygen enhanced combustion

As anticipated, results show that due to increased oxygen content, flue gas recycling is required to increase to cool and keep the same temperature in combustion considering the lower mass of flue gas. However, if the mass flow of flue gas generated is lower, approximately the amount of heat is recovered downstream due to the updated capacity and temperature of flue gas, which only deviate around 2% respectively 1.8% on average. It is notable that the effect of dry and wet recycling have different performances and affect both combustion performance and pollutant levels. The simulation shows that even during peak recycling, the recycling fan does not need to be upgraded to handle the increased volume. Benefits from oxyfuel, except for the lowering of mass in flue gas, in combustion is the increased fuel efficiency, lower fan power requirement, and bypassing drying for high moisture fuel (eg. Bark).

From Figure D1 it can be concluded that a significant increase of CO_2 and H_20 in the flue gas can have a positive impact on the following CCS processing plant. It is also concluded that flue gas condensation energy will not decrease from the loss of mass, and rather increase because of the specific heat capacity in the oxyfuel flue gas, in addition to the slightly higher temperature. It should be considered that the recycled flue gas should have at least 2.8-7 % of oxygen content, to not extinguish the incineration through the combustion chamber, though this number is most likely not relevant when the oxygen content of inlet air is enhanced. In all simulations, the control oxygen level over the heater package is accounted for, as excess oxygen content is not to exceed 3%.

From increasing oxygen levels in the inlet air to combustion, literature (Lupion et al., 2013),(Khavidak et al., 2015) showcase that NO_x, metals, and most other contaminants decrease in content. The only defined negative effect is the higher concentration of sulfur dioxide, some amount of chloride, and proportionally small amounts of mercury. This could be the because of the increased fuel combustion efficiency since the material is more likely to completely combust during oxygen-rich conditions and gasification of inert material.
The fix for the increased levels of SO_x is to ad 10-20 % of limestone to the combustion zone relative to sulfur content, this will decrease SO_x below the initial contaminant level during non-oxyfuel combustion, another possibility is that the increased levels of chlorides will bind to the increased levels of sulfur and therefore decrease limestone demand, alkali chlorides effect on corrosion of the superheaters can also be counteracted with sulfur addition of at least 2-4 mg/MJ heat of fuel. Regarding mercury, the issue could be reduced with increased oxygen control levels in flue gas and slightly higher temperature in downstream operation, due to mercury dissolving in high-temperature process stream. This fix is not certain and further research should investigate the actual effects before implementation (Heden & Saleh., 2021), since a carbon filter may be required to adapt to a new level of contaminant (Stanger et al., 2015).

With values from the literature, inserted in the separate economical models, the price of oxygen per kilogram can be calculated. This value is highly dependent on operational cost(80% of total expenses). The price of oxygen through ASU can be estimated in different cost levels regarding electricity as; 1.44 SEK/kg for the highest(2200 SEK/MWh), 0.84 SEK/kg for mid(1226 SEK/MWh) and lowest 0.66 SEK/kg(900 SEK/MWh). With the price of increased combustion efficiency, which is executed by a previous study (Lindborg, 2023), the

value of oxygen increases to 1.5, 0.9, and 0.72 SEK/kg, which is the final sum of investment and operational saving by utilizing oxygen from electrolysis (Cau et al., 2018) (Cormos, 2016) (Hanak et al., 2017) (Vu et al., 2020) (López et al., 2016) (Pettinau et al., 2017) (Bouillon et al., 2009) (Hu et al., 2013) (Hamadeh et al., 2020) (Heden & Saleh., 2021)

Appendix E

1 Strategic analysis

1.0.1 Reliability data

Table E1: Reliability only Ägir 1 depending on historical data.

Year	**Threshold price (SEK)**	**Availability DH %**	**Availability H_2 %**
2019	500	25.1	43
2020	250	44.5	42.4
2021	560	49.1	39.4
2022	850	46.4	41.9

Table E2: Reliability for mature technology production. (Idun 1a is shortened to I1a and Ägir 1 is Ä1 etc. (*) Indicates if the plant is operating on 90% of maximum output.)

State	**Operation**	**Off**	**Probability DH ζ (%)**	**Probability H_2 ζ (%)**
1	I2a,Ä1	None	45	23.86
2	I2a*,Ä1	None	0	16.79
3	I2a	Ä1	52.09	33.05
4	I2a*	Ä1	0	23.27
5	Ä1	I2a	1.27	1.35
6	None	Ä1,I2a	1.56	1.73

Table E3: Reliability for all technologies Hydrogen production.

State	Operation	Off	Probability DH ζ (%)	Probability H_2 ζ (%)
1	I1a,I1b,I2a,Ä1	None	44.17	11.41
2	I1a,I1b,I2a	Ä1	51.13	15.80
3	I1a,I2a,Ä1	I1b	0.38	10.19
4	I1a,I2a	I1b,Ä1	4.4	14.12
5	I1a,I1b,Ä1	I2a	13.2	6.1
6	I1a,I1b	I2a,Ä1	1.53	8.4
7	I1a,Ä1	I2a,I1b	0.01	0.54
8	I1a	I2a,I1b,Ä1	0.01	0.75
9	I2a,I1b,Ä1	I1a	4.21	1.19
10	I1b,I2a	Ä1,I1a	4.88	1.65
11	I2a,Ä1	I1a,I1b	0.04	6.54
12	I2a	I1a,I1b,Ä1	1.48	1.48
13	I1b,Ä1	I1a,I2a	0.06	0.06
14	I1b	Ä1,I1a,I2a	0.13	1.48
15	Ä1	I1a,I1b,I2a	0	0.06
16	None	Ä1,I1a,I1b,I2a	0	0.08
17	I1a,I1b,I2a*,Ä1	None	0	8.03
18	I1a,I1b,I2a*	Ä1	0	11.12
19	I1a,I2a*,Ä1	I1b	0	7.17
20	I1a,I2a*	I1b,Ä1	0	9.94
21	I2a*,I1b,Ä1	I1a	0	0.084
22	I1b,I2a*	Ä1,I1a	0	1.16
23	I2a*,Ä1	I1a,I1b	0	6.54
24	I2a*	I1a,I1b,Ä1	0	1.04

1.0.2 Benchmark sensitivity diagrams

Sensitivity analysis and benchmark of the different operations are presented in Figure E1 and E2.

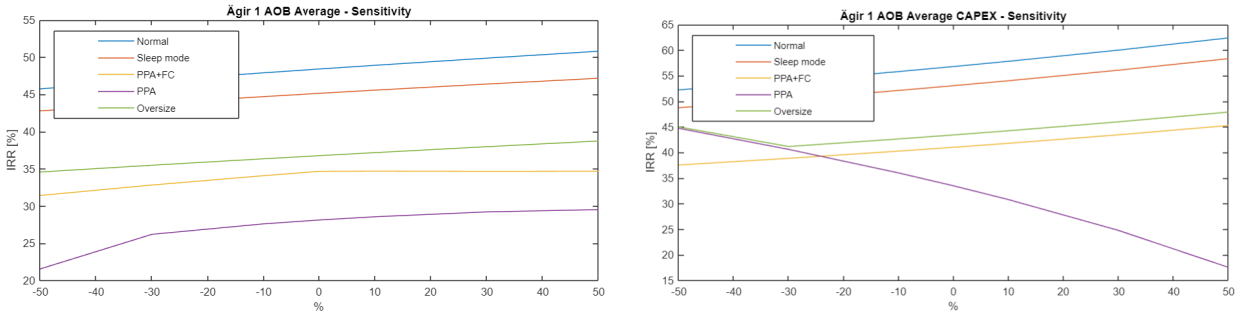

Figure E1: Sensitivity analysis of operations mode related to Ägir 1, presenting the Alternative Operation Benchmark for income variables in the left, respectively subsidies to the right.

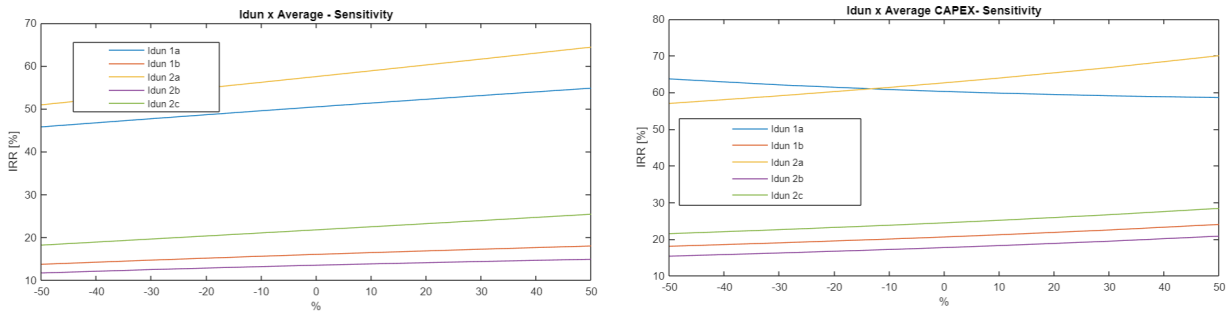

Figure E2: Sensitivity analysis of the gasifier plants, presenting the Benchmark for income variables in the left, respectively subsidies to the right.